Luminescent Composites of Hydroxyapatite Nanoparticles for Theranostic Applications

A Thesis

Submitted in Partial Fulfilment of the Requirements

for the Award of the Degree of

Doctor of Philosophy

by

Anitha T Simon

To

Indian Institute of Technology Guwahati

Centre for Nanotechnology

Indian Institute of Technology Guwahati

Guwahati-781039, Assam, India

January-2022

DECLARATION

I hereby declare that the research work embodied in the thesis entitled "**Luminescent Composites of Hydroxyapatite Nanoparticles for Theranostic Applications**" is the outcome of work carried out by me under the supervision of **Prof. Siddhartha Sankar Ghosh** and **Prof. Arun Chattopadhyay**, **Centre for Nanotechnology, Indian Institute of Technology Guwahati, Assam**, for the award of the degree of Doctor of Philosophy. To the best of my knowledge and belief, the current thesis has not been submitted for any degree, diploma, associateship etc. of any institute or university elsewhere.

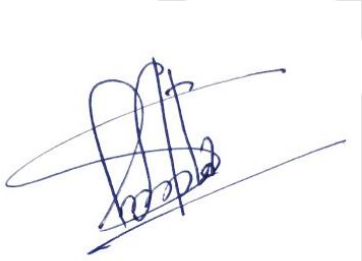

Anitha T Simon (166153005)

Centre for Nanotechnology

Indian Institute of Technology Guwahati

Guwahati-781039

Assam

India

January, 2022
Guwahati

Indian Institute of Technology Guwahati

CERTIFICATE

This is to certify that the thesis entitled "**Luminescent Composites of Hydroxyapatite Nanoparticles for Theranostic Applications",** being submitted to the **Indian Institute of Technology Guwahati** by ***Anitha T Simon*** (Roll No: **166153005**) for the award of the degree of **Doctor of Philosophy** in ***Nanotechnology*** is a bonafide record of research work carried out by her. The information and the data reported by her are solely the results of her original findings. She has meticulously carried out the investigations and followed the guidelines of the laboratory. This work has not been submitted elsewhere for any degree or diploma.

Dr. Siddhartha Sankar Ghosh
Professor
Department of Biosciences and Bioengineering
Indian Institute of Technology Guwahati
Guwahati-781039, Assam, India

Prof. Arun Chattopadhyay
Department of Chemistry
Indian Institute of Technology Guwahati
Guwahati-781 039, INDIA

Prof. Siddhartha Sankar Ghosh
Thesis Supervisor
Department of Biosciences and Bioengineering
Indian Institute of Technology Guwahati
Guwahati-781039, Assam, India

Prof. Arun Chattopadhyay
Thesis Supervisor
Department of Chemistry
Indian Institute of Technology Guwahati
Guwahati-781039, Assam, India

Dedicated to:

All the amazing people who gave me the reason to be hopeful

ACKNOWLEDGEMENT

First and foremost, I thank Christ Jesus my LORD, for this gift of life, His exceedingly abundant grace and immutable faithfulness throughout my life until now and for the days to come.

I extend my sincere gratitude to Prof. Siddhartha Sankar Ghosh and Prof. Arun Chattopadhyay, for giving me the opportunity to learn, work and improve in the field of research as a member of their research family. I am grateful for their mentorship, support and essential drive imparted to me each time, which I believe will always remain valuable in the future. Their constructive concerns, spark in executing new ideas and considerate nature have always been the admirable qualities, I looked up to.

I would like to thank my doctoral committee members: Prof. Lal Mohan Kundu (Chairman), Prof. Tapas Kumar Mandal and Dr. Sunanda Chatterjee for periodically evaluating my thesis work and providing me their necessary inputs.

I want to express my gratitude to Centre for Excellence in Nanoelectronics and Theranostic Devices, Central Instrumentation Facilities, Centre for Nanotechnology, Centre for Excellence DBT Programme Support Biosciences and Bioengineering, and Department of Chemistry for supporting, meeting the essential requirements and providing me all the facilities to pursue my thesis work.

I am enormously indebted to Dr. Deepanjalee Dutta, for guiding me right from the very beginning and helping me understand the critical areas of research, which have been always an inspiration to keep myself moving ahead. Also, I sincerely acknowledge Dr. Sunil Kumar Sailapu, who has also invested his valuable time in sharing his experience and knowledge whenever I approached.

I am thankful to all my seniors: Dr. Upashi Goswami, Dr. Madhumita Das, Dr. Bandhan Chatterjee, Dr. Tamanna Bhuyan, Dr. Neha Arora, Dr. Anil Bidkar and Dr. Srirupa Bhattacharyya, for their timely help and contributions in my learning experience. Also, I want to thank all my previous seniors, who have enormously worked hard to pass on the research environment, so that their subsequent juniors including me, could continue gaining the wonderful experiences of research world.

I am grateful to all my previous, present lab mates and batch mates: Kasturi, Mihir, Dr. Surjendu and Rajib, for gifting me beautiful memories as friends, and helping me learn more as research fellows. I want to thank all my juniors: Debashree, Arupam, Konika, Muktashree, Plaboni, Sayantani, Hirak, Thirukumaran, Soundaram, Shilpi, Sawna and Arisha, for all the wonderful moments shared, as students and friends. We could not only help, but also learn from each other whenever we had our time together.

This journey is quite incomplete without my friends Raji, Pradeep, Jaswant, Purnima, Feba and Christeena who cheered me up, supported me always standing by my side. Each and every moment we had, were really refreshing and would always be cherished in the days to come.

I would have never been "I am", without my precious **family**. Papa and mummy for raising me up with unconditional love, admonishing and teaching the valuable principles of life, dreaming big about me than I myself did and giving me all the required provisions pertaining to personal and professional life. Daddy and mummy, the two incredible souls equivalent to my parents, for hugely caring and encouraging me to pursue my interests of life.

My **husband** (Roy Jones), who promised a wonderful journey with me, for inspiring me with reality of life, uplifting me when I failed and assuring me his unflinching support in my career and life.

My lovely siblings: Feba, Priscilla and Glenson for making my life more interesting with love, fun and knowledge.

I deeply acknowledge the beautiful campus of IIT Guwahati, for gifting me all the amazing memories during the stay of my research journey.

TABLE OF CONTENTS

ABSTRACT

The enormous advancements in pharmaceutical science have been accredited to the nanoscience and technology for improved clinical translation. The improvisations in diagnosis and therapy could be attained through engineered nanomaterials, which were mainly applied as drug delivery vehicles for curative approach. Nanomaterials from inorganic sources owing to their supramolecular structures and physiochemical properties facilitate intended therapeutic functions. Having unique properties, they have been reviewed as multifunctional system by integrating various components involving therapeutic and imaging moieties. A wide range of suitable inorganic nanocarriers have aided in delivering insoluble drugs to the desired sites, through the influence of intracellular microenvironment in a controlled manner. Biocompatible inorganic nanocarriers, modified to accumulate high amount of therapeutic molecules are known to bypass multidrug resistance with less efflux, through their unique composition. In cancer therapy, inorganic nanocarriers are fabricated for passive targeting by making use of EPR (enhanced permeation and retention effect) phenomenon, exhibited by leaky vasculature character of malignant tumours. In addition to internal stimuli like pH and redox conditions, external stimuli based therapy is another approach used for bacterial or cancer therapy, which is featured through inorganic nanocarriers. External stimuli like light, temperature and magnetic field will not only trigger the drug release from such nanocarriers, but also enhance the therapeutic efficiency through combinatorial effect, in conjugation with drug based therapy. Inorganic nanocarriers due to their ease of functionalization host various luminescent probes such as organic fluorophores, quantum dots, metallic nanoclusters and lanthanides, enabling the imaging of desired sites in addition to therapy.

The current thesis mainly focuses on a bioinspired inorganic source such as hydroxyapatite, whose composition resembles to that of human hard tissues, and its development into drug delivery nanocarriers. Having high adsorption property, the nanocarriers were loaded with small drug molecules and evaluated for *in vitro* bacterial and cancer cell treatment. Both mono- and combined therapeutic approaches were investigated, alongside bioimaging with the help of incorporated luminescent nanoclusters.

Chapter 1 is the introduction section of the thesis, which focuses on the progressive advancement of nanotechnology through the development of various multifunctional nanocarriers in the recent past. The chapter covers different classes of nanomaterials from resources belonging to both organic and inorganic materials. Synthesis methodologies, which

influence the tailoring of desired physiochemical properties of a nanocarrier have been discussed. Importantly, inorganic nanocarriers based on hydroxyapatite have been presented along with the possibility of exploring them as therapeutic and imaging system. Furthermore, importance of metallic nanoclusters with their luminescence and therapeutic property has been discussed, that give an insight to the potency of nanosystem in biological field. The chapter discusses widely of the antibacterial and theranostic characteristics exhibited by various drug delivery nanosystems. Finally, scopes and salient features of the entire thesis have been summarized.

Chapter 2 emphasizes on the synthesis and characterisations of hydroxyapatite nanoparticles, doped with copper nanoclusters. The copper nanocluster doped hydroxyapatite nanoparticles were loaded with antibacterial drug namely kanamycin for applying towards antibacterial and antibiofilm applications. The nanoformulation exhibited a drug release in biphasic pattern with an initial burst release, followed by a sustained profile. The copper nanocluster doped hydroxyapatite nanoparticles loaded with kanamycin were found to be active against Gram negative bacteria. Upon interacting with bacteria, the released drug molecules inhibited the bacterial growth, with subsequent cell damage, mostly due to generation of highly reactive form of oxygen. Furthermore, the drug loaded entity was analysed for eradication of biofilms formed by *Pseudomonas aeruginosa*. The entire nanoformulation was suggested to be highly effective in inhibiting the biofilm formation through the release of loaded kanamycin. Additionally, the biocompatibility of copper nanocluster doped hydroxyapatite nanoparticles was confirmed through cell viability assay in HeLa cells. The study suggested the cells to be viable even at higher concentration of copper ions in copper nanocluster doped hydroxyapatite nanoparticles. Moreover, the presence of copper nanoclusters conferred luminescence property to the entire nanocarrier, qualifying them to be a suitable bioimaging entity in bacterial cells.

Chapter 3 presents studies on copper nanocluster doped hydroxyapatite nanoparticles for cancer theranostics. An anticancer flavonoid drug namely quercetin, was loaded into copper nanocluster doped hydroxyapatite nanoparticles and analysed for anti-cell proliferative effects on monolayer culture and tumor spheroids of HeLa cells (cancer cells). A pH dependent drug release profile was observed with maximum release observed at acidic pH. The drug loaded nanocarrier was effectively uptaken by the cancer cells and localized within lysosomal compartments. A significant reduction of cell viability of cancer cells was observed in comparison to unloaded nanocarrier and free drug. The quercetin loaded nanocarrier triggered formation of reactive oxygen species, disrupted the cell cycle pattern with concomitant

induction of apoptosis mediated cell death in treated cancer cells. Also, the cell viability alteration was morphologically evident through the deformation and disruption of cell membrane. However, HEK-293 (normal cells) were viable under similar treated conditions. The drug loaded copper nanocluster doped hydroxyapatite nanoparticles were effective in disrupting and inhibiting the proliferation of tumour spheroids, by releasing the loaded anticancer drug towards their interior. Additionally, the luminescence property inherited through copper nanoclusters enabled intracellular tracking of nanocarrier distribution, suggesting potential use of copper nanocluster doped hydroxyapatite nanoparticles in cancer cell imaging.

Chapter 4 highlights on the combinatorial therapeutic effect implemented through copper nanocluster doped hydroxyapatite nanoparticles through co-delivery approach. The nanoformulation was encapsulated with norfloxacin (NX) and a photosensitizer methylene blue (MB). The nanocarrier carrying two therapeutic molecules was evaluated for combined therapy, conjugating chemotherapy and photodynamic therapy (PDT) on bacteria and cancer cells. A pH driven release profile was observed in case of both NX and MB from copper nanocluster doped hydroxyapatite nanoparticles. In terms of application, the antibacterial therapy with PDT effectively reduced the colonies of Gram negative bacteria in comparison to individual treatments. Further, NX and MB loaded nanocarrier in conjugation with PDT reduced cell viability of HeLa and MCF-7 (cancer cells) significantly at lower doses of drug and photosensitizer. The combined therapy generated reactive oxygen species and altered cell cycle pattern. Significant shrinking, deformation and apoptosis of cancer cells were observed.

Chapter 5 summarizes the major objectives and essential findings reported in the current dissertation. The promising possibilities of hydroxyapatite based nanoparticles as therapeutic and imaging entity have been discussed. The future prospects of the present drug delivery system include monitoring treatment of implant related infections, active targeting for specified therapy, tissue engineering applications and *in vivo* studies. With further understanding of detailed underlying molecular mechanisms of action, hydroxyapatite-based nanomaterials can be used as a suitable platform for future nanomedicine.

Abbreviations

AFM: Atomic force microscopy

AO: Acridine orange

BHI: Brain heart infusion

BSA: Bovine serum albumin

CFU: Colony forming unit

CTAB: Cetyltrimethylammonium bromide

Cu NCs: Copper nanoclusters

DCF: Dichlorofluorescein

DCFH-DA: 2,7-Dichlorofluoresceindiacetate

DMEM: Dulbecco's modified Eagle medium

DMSO: Dimethyl sulfoxide

DPBF: 1,3-Diphenylizobenzofuran

EDTA: Ethylenediamine tetraacetic acid

EDX: Energy-dispersive X-ray

EPR: Enhanced permeation and retention effect

FDA: Food and drug administration

FESEM: Field emission scanning electron microscopy

FQ: Fluoroquinolones

GFP: Green fluorescent protein

HAP NPs: Hydroxyapatite nanoparticles

HEK-293: Human embryonic kidney-293

HeLa: Human cervical carcinoma

HER2: Human epidermal growth factor receptor 2

HRTEM: High resolution transmission electron microscopy

HSA: Human serum albumin

LC-MS: Liquid chromatography-mass spectrometry

LUVs: Large unilmamellar vesicles

MB: Methylene blue

MBC: Minimum bactericidal concentration

$MBIC_{50}$: Minimum biofilm inhibition concentration

MCF-7: Human breast cancer

MDR: Multidrug resistance

MIC: Minimum inhibitory concentration

MLVs: Multilamellar vesicles

MTT: 3-(4,5-Dimethylthiazol 2-yl)-2,5-diphenyltetrazolium bromide

NB: Nutrient broth

NCCS: National Centre for Cell Sciences

NSET: Nanoparticle surface energy transfer

NX: Norfloxacin

OD: Optical density

PBS: Phosphate-buffered saline

PDT: Photodynamic therapy

PEG: Polyethylene glycol

PI: Propidium iodide

PTT: Photothermal therapy

PVA: Polyvinyl alcohol

ROS: Reactive oxygen species

SAED: Selected area electron diffraction

SEDDS: Self-emulsifying drug delivery systems

STM: Scanning tunnelling microscopy

SUVs: Small unilamellar vesicles

TEM: Transmission electron microscopy

TNBS: 2,4,6-Trinitrobenzene-1-sulfonic acid

TRPL: Time-resolved photoluminescence

Chapter 1

Introduction

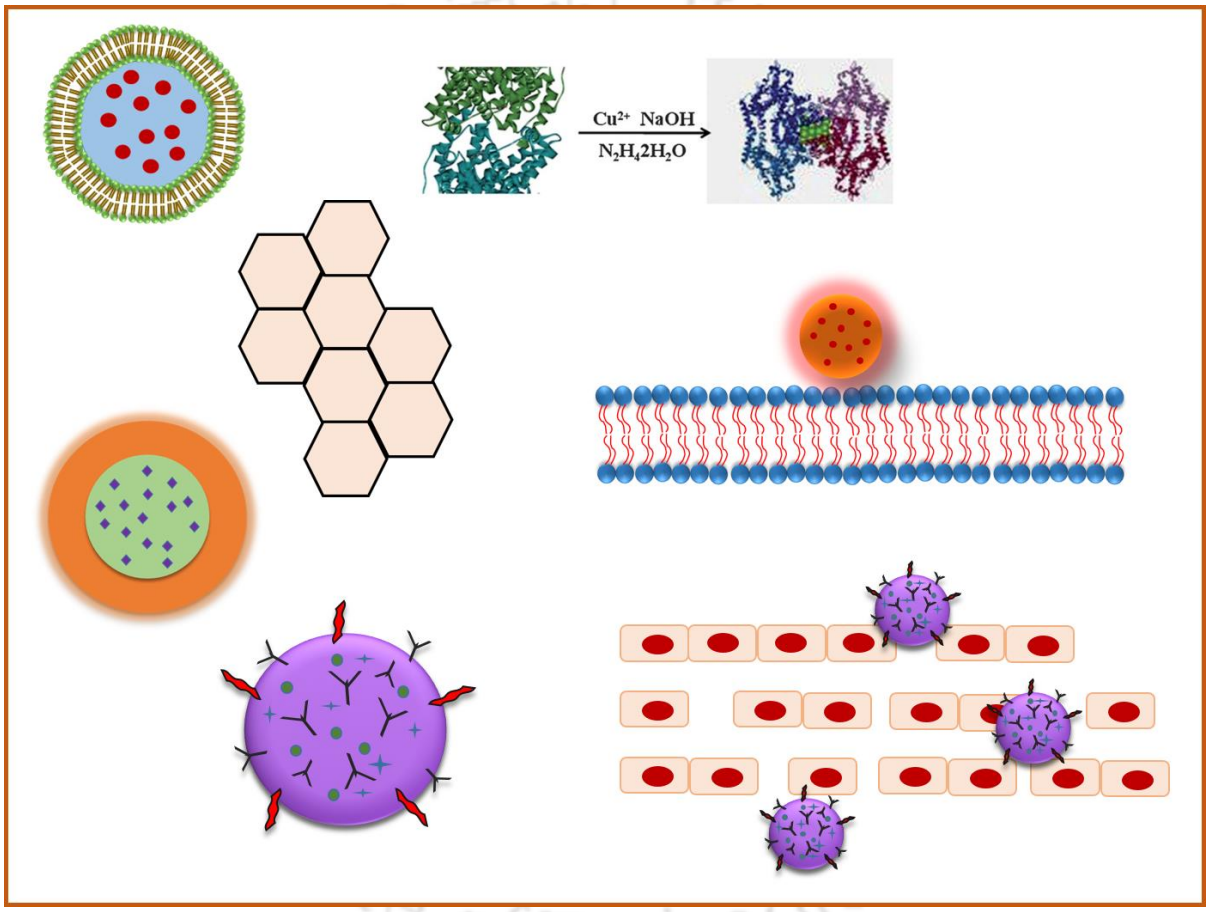

Chapter 1

1.1. Introduction

Nanotechnology is defined as "the understanding and control of matter at dimensions between approximately 1 and 100 nanometers, where unique phenomena enable novel applications" (National Science and Technology Council, 2011).[1] In chemistry, the size range can be related to micelles, polymers, colloids, most recently developed buckytubes, semiconductor based quantum dots and silicon nanorods. The interpretation of nanometre dimension in physics and electrical engineering can be in terms of behavioural patterns of photons, electrons and quantum properties. Biological sciences render the depiction of nanosized materials, which comprise of cellular components including DNA, sub cellular organelles, viruses, flagellar micromotor and intercellular channels. The concept of nanotechnology was introduced by Richard Feynman, and Norio Taniguchi in the year 1974, who advocated nanotechnology as an event of "processing, separation, consolidation and deformation of material by one atom or one molecule".[2,3] The technology covers cluster of fields such as chemistry, physics, biology, principles and tools of engineering and material science, resulting in construction, integration and implementation of nanoscale structure. The intrinsic surface property at the nanoscale differs from bulk form of a material, leading to potential multidisciplinary applications in electronics, computing, communication, manufacturing, energy, environment and life sciences.[4] A timeline representing stepwise advancement of nanotechnology is shown in **Figure 1.1**

With invention of scanning tunnelling microscopy (STM) and atomic force microscopy (AFM) in 1980s, the detailed atomic level studies and development of fabricated structures by manipulation of atoms have been made possible. By exerting an interest in understanding the surface effect, tension, molecular level assembly, innovative exploitations have been taking place to create devices, systems and structures with improvised properties. The golden period of nanotechnology was commenced upon with the discovery of fullerenes by Kroto, Smalley and Curl, followed by development of carbon nanotubes.[5,6] According to initiative of U.S nanotechnology, the nanoscale products can be categorized to be accommodated under four generations. The first generation comprises of passive nanostructures such as nanoparticles and nanosized materials. The second generation holds active nanostructures like targeted drug molecules and actuators.

Third generation contains 3-D nanosystem and systems of nanosystems, generated by synthesis and assembling events. Finally, fourth generation nanostructures are heterogeneous molecular systems, aiming for fundamentally novel approaches.[7]

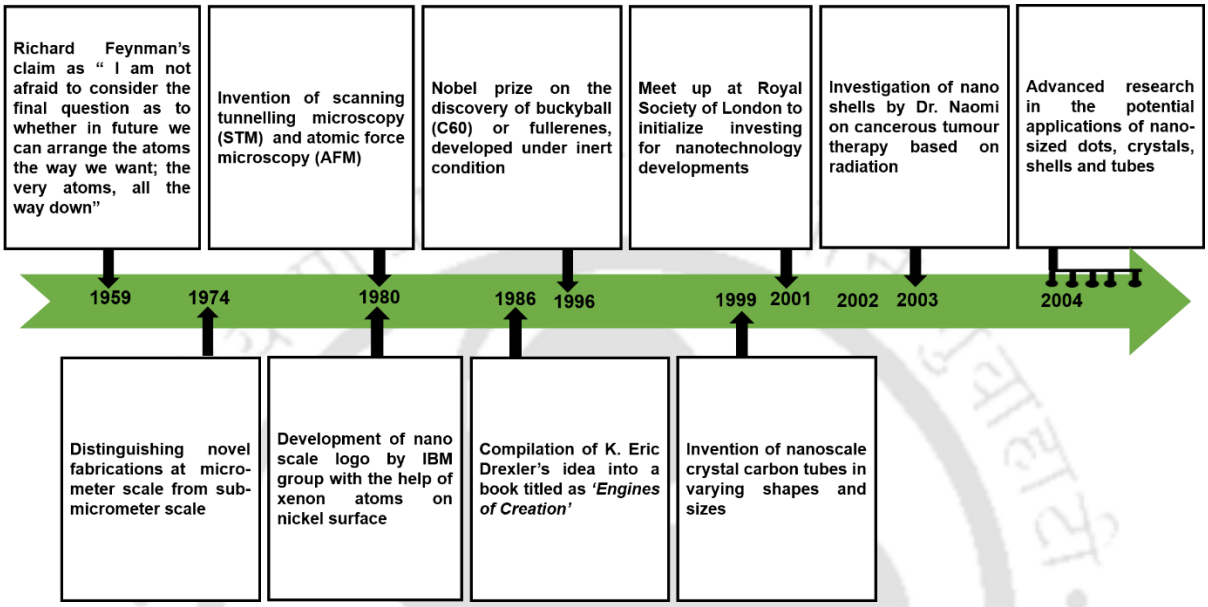

Figure 1.1. A time line illustration of nanoscience developments. Conceptualized and redrawn (reference 5).

In his visionary talk, Feynman laid out the opportunities of molecular level work, visualization and rearrangement of individual atoms and molecules, along with the possible challenges in the field and emphasised fabrication approaches in nanotechnology. Top down and bottom approach are the two fundamental fabrication methods, encompassed by nanotechnology. In top down approach, the larger sized or bulk materials are reduced to nanoscale by applying chemical, mechanical or any energy form. The materials come down to nanoscale with the retention of their original properties, without any alteration in their atomic level. Top down approach mainly uses devices and techniques such as milling, nanolithography, mechanical alloying and shaving, that can generate nanoparticles from mass, which are larger in size. In this approach, nanodevices or patterned nanostructures have been fabricated by etching on semiconductors, thereby accelerating the microelectronics industry. Bottom up approach is widely considered to be an important domain of nanoscience and nanotechnology, which begins with an atom or molecules.

It is a promising and possible strategy to develop two dimensional or three dimensional nanoscale structures, by the exploration of interaction between colloidal particles or molecules. A few of the techniques involved in bottom up approach are desolvation or sedimentation method, chemical vapour deposition process, laser pyrolysis, metal organic decomposition, sol gel, self-assembly and wet synthesis.[8-10] These fabrication approaches, high resolution microscopy, microfluidics and lab on a chip technology enable the exploration and engineering of materials, that yield quantum dots, nanoclusters, nanoparticles, nanorods, nanotubes, nanosheets, nanocarriers, nanocapsules, nanosensors, nanoemulsions and nanodevices. They foster higher impact of advancement in medical, agricultural, environmental, food, cosmetics and electronic applications. Importantly, these resultant products are widely explored as imaging, sensing, tissue engineering, gene and drug delivery means in the area of medical diagnostics.[11, 12]

1.2. Nanoparticles in Drug Delivery

Usage of novel drug delivery system in nanotechnology has altered the prospect of biotechnology and pharmaceutical industries for anticipated future. In 1960s, lipid vesicles later known to be liposomes were considered as the primary drug delivery system in the field. There are major objectives, that can bring an upgraded armamentarium of medical therapeutics through these drug delivery systems. One of them is enhancement in the delivery of sparingly water soluble drugs. Researchers have presented various formulation methodologies to circumvent the issue of delivering poor water soluble drugs among which, self-emulsifying drug delivery systems (SEDDS) are prominent. Such systems are developed by the optimization of suitable lipid mixtures with different emulsifiers for respective drugs. Other approaches such as usage of polymeric micelles, hydrogel, mesoporous carbon silica, various other organic and inorganic based drug delivery systems are also highlighted.[13-15] All these various nanosized formulations are commonly termed as nanoparticles. Interestingly, in comparison to larger-sized particles, the uptake of such nanoparticles by cells is found to be more effective and thus, they are highly preferred in drug delivery applications. Another objective for drug delivery system is to achieve cell or tissue specific targeted drug delivery. Nanocarriers conjugated with ligands or moieties such as peptides, oligonucleotides and antibodies can be directed to the specific cells or tissues, which reduce side effects and enhance

therapeutic efficacy. Non-specific uptake by cells, reduced cellular toxicity as well as long term circulation can be obtained by linking the nanocarrier with compounds like polyethylene glycol. One such example is the development of Doxil, which is a liposome, formulated with PEGylation, that resulted in analogous output in terms of therapy and decreased cardiotoxicity.[16, 17] Nanocarriers can be manipulated for appreciable drug transcytosis through intact endothelial and epithelial barrier. Efforts have also been put forth in implementation of combinatorial therapy through delivery of multiple drugs at the same time. Co-administration of multiple drugs for therapies such as anticancer and antibacterial can aid in overcoming multidrug resistance (MDR), enhanced therapeutic efficacy, alongside tracking the site of drug distribution by linking imaging entities. They can also help in real time monitoring of therapeutic efficiency *in vivo* and bioavailability for longer duration. Based on various physicochemical properties, nanocarriers can be classified into various types (**Figure 1.2)**

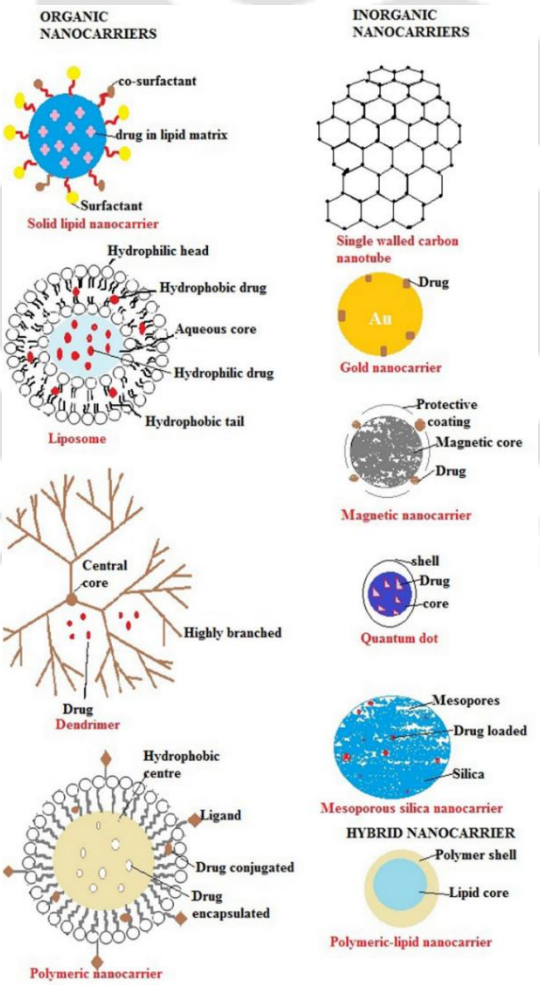

Figure 1.2. A few examples of nanocarriers used in drug delivery. Reprinted by permission from Springer Nature (reference 15), copyright 2018.

1.2.1. Organic Nanocarriers

Most of the organic nanocarriers are carbon based, which accommodate drug molecules within their matrix and are characterized by biocompatible nature. A few of the organic nanocarriers are briefly described below.

Liposomes

The potency of liposomes as drug delivery vehicles was acknowledged for various pharmaceutical applications in broader range. They are mainly spherical systems with a size range of 0.05-5.0 µM, having an aqueous core with outer shell of one or more bilayer lipid configuration. They have been widely investigated for delivering genetic materials, antineoplastic, antimicrobial drug molecules and steroids. Depending on the number of lamellae and size, liposomes are classified into multilamellar vesicles (MLVs), large unilamellar vesicles (LUVs) and small unilamellar vesicles (SUVs). The composition of liposome comprises of either natural or synthetic lipids. The natural lipids utilized for the synthesis of liposomes include phospholipids, sphingolipids and sterols, whereas synthetic lipids include phosphatidylethanolamines, phosphatidylcholines and phosphatidylglycerols. Various synthesis methods such as injection method, dehydration-rehydration method, freeze-thaw method and reverse-phase evaporation method are opted for development of liposomes. Various reports have suggested liposomes to be having increased pharmacokinetic properties, improved cellular uptake, effective penetration property, selective cytotoxic effect, suitable immune response and appreciable immunity against the pathogenic antigens.[18,19]

Dendrimers

Having a branched structure, they are chemically versatile, whose physical or chemical properties can be manipulated by altering the core, branches and functional units. They can be synthesized from sugar molecules, amino acids or nucleotides in a serial manner with the inclusion of extended branches as per requirements. Studies have been documented, where anti-tuberculosis or anticancer drug molecules are entrapped within their interior through covalent or non-covalent interactions. Interestingly, dendrimers are considered as suitable templates for synthesis of various metallic, bimetallic or other inorganic nanoparticles, also stabilize the metal ions in their core, by sequestering them via suitable interactions with their

functional groups. Dendrimers have been surface modified to reduce their surface charge, resulting them to be less toxic and have been linked with targeting ligands or probes for therapy and imaging in biological applications.[20,21]

Polymeric nanocarriers

Polymeric nanocarriers or soft nanocarriers are usually understood to have a core-shell configuration. The core might be made up of components such as catalyst, metals, proteins or peptides and therapeutic ingredients, surrounded by biodegradable polymeric shell. The polymers mostly used are the naturally occurring chitosan, albumin, alginate and collagen or the synthetically derived polyethylene glycol, poly (lactic-co-glycolic acid) and polycaprolactone. They are studied as promising cargos for drugs, which can traverse through the blood stream to desired location within the biological system. Polymeric nanocarriers are also greatly explored for loading hydrophobic molecules. With reduced renal clearance, most of them show stealth property. By modifying their physiochemical property, they are found to have reduced protein adsorption and improved accumulation in the compromised sites.[22, 23]

Micelles

Micelles are mostly amphiphilic molecules with a hydrophilic exterior and hydrophobic interior. Factors such as temperature, pH range and ionic strength play major roles in defining and controlling the morphology and dimension of micellar nanoparticles. The hydrophobic interior encapsulates the sparingly water soluble drugs, whereas the hydrophilic exterior protects the entrapped molecules from the external environment and reduces opsonisation. Micelles are known to be engineered by coupling with various targeting moieties for active targeting and they are considered as suitable drug delivery vehicles for cancer therapy. [24, 25]

1.2.2. Inorganic Nanocarriers

Due to tuneable surface chemistry, larger surface to volume ratio, distinguished size and shape, flexible optical properties or magnetic properties and biological functionalities, development of inorganic nanocarriers has been revealed to be the upgraded strategical headway in the field of nanomedicine. A few examples of inorganic nanocarriers have been briefly discussed below.

Metallic based nanocarriers

In comparison to their bulk counterparts, the nanosized metallic particles emerge themselves as the excellent candidates in clinical applications. Some of the metallic nanocarriers include iron oxide nanoparticles, gold nanoparticles, silver nanoparticles, copper nanoparticles and zinc nanoparticles. Most among them are inert by nature and possess desirable mechanical properties. Oxide forms of certain metallic nanoparticles such as iron inherit superparamagnetic features, providing magnetic field induced signals, qualifying them to be used for magnetic resonance imaging. Iron oxide nanoparticles are applied for drug delivery applications, where one of the studies suggested their fabrication with gemcitabine and usage for osteosarcoma cells. They are known to generate hyperthermia for treatment of various tumours and their different formulations are known to treat iron depletion.[26, 27]

Based on numerous studies conducted, gold nanoparticles have been demonstrated to favour enhanced permeation and retention effect (EPR), multi-functionalization and possess photophysical characteristics, including surface plasmon. Fabrication of gold nanoparticles has been carried out by conjugating with suitable functional moieties and thiol linkers on their surface. They are also engineered to be of different shapes (rods, wires and cubes) and suitable size range between 1 to 200 nm, which are found to be uptaken by cells through pathways such as receptor mediated endocytosis and known to cause size and concentration based cytotoxicity. Gold nanoparticles are investigated for release of small molecules, antibodies, hydrophobic drugs, diatomic therapeutic agents like nitric oxide, large biomolecules such as nucleic acid, peptides and proteins. Additionally, they are understood to cause thermal ablation of cancer cells via external light source, which also could control the drug release in the desired tumour sites.[28, 29]

Having notable surface plasmon phenomenon, surface reactivity and larger surface area, silver nanoparticles have been extensively studied for their application in cosmetics, fabrics industry and biomedical devices. Silver nanoparticles are good antibacterial agents and they have been engineered to form composite systems with chitosan, hydrogel and alginate for drug delivery. Silver nanoparticles have been synthesised chemically as well as from natural sources such as plant extracts. Silver nanoparticle based drug delivery platforms have been observed to offer photothermal, chemical, pH and redox induced drug release intracellularly.

An interesting phenomenon termed as nanoparticle surface energy transfer (NSET), where the fluorescence of conjugated drug is quenched by the nanoparticles, was studied recently in camptothecin linked silver nanoparticles, for controlled drug release.[30, 31]

Similar to silver nanoparticles, copper and zinc nanoparticles have been documented to have prospective applications in the field of medicine, sensing, optics and devices. Researchers have explored biological, chemical and physical methods for synthesis of both copper and zinc nanoparticles. The antimicrobial property of copper nanoparticles has been widely studied in bacteria and fungi. Copper nanoparticles have also been found useful in photoacoustic tomography and molecular imaging in deeper tissue regions. Zinc based nanocarriers have been employed for drug delivery application in antibacterial and antitumor therapy with excellent reactive oxygen species (ROS) generation property. Having excellent ultraviolet (UV) rays capturing ability, they are incorporated in sunscreens and other dermatological products. Both copper and zinc are comparatively cost effective and they are developed to be biocompatible, environment friendly and thus approved by food and drug administration (FDA).[32, 33]

Non-metallic based nanocarriers

Among the broader range of inorganic non-metallic groups, a few of the notable drug delivery nanocarriers are silica based and calcium phosphate based systems. Silica based nanocarriers bestow excellent porosity, biodegradability and larger surface area. Through suitable dry or wet methods such as gas phase decomposition, sol-gel, vapour deposition and chemical precipitation, this amorphous and eco-friendly material is developed to desired nanosystem for numerous research purpose such as biosensing, bio-catalysis, optics and drug delivery. Among solid and mesoporous silica nanoparticles studied, mesoporous formulation had been able to circumvent the various limitations of solid formulation with respect to loading of drug, functionalization and porosity. Mesoporous silica nanoparticles are understood to exhibit crucial merits in enzyme immobilization, bioimaging, intracellular targeting for various disease conditions with appreciable biodistribution and minimal side effects.[34, 35].

One of the booming fields emerged in the expanse of nanomedicine is the calcium phosphate based pharmacotherapy. Calcium and phosphate, being found in the human body as inorganic minerals have close similarity with the compositions of hard tissues such as teeth and

bone. Due to excellent biocompatibility and their degradability to non- hazardous Ca^{2+} and PO_4^{3-} ions that can further involve in human body metabolism, synthetic calcium phosphate has been qualified of their usage in biomedical research. The presence of active ions on their surface promotes electrostatic interaction, which favours the adsorption of drug molecules into their surface. At a lower pH, the solubility of calcium phosphate nanocarriers is enhanced, which aids in pH triggered release of loaded drug.[36, 37] Various advantages of calcium phosphate nanocarrier are shown in **Figure 1.3**

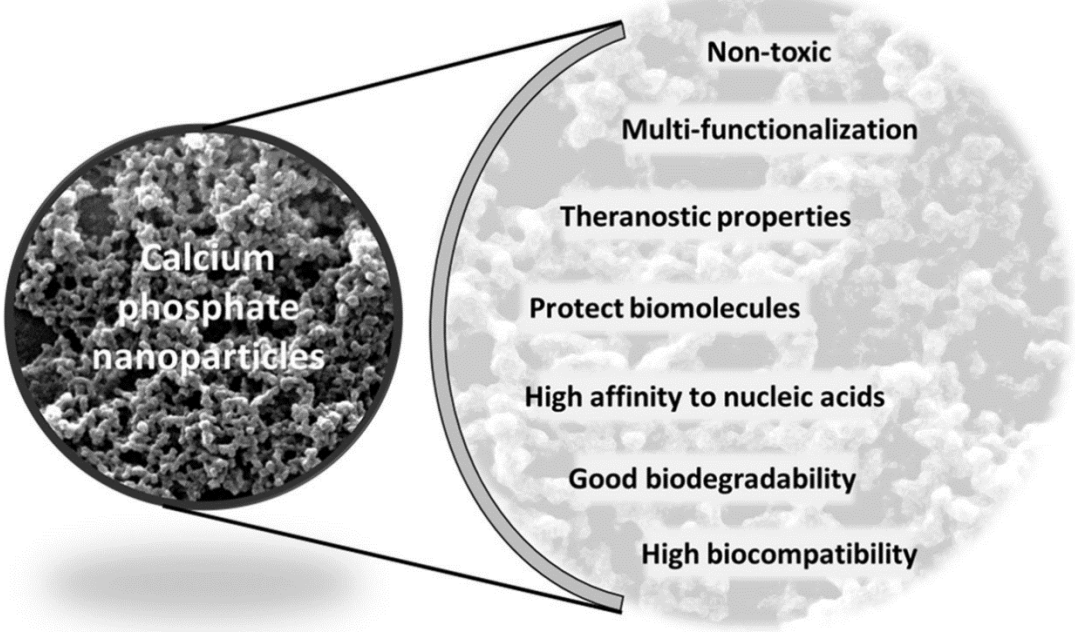

Figure 1.3. Properties of calcium phosphate nanoparticles showing their potential to be used as drug delivery vehicle. Reprinted by permission from John Wiley and Sons (reference 37), copyright 2021.

It is to be noted that, based on the state of protonation and ionic substitution of cations or anions, calcium phosphate exists in different phases. They include amorphous calcium phosphate, mono-hydrate and anhydrate form of mono-calcium phosphate, di-hydrate and anhydrate form of di-calcium phosphate, octa-calcium phosphate, tetra-calcium phosphate and hydroxyapatite. One of the most known phases of calcium phosphate is "hydroxyapatite", which is the nanocrystal form prevalent in mammalian hard tissues, making them stable, intact and functional. Having great bioresorbability and bioactivity, hydroxyapatite based nanomaterials have paved a way in biological fields such as regenerative medicine and nanomedicine as drug delivery vehicle.[38, 39]

Hydroxyapatite-based nanocarrier

Hydroxyapatite ($Ca_{10}(PO_4)_6(OH)_2$) is one of the most thermodynamically stable crystalline form of calcium phosphates in human body. As compared to bulk counterparts, nanophase hydroxyapatite acquires higher surface to volume ratio, biomimetic characteristics, biocompatibility, non-inflammatory and appreciable adsorption properties. These inherent properties have qualified nanosized hydroxyapatite for anti-bacterial, anti-cancerous, antioxidant and anti-inflammatory studies. Various methods have been proposed for synthesis of hydroxyapatite nanoparticles, which have improved the desired properties of the system, satisfying clinical demands. A few methods include hydrothermal techniques, sol-gel method, ultrasound microwave directed, and wet chemical or precipitation synthesis other than availing hydroxyapatite nanoparticles from natural resources or through green synthesis[40] (**Figure 1.4)**

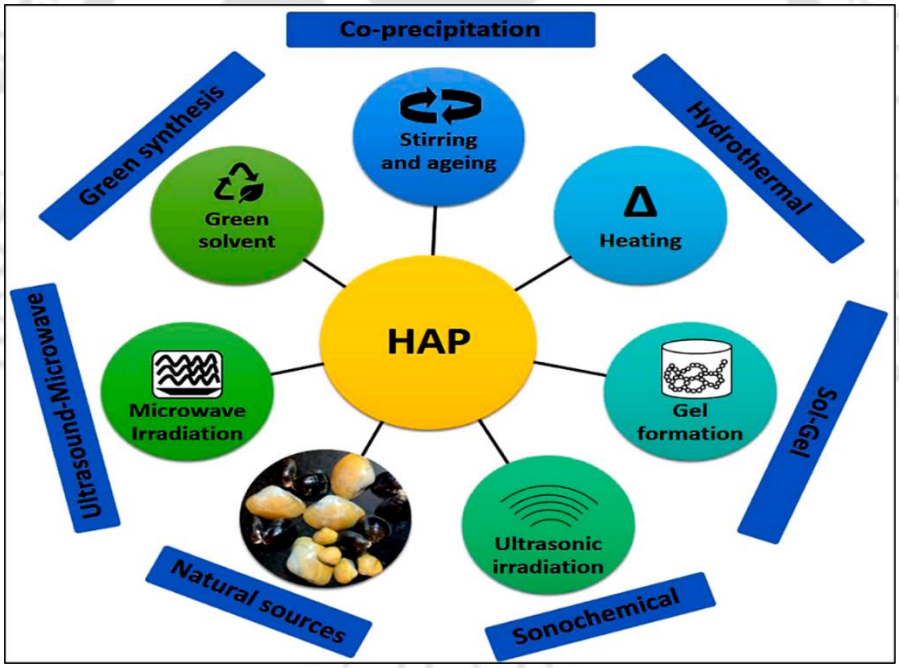

Figure 1.4. General synthesis approaches of hydroxyapatite nanoparticles. Reprinted from reference 40, copyright (2020), with permission from Elsevier.

Hydrothermal method

Hydrothermal method is one of the convenient and effective methods for synthesis of hydroxyapatite nanoparticles, with the employment of high temperature through microwave or autoclave.

This method is intended to develop uniformly dispersed and crystalline hydroxyapatite nanoparticles. Additives such as cationic detergents namely cetyltrimethylammonium bromide (CTAB), vitamin C, and ethylenediamine tetraacetic acid (EDTA) are incorporated as templates to control the morphology, texture and properties of hydroxyapatite nanoparticles. Factors such as pH, temperature and time duration of the whole reaction influence the formulation of hydroxyapatite nanoparticles with suitable Ca/P molar ratio.[41, 42]

Sol-gel method

The method involves the mixing of calcium and phosphate precursors in their stoichiometric ratio of 1.67, resulting in the formation of gel. Under suitable pH conditions and calcination temperature, the technique offers the formation of homogeneous, less agglomerated, pure crystalline hydroxyapatite nanoparticles. With the addition of ultrasonic agitation and stirring, this cost effective method is found to generate mechanically stable hydroxyapatite nanoparticles, with the introduction of upgraded morphological features such as mesoporous properties.[43]

Ultrasound-microwave directed synthesis

Ultrasound aided microwave method is the conjugation of conventional sonochemistry and microwave technique, mostly utilized for the formation of nano-sized powders. Here the reaction mixture is initially introduced to ultrasound process after which, they are subjected to microwave treatment. The technique delivers faster reactivity of integral chemical species, accelerating the formation of final product within a short span of time. Moreover, the execution of ultrasound brings down the size of nanoparticles and controls agglomeration. Jeyapal et al. have reported the synthesis of template assisted synthesis of hydroxyapatite nanoparticles with the aid of ultrasound and microwave irradiation. They could obtain less agglomerated and morphologically sound nanoparticles with reduced size, showing probable potency in biomedical applications.[44, 45]

Wet chemical or precipitation method

Among various executed methods, wet chemical or precipitation method is one of the versatile and notable synthesis procedures widely accepted for the synthesis of hydroxyapatite nanoparticles. Unlike the above methods, which demand the requisite of high temperature and

pressure in customized environment of autoclave or reflux system, the wet chemical method ensures the formation of hydroxyapatite nanoparticles at comparatively lower temperature with mostly no specific pressure requirement. However, this method usually needs suitable pH conditions for promoting the event of precipitation. Additionally, the precursors and other extrinsic conditions applied such as temperature, acidity and rate of reactant addition for the synthesis, play significant role in defining the final morphology, size and crystallinity of obtained nanoparticles. The wet precipitation method employs the usage of templates such as polyvinyl alcohol (PVA), polyethylene glycol (PEG), surfactants such as CTAB, ethanolamine and lecithin, which have been proven to improve the characteristics of the nanoparticles. With the tailoring of various physical, chemical or morphological features using the mentioned process parameters, the wet chemical or precipitation method promises reproducibility, scalability and improved functionality, making the inorganic nanoscale hydroxyapatite material proficient to be of clinical demand, including the field of drug delivery application. Researchers including Yang et al. and Tampieri et al. have suggested wet precipitation method to be the most commendatory and suitable procedure for synthesis of hydroxyapatite nanoparticles.[46-48]

Doping of hydroxyapatite nanoparticles

Doping of hydroxyapatite nanoparticles has been carried out for therapeutic, biosensing, environmental application, tissue engineering and imaging purpose. For aiming therapeutic purpose, hydroxyapatite nanoparticles have been doped with silver for applying against Gram positive and Gram negative bacterial infections. The phenomenon of cationic silver ions, bridging with anionic biological molecules could be explored for antibacterial studies through such doping strategies. Other potential applications of hydroxyapatite nanoparticles have been archived, following their doping with elements such as hafnium and selenium for lung cancer and bone tumour treatment respectively. Kanchana et al. have reported the doping of hydroxyapatite nanoparticles with iron for utilizing them as biosensors for the detection of L-tyrosine. [49-52]

Among various reports on tissue engineering applications, cobalt ions doped hydroxyapatite nanoparticles, synthesised via wet chemical precipitation method were studied for angiogenesis in bone tissue regeneration. Dual doping of hydroxyapatite nanoparticles with

selenium and cationic gold ions was found to increase the microstructural properties of tissue engineering scaffold, favouring enhanced cellular response and mechanical properties. Moreover, doping has been done with rare earth elements such as terbium, europium and gadolinium, transforming hydroxyapatite nanoparticles to be multifunctional nanosystem with magnetic resonance, infrared reflection and X-ray imaging features.[53-55]

Doped hydroxyapatite nanoparticles for bioimaging application

Now, bioimaging is an extremely indispensable application under biological discipline, for elucidating intracellular structure and dynamics, in targeting the desired cells or biologically relevant species or location, for tracking the traversed path of delivery cargo and their intracellular distribution. Rare earth elements or lanthanides based doping has been understood to incorporate excellent bioimaging properties to the hydroxyapatite nanoparticles, making them attractive and potential in fluorescent based biological labelling. Rare earth elements such as erbium (**Figure 1.5)**, europium, neodymium and ytterbium enable luminescent emission in visible range, limited light scattering, narrow emission, wider absorption area and no-blinking emission.[56] Quantum dots are another class of luminescent materials, focused for conjugating into hydroxyapatite nanoparticles. Zhou et al. have explored the possibilities of linking nano hydroxyapatite with Mn-doped ZnSe@ZnS quantum dot for cellular imaging.[57] Another study involving barium doped nano hydroxyapatite, conjugated with copper doped quantum dots was evaluated for near infrared bioimaging, in addition to tumour targeting. The usage of quantum dots has been driven due to their size-tuneable emission, interesting photo-physical nature and broader excitation. Likewise, organic fluorophore such as indocyanine green has also been keenly considered for doping and intracellular imaging of various cancer cells.[58, 59] Reports have suggested that the above dopants used in hydroxyapatite nanoparticles for bioimaging purpose have both advantages and disadvantages. Apart from the advantages mentioned, some of the major concerns are potential cellular toxicity, negligible homogeneous dispersion, aggregation, rapid clearance, photobleaching, low molar extinction coefficient and sometimes low quantum yield. An interesting divergence unearthed for expanding the phenomenon of doping of hydroxyapatite nanoparticles is the introduction of metallic nanoclusters.

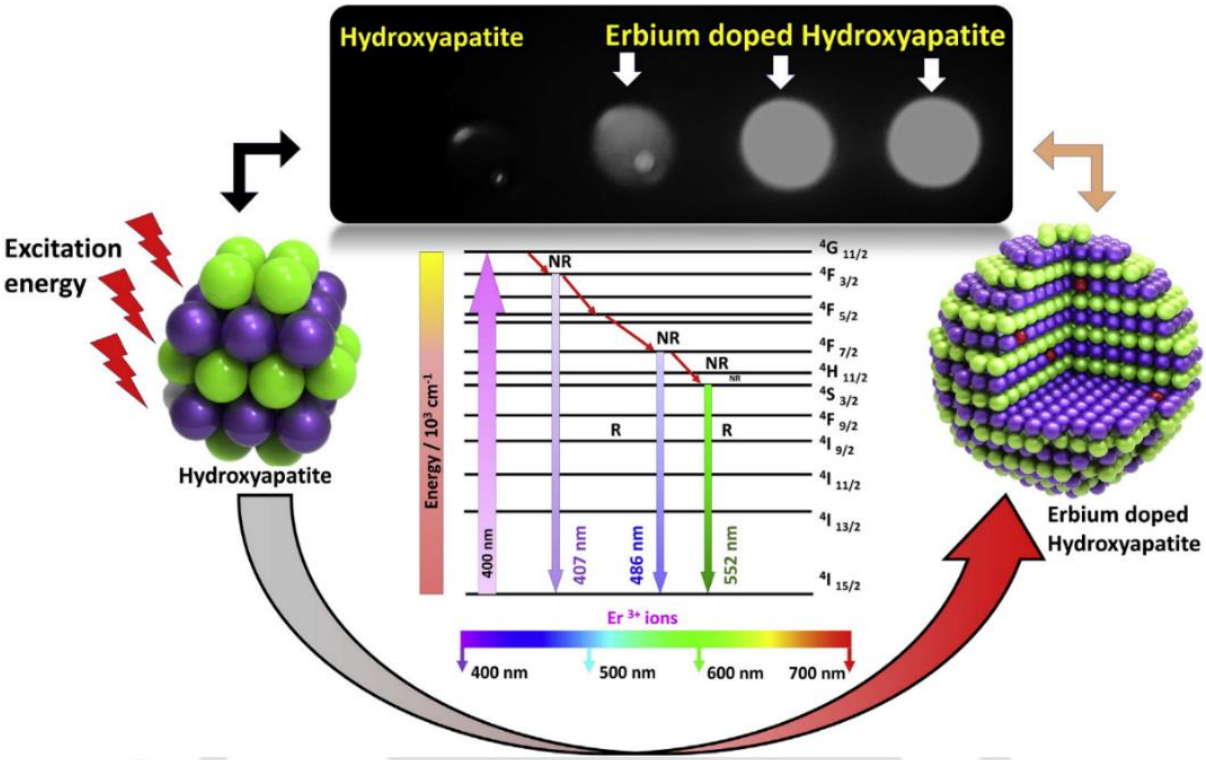

Figure 1.5. An illustration of erbium doped hydroxyapatite nanoparticles with their luminescent property. Reprinted from reference 56, copyright (2020), with permission from Elsevier.

A brief description about the prospect of metallic nanoclusters and their examples is detailed below.

1.2.3. Metallic Nanoclusters

Metal nanoclusters or ultra small metal nanoparticles are distinctive class of materials comprising of several to a few atoms with size less than 2 nm. They are generally considered as connecting bridge between metal nanoparticles and single atomic species. Unlike the metal nanoparticles having larger size range, these metal nanoclusters, due to their extremely reduced size become deprived of surface plasmon effect and exhibit discrete energy levels. Nanoclusters inherit molecule like structure and their electrons are localized to a few atom width space, thus giving rise to quantum confinement effect. The excellent physio-chemical properties bestowed by the metal nanoclusters are distinctive from their bulk counterparts, commending them as excellent fluorescent nanostructures for bioimaging. In an era, where non-invasive fluorescent imaging is highly prevalent, metal nanoclusters are highly regarded

to be accomplishing the aim of diagnosis in medical field. A few examples of metallic nanoclusters include gold, silver, platinum and copper nanoclusters **(Figure 1.6)**.[60, 61]

Gold nanoclusters are popularly known among the emerging fluorophores, owing to their ultra smaller size and hydrophilicity. They are known for longer emission rate, optical chirality, higher photostability and two-photon excitation. The properties such as emission range, luminescence intensity, stability, biocompatibility and solubility can be tuned with the usage of various ligands, stabilizer or capping agents. Researchers have delineated the synthesis of gold nanoclusters functionalized with oligosaccharide, amino acids, proteins or peptides such as cyclodextrin, tyrosine, phenylalanine, tryptophan, BSA, insulin and lysozyme. Another set of stabilizing agents widely explored is thiol containing compound such as mercaptopropionic acid, glutathione and dihydrolipoic acid, which assist chemical reduction and form covalent bridging between Au and S. Wang et al. have documented the bioimaging application of gold nanoclusters, fabricated with transferrin functionalization, converting them to a composite system in association with graphene oxide. The report suggests that transferrin not only stabilized the clusters, but also aided in target based approach, making the entire system eligible for imaging in transferrin overexpressed cancer cells and small animals.[62, 63]

Silver nanoclusters have been studied for catalysis, sensing, antibacterial therapy and bioimaging. Similar to the gold nanoclusters, silver nanoclusters are also characterised with appreciable luminescence, ultra small size and other interesting electronic and optical phenomenon. However, at zero-valent state, silver is susceptible to reactivity and prone to getting oxidized, unlike the analogues of gold, making the synthesis process comparatively challenging. Various protocols have been upgraded with the aim of developing stable version of silver nanoclusters through direct reduction, exchange of ligand, chemical etching, solid state and gel route method. Reports suggest that stabilisation of silver nanoclusters with the help of carboxylic and amine group imparts them red and yellow emission respectively. A few of the stabilizing agents include, chitosan, human serum albumin (HSA) and DNA, ameliorating the resultant silver nanoclusters to be biocompatible. Lyu et al. have reported the synthesis of silver nanoclusters, templated with DNA, followed by their conjugation with polyelectrolyte for cellular imaging. Interestingly, a recent study conducted by Santillan et al.

put forward ligand free synthesis of silver nanoclusters, activated by short duration laser pulse showing excellent fluorescence intensity.[64-67]

Platinum nanoclusters among the noble metals are also explored for bioimaging applications and are developed by wet-chemical, green and *in situ* synthesis methods. Common ligands introduced for synthesis include thiols, polymers, proteins and dendrimers, also ligand free methods have been adapted for platinum nanoclusters synthesis. Chen et al. have proposed an *in situ* based synthesis of platinum nanoclusters with blue emission, which was further used for *in vivo* bioimaging. Tanaka et al. have developed platinum nanoclusters having red emission, which were eventually used for imaging and detection of human epidermal growth factor receptor 2 (HER2) in breast cancer cells. Antibody conjugated platinum nanoclusters with yellow emission have been fabricated by Huang et al. for bioimaging in HeLa cells.[68-70]

Apart from therapeutic application, metal nanoclusters such as gold and silver nanoclusters are comprehensively evaluated for bioimaging, with rare reports on copper nanoclusters. In recent days, the scientific community has begun to focus on the potential properties of copper nanoclusters due to their abundance, cost effective precursors and moderate synthesis parameters. Importantly, unlike gold, silver and platinum, copper is one of the important trace elements in human system. Metal such as gold is understood to cause toxicity due to liver retention, whereas there are physiological means to excrete excess copper from the body. Interestingly, copper nanoclusters with accurate composition and unique packing of atoms, have been considered as an exemplary model for scrutinizing various morphological characteristics of metal nanoparticles. Making advantage of their quantum size effect, optical properties and considerable biocompatibility, efforts have been exerted to widely explore copper nanoclusters in therapy and imaging.[71-73]

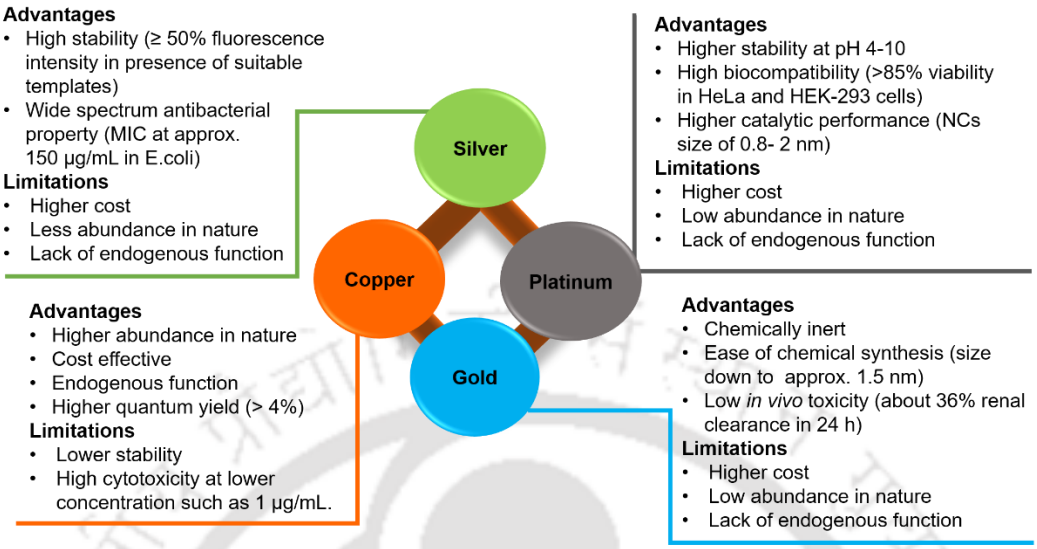

Figure 1.6. Metallic nanoclusters with their merits and demerits. Conceptualized and redrawn (reference 71).

Different synthesis approaches have been developed in improving the stability, luminescence intensity and quantum yield of copper nanoclusters (**Figure 1.7)**. A few of them include ligand directed synthesis where glutathione, D-pencillamine, mercaptosuccinic acid and thiosalicylic acid are used as ligands. Template mediated synthesis is another effective approach in synthesis of copper nanoclusters. The templates studied are DNA, polymers, peptides and proteins. Such templates enable the interaction of Cu^{2+} ions into them, reducing the possibility of agglomeration through steric hindrance. Usage of suitable templates and corresponding reducing agents determines the emission range of nanoclusters. BSA is one of the most favourable protein templates used for synthesizing copper nanoclusters due to its aqueous solubility, binding ability, cysteine residues. Using suitable pH, temperature and reducing agents, the dissociation, coupling and further reduction events take place, favouring cluster formation. In one of the studies, BSA used as template in combination with sodium thiosulfate as reducing agent, gave rise to blue emitting copper nanoclusters.[74, 75]

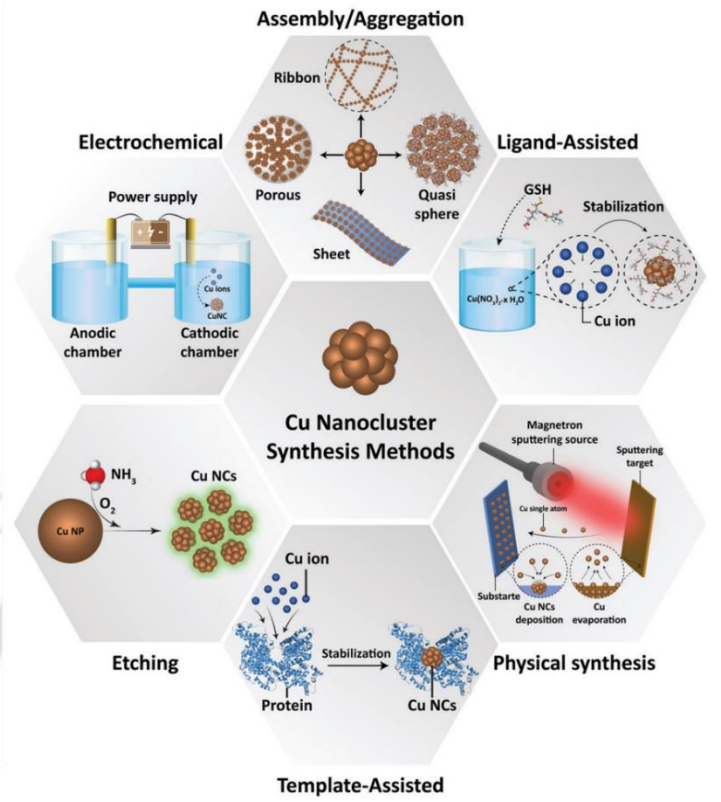

Figure 1.7. Various methods adopted for copper nanoclusters synthesis. Reprinted with permission of Royal Society of Chemistry, from reference 74. Copyright 2019.

Similarly, BSA templated copper nanoclusters, having hydrazine hydrate used as reducing agent, emerged out with red emitting fluorescence property. Hydrazine hydrate is understood to cause structural transformation in α-helix of BSA, availing their functional groups to interact and encourage formation of nanoclusters (**Figure 1.8)**. Additionally, red and near infra emissive materials are highly considered for *in vitro* and *in vivo* imaging, due to deep tissue penetrability and negligible autofluorescence interference.[76]

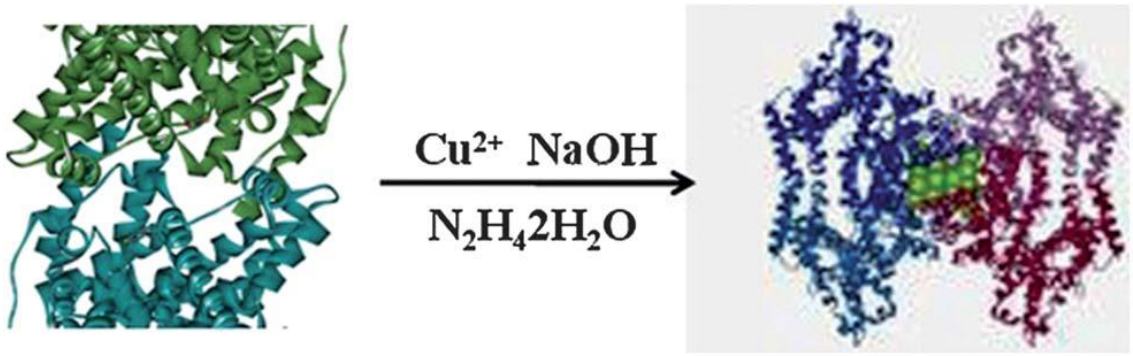

Figure 1.8. Influence of hydrazine hydrate ($N_2H_4.2H_2O$) in protein directed synthesis of red emitting copper nanoclusters. Reprinted with permission of Royal Society of Chemistry, from reference 76. Copyright 2014.

Other methods employed for copper nanoclusters are electrochemical, etching, microemulsion and microwave assisted synthesis.

1.3. Therapeutic Applications of Nanocarriers

The astounding physio-chemical properties imparted to the manipulated nanoscale structures have brought promising outcomes in therapeutic applications *in vivo* and *in vitro*. Upgradation of conventional medical techniques and tools could be achieved through the numerous discoveries made at nano-bio interface, especially through the newly fabricated nanosytems. These developments have been implemented for diagnosis and treatment of bacterial or biofilm infections, chronic diseases such as cancer and other inflammatory diseases, in addition to biosensing of desired molecules and tracking the dissemination of our engineered system *in vitro* and *in vivo*. Major contributions can be observed in other sectors of medicine such as orthopaedics, regenerative medicine including tissue engineering and area of medical implants.

1.3.1. Antibacterial Applications

The persistent antibacterial infections across the Globe have been accredited to the development of MDR, escape from host immune system, occurrence of new mutant strains and lack of suitable remedy for the cause. The prescribed antimicrobials for the cure are mostly recommended at higher concentration with repeated dosage, which probably leads to reduced retention, lower penetration and systemic toxicity. Engineered nanomaterials have been documented to circumvent such threats and improve the pharmacokinetics. Organic nanocarrier such as liposome having a composition of phospholipids and cholesterol, similar

to the composition of cell membrane, can easily fuse with the bacterial membrane and thus mostly are biocompatible and biodegradable (**Figure 1.9)**. Taking that phenomenon as an advantage, antibiotics are encapsulated into liposomes for delivery against bacterial infection.[77]

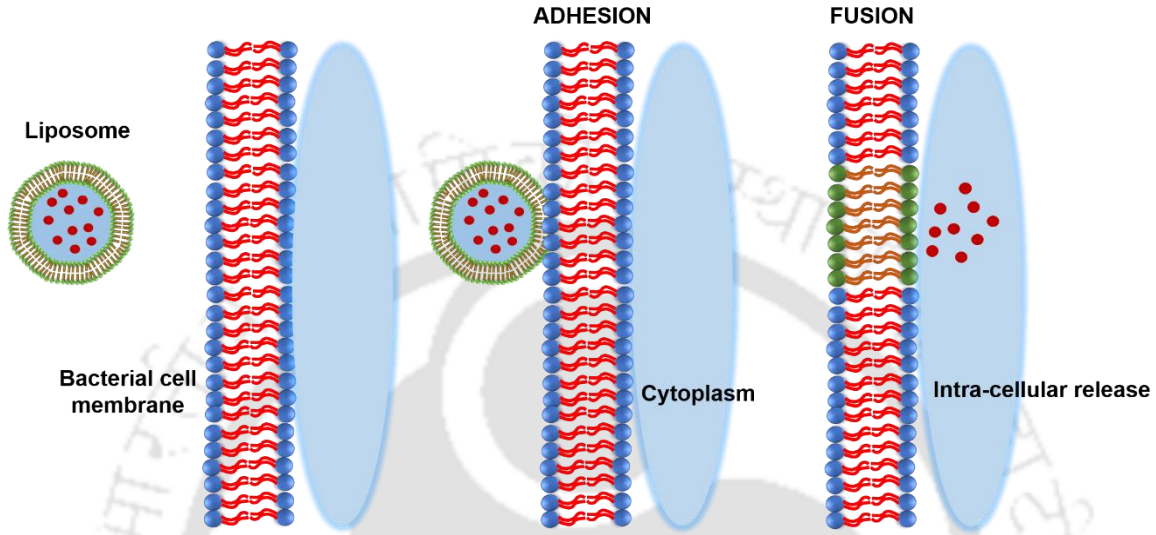

Figure 1.9. Illustration showing bacterial membrane fusion of liposome based nanocarrier. Conceptualized and redrawn (reference 77).

However, the entrapment efficiency was found to be low, especially for aqueous soluble drugs, which was attempted to improve by opting different synthesis parameters. In one of the studies, vancomycin encapsulated liposome was developed, which was further coated with positively charged chitosan whose encapsulation efficiency was found to be improved. Their pharmacokinetics results suggested, sustained release of drug promising reduced nephrotoxicity and reduced pulmonary infection.[78] Another effective strategy of antibiotic therapy is the development of polymers and proteins based nanocarriers, which can be easily internalized and biodegradable. Chitosan, being one of the most commonly explored natural polysaccharide with its inherent antimicrobial property, is considered to be suitable as nanocarrier, which also can adhere non-covalently to epithelial tissues. One of the reports suggested the employment of a synthetic polymer namely poly (lactic-co-glycolic acid) as drug delivery system of clarithromycin for treating *Helicobacter pylori* infection, which showed excellent drug loading efficiency and therapeutic effect.[79] An earlier study conducted by Majumdar and co-worker proposed the development of BSA based nanocarrier loaded with p-aminosalicylic acid, having high affinity for macrophages in treatment of *Mycobacterium tuberculosis*.[80]

A large number of bacterial strains tend to form biofilms on solid surface under favourable conditions. Biofilms, which are formed by the adherence of bacteria on surface, form into a 3-D structure, where numerous bacterial cells are encased within an extracellular matrix composed of secreted proteins, DNA and polysaccharides. Such biofilms are prone to cause nosocomial infections, chronic infections in mucous membrane and wounds as well as contamination on medical devices such as catheter and orthopaedic implants. Having a very complex niche, antibiotic therapy is mostly resisted by biofilm by blocking antibiotic penetration, antibiotic adsorption and its degradation by biofilm components. Introduction of drug loaded nanomaterials has improved antibiofilm therapy, through active delivery of drug to site of infection. A micelle based formulation was developed for the treatment of oral biofilm through loaded triclosan, which was known to strongly impair biofilm formation. Another study suggested efficiency of a PLGA based nanocarrier loaded with a fluoroquinolone namely ciprofloxacin, which was further functionalized with DNase I for the eradication of *Pseudomonas aeruginosa* biofilm.[81, 82]

Inorganic nanocarriers having different compositions based on silver, silica and calcium phosphates are widely explored for both antibacterial and antibiofilm therapy. The widely known inorganic metallic nanoparticles based on silver display wide spectrum antibacterial property against Gram positive and Gram negative strains. One of the research groups had proposed an antibacterial platform with carbon nanotube coated with mesoporous silica, which was further decorated with silver nanoparticles. The entire formulation was found to be therapeutically excellent for MDR Gram negative and Gram positive strains, along with improved wound healing property and excellent bio- safety *in vivo*.[83] Mesoporous inorganic structures such as silica are another focussed nanocarrier system in which manipulations are done for loading both high molecular weight compound and smaller molecules. The loaded antimicrobial compounds by triggered release of external stimuli such as heat, magnetic field, light and pathogenic response, can eradicate pathogenic bacteria and biofilms with disintegration of their cells (**Figure 1.10)**.[84] Light based external stimuli mainly employs photodynamic therapy (PDT) approach, which involves a photosensitizer, light source and molecular oxygen. Upon irradiation of photosensitizer using light of suitable wavelength, generation of ROS occur, that can disrupt the bacterial intracellular content and cell membrane.

Another interesting phenomenon of certain chosen inorganic nanomaterial is their effect towards loaded molecule resulting in electron exchange, which can be made advantage in applying for broad spectrum antibacterial therapy.[85]

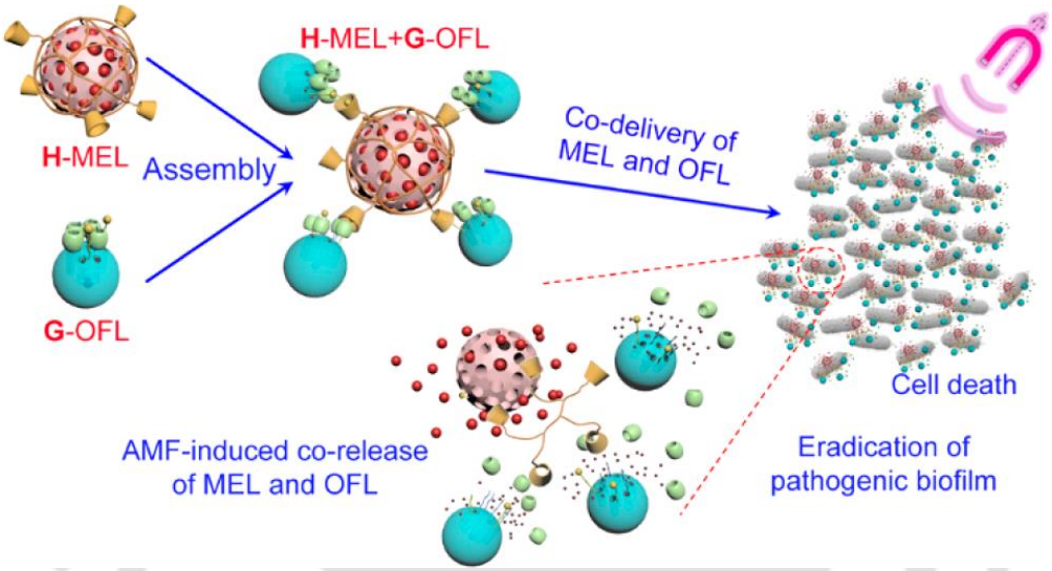

Figure 1.10. Depiction of an inorganic nanocarrier based on mesoporous silica applied for antibiofilm in combination with external stimuli. Reprinted with permission from reference 84. Copyright (2020) American Chemical Society.

The biomimetic and biocompatible hydroxyapatite based nanocarriers are explored for delivery of enzymes, proteins, genes and drugs. They are also known for having pathogenic affinity, excellent ion exchange with metals and ability to develop chemical interaction with hard tissues. The bond with hard tissues promotes their usage against various bone infection causing micro-organisms such as *Bacillus subtilis* and *Klebsiella pneumoniae*. Due to their sparingly soluble nature in physiological condition and microporous structure, hydroxyapatite nanocarriers are analysed for localized, slow and controlled drug delivery at infection sites. Such localized mode of drug release avoids its systemic toxicity and excess accumulation in blood stream.[86, 87] Interestingly, electron exchange events have been studied in hydroxyapatite nanoparticles, where introduction of antimicrobial elements kindled the leakage of internal sugar by disrupting cell membrane of clinically relevant strains such as *Pseudomonas aeruginosa* and *Staphylococcus aureus*.[88] Doping of hydroxyapatite using various elements has been found to enhance its mechanical property and biological activity in antibacterial and antibiofilm drug delivery.

Doping facilitates the interaction of functional group present in loaded molecule with ions present in hydroxyapatite. Such interaction of positively charged calcium and negatively charged phosphate ions of hydroxyapatite with deprotonated carboxyl and protonated amines of drug molecules respectively repels bacterial adhesion, thereby being approved for medical usage. One of the studies revealed that doping with rare earth element such as europium rendered hydroxyapatite nanoparticles of bioimaging characteristics, which aided in detection of bacterial spore constituent.[89]

A plethora of scientific studies have been archived on nanosized delivery cargos about their size controllable property, functionalisation ability, appreciable entrapment efficiency, electrostatic cell membrane interaction and penetrability, causing membrane disruption and inhibition of essential protein synthesis. Thus they have been ratified for implementing as promising treatment tools for various pathogenic strains.

1.3.2. Cancer Theranostics

Cancer theranostics is an evolved concept, which is understood to be a combination of therapy and diagnosis occurring as concomitant activities (**Figure 1.11**). The intrinsic anomalous behaviour, dynamic heterogeneity and complex tumour environment of cancer cells have added significant concerns and challenges in conventional treatment methods such as chemotherapy, radiation therapy and immune therapy. Though these methods help in eradicating the malignancy to a greater extent, there are other major concerns related to side effects, systemic toxicity and non-specific interaction. Since there are monotonous complications in formulating novel anticancer drugs from scratch, scientific community has diverted their interest towards nano-sized carriers.[90, 91]

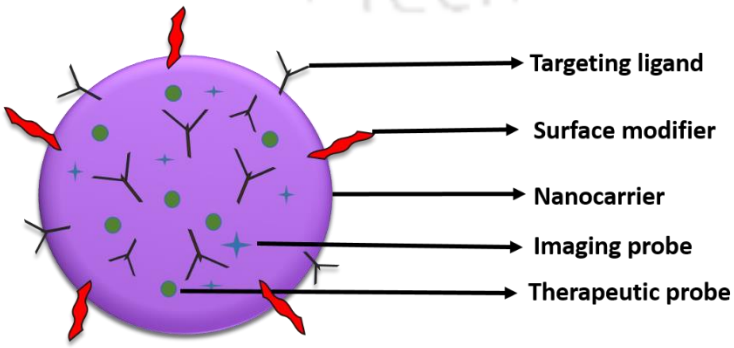

Figure 1.11. A representation of theranostic system. Conceptualized and redrawn (reference 90)

Making advantage of the fact that nano-sized materials resemble to the size of intracellular biological structures and molecules, nanomedicine advancement has prodigiously explored the possibilities of nanocarriers for personalized treatment of cancer. Diverse ranges of nano theranostic systems based on organic and inorganic precursors have been engineered to combat MDR, permit localized delivery, promote earlier detection through imaging and enable targeted therapy. MDR in cancer cells occurs mostly due to excess expression of glycoprotein on the cell membrane, causing high rate of drug efflux and reduced drug uptake. MDR can also result from exhibition of pleotropic effects, activation of detoxifying enzymes and endogenous lipid constituent, which send defective signals in cancer cells. Li and co-workers have proposed the development of fluorescent nano-hybrid based on carbon dot conjugated dendrimer, loaded with anticancer drug doxorubicin for circumventing MDR and inhibiting the tumour growth. The incorporated carbon dot provided fluorescence, which was employed for imaging the tumour. External ultrasound enhanced the cellular uptake with pH driven drug release profile, suggesting appreciable therapeutic efficiency.[92] Nanocarriers have also been developed to bypass the *in vivo* nephrotoxicity and neurotoxicity of certain drugs such as cisplatin and oxaliplatin.[93] Tailoring of synthesis environment, templates, morphological characteristics facilitates prolonged circulation, permitting active and passive targeting of tumour. In the recent past, nanocarriers based on liposome, polymers, micelles and solid lipid nanoparticles have been synthesised for accommodating water insoluble drugs, co-delivery application, achieving synergetic effect, activating endocytosis mediated uptake and inducing apoptotic pathways. Though these nanocarriers are widely accepted and have been clinically approved, there are a few concerns on drug encapsulation efficiency, controlled delivery, instability causing leakage, usage of toxic surfactants as templates, complex and time consuming synthesis procedures. Therefore, focus has been driven to scrutinize the prospects of inorganic nanocarriers.[94, 95]

Presenting clinically relevant drugs in a modified version to abnormal cells could be appreciably achieved through inorganic nanocarriers. Plasmonic inorganic nanocarriers based on gold and silver are intensively studied for cancer therapy and diagnosis, by stabilizing them with various capping agents and templates, moulding them to be loaded with various compounds via physical, covalent and ionic interaction. They have been reported to unload the cargo in the internal cellular space, stimulating higher accumulation and reverting MDR.[96]

Inorganic nanocarriers have been functionalized using clinically approved polymers such as polyethylene glycol (PEG) for imparting colloidal stability in physiological environment, long term circulation and biocompatibility. Modifications have been introduced, which facilitated the transport of loaded drug, eluding from MDR receptors and finally traversing through the membrane to cytoplasm.[97] One of the research groups has showcased the active targeting of antineoplastic drug loaded inorganic nanocarrier, conjugated with antibody towards cancer stem cells, demonstrating the possibility of preventing cancer recurrence and reduced toxicity of drug towards healthy tissues.[98] Passive targeting is another theranostic approach for treating cancer, which is promoted by EPR effect. In order to supply sufficient nutrient and oxygen, new blood vessels have been recruited by tumour cells, which swarm around the already existing vessels. But the newly formed tumour blood vessels develop larger pores, due to partially completed endothelial lining, making the vasculature leaky. The abnormal vasculature is characterised with disorganized structure, non-uniform distribution, asymmetric branching, increasing their permeability. In addition to factors accelerating permeability, an impairment in lymphatic drainage mechanism is observed, which stimulates the extravasation of uptaken nanoparticles towards tumour region.[99] Using self-assembly approach, researchers have fabricated quantum dot based nanocarrier, which showed excellent fluorescence characteristics and tumour environment sensitivity, for imaging tumour site and delivering anticancer drug respectively. EPR effect with *in vivo* curative property was observed, in case of drug loaded carrier than free drug, also diagnosis of both early and advanced tumour was ensured. [100] In another study, a poorly bioavailable chemotherapeutic drug was encapsulated using a single step procedure into strontium based nanocarrier, which showed EPR and therapeutic effect towards gastric carcinoma cells.[101] Physiochemical features such as size, shape and charge also play significant role in enabling cellular uptake and theranostic effect of nanocarriers. Based on different compositions, synthesis strategies and functionalization of inorganic nanocarriers, various conclusions on physiochemical properties have been documented, that mention of overcoming biological barriers, internalization, systemic delivery, bioavailability, retention and excretion.[102] Synergy is another important phenomenon achieved by inorganic theranostic systems in conjunction with the loaded drugs and other additional factors. Another multifunctional inorganic theranostic platform based on silica had been developed, for co-delivery of two chemotherapeutic drugs such as gemcitabine and doxorubicin, which was found

to be more robust than a few reported organic nanocarrier made of liposome and polymer. The gold nanoclusters incorporated in this nanocarrier rendered exclusive tumour diagnosis and the two loaded drugs imparted synergistic therapeutic effect.[103] Sometimes, doping with suitable luminescent materials not only impart bioimaging property, but also augment synergistic therapy in conjugation with loaded drug towards cancer cells.

Pre-clinical investigations have been employed on the response of external stimuli to boost the performance of theranostic system. The external stimuli mostly include ultrasound, magnetic field and light, which induce localized treatment, with negligible effect towards adjacent regions. In light induced therapy, photothermal therapy (PTT) and PDT are involved, among which PDT is considered to be a mature non-invasive approach accepted in clinical realm for cancer therapy. With the combination of photosensitizers and suitable light source, conversion of molecular oxygen to cytotoxic ROS takes place through series of reaction cascade prompting apoptosis, tumour destruction and host immune system activation. One of the mostly studied inorganic nanocarriers for PDT is gold nanoparticles, using which, research groups have demonstrated the functionalization of ligand and photosensitizer for targeted imaging and irradiation based therapy. Such formulations were found to be biologically stable, showing greater accumulation at tumour sites, negligible dark toxicity, irreversible cancer therapy and imaging property, eligible for surgical guidance. [104] The promising therapeutic aspect of PDT was demonstrated using other inorganic nanocarriers involving iron oxide, quantum dot and silica precursors. Through PDT approach, these nanocarriers revealed serum stability, synergistic effect, minimal collateral damage, excess ROS production, apoptosis, DNA damage and tumour ablation.

Apart from the reported metallic and non-metallic inorganic nanocarriers, bioinspired nanocarriers from inorganic source such as hydroxyapatite with calcium-phosphate proportions are also accepted for clinical translation. Resemblance to hard tissue composition is one of the key factors for hydroxyapatite materials to be considered for engineering into nanocarrier, without having them to be modified for making them biocompatible and biodegradable. Its well-defined porous nanostructure and controllable physio-chemical properties accommodate therapeutic molecules, targeting ligands, fluorescent compounds, dopants and photosensitizers for theranostic application. The pH sensitive degradation of hydroxyapatite nanocarrier induces

pH triggered drug release, making drug molecules available at the abnormal sites. The greater affinity of hydroxyapatite towards bone tissues was explored in one of the studies, for making them into a carrier and loading an anticancer drug vincristine for bone cancer therapy, which significantly prevented angiogenesis.[105] Another scientific group has demonstrated site specific delivery of drug loaded hydroxyapatite nanoparticles towards mitochondria and nuclei with sufficient distribution and potential anti-tumorigenic effect in hepatic cancer cell line.[106] **(Figure 1.12)**

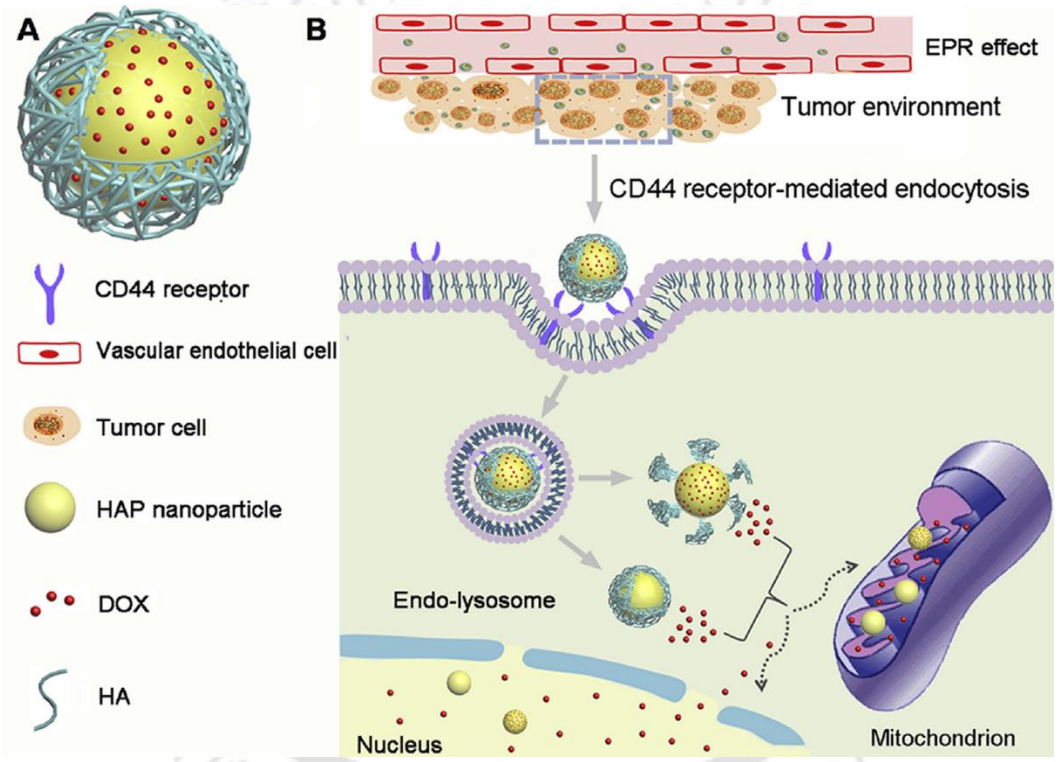

Figure 1.12. Drug loaded hydroxyapatite nanoparticles analysed for cancer therapy with the influence of EPR effect. Reprinted from reference 106, copyright (2016), with permission from Elsevier.

Hydroxyapatite nanoparticles are excellent hosting materials for various elements, qualifying them as diagnostic tool for radiolabelling, magnetic resonance imaging and bioimaging, alongside therapy. Bioimaging property activated in hydroxyapatite nanoparticles through dopants and organic fluorophores could be used for image guided therapy. Rare earth elements or lanthanides doped hydroxyapatite nanoparticles loaded with anticancer drugs are found to render *in vitro* and *in vivo* imaging property as well as pH dependent sustained drug

release profile.[107] In one of the studies, cellular uptake and trafficking possibilities were investigated on fluorophore conjugated hydroxyapatite nanoparticles, which bestowed lung cancer specific toxicity in response to dosage and time. By altering the membrane potential, activating the apoptotic enzymes and interrupting calcium ion homeostasis, the entire nano hydroxyapatite formulation could intensify the anticancer effect.[108] Light induced therapy involving PDT approach has also been explored using hydroxyapatite. A few reports suggest the photosensitizer loading and generation of singlet oxygen, shedding lights on fabrication of nanocarrier which restricts aggregation, promoting therapy and diagnosis (**Figure 1.13)**.[109]

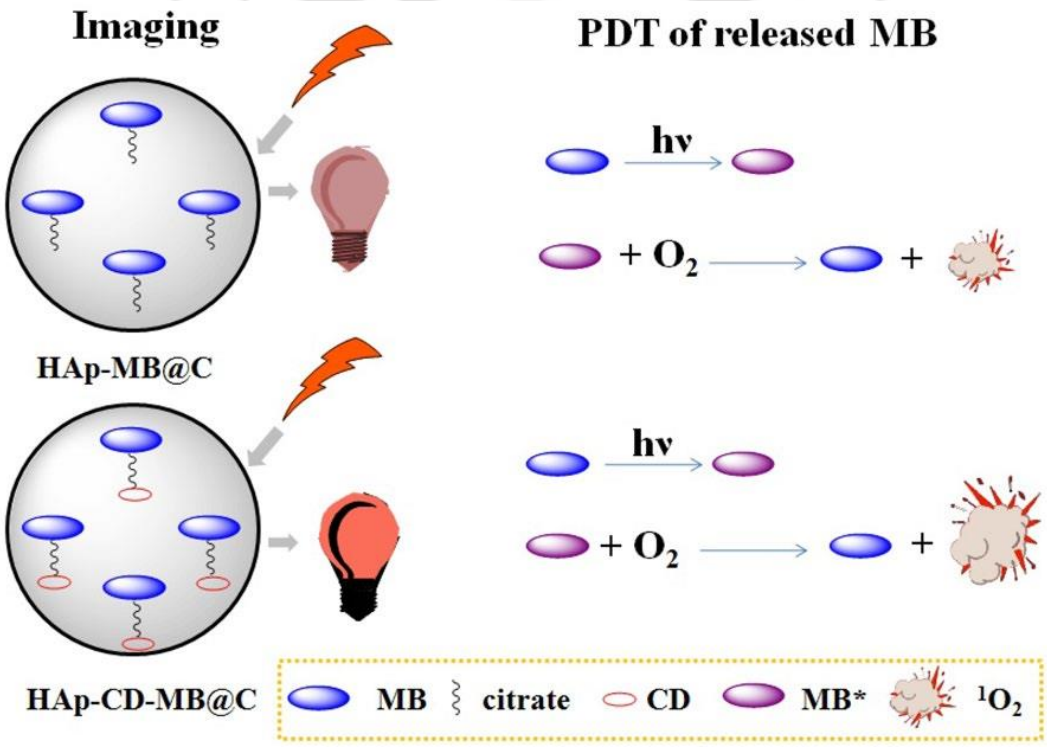

Figure 1.13. Illustration showing PDT application of hydroxyapatite nanoparticles applied as nanocarrier. Reprinted by permission from Springer Nature (reference 109), copyright 2021.

Having manifested most of the clinically required salient features from various scientific studies conducted, inorganic nanocarriers are thus promised to be versatile means of multifunctional therapeutic tools, expediting their dominance in translational medicine.

1.4. Scope and Challenges

Inspired by numerous literature surveys on inorganic nanocarriers, especially based on hydroxyapatite, the following were considered for examination.

- Developing hydroxyapatite based nanocarrier as drug delivery vehicle.
- Upgradation of hydroxyapatite based nanocarrier to theranostic nanosystem for therapeutic and bioimaging applications.
- Loading of hydrophilic and hydrophobic drugs for antibacterial, antibiofilm or anticancer applications.
- Exploration of external stimuli based therapy using hydroxyapatite based nanocarrier for antibacterial and anticancer therapy.

1.5. Salient Features of the Current Study

- Wet chemical synthesis of hydroxyapatite nanoparticles doped with luminescent copper nanoclusters for bioimaging application in bacterial cells.
- Investigations performed on loading hydrophilic antibacterial drugs into the nanoformulation and *in vitro* applications for antibacterial and biofilm therapy.
- Inspection of luminescent hydroxyapatite nanocarrier for loading hydrophobic anticancer drug and bioimaging in cancer cells. Evaluation of therapeutic aspect on the present nanocarrier on monolayer as well as tumor spheroids.
- Employment of co-delivery module using luminescent hydroxyapatite nanocarrier for antibacterial and anticancer photodynamic therapy (PDT).

1.6. References

1. Nazarenko, Y.; Han, T. W.; Lioy, P. J.; Mainelis, G., Potential for exposure to engineered nanoparticles from nanotechnology-based consumer spray products. *J Expo Sci Environ Epidemiol* **2011,** *21* (5), 515-28.
2. Whitesides, G. M., Nanoscience, Nanotechnology, and Chemistry. **2005,** *1* (2), 172-179.
3. Hulla, J. E.; Sahu, S. C.; Hayes, A. W., Nanotechnology: History and future. *Hum Exp Toxicol* **2015,** *34* (12), 1318-21.

4. Miyazaki, K.; Islam, N., Nanotechnology systems of innovation—An analysis of industry and academia research activities. *Technovation* **2007,** *27* (11), 661-675
5. Shea, C. M., Future management research directions in nanotechnology: A case study. *Journal of Engineering and Technology Management* **2005,** *22* (3), 185-200.
6. Kroto, H. W.; Heath, J. R.; O'Brien, S. C.; Curl, R. F.; Smalley, R. E., C60: Buckminsterfullerene. *Nature* **1985,** *318* (6042), 162-163.
7. Schaper-Rinkel, P. J. T. F.; Change, S., The role of future-oriented technology analysis in the governance of emerging technologies: The example of nanotechnology. **2013,** *80*, 444-452.
8. Iqbal, P.; Preece, J. A.; Mendes, P. M., Nanotechnology: The "Top-Down" and "Bottom-Up" Approaches. In *Supramolecular Chemistry*, 2012.
9. Fu, X.; Cai, J.; Zhang, X.; Li, W.-D.; Ge, H.; Hu, Y., Top-down fabrication of shape-controlled, monodisperse nanoparticles for biomedical applications. *Advanced Drug Delivery Reviews* **2018,** *132*, 169-187.
10. Kumar, S.; Bhushan, P.; Bhattacharya, S., Fabrication of Nanostructures with Bottom-up Approach and Their Utility in Diagnostics, Therapeutics, and Others. 2018; pp 167-198.
11. Huang, W.; Ling, S.; Li, C.; Omenetto, F. G.; Kaplan, D. L., Silkworm silk-based materials and devices generated using bio-nanotechnology. *Chemical Society Reviews* **2018,** *47* (17), 6486-6504.
12. Khomutov, G. B.; Kislov, V. V.; Antipina, M. N.; Gainutdinov, R. V.; Gubin, S. P.; Obydenov, A. Y.; Pavlov, S. A.; Rakhnyanskaya, A. A.; Sergeev-Cherenkov, A. N.; Soldatov, E. S.; Suyatin, D. B.; Tolstikhina, A. L.; Trifonov, A. S.; Yurova, T. V., Interfacial nanofabrication strategies in development of new functional nanomaterials and planar supramolecular nanostructures for nanoelectronics and nanotechnology. *Microelectronic Engineering* **2003,** *69* (2), 373-383.
13. Farokhzad, O. C.; Langer, R., Impact of nanotechnology on drug delivery. *ACS Nano* **2009,** *3* (1), 16-20.
14. Abdalla, A.; Klein, S.; Mader, K., A new self-emulsifying drug delivery system (SEDDS) for poorly soluble drugs: characterization, dissolution, in vitro digestion and incorporation into solid pellets. *Eur J Pharm Sci* **2008,** *35* (5), 457-64.
15. Chamundeeswari, M.; Jeslin, J.; Verma, M. L., Nanocarriers for drug delivery applications. *Environmental Chemistry Letters* **2019,** *17* (2), 849-865.
16. Sapsford, K. E.; Algar, W. R.; Berti, L.; Gemmill, K. B.; Casey, B. J.; Oh, E.; Stewart, M. H.; Medintz, I. L., Functionalizing nanoparticles with biological molecules: developing chemistries that facilitate nanotechnology. *Chem Rev* **2013,** *113* (3), 1904-2074.
17. Park, K., Facing the Truth about Nanotechnology in Drug Delivery. *ACS Nano* **2013,** *7* (9), 7442-7447.
18. Sharma, A.; Sharma, U. S., Liposomes in drug delivery: Progress and limitations. *International Journal of Pharmaceutics* **1997,** *154* (2), 123-140.

19. Chonn, A.; Cullis, P. R., Recent advances in liposomal drug-delivery systems. *Current opinion in biotechnology* **1995,** *6* (6), 698-708.
20. Shen, M.; Shi, X., Dendrimer-based organic/inorganic hybrid nanoparticles in biomedical applications. *Nanoscale* **2010,** *2* (9), 1596-610.
21. Jain, N. K.; Gupta, U., Application of dendrimer-drug complexation in the enhancement of drug solubility and bioavailability. *Expert Opin Drug Metab Toxicol* **2008,** *4* (8), 1035-52.
22. Kowalczuk, A.; Trzcinska, R.; Trzebicka, B.; Müller, A. H. E.; Dworak, A.; Tsvetanov, C. B., Loading of polymer nanocarriers: Factors, mechanisms and applications. *Progress in Polymer Science* **2014,** *39* (1), 43-86.
23. Chen, W.; Zhou, S.; Ge, L.; Wu, W.; Jiang, X., Translatable High Drug Loading Drug Delivery Systems Based on Biocompatible Polymer Nanocarriers. *Biomacromolecules* **2018,** *19* (6), 1732-1745.
24. Qiu, L.; Zheng, C.; Jin, Y.; Zhu, K., Polymeric micelles as nanocarriers for drug delivery. *Expert Opinion on Therapeutic Patents* **2007,** *17* (7), 819-830.
25. Kedar, U.; Phutane, P.; Shidhaye, S.; Kadam, V., Advances in polymeric micelles for drug delivery and tumor targeting. *Nanomedicine* **2010,** *6* (6), 714-29.
26. Wang, S. Y.; Hu, H. Z.; Qing, X. C.; Zhang, Z. C.; Shao, Z. W., Recent advances of drug delivery nanocarriers in osteosarcoma treatment. *Journal of Cancer* **2020,** *11* (1), 69-82.
27. Chariou, P. L.; Ortega-Rivera, O. A.; Steinmetz, N. F., Nanocarriers for the Delivery of Medical, Veterinary, and Agricultural Active Ingredients. *ACS Nano* **2020,** *14* (3), 2678-2701.
28. Tréguer-Delapierre, M.; Majimel, J.; Mornet, S.; Duguet, E.; Ravaine, S., Synthesis of non-spherical gold nanoparticles. *Gold Bulletin* **2008,** *41* (2), 195-207.
29. Ghosh, P.; Han, G.; De, M.; Kim, C. K.; Rotello, V. M., Gold nanoparticles in delivery applications. *Adv Drug Deliv Rev* **2008,** *60* (11), 1307-1315.
30. Brown, P. K.; Qureshi, A. T.; Moll, A. N.; Hayes, D. J.; Monroe, W. T., Silver nanoscale antisense drug delivery system for photoactivated gene silencing. *ACS Nano* **2013,** *7* (4), 2948-59.
31. Qiu, L.; Li, J.-W.; Hong, C.-Y.; Pan, C.-Y., Silver Nanoparticles Covered with pH-Sensitive Camptothecin-Loaded Polymer Prodrugs: Switchable Fluorescence "Off" or "On" and Drug Delivery Dynamics in Living Cells. *ACS Applied Materials & Interfaces* **2017,** *9* (46), 40887-40897.
32. Rubilar, O.; Rai, M.; Tortella, G.; Diez, M. C.; Seabra, A. B.; Durán, N., Biogenic nanoparticles: copper, copper oxides, copper sulphides, complex copper nanostructures and their applications. *Biotechnol Lett* **2013,** *35* (9), 1365-1375.
33. Mishra, P. K.; Mishra, H.; Ekielski, A.; Talegaonkar, S.; Vaidya, B., Zinc oxide nanoparticles: a promising nanomaterial for biomedical applications. *Drug Discovery Today* **2017,** *22* (12), 1825-1834.

34. Fan, J.; Wang, S.; Sun, W.; Guo, S.; Kang, Y.; Du, J.; Peng, X., Anticancer drug delivery systems based on inorganic nanocarriers with fluorescent tracers. **2018,** *64* (3), 835-859.
35. Chen, Y.-C.; Huang, X.-C.; Luo, Y.-L.; Chang, Y.-C.; Hsieh, Y.-Z.; Hsu, H.-Y., Non-metallic nanomaterials in cancer theranostics: a review of silica- and carbon-based drug delivery systems. *Science and Technology of Advanced Materials* **2013,** *14* (4), 044407.
36. Huang, D.; He, B.; Mi, P., Calcium phosphate nanocarriers for drug delivery to tumors: imaging, therapy and theranostics. *Biomaterials Science* **2019,** *7* (10), 3942-3960.
37. Sokolova, V.; Epple, M., Biological and Medical Applications of Calcium Phosphate Nanoparticles. *Chemistry (Weinheim an der Bergstrasse, Germany)* **2021,** *27* (27), 7471-7488.
38. Ferna´ndez, E.; Gil, F. J.; Ginebra, M. P.; Driessens, F. C. M.; Planell, J. A.; Best, S. M., Calcium phosphate bone cements for clinical applications. Part I: Solution chemistry. *Journal of Materials Science: Materials in Medicine* **1999,** *10* (3), 169-176.
39. Levingstone, T. J.; Herbaj, S.; Dunne, N. J., Calcium Phosphate Nanoparticles for Therapeutic Applications in Bone Regeneration. **2019,** *9* (11), 1570.
40. Pai, S.; M Kini, S.; Selvaraj, R.; Pugazhendhi, A., A review on the synthesis of hydroxyapatite, its composites and adsorptive removal of pollutants from wastewater. *Journal of Water Process Engineering* **2020,** *38*, 101574.
41. Ebrahimi, S.; Stephen Sipaut@ Mohd Nasri, C.; Bin Arshad, S. E., Hydrothermal synthesis of hydroxyapatite powders using Response Surface Methodology (RSM). *PLOS ONE* **2021,** *16* (5), e0251009.
42. Zhang, H.-b.; Zhou, K.-c.; Li, Z.-y.; Huang, S.-p., Plate-like hydroxyapatite nanoparticles synthesized by the hydrothermal method. *Journal of Physics and Chemistry of Solids* **2009,** *70* (1), 243-248.
43. Vijayalakshmi Natarajan, U.; Rajeswari, S., Influence of calcium precursors on the morphology and crystallinity of sol–gel-derived hydroxyapatite nanoparticles. *Journal of Crystal Growth* **2008,** *310* (21), 4601-4611.
44. Liang, T.; Qian, J.; Yuan, Y.; Liu, C., Synthesis of mesoporous hydroxyapatite nanoparticles using a template-free sonochemistry-assisted microwave method. *Journal of Materials Science* **2013,** *48* (15), 5334-5341.
45. Jeyapal, I.; Malathi, K. S., Comparison of template mediated ultrasonic and microwave irradiation method on the synthesis of hydroxyapatite nanoparticles for biomedical applications. *Materials Today: Proceedings* **2021**.
46. Yelten-Yilmaz, A.; Yilmaz, S., Wet chemical precipitation synthesis of hydroxyapatite (HA) powders. *Ceramics International* **2018,** *44* (8), 9703-9710.
47. Michał, W.; Ewa, D.; Tomasz, C., Lecithin-based wet chemical precipitation of hydroxyapatite nanoparticles. *Colloid and Polymer Science* **2015,** *293* (5), 1561-1568.
48. Goh, K.; Wong, Y. H.; Singh, R.; Thambinayagam, H.; Krishnasamy, S.; Sidhu, A. S.; Teng, W., Effect of pH on the properties of eggshell-derived hydroxyapatite bioceramic

synthesized by wet chemical method assisted by microwave irradiation. *Ceramics International* **2020,** *47*.

49. Franci, G.; Falanga, A.; Galdiero, S.; Palomba, L.; Rai, M.; Morelli, G.; Galdiero, M., Silver Nanoparticles as Potential Antibacterial Agents. **2015,** *20* (5), 8856-8874.

50. Chen, M. H.; Hanagata, N.; Ikoma, T.; Huang, J. Y.; Li, K. Y.; Lin, C. P.; Lin, F. H., Hafnium-doped hydroxyapatite nanoparticles with ionizing radiation for lung cancer treatment. *Acta biomaterialia* **2016,** *37*, 165-73.

51. Barbanente, A.; Palazzo, B.; Esposti, L. D.; Adamiano, A.; Iafisco, M.; Ditaranto, N.; Migoni, D.; Gervaso, F.; Nadar, R.; Ivanchenko, P.; Leeuwenburgh, S.; Margiotta, N., Selenium-doped hydroxyapatite nanoparticles for potential application in bone tumor therapy. *Journal of Inorganic Biochemistry* **2021,** *215*, 111334.

52. Kanchana, P.; Lavanya, N.; Sekar, C., Development of amperometric l-tyrosine sensor based on Fe-doped hydroxyapatite nanoparticles. *Materials Science and Engineering: C* **2014,** *35*, 85-91.

53. Kulanthaivel, S.; Roy, B.; Agarwal, T.; Giri, S.; Pramanik, K.; Pal, K.; Ray, S. S.; Maiti, T. K.; Banerjee, I., Cobalt doped proangiogenic hydroxyapatite for bone tissue engineering application. *Materials Science and Engineering: C* **2016,** *58*, 648-658.

54. Ahmed, M. K.; Mansour, S. F.; Al-Wafi, R.; Afifi, M.; Uskoković, V., Gold as a dopant in selenium-containing carbonated hydroxyapatite fillers of nanofibrous ε-polycaprolactone scaffolds for tissue engineering. *Int J Pharm* **2020,** *577*, 118950.

55. Zhigang, L.; Wang, Q.; Shaowei, Y.; Lirong, Y.; Shouwu, Y.; Xiaoxin, F.; Li, F.-f. J. C. I., Synthesis and characterization of Tb3+/Gd3+ dual-doped multifunctional hydroxyapatite nanoparticles. **2014,** *40*, 2613-2617.

56. Mondal, S.; Nguyen, V. T.; Park, S.; Choi, J.; Tran, L. H.; Yi, M.; Shin, J. H.; Lee, C.-Y.; Oh, J., Bioactive, luminescent erbium-doped hydroxyapatite nanocrystals for biomedical applications. *Ceramics International* **2020,** *46* (10, Part B), 16020-16031.

57. Zhou, R.; Li, M.; Wang, S.; Wu, P.; Wu, L.; Hou, X., Low-toxic Mn-doped ZnSe@ZnS quantum dots conjugated with nano-hydroxyapatite for cell imaging. *Nanoscale* **2014,** *6* (23), 14319-14325.

58. Zeng, S.; Zhou, R.; Zheng, X.; Wu, L.; Hou, X., Mono-dispersed Ba 2+ -doped Nano-hydroxyapatite conjugated with near-infrared Cu-doped CdS quantum dots for CT/fluorescence bimodal targeting cell imaging. *Microchemical Journal* **2017,** *134*.

59. Altınoğlu, E. I.; Russin, T. J.; Kaiser, J. M.; Barth, B. M.; Eklund, P. C.; Kester, M.; Adair, J. H., Near-Infrared Emitting Fluorophore-Doped Calcium Phosphate Nanoparticles for In Vivo Imaging of Human Breast Cancer. *ACS Nano* **2008,** *2* (10), 2075-2084.

60. Du, Y.; Sheng, H.; Astruc, D.; Zhu, M., Atomically Precise Noble Metal Nanoclusters as Efficient Catalysts: A Bridge between Structure and Properties. *Chemical Reviews* **2020,** *120* (2), 526-622.

61. Kailasa, S. K.; Borse, S.; Koduru, J. R.; Murthy, Z. V. P., Biomolecules as promising ligands in the synthesis of metal nanoclusters: Sensing, bioimaging and catalytic applications. *Trends in Environmental Analytical Chemistry* **2021,** *32*, e00140.
62. El-Sayed, N.; Trouillet, V.; Clasen, A.; Jung, G.; Hollemeyer, K.; Schneider, M., NIR-Emitting Gold Nanoclusters–Modified Gelatin Nanoparticles as a Bioimaging Agent in Tissue. **2019,** *8* (24), 1900993.
63. Wang, Y.; Chen, J.-T.; Yan, X.-P., Fabrication of Transferrin Functionalized Gold Nanoclusters/Graphene Oxide Nanocomposite for Turn-On Near-Infrared Fluorescent Bioimaging of Cancer Cells and Small Animals. *Analytical Chemistry* **2013,** *85* (4), 2529-2535.
64. Xie, Y.-P.; Shen, Y.-L.; Duan, G.-X.; Han, J.; Zhang, L.-P.; Lu, X., Silver nanoclusters: synthesis, structures and photoluminescence. *Materials Chemistry Frontiers* **2020,** *4* (8), 2205-2222.
65. Nakal-Chidiac, A.; García, O.; García-Fernández, L.; Martín-Saavedra, F. M.; Sánchez-Casanova, S.; Escudero-Duch, C.; San Román, J.; Vilaboa, N.; Aguilar, M. R., Chitosan-stabilized silver nanoclusters with luminescent, photothermal and antibacterial properties. *Carbohydrate Polymers* **2020,** *250*, 116973.
66. Lyu, D.; Li, J.; Wang, X.; Guo, W.; Wang, E., Cationic-Polyelectrolyte-Modified Fluorescent DNA–Silver Nanoclusters with Enhanced Emission and Higher Stability for Rapid Bioimaging. *Analytical Chemistry* **2019,** *91* (3), 2050-2057.
67. Santillán, J. M. J.; Muñetón Arboleda, D.; Muraca, D.; Schinca, D. C.; Scaffardi, L. B., Highly fluorescent few atoms silver nanoclusters with strong photocatalytic activity synthesized by ultrashort light pulses. *Scientific Reports* **2020,** *10* (1), 8217.
68. George, A.; Gopalakrishnan, H.; Mandal, S., Surfactant free platinum nanocluster as fluorescent probe for the selective detection of Fe (III) ions in aqueous medium. *Sensors and Actuators B: Chemical* **2017,** *243*, 332-337.
69. Chen, D.; Zhao, C.; Ye, J.; Li, Q.; Liu, X.; Su, M.; Jiang, H.; Amatore, C.; Selke, M.; Wang, X., In Situ Biosynthesis of Fluorescent Platinum Nanoclusters: Toward Self-Bioimaging-Guided Cancer Theranostics. *ACS Applied Materials & Interfaces* **2015,** *7* (32), 18163-18169.
70. Tanaka, S.-i.; Wadati, H.; Sato, K.; Yasuda, H.; Niioka, H., Red-Fluorescent Pt Nanoclusters for Detecting and Imaging HER2 in Breast Cancer Cells. *ACS Omega* **2020,** *5* (37), 23718-23723.
71. Lai, W.-F.; Wong, W.-T.; Rogach, A. L., Development of Copper Nanoclusters for In Vitro and In Vivo Theranostic Applications. **2020,** *32* (9), 1906872.
72. Heo, G. S.; Zhao, Y.; Sultan, D.; Zhang, X.; Detering, L.; Luehmann, H. P.; Zhang, X.; Li, R.; Choksi, A.; Sharp, S.; Levingston, S.; Primeau, T.; Reichert, D. E.; Sun, G.; Razani, B.; Li, S.; Weilbaecher, K. N.; Dehdashti, F.; Wooley, K. L.; Liu, Y., Assessment of Copper Nanoclusters for Accurate in Vivo Tumor Imaging and Potential for Translation. *ACS Applied Materials & Interfaces* **2019,** *11* (22), 19669-19678.

73. Liu, X.; Astruc, D., Atomically precise copper nanoclusters and their applications. *Coord. Chem. Rev*. **2018,** *359*, 112.
74. Shahsavari, S.; Hadian-Ghazvini, S.; Hooriabad Saboor, F.; Menbari Oskouie, I.; Hasany, M.; Simchi, A.; Rogach, A. L., Ligand functionalized copper nanoclusters for versatile applications in catalysis, sensing, bioimaging, and optoelectronics. *Materials Chemistry Frontiers* **2019,** *3* (11), 2326-2356.
75. Kong, B.; Cao, Y.; Yu, Y.; Zhao, S., Synthesis of sodium thiosulfate-reduced copper nanoclusters using bovine serum albumin as a template and their applications in the fluorometric detection of minocycline. *Microchemical Journal* **2020,** *159*, 105388.
76. Wang, C.; Wang, C.; Xu, L.; Cheng, H.; Lin, Q.; Zhang, C., Protein-directed synthesis of pH-responsive red fluorescent copper nanoclusters and their applications in cellular imaging and catalysis. *Nanoscale* **2014,** *6* (3), 1775-1781.
77. Wang, D. Y.; van der Mei, H. C.; Ren, Y.; Busscher, H. J.; Shi, L., Lipid-Based Antimicrobial Delivery-Systems for the Treatment of Bacterial Infections. *Frontiers in chemistry* **2019,** *7*, 872.
78. Yang, Z.; Liu, J.; Gao, J.; Chen, S.; Huang, G., Chitosan coated vancomycin hydrochloride liposomes: Characterizations and evaluation. *Int J Pharm* **2015,** *495* (1), 508-515.
79. Parisi, O. I.; Scrivano, L.; Sinicropi, M. S.; Puoci, F., Polymeric nanoparticle constructs as devices for antibacterial therapy. *Current opinion in pharmacology* **2017,** *36*, 72-77.
80. Majumdar, S.; Basu, S. K., Killing of intracellular Mycobacterium tuberculosis by receptor-mediated drug delivery. *Antimicrob Agents Chemother* **1991,** *35* (1), 135-40.
81. Chen, F.; Rice, K. C.; Liu, X.-M.; Reinhardt, R. A.; Bayles, K. W.; Wang, D., Triclosan-loaded tooth-binding micelles for prevention and treatment of dental biofilm. *Pharm Res* **2010,** *27* (11), 2356-2364.
82. Baelo, A.; Levato, R.; Julián, E.; Crespo, A.; Astola, J.; Gavaldà, J.; Engel, E.; Mateos-Timoneda, M. A.; Torrents, E., Disassembling bacterial extracellular matrix with DNase-coated nanoparticles to enhance antibiotic delivery in biofilm infections. *J Control Release* **2015,** *209*, 150-8.
83. Zhu, Y.; Xu, J.; Wang, Y.; Chen, C.; Gu, H.; Chai, Y.; Wang, Y., Silver nanoparticles-decorated and mesoporous silica coated single-walled carbon nanotubes with an enhanced antibacterial activity for killing drug-resistant bacteria. *Nano Research* **2020,** *13* (2), 389-400.
84. Yu, Q.; Deng, T.; Lin, F.-C.; Zhang, B.; Zink, J. I., Supramolecular Assemblies of Heterogeneous Mesoporous Silica Nanoparticles to Co-deliver Antimicrobial Peptides and Antibiotics for Synergistic Eradication of Pathogenic Biofilms. *ACS Nano* **2020,** *14* (5), 5926-5937.

85. Sun, J.; Fan, Y.; Ye, W.; Tian, L.; Niu, S.; Ming, W.; Zhao, J.; Ren, L., Near-infrared light triggered photodynamic and nitric oxide synergistic antibacterial nanocomposite membrane. *Chemical Engineering Journal* **2021,** *417*, 128049.
86. Stanić, V.; Dimitrijević, S.; Antić-Stanković, J.; Mitrić, M.; Jokić, B.; Plećaš, I. B.; Raičević, S., Synthesis, characterization and antimicrobial activity of copper and zinc-doped hydroxyapatite nanopowders. *Applied Surface Science* **2010,** *256* (20), 6083-6089.
87. Prasanna, A. P. S.; Venkatasubbu, G. D., Sustained release of amoxicillin from hydroxyapatite nanocomposite for bone infections. *Progress in biomaterials* **2018,** *7* (4), 289-296.
88. Placente, D.; Ruso, J.; Baldini, M.; Sieben, J.; Laiuppa, J.; Santillan, G.; Messina, P., Self-fluorescent Antibiotic MoOx-Hydroxyapatite: A Nano- theranostic Platform for Bone Infection Therapies. *Nanoscale* **2019,** *11*.
89. Li, Y.; Li, X.; Wang, D.; Shen, C.; Yang, M., Hydroxyapatite nanoparticle based fluorometric turn-on determination of dipicolinic acid, a biomarker of bacterial spores. *Microchimica Acta* **2018,** *185* (9), 435.
90. Prasad, R.; Jain, N. K.; Conde, J.; Srivastava, R., Localized nanotheranostics: recent developments in cancer nanomedicine. *Materials Today Advances* **2020,** *8*, 100087.
91. Taylor, D., The Pharmaceutical Industry and the Future of Drug Development. In *Pharmaceuticals in the Environment*, The Royal Society of Chemistry: 2016; pp 1-33.
92. Li, D.; Lin, L.; Fan, Y.; Liu, L.; Shen, M.; Wu, R.; Du, L.; Shi, X., Ultrasound-enhanced fluorescence imaging and chemotherapy of multidrug-resistant tumors using multifunctional dendrimer/carbon dot nanohybrids. *Bioactive Materials* **2021,** *6* (3), 729-739.
93. Liu, D.; Poon, C.; Lu, K.; He, C.; Lin, W., Self-assembled nanoscale coordination polymers with trigger release properties for effective anticancer therapy. *Nature Communications* **2014,** *5* (1), 4182.
94. Mei, D.; Chen, B.; He, B.; Liu, H.; Lin, Z.; Lin, J.; Zhang, X.; Sun, N.; Zhao, L.; Wang, X.; Zhang, Q., Actively priming autophagic cell death with novel transferrin receptor-targeted nanomedicine for synergistic chemotherapy against breast cancer. *Acta Pharmaceutica Sinica B* **2019,** *9* (5), 1061-1077.
95. Hajipour, H.; Ghorbani, M.; Kahroba, H.; Mahmoodzadeh, F.; Emameh, R. Z.; Taheri, R. A., Arginyl-glycyl-aspartic acid (RGD) containing nanostructured lipid carrier co-loaded with doxorubicin and sildenafil citrate enhanced anti-cancer effects and overcomes drug resistance. *Process Biochemistry* **2019,** *84*, 172-179.
96. Min, Y.; Mao, C.; Xu, D.; Wang, J.; Liu, Y., Gold nanorods for platinum based prodrug delivery. *Chemical Communications* **2010,** *46* (44), 8424-8426.
97. Lombardo, D.; Kiselev, M. A.; Caccamo, M. T.; Fratoddi, I., Smart Nanoparticles for Drug Delivery Application: Development of Versatile Nanocarrier Platforms in Biotechnology and Nanomedicine. **2019,** *2019*, 26.

98. Yang, C.; Xiong, F.; Wang, J.; Dou, J.; Chen, J.; Chen, D.; Zhang, Y.; Luo, S.; Gu, N., Anti-ABCG2 monoclonal antibody in combination with paclitaxel nanoparticles against cancer stem-like cell activity in multiple myeloma. *Nanomedicine (Lond)* **2014,** *9* (1), 45-60.
99. Nakamura, Y.; Mochida, A.; Choyke, P. L.; Kobayashi, H., Nanodrug Delivery: Is the Enhanced Permeability and Retention Effect Sufficient for Curing Cancer? *Bioconjugate Chem*. **2016,** *27*, 2225.
100. Deng, T.; Wang, J.; Li, Y.; Han, Z.; Peng, Y.; Zhang, J.; Gao, Z.; Gu, Y.; Deng, D., Quantum Dots-Based Multifunctional Nano-Prodrug Fabricated by Ingenious Self-Assembly Strategies for Tumor Theranostic. *ACS Applied Materials & Interfaces* **2018,** *10* (33), 27657-27668.
101. Qian, W. Y.; Sun, D. M.; Zhu, R. R.; Du, X. L.; Liu, H.; Wang, S. L., pH-sensitive strontium carbonate nanoparticles as new anticancer vehicles for controlled etoposide release. *Int J Nanomedicine* **2012,** *7*, 5781-92.
102. Kang, H.; Mintri, S.; Menon, A. V.; Lee, H. Y.; Choi, H. S.; Kim, J., Pharmacokinetics, pharmacodynamics and toxicology of theranostic nanoparticles. *Nanoscale* **2015,** *7* (45), 18848-62.
103. Croissant, J. G.; Zhang, D.; Alsaiari, S.; Lu, J.; Deng, L.; Tamanoi, F.; AlMalik, A. M.; Zink, J. I.; Khashab, N. M., Protein-gold clusters-capped mesoporous silica nanoparticles for high drug loading, autonomous gemcitabine/doxorubicin co-delivery, and in-vivo tumor imaging. *J Control Release* **2016,** *229*, 183-191.
104. Zhao, L.; Kim, T. H.; Kim, H. W.; Ahn, J. C.; Kim, S. Y., Enhanced cellular uptake and phototoxicity of Verteporfin-conjugated gold nanoparticles as theranostic nanocarriers for targeted photodynamic therapy and imaging of cancers. *Materials science & engineering. C, Materials for biological applications* **2016,** *67*, 611-622.
105. Maia, A. L. C.; Ferreira, C. A.; Barros, A. L. B.; ATM, E. S.; Ramaldes, G. A.; Silva Cunha Júnior, A. D.; Oliveira, D. C. P.; Fernandes, C.; Ferreira Soares, D. C., Vincristine-loaded hydroxyapatite nanoparticles as a potential delivery system for bone cancer therapy. *J Drug Target* **2018,** *26* (7), 592-603.
106. Xiong, H.; Du, S.; Ni, J.; Zhou, J.; Yao, J., Mitochondria and nuclei dual-targeted heterogeneous hydroxyapatite nanoparticles for enhancing therapeutic efficacy of doxorubicin. *Biomaterials* **2016,** *94*, 70-83.
107. Chen, M.-H.; Yoshioka, T.; Ikoma, T.; Hanagata, N.; Lin, F.-H.; Tanaka, J., Photoluminescence and doping mechanism of theranostic Eu(3+)/Fe(3+) dual-doped hydroxyapatite nanoparticles. *Science and technology of advanced materials* **2014,** *15* (5), 055005-055005.
108. Sun, Y.; Chen, Y.; Ma, X.; Yuan, Y.; Liu, C.; Kohn, J.; Qian, J., Mitochondria-Targeted Hydroxyapatite Nanoparticles for Selective Growth Inhibition of Lung Cancer in Vitro and in Vivo. *ACS Applied Materials & Interfaces* **2016,** *8* (39), 25680-25690.

109. Zhang, K.; Sun, H.; Li, X.; Bai, J.; Du, Q.; Li, C., Increased photoluminescence and photodynamic therapy efficiency of hydroxyapatite-β-cyclodextrin-methylene blue@carbon powders with the favor of hydrogen bonding effect. *Photochemical & photobiological sciences : Official journal of the European Photochemistry Association and the European Society for Photobiology* **2021,** *20* (10), 1323-1331.

Chapter 2

Copper Nanocluster-Doped Luminescent Hydroxyapatite Nanoparticles for Antibacterial and Antibiofilm Applications

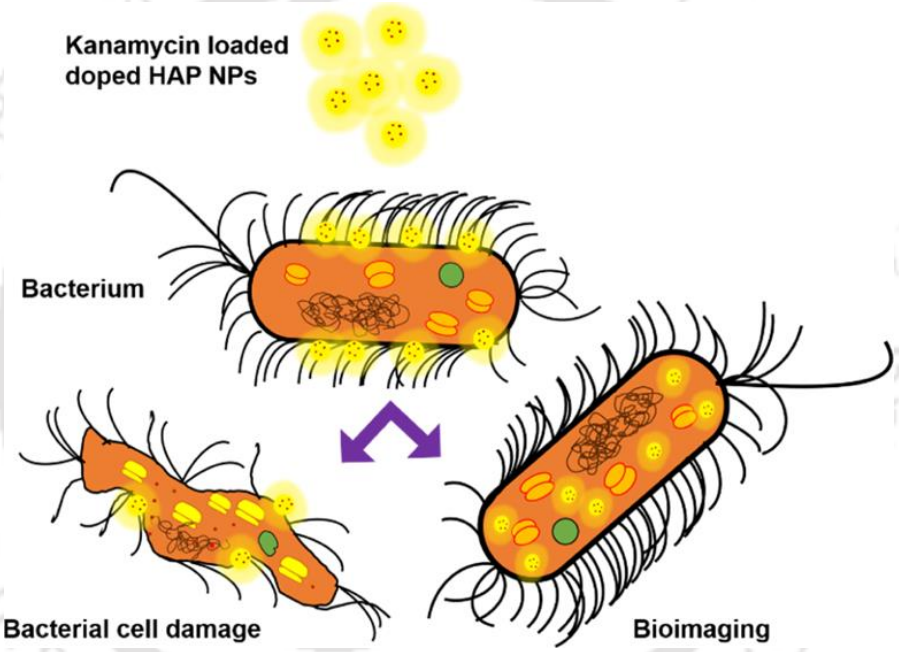

https://pubs.acs.org/doi/full/10.1021/acsomega.8b03076

Chapter 2

Copper Nanocluster-Doped Luminescent Hydroxyapatite Nanoparticles for Antibacterial and Antibiofilm Applications

Abstract

Novel strategies in the field of nanotechnology for the development of suitable multifunctional drug delivery vehicles have been pursued with promising upshots. Luminescent copper nanocluster-doped hydroxyapatite nanoparticles (HAP NPs) were synthesized and applied for the delivery of antibacterial drug kanamycin. The negatively charged doped HAP NPs could electrostatically interact with the positively charged kanamycin. The kanamycin-loaded doped HAP NPs showed pronounced activity in the case of Gram-negative bacteria compared to that in Gram-positive bacteria. Upon interaction with the bacteria, kanamycin could probably generate harmful agents such as hydroxyl radical that leads to bacterial cell damage. After being incorporated with copper nanoclusters (Cu NCs), the doped HAP NPs were applied for the bioimaging of bacterial cells. The biocompatibility of doped HAP NPs was also studied in HeLa cells. As compared to copper nanoclusters, the doped HAP NPs showed excellent biocompatibility even at higher concentrations of copper. The kanamycin-loaded doped HAP NPs were further applied toward *Pseudomonas aeruginosa* biofilm eradication. Thus, the as-synthesized copper nanocluster-doped HAP NPs were applied as nanocarriers for antibiotic drug delivery, bioimaging, and antibiofilm applications.

2.1. Introduction

Multidrug resistance in bacteria is an emerging serious concern, which has been prevailing because of the development of resistant genes, by the action of multidrug efflux pumps that eliminate the uptaken drug, and through modification in the drug target site. The cure of multidrug resistant bacterial infections demands multiple treatments with a broad spectrum of drugs that are quite expensive and toxic.[1-4]

Nanotechnology has become a promising field in handling the challenge for the development of nano-sized materials that can vanquish such serious threat to an extent. The increasing resistance of bacterial strains toward a wide range of drugs has prompted the researchers to pursue various drug delivery methods where focus has been driven to sustained release of drug and biocompatibility of drug delivery vehicles.[5] There has been an accelerated interest toward inorganic material-based nanoparticles as carriers, which can be modified to resist enzymatic degradation with improved affinity between carriers and macromolecules, sustained drug delivery, and reduced renal clearance. Inorganic nanoparticles have got several advantages over polymer-based nanocarrier systems and organic nanoparticles by exhibiting multifunctionality, less toxicity, and lower immune response. Unlike liposome-based carriers, they show lipase resistance and stability toward bile salts.[6,7]

In nature, there are a diverse range of highly ordered inorganic materials with a well-defined structure, which can be manipulated to engineer suitable nanocrystals.[8] Hydroxyapatite (HAP) among the inorganic materials is an important constituent in the hard tissues of human such as bone and tooth. Being a bioceramic material, it has excellent biocompatibility, nonimmunogenicity, and high osteoconductivity, which make it an ideal material for bone implants and dental implants. The chemical resemblance of HAP with the naturally existing bone matrix enables it to be used in tissue regeneration or bone implants. The excellent nanoscale properties of HAP, which differ from that of their bulk form, have attained wider attention in the area of inorganic nanoparticle-based applications.[9,10] Importantly, the rough surface texture, high adsorption capacity, and nontoxicity qualify their usage as *in vitro* and *in vivo* carriers for proteins, growth factors, and drugs.[11,12] The cell membrane penetrability and *in vivo* solubility favor HAP-based nanocarriers to carry out both localized and systemic delivery of drugs. HAP nanocarriers are found to facilitate sustained drug delivery with appreciable therapeutic response.[13,14] Studies had been conducted to investigate the loading and release of bovine serum albumin (BSA)[15] and insulin[16] from HAP nanoparticles (HAP NPs) and HAP-based scaffolds, respectively. Investigations have revealed the loading and release efficiency of drugs such as cisplatin[17] and ibuprofen[18] from HAP NPs. In various studies, the HAP NPs are doped with different metal ions for applications including loading and release of biomolecules, bioimaging, biolabeling, as well as adsorption of toxic metal ions

from the environment.[19] One of the dominant, reliable, inexpensive, and fast methods for the detection of bacteria in the field of sensing technology is luminescence-based detection. Metal nanoclusters comprising a few to hundred atoms are excellent fluorescent materials with high photoluminescence, excellent photostability, lower toxicity, and high water solubility. Among the metal nanoclusters, copper nanoclusters (Cu NCs) are explored with great attention in the area of bioimaging *in vitro* and *in vivo*. Copper nanoclusters have another advantage of being used *in vivo* as there are cellular and molecular mechanisms that regulate the uptake and efflux of copper unlike gold and silver metal ions.[20-22] The HAP nanomaterial, ideally not being a luminescent material, has been converted into luminescent probes after doping it with organic dyes and lanthanides for bioimaging and biolabeling applications. However, the HAP NPs doped with lanthanides have limited *in vivo* applications because of their toxicity, so as the case with organic dyes due to the drawbacks of photobleaching and poor stability. HAP owing to its high biocompatibility and adsorption property can be used for doping with metal nanoclusters such as copper. [23-25] Herein, we report the synthesis of copper nanocluster-doped HAP NPs, which acted as nanocarriers for antibacterial drug delivery (**Figure 2.1**). The negatively charged doped HAP NPs could be loaded with the positively charged antibacterial drug kanamycin. Kanamycin is one of the aminoglycosides, which can irreversibly bind with the 30S ribosomal subunit, further inactivating the bacterium for the synthesis of vital protein required for its growth. Having been included within the WHO list of important medicines, kanamycin is considered as an essential antibiotic for various bacterial infections.[26] Here, the drug loaded doped HAP NPs showing biphasic mode of antibacterial drug release exhibited both antibacterial and antibiofilm property. The as-synthesized doped HAP NPs were biocompatible, and they were also found to be useful for the bioimaging of bacterial cells.

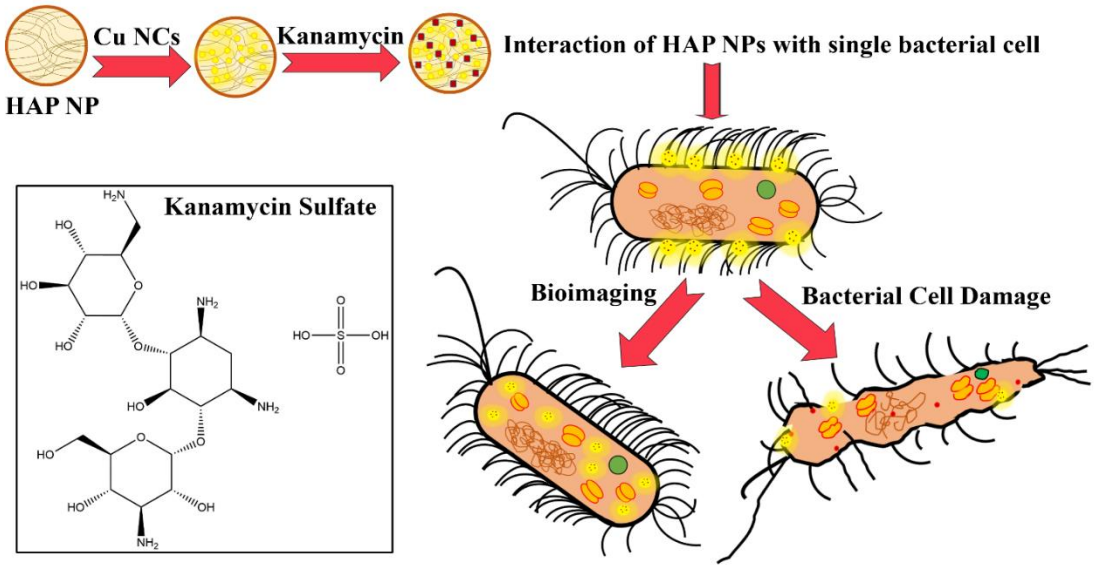

Figure 2.1. Synthesis of kanamycin-loaded doped HAP NPs which on interacting with bacterial cells show both antibacterial and bioimaging potency.

2.2. Materials and Methods

2.2.1. Chemicals

The experimental procedures detailed below include the usage of the following chemicals as-purchased: calcium chloride dihydrate (Merck), potassium dihydrogen phosphate (Merck), strontium nitrate pure (Merck), poly- (ethylene glycol) (PEG) 400 (Merck), ammonia 25% (Merck), hydrazine hydrate 80% (Merck), poly(vinyl alcohol) (PVA) 87-89% hydrolyzed (Sigma-Aldrich), glacial acetic acid (Rankem), sodium hydroxide pellet (Rankem), copper(II) sulfate pentahydrate pure (Merck), BSA (Himedia), kanamycin sulfate (Himedia), Luria Bertani (LB) broth (Himedia), nutrient broth (NB) (Sigma-Aldrich), brain heart infusion (BHI) broth (Sigma-Aldrich), and agar powder (bacteriological grade, Himedia). Milli-Q grade water (>18 MΩ cm-1, Millipore) was used in all the experiments.

2.2.2. Synthesis of HAP NPs

The HAP NPs were synthesized by a wet chemical synthesis method by slightly modifying a known protocol.[27] In this synthesis, 0.2 M (0.176 g) calcium chloride dihydrate, 0.12 M (0.098 g) potassium dihydrogen phosphate, and 0.12 M (0.15 g) strontium nitrate were mixed in 6 mL

of water. While the mixture was kept for stirring, 7 mL of PEG 400 was added into it. The pH of the solution was adjusted to 11 by using 5 M NaOH. While the pH was brought to 11, the mixture turned to a white turbid dispersion and was allowed to stir for 10 min. This formed the first set of dispersion. A second set of solution was prepared where 20 mL of PVA solution, 500 µL of 2.5% diluted glacial acetic acid, and 400 µL of 0.5% ammonia were mixed together and stirred. Further, the second set was added to the first set of dispersion and stirred for 10 min, followed by heating at 85 °C for 2 min. Thereafter, the final dispersion was cooled and centrifuged at 5000 rpm for 10 min to remove the unreacted PVA and PEG. After discarding the supernatant, the pellet was washed and redispersed into water, followed by centrifugation at the same speed for 5 min. The obtained pellet was suspended in water and stored at 4 °C for further use. Instead of N-cetyl-N,N,Ntrimethylammonium bromide reported in the referred protocol, we have used PEG, which is reported to favor the formation of spherical morphology of the HAP NPs.[28] Moreover, both PEG and PVA contribute to the biocompatibility and stability of nanoparticles.

2.2.3. Synthesis of Copper Nanoclusters

The copper nanoclusters were synthesized by modifying a known protocol.[29] In this method, 300 mg of BSA was added to 30 mL of water, followed by the addition of 30 mg of CuSO4. The reaction was kept stirring, which led to the formation of bluish turbid dispersion. To this, 1 M NaOH was added drop by drop, until the color of the medium turned from blue to purple. Further, 180 µL of 80% hydrazine hydrate was added to the purple colored solution, until the color became pale brown. The entire reaction was kept stirring at 80 °C for 15 min. After cooling down, the as-synthesized BSA-templated copper nanoclusters were stored at 4 °C for further use.

2.2.4. Synthesis of Doped HAP NPs

For the synthesis of the doped HAP NPs, 0.2 M calcium chloride dihydrate and 0.12 M strontium nitrate were mixed in 3 mL of water. To this, 7 mL of PEG 400 was added and stirred. The pH was kept at 11 using 1 M NaOH. While the reaction mixture was kept stirring, the synthesized copper nanocluster dispersion was added, followed by the addition of 3 mL of 0.12 M potassium dihydrogen phosphate. This formed the first set of dispersion.

The second set contained 20 mL of the PVA solution, where 500 µL of 2.5% diluted glacial acetic acid and 400 µL of 0.5% ammonia were mixed and stirred. The pH of the second solution was brought to 11 using 1 M NaOH. Finally, the second set and the first set were mixed together and heated at 85 °C for 2 min. After the synthesis, the reaction mixture was cooled down to room temperature and centrifuged at 5000 rpm for 10 min. The pellet was redispersed into water, centrifuged at 5000 rpm for 5 min, and again redispersed in water. The final dispersion was stored at 4 °C for further studies.

2.2.5. Drug-Binding Efficiency of Doped HAP NPs

For performing the binding experiment, different concentrations of doped HAP NPs with varying calcium concentrations (0.76, 1.06, 2.28, and 3.04 mg/mL) were taken with the addition of 500 µL of 20 mg/mL of kanamycin. Incubation was carried out at 37 °C for 45 min. By centrifuging at 5000 rpm for 5 min, the supernatant was collected and the binding efficiency was checked by the 2,4,6-trinitrobenzene-1-sulfonic acid (TNBS) assay.[30]

2.2.6. TNBS Assay

The TNBS assay was used for the detection of primary amines. The kanamycin standards ranging from 2, 5, 10, 15, 20, to 25 mg/mL were prepared. To each well in a 96- well plate, 20 µL of each standard as well as sample with the unknown concentration of kanamycin was added, followed by the addition of 160 µL of 2% sodium bicarbonate to each well. Finally, we added 20 µL of 1% TNBS to all the wells and waited for 5 min for the yellow color to develop. After the color was developed, the absorbance was measured at 450 nm in a microtiter plate reader. Here, TNBS reacts with the amino sugar moieties in kanamycin to give a product of trinitrophenylated derivatives, which then could be spectrophotometrically detected at 450 nm. The efficiency was calculated by the following formula:

$$\% \text{ of loading efficiency} = \frac{KAN_i - KAN_f}{KAN_i} x100$$

Here, KANi refers to the concentration of drug used for binding and KAN_f refers to the concentration of drug in the supernatant.

2.2.7. Release Kinetics of the Antibacterial Drug

The release study was quantified in three different pHs, which include pH 4 (acetate buffer), pH 7.4 phosphate-buffered saline (PBS), and pH 8.4 (PBS). Initially, the doped HAP NPs loaded with kanamycin were incubated for 45 min at 37 °C for binding to take place. After incubation, centrifugation was carried out, and the supernatant was discarded. The obtained pellet was redispersed in different pH buffers and incubated at 37 °C up to 12 h. The sample was withdrawn at each time interval and centrifuged at 5000 rpm for 5 min. The supernatant was collected, and kanamycin was released from the doped HAP NPs analyzed by the TNBS assay

$$\text{Cumulative release } \% = \frac{\text{drug released in supernatant}}{\text{drug loaded in nanocarrier}} \text{x } 100$$

2.2.8. UV-Vis Spectroscopy

The absorbance characteristics of the as-synthesized HAP NPs, copper nanoclusters, and doped HAP NPs in the UV-vis range were recorded using UV-visible spectroscopy (by using a Jasco V-630 spectrophotometer).

2.2.9. Luminescence Measurements

All the luminescence measurements were recorded by a fluorescence spectrophotometer (by using a PerkinElmer LS55 spectrofluorometer).

2.2.10. Quantum Yield Measurements

The quantum yield measurements of doped HAP NPs were carried out using a standard protocol. Quinine sulfate in 0.1 M H_2SO_4 was used as a reference for the study. On the basis of the following equation, the quantum yield was calculated for doped HAP NPs.

$$QY = QY_r \frac{m}{m_r} \frac{n^2}{n_r^2}$$

Here, QY refers to the quantum yield of doped HAP NPs, QY_r refers to the quantum yield of quinine sulfate, which was used as a reference, m and m_r refer to the slope of plot obtained

from integrated luminescence intensity versus absorbance for doped HAP NPs and quinine sulfate, respectively, and n and n_r refer to the refractive indices of doped HAP NPs and quinine sulfate, respectively. QY_r has a quantum yield of 0.54, and solvent (water) has a refractive index of 1.33.

2.2.11. Transmission Electron Microscopy

The as-synthesized HAP NPs, copper nanoclusters, and doped HAP NPs were analyzed under a transmission electron microscope, which was operating at a maximum accelerating voltage of 200 keV (JEM 2100; JEOL, Peabody, MA). For the transmission electron microscopy (TEM) analysis, 7 μL of the sample was drop-cast to a carbon-coated copper grid and air-dried overnight. The HAP NPs and doped HAP NPs were sonicated in an ultrasonic bath (TELSONIC) for 40 min before drop-casting on the grid.

2.2.12. Field Emission Scanning Electron Microscopy

The surface morphology of doped HAP NPs was studied using field emission scanning electron microscopy (FESEM) (JEOL JSM-7610F). The sample for FESEM was prepared by drop-casting 20 μL of the sample to an aluminum foil-covered glass slide and air-drying it overnight. The sample was sonicated for 40 min before being drop-cast. The morphologies of both treated and control bacteria were also studied using FESEM. During the analysis, the bacteria were treated with kanamycin-loaded doped HAP NPs at their minimum inhibitory concentration (MIC). Both the treated and control bacteria were incubated for 10 h at 37 °C (180 rpm). For analysis, 100 μL of the culture was taken and centrifuged at 10 000 rpm for 1 min. After the removal of the supernatant, the pellet was washed and suspended in water. A 20 μL of the diluted culture was drop-cast on an aluminium foil-covered glass slide and air-dried overnight.

2.2.13. Zeta Potential

The zeta potential of doped HAP NPs, undoped HAP NPs, copper nanoclusters, and kanamycin loaded doped HAP NPs was recorded using a Malvern Zetasizer Nano ZS.

2.2.14. Atomic Absorption Spectroscopy

The amount of copper present in the doped HAP NPs was determined using an atomic absorption spectrophotometer (AA240-Varian Inc.)

2.2.15. Liquid Chromatography-Mass Spectrometry

Using liquid chromatography-mass spectrometry (LC-MS) (Q-Tof Premier), the interaction of kanamycin with kanamycin-loaded doped HAP NPs was studied. The analysis was carried out for kanamycin, kanamycin-loaded doped HAP NPs, and doped HAP NPs.

2.2.16. Biocompatibility Assay of Doped HAP NPs

The biocompatibility study was done on HeLa cells by carrying out the 3-(4,5-dimethylthiazol 2-yl)-2,5-diphenyltetrazolium bromide (MTT) assay. For the assay, 1×10^4 HeLa cells/ well were seeded into a 96-well plate and cultured in Dulbecco's modified Eagle medium (DMEM) inside a 5% CO_2 humidified incubator overnight at 37 °C for 24 h. The cells were treated with copper nanoclusters and doped HAP NPs of varying copper concentrations (ranging from 1 to 10 µg/mL). The treated cells were incubated overnight at 37 °C for 24 h. The MTT assay was carried out after 24 h. The respiratory mitochondrial enzyme in the live cells reduces the MTT to a formazan product, which can be detected spectrophotometrically at 570 nm with the reference filter at 655 nm. The amount of formazan formed is directly proportional to the number of live cells. The percentage (%) of cell viability was calculated as follows:

$$\% \text{ of viable cells} = \frac{(\text{A570-A690}) \text{ of treated cells}}{(\text{A570-A690}) \text{ of control cells}} \text{ x } 100$$

2.2.17. Antibacterial Studies

For the antibacterial studies, the following strains were used, which include Gram-positive bacteria (*Staphylococcus aureus* MTCC 96 and *Bacillus subtilis* MTCC 1305) and Gram negative bacteria [green fluorescent protein (GFP) expressing recombinant *Escherichia coli*, *Pseudomonas aeruginosa* MTCC 2488, and *E. coli* DH5α]. *S. aureus* MTCC 96 was grown in BHI at 37 °C (180 rpm) for 12 h. *B. subtilis* MTCC 1305 and *P. aeruginosa* MTCC 2488 were propagated in NB at 37 °C (180 rpm) for 12 h. GFP expressing recombinant *E. coli* was grown in ampicillin containing LB media at 37 °C (180 rpm) for 12 h and *E. coli* DH5α was grown in

LB at 37 °C (180 rpm) for 12 h. The bacterial strains were treated with different concentrations of kanamycin-loaded doped HAP NPs (kanamycin concentration ranging from 3 to 50 µg/mL) and free kanamycin (3 to 50 µg/ mL). The bacterial growth was monitored by recording the optical density (OD) at 595 nm using the UV-visible spectrophotometer (Jasco V-630). The measurements were recorded in triplicates. Further, the MIC and the minimum bactericidal concentration (MBC) were again confirmed by plating the bacteria on nutrient agar media. Here, 100 µL of bacteria treated with the MIC and MBC of kanamycin-loaded doped HAP NPs was spread-plated on the media using L-rod. Similarly, the bacteria treated with the MIC and MBC of free kanamycin were also plated and incubated. The incubation was carried out at 37 °C for 12 h.

2.2.18. Growth Kinetics Study

The growth curve was analysed for *P. aeruginosa* MTCC 2488 after treating the bacteria with the MIC and MBC of kanamycin-loaded doped HAP NPs and free kanamycin, followed by monitoring the growth for 12 h at 37 °C (180 rpm).

2.2.19. Confocal Laser Scanning Microscopy

The confocal experiment was done by treating the bacterial cells with doped HAP NPs at the MIC of kanamycin-loaded doped HAP NPs and incubating for 3 h at 37 °C (180 rpm). The samples were viewed under a Zeiss LSM 880 microscope (at an excitation of 365 nm).

2.2.20. Bacterial Biofilm Assay

The bacteria were diluted to 1×10^6 cfu/mL using the NB media from which 100 µL of bacteria was added to a 96-well plate and incubated at 37 °C in static condition. After 24 h, the medium was removed and fresh medium was added. To this, different concentrations of kanamycin-loaded doped HAP NPs (kanamycin concentration ranging from 12 to 400 µg/mL) and free kanamycin (concentration ranging from 12 to 400 µg/mL) were added and incubated for 12 h. After incubation, the medium was removed, and biofilm was stained with 0.01% crystal violet. The stained biofilm was incubated for 15 min at 37 °C. The crystal violet was dissolved using 95% ethanol, and the absorbance was measured at 595 nm using the microplate reader. The measurements were recorded in triplicates.[31]

2.2.21. Lipid Content Detection

The bacteria grown overnight were diluted to 1×10^6 cfu/mL, and 100 µL was then added to the 96-well plate and incubated for 24 h. Following incubation, the biofilm was treated with kanamycin loaded doped HAP NPs at their minimum biofilm inhibition concentration ($MBIC_{50}$) and incubated for 12 h. The cells were stained with 0.01 mg/mL of Nile red and incubated in dark. The excess dye was removed, and imaging was carried out with an epifluorescence microscope (Nikon ECLIPSE, TS100, Tokyo) at an excitation filter of 540/25 nm.

2.2.22. Acridine Orange/Propidium Iodide Dual Staining Assay

The bacteria were grown overnight, and the culture was diluted to 1×10^6 cfu/mL. A 100 µL of the diluted culture was added to the 96-well plate and incubated for 24 h. After incubation, the grown biofilm was treated with kanamycin loaded doped HAP NPs at their $MBIC_{50}$ and incubated for 12 h. The biofilm was then gently washed and stained with 0.01 mg/mL of propidium iodide (PI) and 0.01 mg/mL of acridine orange (AO), followed by the incubation in dark. The excess dye was removed, and imaging was done at an excitation filter of 465-495 nm for AO and 540/25 nm for PI.

2.3. Results and Discussion

2.3.1. Synthesis and Characterisations

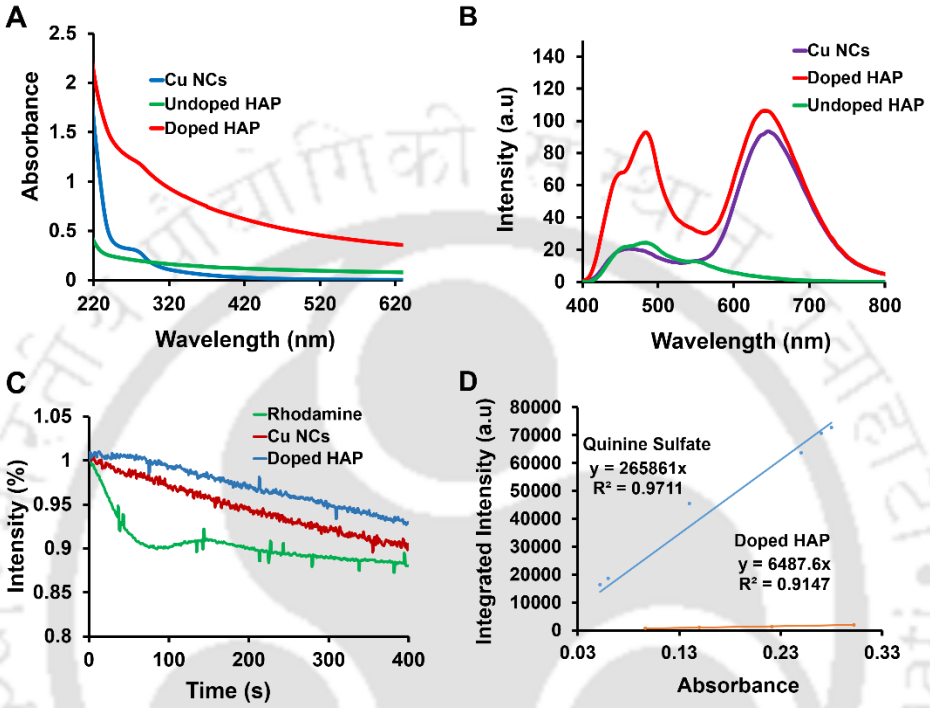

Figure 2.2. (A) UV-vis absorption spectra of copper nanoclusters, undoped HAP NPs and doped HAP NPs. (B) Emission spectra of copper nanoclusters and doped HAP NPs showing the emission peak at 650 nm when excited at 365 nm. (C) Photostability of copper nanoclusters and doped HAP NPs. The organic fluorophore rhodamine was used as standard. As compared to copper nanoclusters or rhodamine (organic dye), doped HAP NPs were found to be more stable. (D) Quantum yield measurement of doped HAP NPs using quinine sulfate as the reference.

The as-synthesized doped HAP NP dispersion was turbid and brown in color. The UV-vis spectrum of doped HAP NPs, HAP NPs (undoped), or copper nanoclusters (**Figure 2.2A**) did not exhibit any significant peak in the visible region of wavelengths. However, a peak could be observed at around 280 nm in the case of doped HAP NPs or copper nanoclusters. The observed peak at 280 nm in the case of doped HAP NPs is attributed to BSA, which is used as the template in the synthesis of copper nanoclusters and thus suggests the incorporation of BSA-templated copper nanoclusters into HAP NPs. Importantly, copper nanoclusters, when excited at 365 nm, exhibited an emission peak at around 650 nm (**Figure 2.2B**). A similar luminescence emission peak was also observed at 650 nm when doped HAP NPs were excited

at 365 nm. This also indicated successful incorporation of BSA-templated copper nanoclusters into HAP NPs. As compared to the copper nanoclusters, the doped HAP NPs exhibited apparent higher luminescence intensity. This was resulted probably due to the aggregation-induced emission enhancement of nanoclusters.[32,33] Additionally, the photostability study revealed that the doped HAP NPs were comparatively more stable than copper nanoclusters or the organic luminescent dye rhodamine 6G (**Figure 2.2C**). In the case of doped HAP NPs, there was reduction in the luminescent intensity (F/F_0) at a rate of only 1.06% per minute. However, copper nanoclusters and the organic dye showed the decrease of intensity at a rate of 1.4% per minute and 1.8% per minute, respectively. The stability of doped HAP NPs toward photobleaching can be considered for their bioimaging application. Using quinine sulfate as the reference, the quantum yield of doped HAP NPs was obtained to be 1.2% (**Figure 2.2D**) and thus can be considered for bioimaging applications.[34]

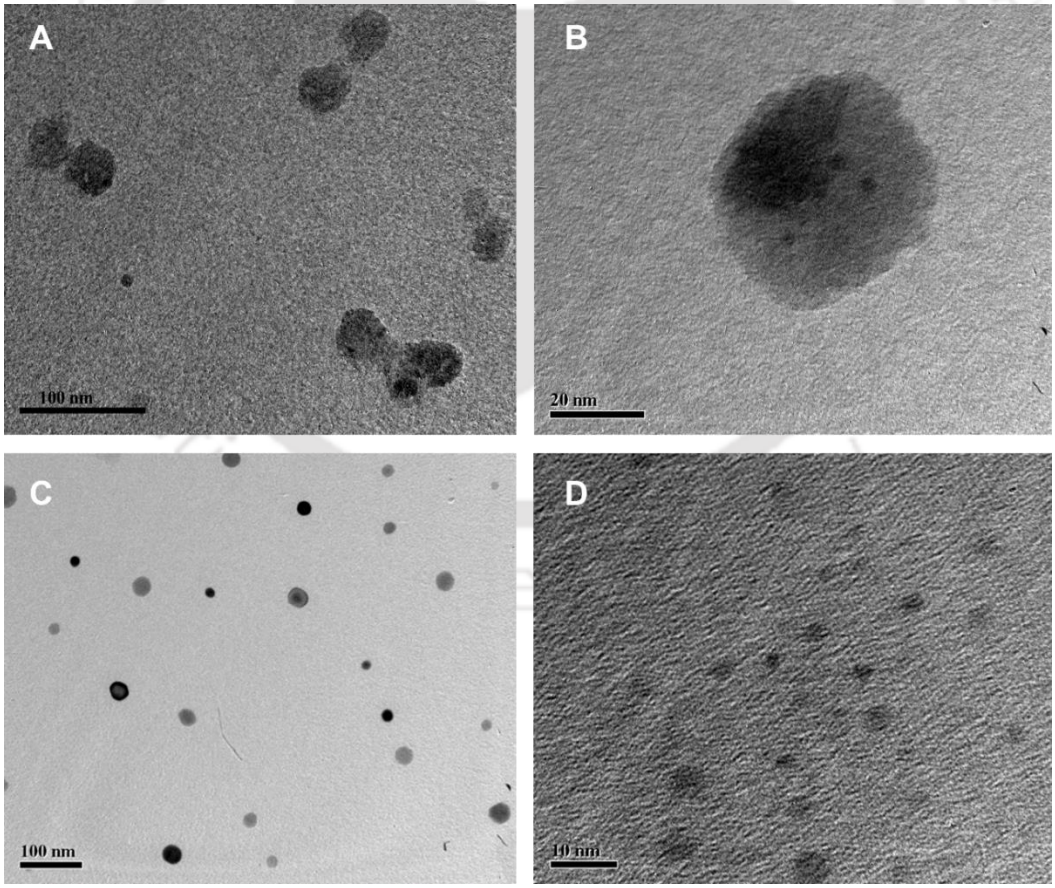

Figure 2.3. (A) TEM image of doped HAP NPs at a scale bar of 100 nm. TEM image of (B) a single doped HAP NP showing incorporated copper nanoclusters at 20 nm scale bar, (C) undoped HAP NPs (scale bar at 100 nm) and (D) copper nanoclusters (scale bar at 10 nm).

TEM images revealed doped HAP NPs (**Figure 2.3A and B**) and undoped HAP NPs (**Figure 2.3C**) with an average size of 32.64 ± 7.0 and 24.0 ± 6.0 nm, respectively. Likewise, the average size of copper nanoclusters (**Figure 2.3D**) was measured to be 1.75 ± 0.3 nm. The copper nanoclusters incorporated into doped HAP NPs were found to have an average size of 1.71 ± 0.5 nm, which is almost similar to the size of as-synthesized copper nanoclusters. The size calculations were carried out using the ImageJ software. The comparatively larger size of the doped HAP NPs might be probably due to the incorporation of copper nanoclusters, which contain the high-molecular-weight BSA as the template. Thus, from the TEM images obtained, it was confirmed that the copper nanoclusters were successfully incorporated into the doped HAP NPs.

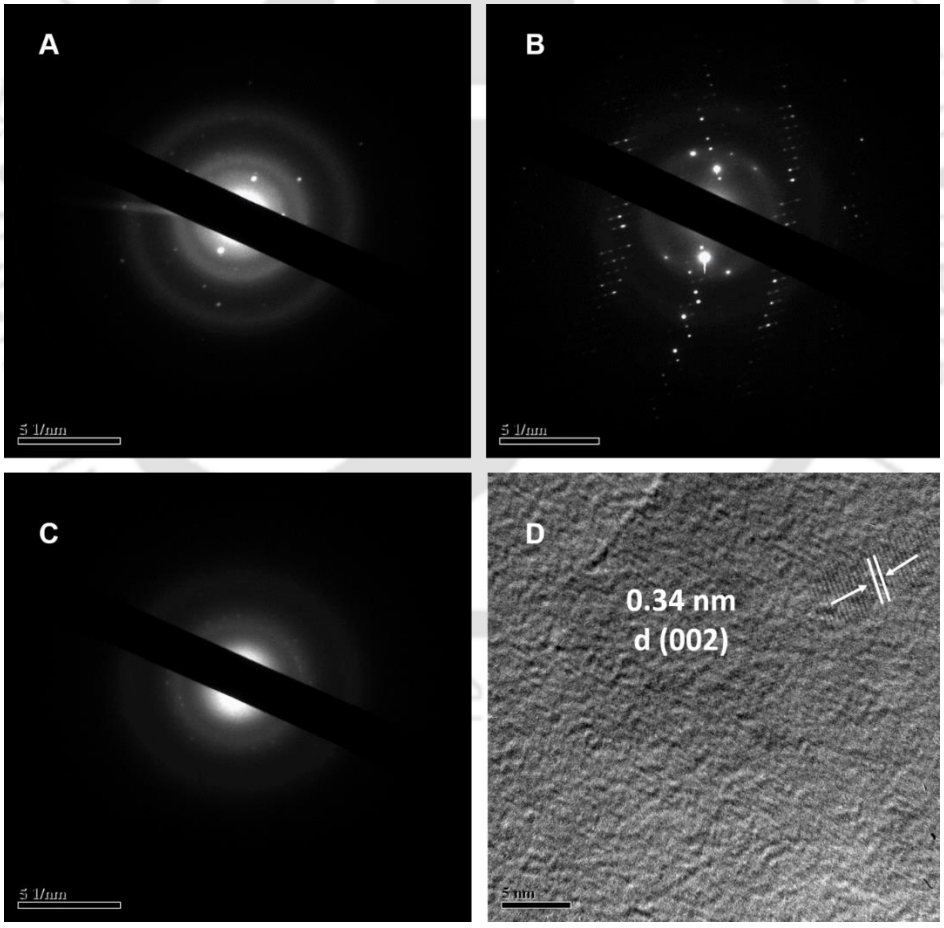

Figure 2.4. SAED images of (A) doped HAP NPs, (B) undoped HAP NPs and (C) copper nanoclusters. (D) HRTEM image of doped HAP NPs (scale bar at 5 nm).

The selected area electron diffraction (SAED) patterns obtained for doped (300), (310), and (410) and undoped HAP NPs (310), (320), and (410) corroborated the formation of HAP material as per the earlier reports[35] (**Figure 2.4A and B**). The copper nanoclusters themselves did not show any significant SAED pattern (**Figure 2.4C**). The high resolution TEM (HRTEM) image of the doped HAP NPs (**Figure 2.4D**) exhibited a lattice spacing of 0.34 nm that corresponds to the (002) plane of HAP.[36]

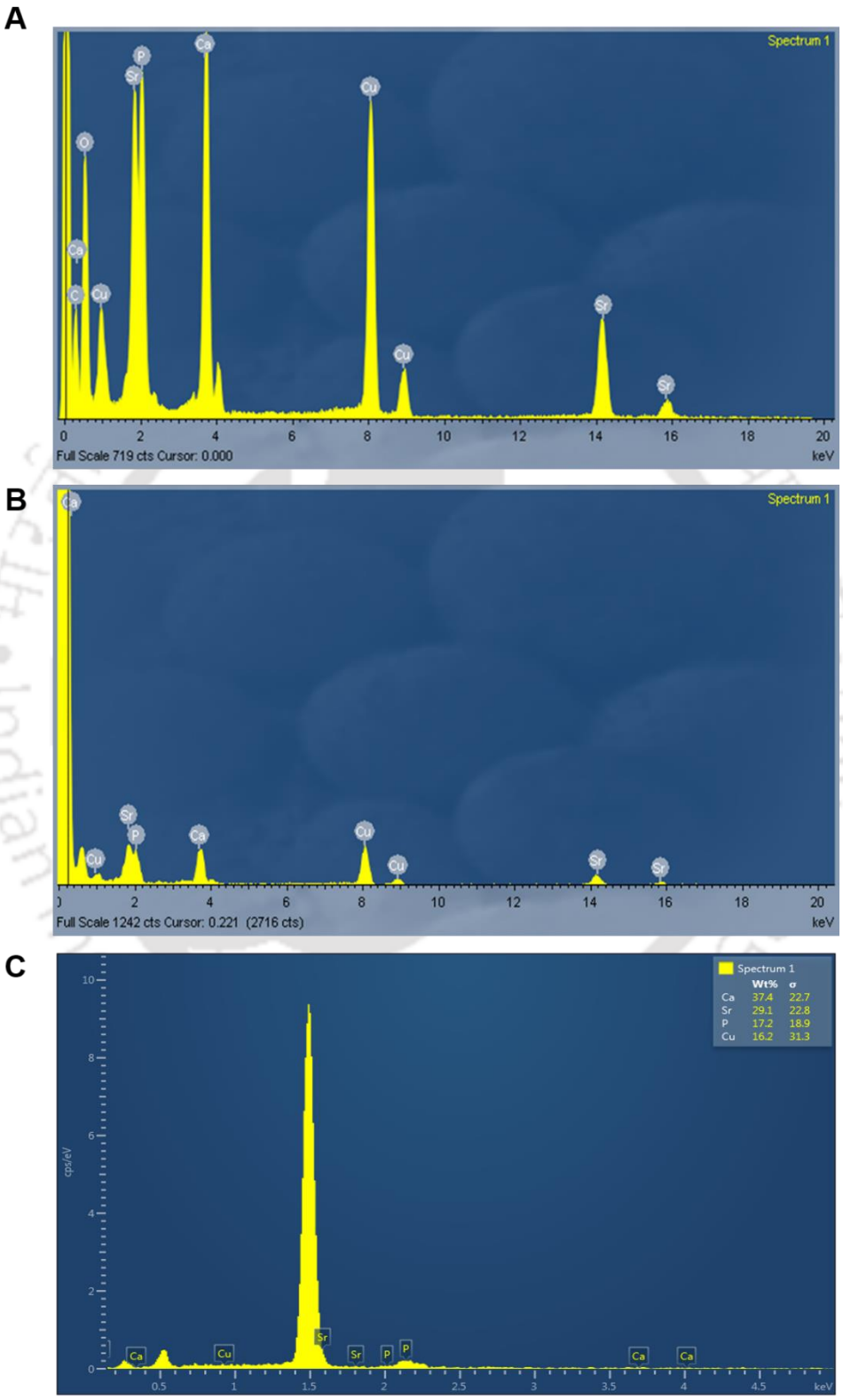

Figure 2.5. TEM-EDX spectra showing elemental composition of (A) doped HAP NPs with higher copper concentration and (B) undoped HAP NPs. (C) FESEM-EDX spectrum of doped HAP NPs

The energy-dispersive X-ray (EDX) spectroscopy analysis revealed the presence of metal ions used in the synthesis of doped and undoped HAP NPs (**Figure 2.5A-C**). The elemental composition confirms the presence of calcium, phosphorous, strontium, and copper ions at higher amount in doped HAP NPs. The FESEM images obtained further revealed the formation of doped HAP NPs with an average size of 32.07 ± 7.0 nm (**Figure 2.6A and B**). The size calculated using the ImageJ software corresponded with the sizes obtained by TEM analysis.

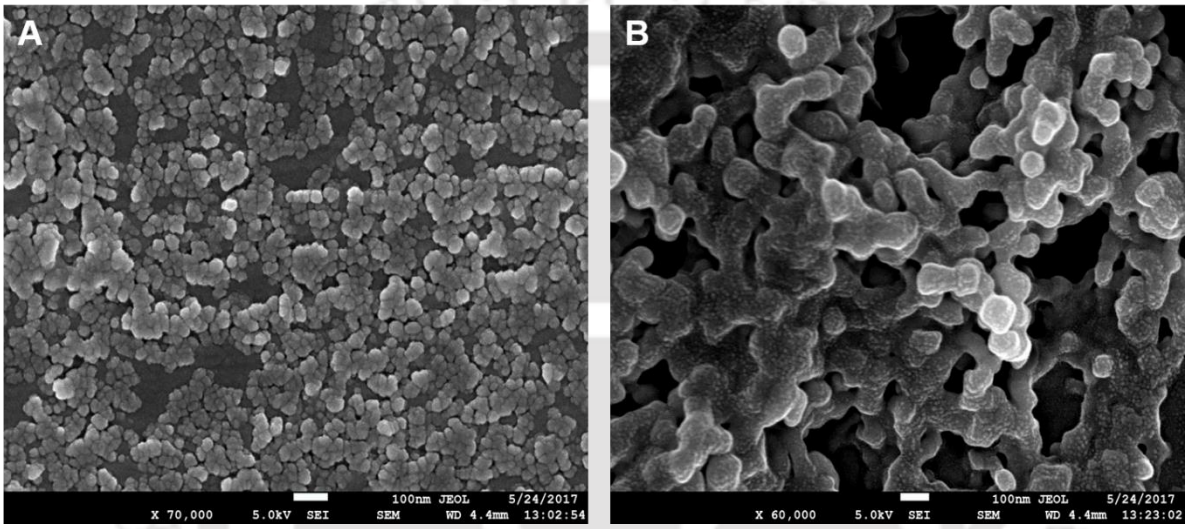

Figure 2.6. FESEM images of doped HAP NPs at (A) low magnification and (B) high magnification (scale bar at 100 nm).

The zeta potential analysis confirmed that doped HAP NPs had a net negative charge of -3.14 ± 0.17 mV (**Figure 2.7A**). Also, both undoped HAP NPs and BSA-templated copper nanoclusters had zeta potential values of -0.08037 ± 0.03 and -4.17 ± 0.7 mV, respectively (**Figure 2.7B and C**). Further, kanamycin-loaded doped HAP NPs were found to possess a negative charge of -2.3 ± 0.58 mV (**Figure 2.7D**). The reduction in the negative charge of the kanamycin loaded doped HAP NPs as compared to doped HAP NPs was due to bound kanamycin, which is positively charged. This result suggests that kanamycin was successfully loaded into the doped HAP NPs. The negative charge on the nanoparticles is beneficial to be used as a drug cargo where positively charged drug can be loaded through electrostatic interaction. The negatively charged nanoparticles exhibit reduced adsorption of plasma protein on their surface. This in fact leads to reduced opsonization and reduced clearance of the nanoparticles from the blood stream, retaining their circulation for a longer time period.

It would also aid in reduced nonspecific cellular uptake, unlike the positively charged nanoparticles.[37,38]

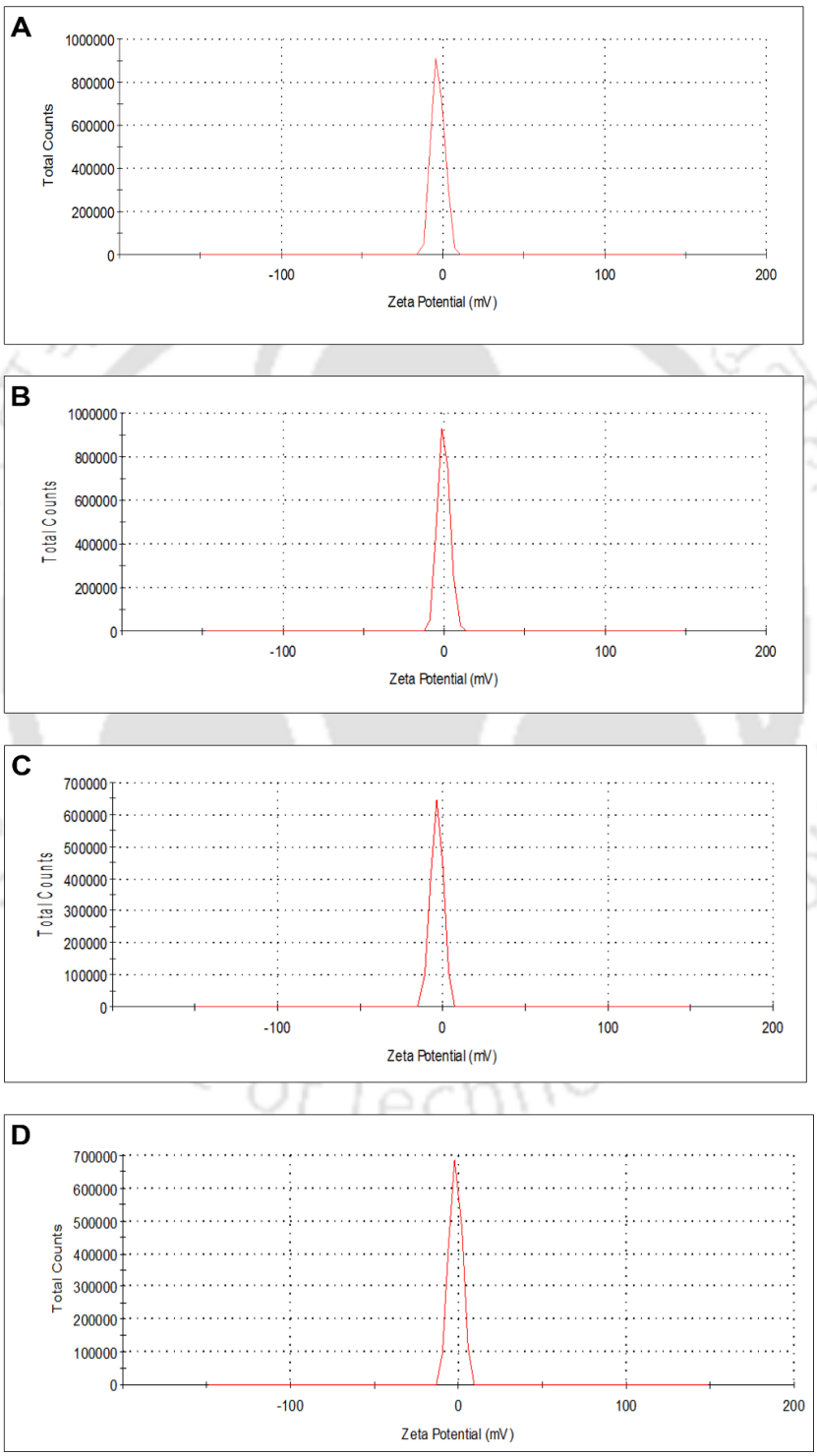

Figure 2.7. Zeta potential measurements of (A) doped HAP NPs, (B) undoped HAP NPs, (C) copper nanoclusters and (D) kanamycin loaded doped HAP NPs.

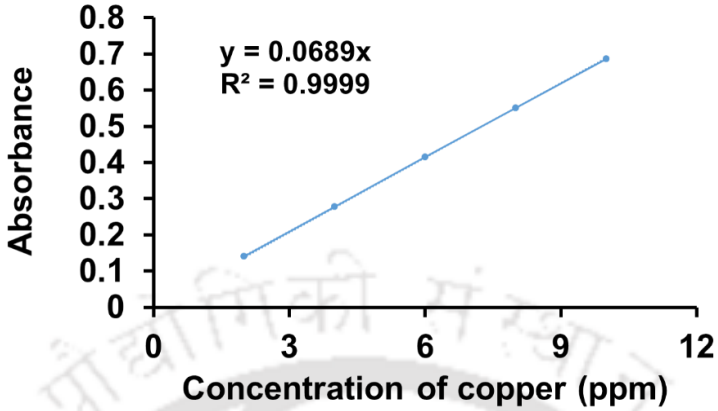

Figure 2.8. Concentration of copper calculated based on the standard curve obtained from atomic absorption spectroscopy.

Following this, atomic absorption spectroscopy was carried out, and the copper concentration in doped HAP NPs was found to be 37.8 µg/mL (**Figure 2.8**). The LC-MS analysis exhibited an m/z value of 483.26 for free kanamycin, which corroborated with the m/z value (483.27) of kanamycin loaded doped HAP NPs (**Figure 2.9A and B**). However, similar values were not obtained for the doped HAP NPs **(Figure 2.9C**). Thus, the result obtained from LC-MS suggested the interaction of kanamycin with kanamycin-loaded doped HAP NPs.[39]

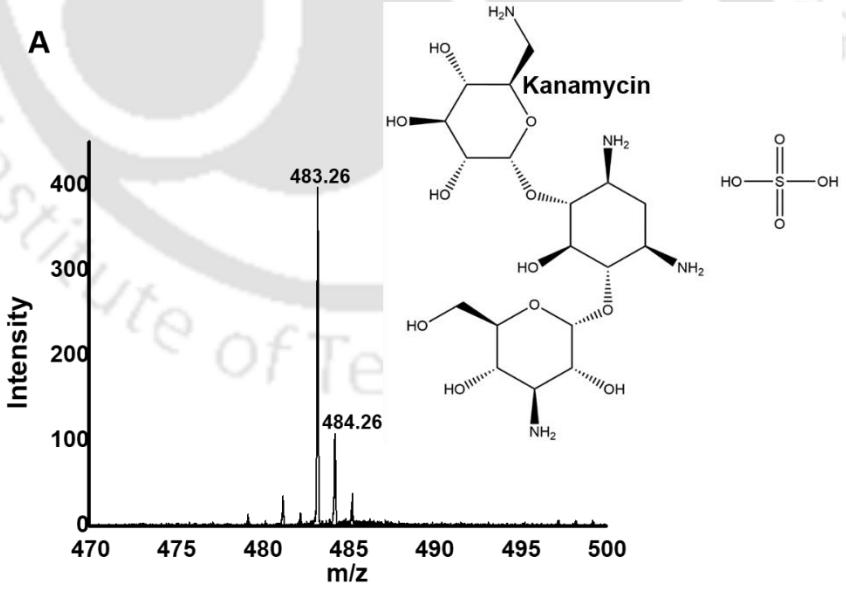

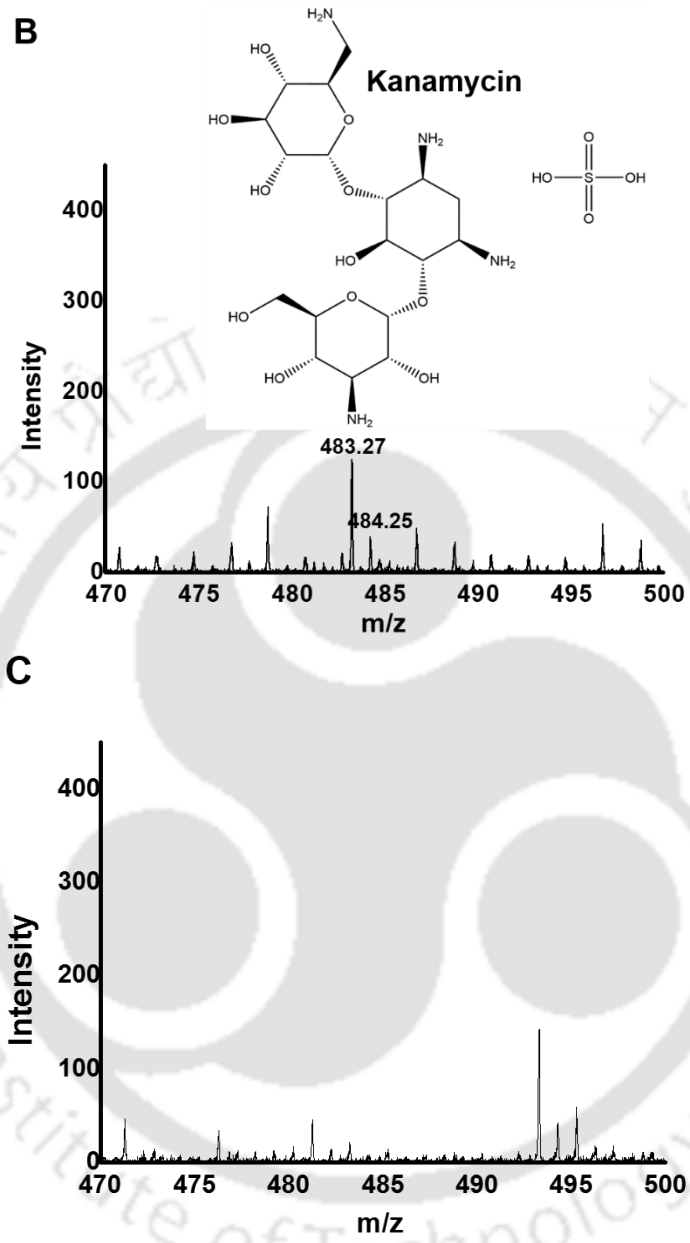

Figure 2.9. LCMS spectra of (A) free Kanamycin (structure of kanamycin is shown), (B) kanamycin loaded doped HAP NPs (kanamycin structure is shown corresponding to the m/z value = 483.27) and (C) doped HAP NPs.

2.3.2. Bioimaging Study

The luminescence characteristics exhibited by doped HAP NPs led to exploring its bioimaging aptness in the bacterial cells probing through confocal microscopy. The bacteria were treated for 3 h at 37 °C, and the imaging was done at an excitation filter of 365 nm. The images obtained showed the control bacterial cells with no luminescence (**Figure 2.10A-C**). However,

luminescence was observed in the case of doped HAP NP-treated bacterial cells, implying the fact that doped HAP NPs had been successfully incorporated in the bacteria (**Figure 2.10D-F**). The interaction between doped HAP NPs and the bacteria could be due to the influence of bridging of calcium ions with the bacterial cell wall.[40] As inferred from the confocal images, the as-synthesized doped HAP NPs were found to be attractive candidates for the bioimaging of bacterial cells. Such a nanoparticle-based bacterial imaging system would be highly advantageous in identifying pathological strains in clinical diagnosis and environmental monitoring without having to resort to time-consuming procedures.[41]

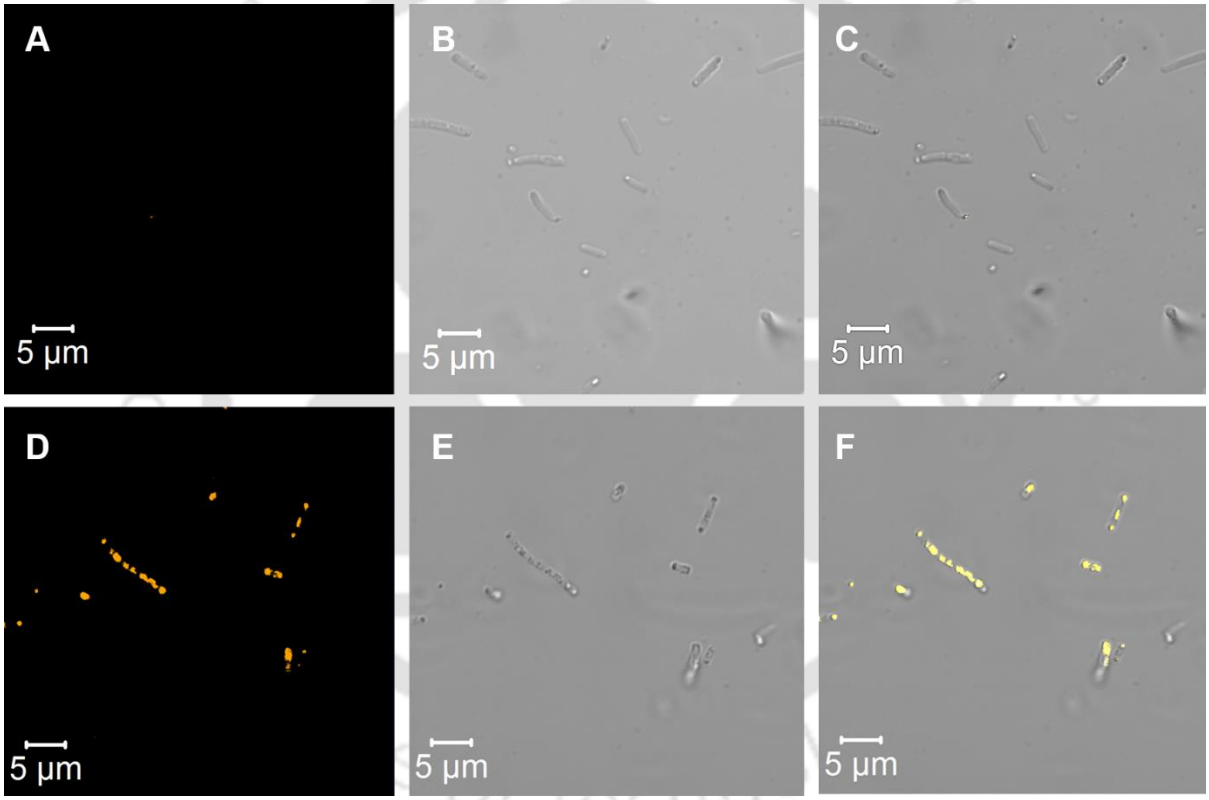

Figure 2.10. Confocal images showing the control bacterial cells (*Pseudomonas aeruginosa*) without the uptake of doped HAP NPs. (A) Fluorescence image, (B) bright field image and (C) merged image. Confocal images showing the bacterial uptake of doped HAP NPs. (D) Fluorescence image, (E) bright-field image and (F) merged image of treated bacteria. The bacteria were treated with doped HAP NPs at the MIC of kanamycin-loaded doped HAP NPs. The images were taken at a scale bar of 5 µm. An excitation filter of 365 nm was used for imaging.

2.3.3. Drug Release Study

Besides the bioimaging property, the doped HAP NPs were investigated for their efficiency to act as nanocarriers for antibacterial drug delivery. The as-synthesized doped HAP NPs, which had a negative charge, were loaded with the antibacterial drug kanamycin sulfate The efficiency of the doped HAP NPs to bind with kanamycin was investigated using the TNBS assay. The binding efficiency of doped HAP NPs was found to be 57%, and the concentration of bound kanamycin was found to be 9.3 mg/mL. To quantify the *in vitro* release of kanamycin from doped HAP NPs, the release profile was studied. The time-dependent release profile (**Figure 2.11A-C**) showed that the kanamycin release was found to be more significant in acidic pH 4 with a maximum release of 62% at 6^{th} h and gradually reducing to 40% at the end of 12^{th} h. At pH 7.4, a maximum release of only 6% was found at 8^{th} h, which gradually was reduced by 12^{th} h. At pH 8.4, 18% of release was observed at 6^{th} h, which remained constant up to 8^{th} h followed by slow reduction and finally became constant up to 12^{th} h. Here, a biphasic release pattern was observed at the acidic pH (pH 4) with an initial burst release, followed by the sustained release of antibiotic drug. An initial burst release is important to prevent the intruded bacteria from initiating their proliferation, thereby eliminating them from the infectious sites. The sustained release would further inhibit the infection with reduced toxicity having effective therapeutic index and reduced wastage of drug. The extended antibiotic delivery is also found to be advantageous over long-term oral antibiotic intake.[42-44] The sustained release of kanamycin observed after 6^{th} h at acidic pH (pH 4) is fortuitous for its action against pathogenic bacteria growing at acidic conditions.

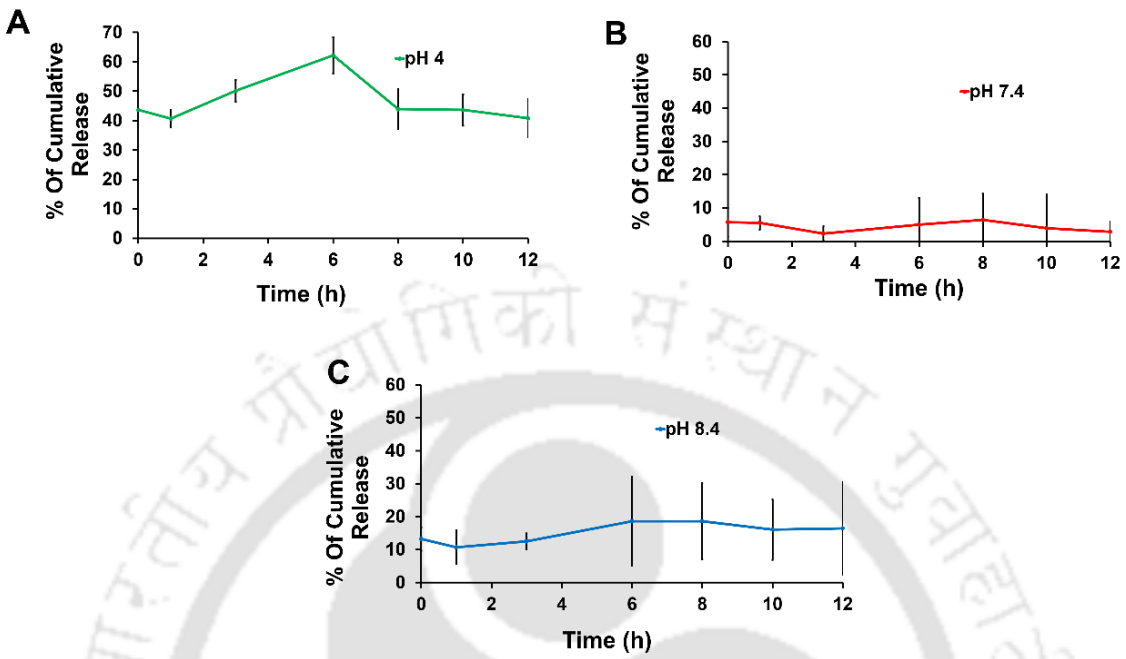

Figure 2.11. Antibacterial drug release study carried out at (A) pH 4 (acetate buffer), (B) pH 7.4 (PBS) and (C) pH 8.4 (PBS). The release study suggested maximum release at acidic pH 4 (62% at 6th h) as compared to release conducted at pH 7.4 (6% at 8th h) and pH 8.4 (18% at 6th h).

2.3.4. Biocompatibility Study

Cell cytotoxicity study is essential in understanding the biocompatibility of doped HAP NPs for their application as nanocarriers. The investigations performed revealed that the as-synthesized copper nanoclusters were toxic even at their lowest concentration (copper concentration of 1 µg/mL), whereas when doped into the HAP NPs, the toxicity was found to be negligible. Interestingly, when HeLa cells were treated with doped HAP NPs with varying copper concentrations (ranging from 1 to 10 µg/mL), the cells were observed to be viable up to 10 µg/mL of copper with minimum toxicity ((**Figure 2.12**). The procured result suggested that the doped HAP NPs qualify for their use in bioimaging applications.

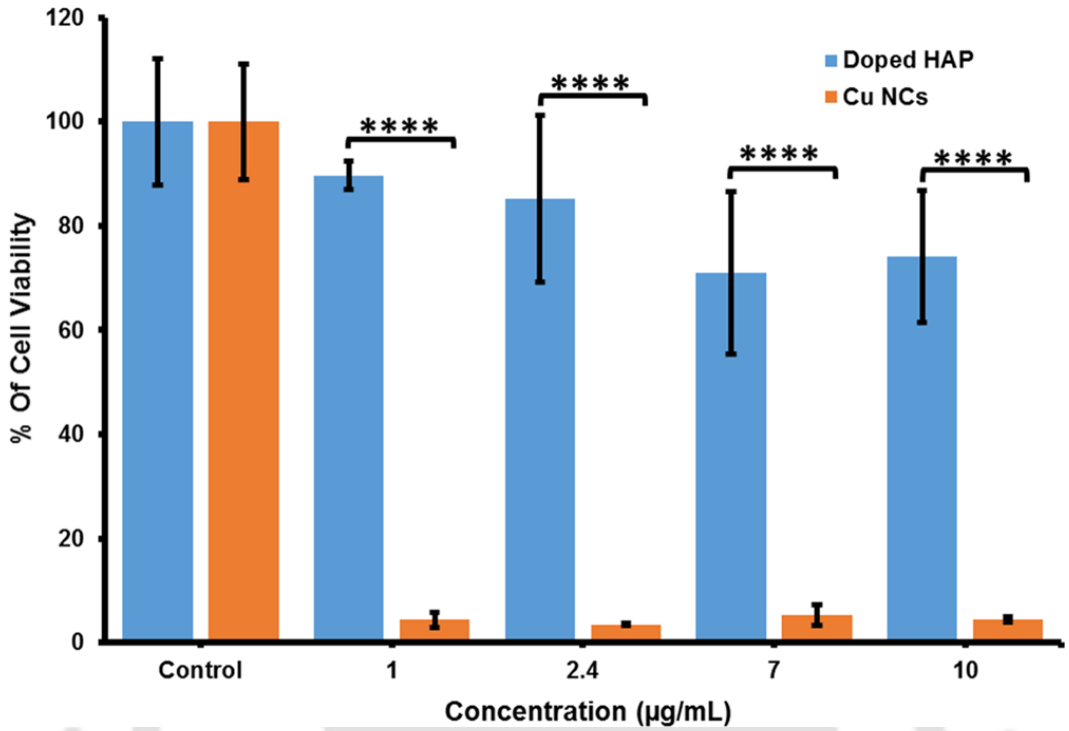

Figure 2.12. Biocompatibility of doped HAP NPs carried out on HeLa cells at different concentrations. The HeLa cells were cultured in DMEM after treatment with different concentrations of copper nanocluster-doped HAP NPs (with varying copper concentrations) and only copper nanoclusters. The MTT assay was carried out after 24 h of incubation at 37 °C. The cells were found to be viable upon treating with copper nanocluster-doped HAP NPs having a concentration of copper up to 10 µg/mL, whereas only copper nanoclusters even at their lowest copper concentration (1 µg/mL) exhibited significant toxicity toward cells. The statistical significance between copper nanocluster-doped HAP NP-treated samples and copper nanocluster-treated samples was revealed by the analysis of variance (ANOVA) test, which is denoted by **** ($p < 0.0001$). The values are represented as mean ± standard deviation (SD) of three individual experiments.

2.3.5. Antibacterial and Antibiofilm Studies

After successful loading of kanamycin, the antibacterial activity was further investigated. The antibacterial study was carried out on both Gram-positive and Gram-negative bacteria where the selected Gram-positive strains included *S. aureus* MTCC 96 and *B. subtilis* MTCC 1305. Gram-negative strains included GFP expressing recombinant *E. coli*, *P. aeruginosa* MTCC 2488, and *E. coli* DH5α. The MIC obtained for the kanamycin-loaded doped HAP NPs and free kanamycin for all the selected bacteria is given in the table (**Table 2.1**).

Among all the bacteria that were treated, the MIC of kanamycin loaded doped HAP NPs obtained for *P. aeruginosa* MTCC 2488 was found to be the least. Thus, for further studies, the Gram-negative strain *P. aeruginosa* MTCC 2488 was selected. Among the various concentrations tested, the minimum concentration of kanamycin-loaded doped HAP NPs that measurably inhibited the growth of *P. aeruginosa* was considered as the MIC. Further, by reinoculating from the culture, which lacked turbidity to a fresh medium, the MBC for the kanamycin-loaded doped HAP NPs was confirmed.

	Bacterial strains	Doped HAP + Drug (MIC)	Drug (MIC)
Gram negative	*Escherichia coli* (GFP)	20 µg/mL	4 µg/mL
	Pseudomonas aeruginosa MTCC 2488	12 µg/mL	3 µg/mL
	Escherichia coli (DH5α)	400 µg/mL	290 µg/mL
Gram positive	*Staphylococcus aureus* MTCC 96	>900 µg/mL	400 µg/mL
	Bacillus subtilis MTCC 1305	>900 µg/mL	400 µg/mL

Table 2.1. Data representing the minimum inhibition concentration (MIC) of kanamycin loaded doped HAP NPs and free kanamycin for both Gram positive and Gram negative bacteria. MIC for kanamycin loaded doped HAP NPs could be determined only for Gram negative bacteria whereas no MIC was obtained in case of Gram positive bacteria.

The growth curve studies on *P. aeruginosa* revealed that at MIC (12 µg/mL) of kanamycin-loaded doped HAP NPs, there was arrest of bacterial growth, and at its MBC (35 µg/mL), the growth was completely prevented. The free kanamycin exhibited an MIC and MBC of 3 and 6 µg/mL, respectively (**Figure 2.13A**). As observed in the figure (**Figure 2.13A**), there was no bactericidal activity for doped HAP NPs unlike kanamycin loaded doped HAP NPs. The bacteria were plated on nutrient agar media to further confirm the MIC and MBC where only few bacterial colonies were observed in the case of kanamycin loaded doped HAP NPs at their MIC and no bacterial colony at their MBC (**Figure 2.13B (I-III)**). Similar results were obtained

when bacteria were treated with the MIC and MBC of free kanamycin (**Figure 2.13B (IV and V)**).

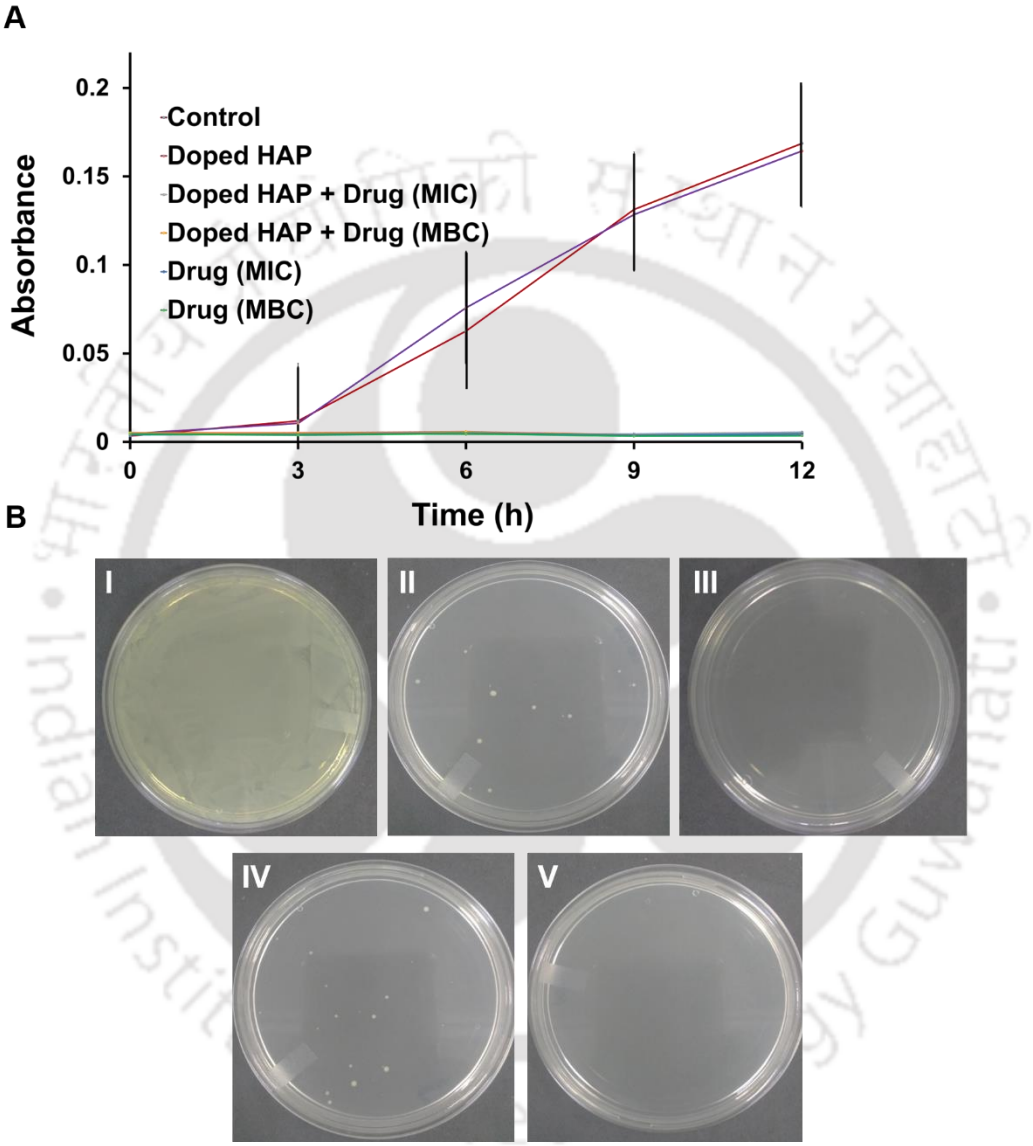

Figure 2.13. (A) Growth curve study showing the inhibitory and killing effect of doped HAP NPs, kanamycin-loaded doped HAP NPs and free kanamycin on *P. aeruginosa* by measuring the OD at 595 nm. The kanamycin concentration was 12 µg/mL (MIC) and 35 µg/mL (MBC) in kanamycin-loaded doped HAP NPs, 3 µg/mL (MIC) and 6 µg/mL (MBC) in free kanamycin and 0 µg/mL in doped HAP NPs. (B) Bacteria (*Pseudomonas aeruginosa*) grown on nutrient agar. (I) Control, bacteria treated with kanamycin loaded doped HAP NPs at their (II) MIC-12 µg/mL and (III) MBC-35 µg/mL; bacteria treated with free kanamycin at its (IV) MIC-3 µg/mL and (V) MBC-6 µg/mL.

The pattern of activity exhibiting slightly higher detrimental effect by free drug than the drug-loaded carrier is found to be similar with various previously reported studies conducted on nanocarrier-based drug delivery.[45-49] The higher MIC of kanamycin-loaded doped HAP NPs as compared to the lower MIC of free kanamycin was probably due to the partial release of kanamycin from the kanamycin-loaded doped HAP NPs.[50] The antibiotics bound to nanocarriers have several merits over free antibiotics in terms of reduced side effects and stability. Such antibiotic-loaded nanocarriers are beneficial as they play the role of protecting the bound antibiotic from early degradation upon interacting with molecules present in the physiological environment.[51-53] Further, the interaction of kanamycin loaded doped HAP NPs with bacteria was studied using the FESEM analysis. When compared with control bacterial cells, which had smooth cell surfaces (**Figure 2.14A**), the treated bacterial cell showed disrupted cell wall (**Figure 2.14B**) because of their interaction with kanamycin-loaded doped HAP NPs. This strongly suggested that the kanamycin-loaded doped HAP NPs could effectively release kanamycin that interacted with the bacteria. The kanamycin could probably use the internal iron from the iron-sulfur cluster, leading to the formation of hydroxyl radicals mediated by the tricarboxylic acid cycle. This finally results in the depletion of NADH and cell damage.[54] The bactericidal activity and the higher susceptibility of *P. aeruginosa* over all other tested bacterial species toward as-synthesized kanamycin-loaded doped HAP NPs suggested their use in advanced applications.

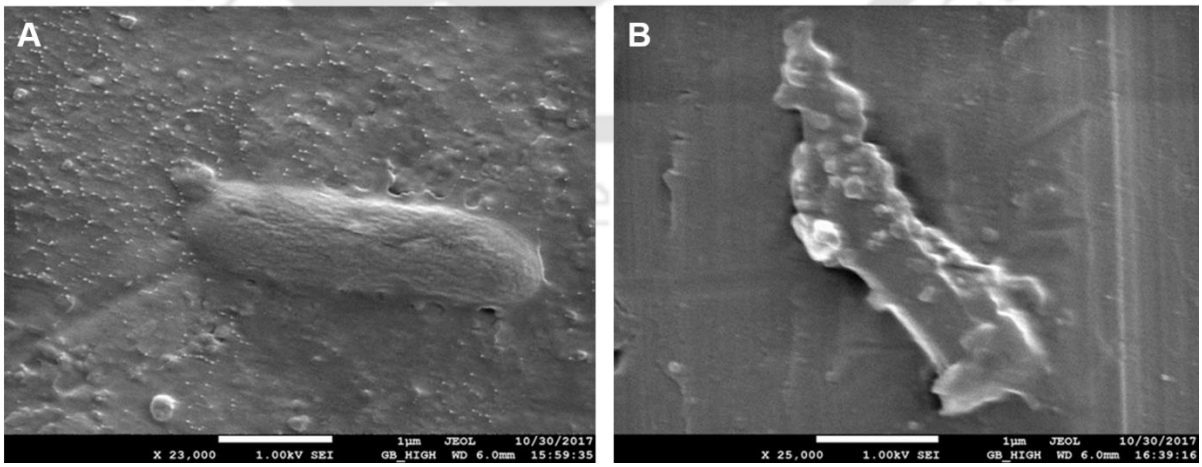

Figure 2.14. FESEM images of (A) control bacteria (*Pseudomonas aeruginosa*) and (B) bacteria treated by kanamycin loaded doped HAP NPs at their MIC. The images are taken at a scale bar of 1 µm.

This led us to investigate the activity of kanamycin-loaded doped HAP NPs against *P. aeruginosa* biofilm as a proof of principle for application of these nanocarriers in antibiofilm activity. Adhesion of bacteria followed by their colonization and formation of biofilms on either animate or inanimate surfaces can cause serious complications which are actively studied upon.[55] *P. aeruginosa*, being an opportunistic pathogen, is capable of forming robust biofilms and is responsible for various life-threatening infections.[56] The antibiofilm studies carried out on *P. aeruginosa* at different concentrations of kanamycin (12, 35, 100, and 400 µg/mL) revealed 50% ($MBIC_{50}$) inhibition by the kanamycin-loaded doped HAP NPs at a concentration of 400 µg/mL (**Figure 2.15**). Treatment with free kanamycin exhibited 50% ($MBIC_{50}$) inhibition at 100 µg/mL. The results obtained for the antibiofilm activity corroborated the results of antibacterial studies conducted on *P. aeruginosa*.

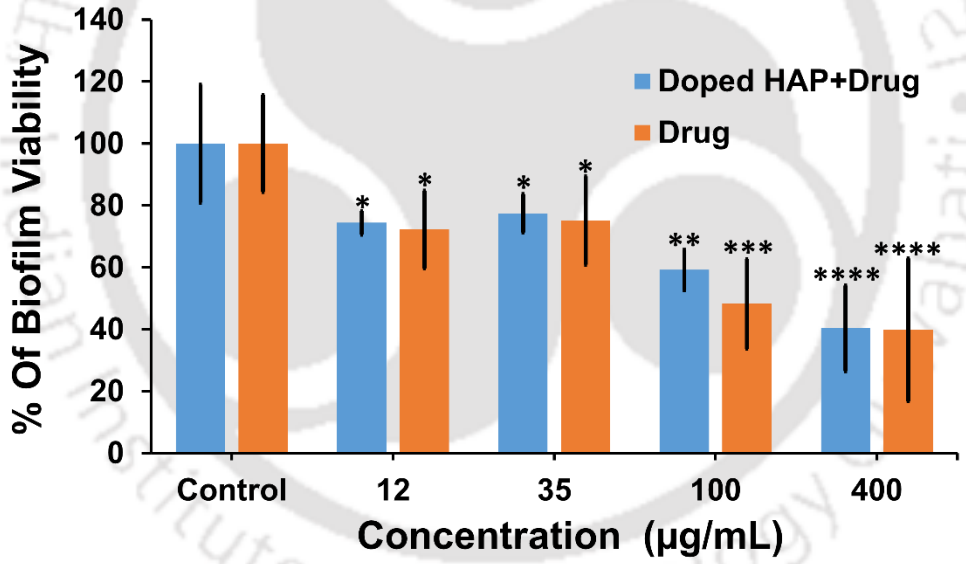

Figure 2.15. Antibiofilm activity of both kanamycin-loaded doped HAP NPs and free kanamycin on *P. aeruginosa*. The ANOVA test revealed the statistical significance of kanamycin-loaded doped HAP NP-treated samples and free kanamycin-treated samples with respect to control sample. Statistical significance is denoted by * ($p < 0.05$), ** ($p < 0.005$), *** ($p < 0.001$), and **** ($p < 0.0001$). The data are represented as mean ± SD of three individual experiments.

The antibiofilm activity was further characterized by epifluorescence imaging where Nile red staining was used to study the lipid content. *P. aeruginosa* being a Gram-negative bacterium possesses an outer membrane highly rich in lipid content.[57] In the case of the control biofilm, the epifluorescence images obtained showed high lipid content covering almost the entire area

of individual wells in a 96-well plate emitting high fluorescence (**Figure 2.16A**). In the case of biofilm treated with the $MBIC_{50}$ (400 µg/mL) of kanamycin loaded doped HAP NPs, reduced fluorescence intensity (**Figure 2.16B**) was observed. This suggested that kanamycin released from the doped HAP NPs could prevent the proliferation of bacteria, leading to reduced biofilm mass as indicated by the diminished lipid content. The epifluorescence image showing Nile red stained biofilm treated with free kanamycin is given (**Figure 2.16C**). The bright-field images of the control biofilm, biofilm treated with kanamycin-loaded doped HAP NPs and free kanamycin are shown (**Figure 2.16D-F)**

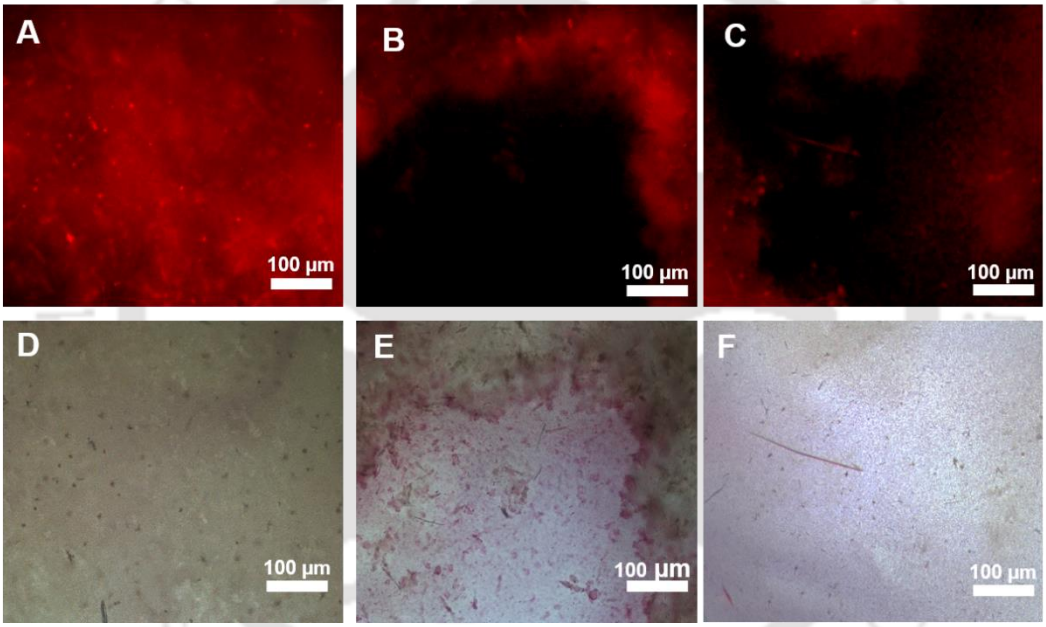

Figure 2.16. Epifluorescence images of *P. aeruginosa* biofilm stained with Nile red at an excitation and emission wavelength of 540/25 nm and 605/55 nm, respectively. (A) Control biofilm, biofilm treated with (B) kanamycin-loaded doped HAP NPs and (C) free kanamycin at its $MBIC_{50}$ for 12 h. The corresponding bright-field image of (D) control biofilm, biofilm treated with (E) kanamycin-loaded doped HAP NPs and (F) free kanamycin. The control biofilm having high lipid content exhibited high fluorescence, whereas diminished fluorescence was observed in the treated biofilm because of reduced lipid content. The epifluorescence images were taken at a scale bar of 100 µm.

The dual staining study carried out using the AO/PI dyes indicated that the kanamycin-loaded doped HAP NPs could reduce the biofilm mass. As visualized, the control cells after being treated with AO/PI dual stain could take up the stains and emit out green fluorescence because of the uptake of AO stain by live bacterial cells.

There was only negligible red fluorescence (due to PI) from the control cells, possibly due to very less number of dead bacterial cells (**Figure 2.17A (I-III)**). In the case of the biofilm treated with the $MBIC_{50}$ of kanamycin loaded doped HAP NPs (**Figure 2.17B (I-III)**), a prominent red fluorescence could be visualized possibly due to the penetration of PI stain through the damaged bacterial cell membrane. Only a limited area showed green fluorescence where a few viable bacterial cells were present. The epifluorescence images of the biofilm treated with free kanamycin are given (**Figure 2.17C (I-III)**). From the epifluorescence characterization, the reduction in the biofilm mass observed by both Nile red and AO/PI-based staining suggested that doped HAP NPs releasing kanamycin are promising therapeutic agents against recurrent biofilm infections.

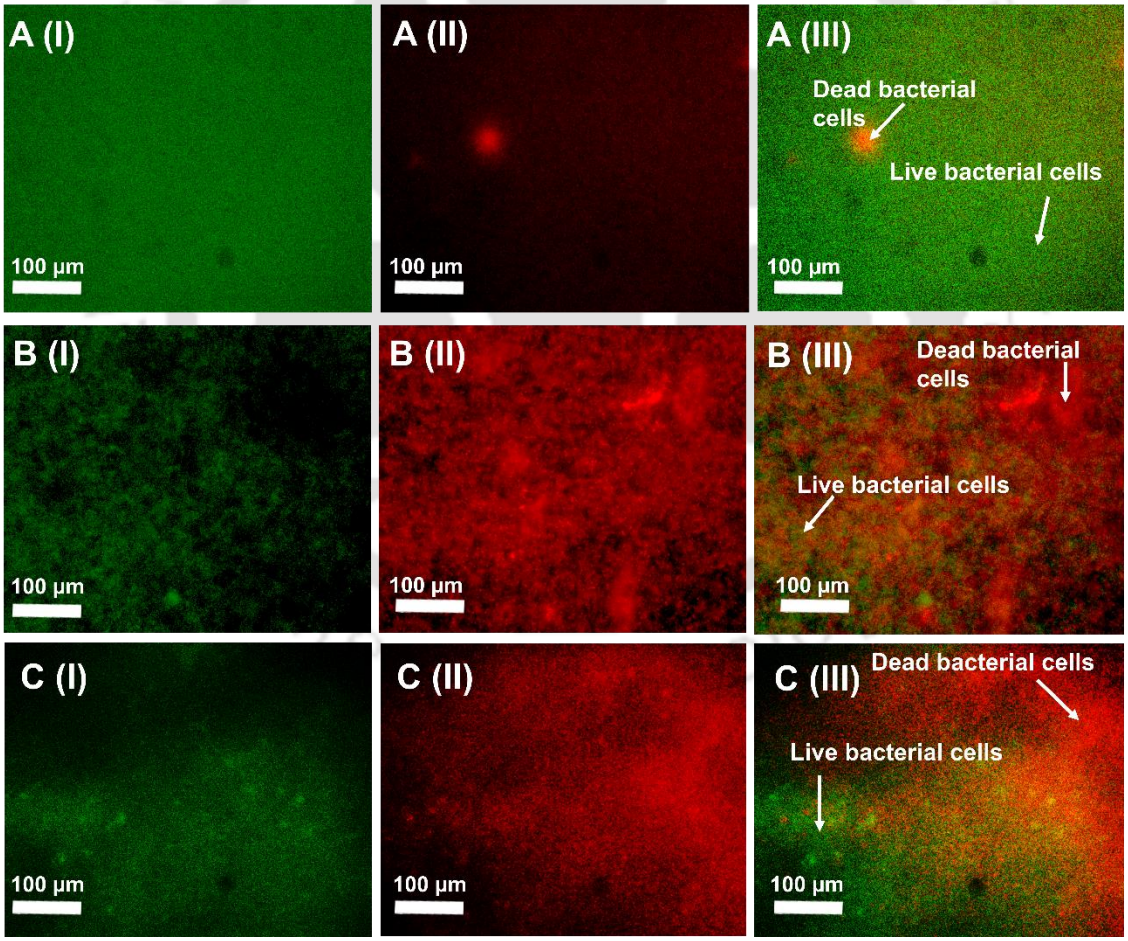

Figure 2.17. [A(I-III)] Epifluorescence images of AO/PI stained control biofilm: [A(I)] AO stained, [A(II)] PI stained and [A(III)] merged image. The arrows in the merged image of the control biofilm denote the regions with dead and live bacterial cells. [B(I-III)] *Pseudomonas aeruginosa* biofilm treated with kanamycin-loaded doped HAP NPs: [B(I)] AO stained, [B(II)]

PI stained and [B(III)] merged image. The arrows in the merged image of the treated biofilm denote the regions with dead and live bacterial cells. For imaging, the biofilm was treated with kanamycin-loaded doped HAP NPs at their $MBIC_{50}$ for 12 h. [C(I-III)] Epifluorescence images of AO/PI stained biofilm treated with free kanamycin. [C(I)] AO stained, [C(II)] PI stained and [C(III)] merged image of biofilm. The red region in the merged image marks the area with dead bacterial cells whereas green marks the area with live cells. The excitation/emission of AO is 465-495/515-55 nm. PI was excited at 540/25 nm with an emission at 605/55 nm. The control biofilm with negligible number of dead bacterial cells emitted green fluorescence because of AO uptake by live bacterial cells. The red fluorescence emitted from the treated biofilm is due to dead bacterial cells stained by PI. The images were taken at a scale bar of 100 µm.

2.4. Conclusions

In brief, HAP NPs were synthesized and further doped with luminescent copper nanoclusters. The doped HAP NPs being negatively charged were successfully loaded with positively charged antibacterial drug kanamycin. Having been explored for their antibacterial activity against both Gram-positive and Gram-negative bacteria, the kanamycin-loaded doped HAP NPs were found to be more effective against Gram-negative bacteria as compared to Gram positive bacteria. The doping of luminescent copper nanoclusters on the as-synthesized HAP NPs endowed the entire nanoformulation with the possibility of bioimaging of bacterial cells. The investigation on biocompatibility of doped HAP NPs in HeLa cells revealed their negligible toxic nature even at higher concentrations of copper. This result was in contradiction with the significant toxicity exhibited on HeLa cells by copper nanoclusters at their lowest copper concentration. The sustained release of kanamycin from kanamycin-loaded doped HAP NPs was found to eradicate *P. aeruginosa* biofilm. Thus, the present copper nanocluster-doped HAP NPs qualify to be used as a drug cargo as a proof of principle for application in nanocarrier-based antibiotic delivery with bioimaging property, antibacterial, and antibiofilm applications.

2.5. References

1. Nikaido, H., Multidrug Resistance in Bacteria. *Annu Rev Biochem* **2009,** *78*, 119-146.
2. Rai, M. K.; Deshmukh, S. D.; Ingle, A. P.; Gade, A. K., Silver nanoparticles: the powerful nanoweapon against multidrug-resistant bacteria. *J Appl Microbiol* **2012,** *112* (5), 841-852.

3. Li, X.; Robinson, S. M.; Gupta, A.; Saha, K.; Jiang, Z.; Moyano, D. F.; Sahar, A.; Riley, M. A.; Rotello, V. M., Functional gold nanoparticles as potent antimicrobial agents against multi-drug-resistant bacteria. *Acs Nano* **2014,** *8* (10), 10682-6.
4. Ding, X. K.; Duan, S.; Ding, X. J.; Liu, R. H.; Xu, F. J., Versatile Antibacterial Materials: An Emerging Arsenal for Combatting Bacterial Pathogens. *Adv Funct Mater* **2018,** *28* (40), 1802140.
5. Radovic-Moreno, A. F.; Lu, T. K.; Puscasu, V. A.; Yoon, C. J.; Langer, R.; Farokhzad, O. C., Surface Charge-Switching Polymeric Nanoparticles for Bacterial Cell Wall-Targeted Delivery of Antibiotics. *Acs Nano* **2012,** *6* (5), 4279-4287.
6. Xu, Z. P.; Zeng, Q. H.; Lu, G. Q.; Yu, A. B., Inorganic nanoparticles as carriers for efficient cellular delivery. *Chem Eng Sci* **2006,** *61* (3), 1027-1040
7. Dasgupta, S.; Banerjee, S. S.; Bandyopadhyay, A.; Bose, S., Zn- and Mg-Doped Hydroxyapatite Nanoparticles for Controlled Release of Protein. *Langmuir* **2010,** *26* (7), 4958-4964.
8. Rusu, V. M.; Ng, C. H.; Wilke, M.; Tiersch, B.; Fratzl, P.; Peter, M. G., Size-controlled hydroxyapatite nanoparticles as self-organized organic-in organic composite materials. *Biomaterials* **2005,** *26* (26), 5414-5426.
9. Zhou, H.; Lee, J., Nanoscale hydroxyapatite particles for bone tissue engineering. *Acta Biomater* **2011,** *7* (7), 2769-2781.
10. Han, Y.; Wang, X.; Dai, H.; Li, S., Nanosize and surface charge effects of hydroxyapatite nanoparticles on red blood cell suspensions. *ACS Appl Mater Interfaces* **2012,** *4* (9), 4616-22.
11. Wei, G. B.; Ma, P. X., Structure and properties of nano-hydroxyapatite/polymer composite scaffolds for bone tissue engineering. *Biomaterials* **2004,** *25* (19), 4749-4757.
12. Haider, A.; Haider, S.; Han, S. S.; Kang, I. K., Recent advances in the synthesis, functionalization and biomedical applications of hydroxyapatite: a review. *Rsc Adv* **2017,** *7* (13), 7442-7458.
13. Syamchand, S. S.; Sony, G., Multifunctional hydroxyapatite nanoparticles for drug delivery and multimodal molecular imaging. *Microchim Acta* **2015,** *182* (9-10), 1567-1589.
14. Venkatasubbu, G. D.; Ramasamy, S.; Avadhani, G. S.; Ramakrishnan, V.; Kumar, J., Surface modification and paclitaxel drug delivery of folic acid modified polyethylene glycol functionalized hydroxyapatite nanoparticles. *Powder Technol* **2013,** *235*, 437-442.
15. Boonsongrit, Y.; Abe, H.; Sato, K.; Naito, M.; Yoshimura, M.; Ichikawa, H.; Fukumori, Y., Controlled release of bovine serum albumin from hydroxyapatite microspheres for protein delivery system. *Mater Sci Eng B-Adv* **2008,** *148* (1-3), 162-165.
16. Wang, X.; Wu, X.; Xing, H. L.; Zhang, G. L.; Shi, Q.; E, L. L.; Liu, N.; Yang, T. Y.; Wang, D. S.; Qi, F.; Wang, L. Y.; Liu, H. C., Porous Nanohydroxyapatite/Collagen Scaffolds

Loading Insulin PLGA Particles for Restoration of Critical Size Bone Defect. *Acs Appl Mater Inter* **2017,** *9* (13), 11380-11391.

17. Iafisco, M.; Palazzo, B.; Marchetti, M.; Margiotta, N.; Ostuni, R.; Natile, G.; Morpurgo, M.; Gandin, V.; Marzano, C.; Roveri, N., Smart delivery of antitumoral platinum complexes from biomimetic hydroxyapatite nanocrystals. *J Mater Chem* **2009,** *19* (44), 8385-8392.

18. Chen, F.; Huang, P.; Zhu, Y. J.; Wu, J.; Zhang, C. L.; Cui, D. X., The photoluminescence, drug delivery and imaging properties of multifunctional Eu3+/Gd3+ dual-doped hydroxyapatite nanorods. *Biomaterials* **2011,** *32* (34), 9031-9039.

19. Liu, G.; Talley, J. W.; Na, C.; Larson, S. L.; Wolfe, L. G., Copper doping improves hydroxyapatite sorption for arsenate in simulated groundwaters. *Environ Sci Technol* **2010,** *44* (4), 1366-72.

20. Xie, J. P.; Zheng, Y. G.; Ying, J. Y., Protein-Directed Synthesis of Highly Fluorescent Gold Nanoclusters. *J Am Chem Soc* **2009,** *131* (3), 888-889.

21. de Romana, D. L.; Olivares, M.; Uauy, R.; Araya, M., Risks and benefits of copper in light of new insights of copper homeostasis. *J Trace Elem Med Bio* **2011,** *25* (1), 3-13.

22. Das, N. K.; Ghosh, S.; Priya, A.; Datta, S.; Mukherjee, S., Luminescent Copper Nanoclusters as a Specific Cell-Imaging Probe and a Selective Metal Ion Sensor. *J Phys Chem C* **2015,** *119* (43), 24657-24664.

23. Li, L.; Liu, Y. K.; Tao, J. H.; Zhang, M.; Pan, H. H.; Xu, X. R.; Tang, R. K., Surface modification of hydroxyapatite nanocrystallite by a small amount of terbium provides a biocompatible fluorescent probe. *J Phys Chem C* **2008,** *112* (32), 12219-12224.

24. Zhang, Q.; Dan, S. M.; Du, K. F., Fabrication and Characterization of Magnetic Hydroxyapatite Entrapped Agarose Composite Beads with High Adsorption Capacity for Heavy Metal Removal. *Ind Eng Chem Res* **2017,** *56* (30), 8705-8712.

25. Deshmukh, K.; Shaik, M. M.; Ramanan, S. R.; Kowshik, M., Self-Activated Fluorescent Hydroxyapatite Nanoparticles: A Promising Agent for Bioimaging and Biolabeling. *Acs Biomater Sci Eng* **2016,** *2* (8), 1257-1264.

26. Bashir, K. M. I.; Cho, M. G., The Effect of Kanamycin and Tetracycline on Growth and Photosynthetic Activity of Two Chlorophyte Algae. *Biomed Res Int* **2016**.

27. Liu, Y. K.; Hou, D. D.; Wang, G. H., A simple wet chemical synthesis and characterization of hydroxyapatite nanorods. *Mater Chem Phys* **2004,** *86* (1), 69-73.

28. Bharath, G.; Kumar, A. J.; Karthick, K.; Mangalaraj, D.; Viswanathan, C.; Ponpandian, N., Shape evolution and size controlled synthesis of mesoporous hydroxyapatite nanostructures and their morphology dependent Pb(II) removal from waste water. *Rsc Adv* **2014,** *4* (70), 37446-37457.

29. Wang, C.; Wang, C. X.; Xu, L.; Cheng, H.; Lin, Q.; Zhang, C., Protein-directed synthesis of pH-responsive red fluorescent copper nanoclusters and their applications in cellular imaging and catalysis. *Nanoscale* **2014,** *6* (3), 1775-1781.

30. Benjamin, D. M.; Mccormack, J. J.; Gump, D. W., Use of Newer Amino Group Reagents for Detection and Determination of Kanamycin. *Anal Chem* **1973,** *45* (8), 1531-1534.

31. Kapoor, V.; Rai, R.; Thiyagarajan, D.; Mukherjee, S.; Das, G.; Ramesh, A., A Nonbactericidal Zinc-Complexing Ligand as a Biofilm Inhibitor: Structure-Guided Contrasting Effects on Staphylococcus aureus Biofilm. *Chembiochem: a European journal of chemical biology* **2017,** *18* (15), 1502-1509.

32. Zhang, X.; Wang, K.; Liu, M.; Zhang, X.; Tao, L.; Chen, Y.; Wei, Y., Polymeric AIE-based nanoprobes for biomedical applications: recent advances and perspectives. *Nanoscale* **2015,** *7* (27), 11486-508.

33. Goswami, N.; Yao, Q.; Luo, Z.; Li, J.; Chen, T.; Xie, J., Luminescent Metal Nanoclusters with Aggregation-Induced Emission. *The journal of physical chemistry letters* **2016,** *7* (6), 962-75.

34. Wang, C. X.; Wang, Y.; Xu, L.; Zhang, D.; Liu, M. X.; Li, X. W.; Sun, H. C.; Lin, Q.; Yang, B., Facile Aqueous-Phase Synthesis of Biocompatible and Fluorescent Ag_2S Nanoclusters for Bioimaging: Tunable Photoluminescence from Red to Near Infrared. *Small* **2012,** *8* (20), 3137-3142.

35. Farzadi, A.; Bakhshi, F.; Solati-Hashjin, M.; Asadi-Eydivand, M.; abu Osman, N. A., Magnesium incorporated hydroxyapatite: Synthesis and structural properties characterization. *Ceram Int* **2014,** *40* (4), 6021-6029.

36. Amer, W.; Abdelouahdi, K.; Ramananarivo, H. R.; Zahouily, M.; Fihri, A.; Djessas, K.; Zahouily, K.; Varma, R. S.; Solhy, A., Microwave-assisted synthesis of mesoporous nano-hydroxyapatite using surfactant templates. *Crystengcomm* **2014,** *16* (4), 543-549.

37. Blanco, E.; Shen, H.; Ferrari, M., Principles of nanoparticle design for overcoming biological barriers to drug delivery. *Nat Biotechnol* **2015,** *33* (9), 941-951.

38. Alexis, F.; Pridgen, E.; Molnar, L. K.; Farokhzad, O. C., Factors affecting the clearance and biodistribution of polymeric nanoparticles. *Mol Pharm* **2008,** *5* (4), 505-15.

39. Shymanski, E.L.; Neumann, S., The critical assessment of small molecule identification (CASMI): challenges and solutions. *Metabolites* **2013,** *3*,517-538

40. Clark, W. B.; Bammann, L. L.; Gibbons, R. J., Comparative Estimates of Bacterial Affinities and Adsorption Sites on Hydroxyapatite Surfaces. *Infect Immun* **1978,** *19* (3), 846-853.

41. Wang, L.; Zhao, W.; O'Donoghue, M. B.; Tan, W., Fluorescent nanoparticles for multiplexed bacteria monitoring. *Bioconjugate chemistry* **2007,** *18* (2), 297-301.

42. Cui, W.; Li, X.; Zhu, X.; Yu, G.; Zhou, S.; Weng, J., Investigation of drug release and matrix degradation of electrospun poly(DL-lactide) fibers with paracetanol inoculation. *Biomacromolecules* **2006,** *7* (5), 1623-9.

43. Song, J.; Chen, Q.; Zhang, Y.; Diba, M.; Kolwijck, E.; Shao, J.; Jansen, J. A.; Yang, F.; Boccaccini, A. R.; Leeuwenburgh, S. C., Electrophoretic Deposition of Chitosan Coatings Modified with Gelatin Nanospheres To Tune the Release of Antibiotics. *ACS Appl Mater Interfaces* **2016,** *8* (22), 13785-92.

44. Chen, H.; Wang, L.; Yeh, J.; Wu, X.; Cao, Z.; Wang, Y. A.; Zhang, M.; Yang, L.; Mao, H., Reducing non-specific binding and uptake of nanoparticles and improving cell targeting with an antifouling PEO-b-PgammaMPS copolymer coating. *Biomaterials* **2010,** *31* (20), 5397-407.

45. Li, L. L.; Xu, J. H.; Qi, G. B.; Zhao, X. Z.; Yu, F. Q.; Wang, H., Core-Shell Supramolecular Gelatin Nanoparticles for Adaptive and "On-Demand" Antibiotic Delivery. *Acs Nano* **2014,** *8* (5), 4975-4983.

46. Botella, P.; Abasolo, I.; Fernandez, Y.; Muniesa, C.; Miranda, S.; Quesada, M.; Ruiz, J.; Schwartz, S.; Corma, A., Surface-modified silica nanoparticles for tumor-targeted delivery of camptothecin and its biological evaluation. *J Control Release* **2011,** *156* (2), 246-257.

47. Cho, H. S.; Dong, Z. Y.; Pauletti, G. M.; Zhang, J. M.; Xu, H.; Gu, H. C.; Wang, L. M.; Ewing, R. C.; Huth, C.; Wang, F.; Shi, D. L., Fluorescent, Superparamagnetic Nanospheres for Drug Storage, Targeting, and Imaging: A Multifunctional Nanocarrier System for Cancer Diagnosis and Treatment. *Acs Nano* **2010,** *4* (9), 5398-5404.

48. Dai, Y. L.; Ma, P. A.; Cheng, Z. Y.; Kang, X. J.; Zhang, X.; Hou, Z. Y.; Li, C. X.; Yang, D. M.; Zhai, X. F.; Lin, J., Up-Conversion Cell Imaging and pH-Induced Thermally Controlled Drug Release from NaYF4:Yb3+/Er3+@Hydrogel Core-Shell Hybrid Microspheres. *Acs Nano* **2012,** *6* (4), 3327-3338.

49. Guo, Y.; Shi, D. L.; Cho, H. S.; Dong, Z. Y.; Kulkarni, A.; Pauletti, G. M.; Wang, W.; Lian, J.; Liu, W.; Ren, L.; Zhang, Q. Q.; Liu, G. K.; Huth, C.; Wang, L. M.; Ewing, R. C., *In vivo* imaging and drug storage by quantum-dot-conjugated carbon nanotubes. *Adv Funct Mater* **2008,** *18* (17), 2489-2497.

50. Khandelia, R.; Bhandari, S.; Pan, U. N.; Ghosh, S. S.; Chattopadhyay, A., Gold Nanocluster Embedded Albumin Nanoparticles for Two-Photon Imaging of Cancer Cells Accompanying Drug Delivery. *Small* **2015,** *11* (33), 4075-4081.

51. Peer, D.; Karp, J. M.; Hong, S.; FaroKHzad, O. C.; Margalit, R.; Langer, R., Nanocarriers as an emerging platform for cancer therapy. *Nat Nanotechnol* **2007,** *2* (12), 751-760.

52. Khandelia, R.; Jaiswal, A.; Ghosh, S. S.; Chattopadhyay, A., Polymer coated gold nanoparticle-protein agglomerates as nanocarriers for hydrophobic drug delivery. *J Mater Chem B* **2014,** *2* (38), 6472-6477.

53. Pan, U. N.; Khandelia, R.; Sanpui, P.; Das, S.; Paul, A.; Chattopadhyay, A., Protein-Based Multifunctional Nanocarriers for Imaging, Photothermal Therapy, and Anticancer Drug Delivery. *Acs Appl Mater Inter* **2017,** *9* (23), 19495-19501.

54. Kohanski, M. A.; Dwyer, D. J.; Hayete, B.; Lawrence, C. A.; Collins, J. J., A common mechanism of cellular death induced by bactericidal antibiotics. *Cell* **2007,** *130* (5), 797-810.
55. Wei, T.; Tang, Z. C.; Yu, Q.; Chen, H., Smart Antibacterial Surfaces with Switchable Bacteria-Killing and Bacteria-Releasing Capabilities. *Acs Appl Mater Inter* **2017,** *9* (43), 37511-37523.
56. Ritenberg, M.; Nandi, S.; Kolusheva, S.; Dandela, R.; Meijler, M. M.; Jelinek, R., Imaging *Pseudomonas aeruginosa* Biofilm Extracellular Polymer Scaffolds with Amphiphilic Carbon Dots. *ACS chemical biology* **2016,** *11* (5), 1265-70.
57. Beveridge, T. J., Structures of gram-negative cell walls and their derived membrane vesicles. *Journal of bacteriology* **1999,** *181* (16), 4725-33.

Chapter 3

Quercetin-Loaded Luminescent Hydroxyapatite Nanoparticles for Theranostic Application in Monolayer and Spheroid Cultures of Cervical Cancer Cell Line *In Vitro*

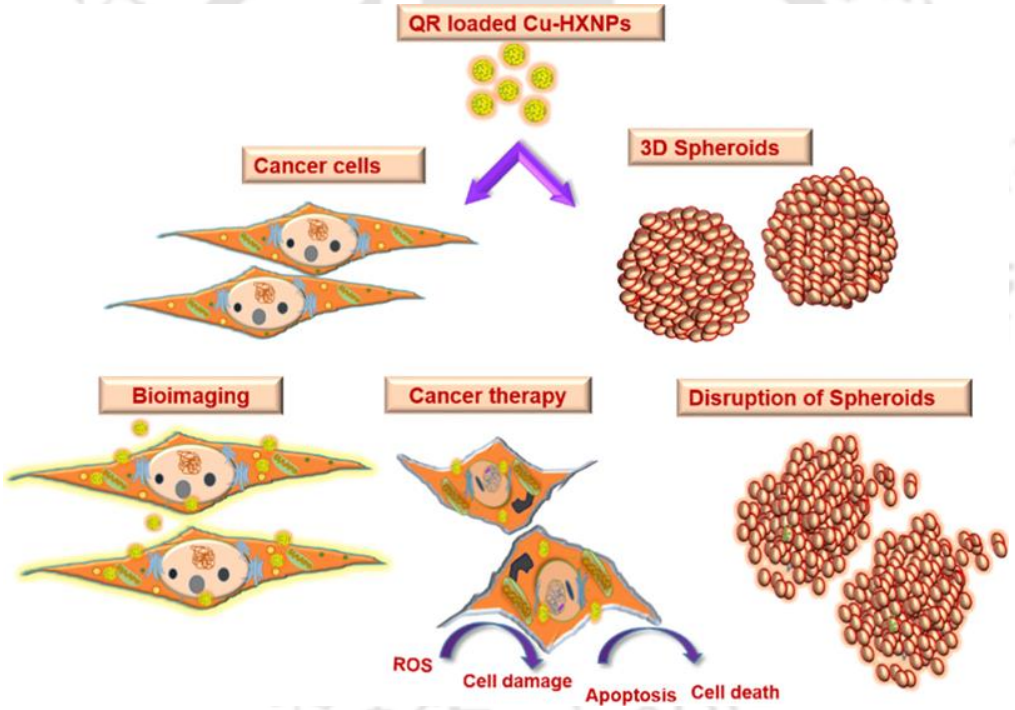

https://doi.org/10.1021/acsabm.1c00255

Chapter 3

Quercetin-Loaded Luminescent Hydroxyapatite Nanoparticles for Theranostic Application in Monolayer and Spheroid Cultures of Cervical Cancer Cell Line *In Vitro*

Abstract

Nanoscale materials have been explored as better alternatives to conventional therapeutic agents in cancer theranostics in the recent period due to efficacy in overcoming biological, biomedical, and biophysical barriers. Analysis on the ability of copper nanocluster (CuNC)-doped hydroxyapatite nanoparticles (Cu-HXNPs) as suitable nanocarriers for anti-cell proliferative application was carried out. Having high adsorption capacity, the Cu-HXNPs could be loaded with the anticancer drug quercetin, which is a polyphenolic flavonoid compound, and were used as nanocarriers to be applied on HeLa (cancer cells) and HEK-293 (normal cells). The drug release profile was found to be pH-dependent, where maximum release of quercetin from quercetin-loaded Cu-HXNPs was observed in acidic pH as compared to physiological pH. The Cu-HXNPs could release quercetin, which could effectively decline proliferation of cancer cells via generation of reactive oxygen species. Moreover, the released quercetin significantly altered the cell cycle pattern and triggered the cells to undergo apoptosis. Additionally, the efficacy of Cu-HXNPs as a nanocarrier to release quercetin on 3D spheroids of HeLa had been checked, which demonstrated significant reduction in the viability of 3D spheroids. The luminescent CuNCs used for doping HXNPs endowed the nanocarrier with the imaging property, which was an excellent feature in confirming their uptake by the cells. Thus, the study suggested Cu-HXNPs to be a beneficial nanocarrier for both bioimaging and therapeutic purpose in the field of cancer theranostics.

3.1. Introduction

The amalgamation of diverse scientific disciplines has expedited the generation of novel medicines bridging science and clinical applications, resulting in the emergence of the field of nanomedicines.[1] The area of cancer nanomedicine is aimed to address a majority of pharmacological limitations of conventional drugs.

Nanoformulation of naturally or synthetically derived materials has been found to be effective for attaining cancer therapy using them as drug delivery vehicles. Both organic and inorganic nanomaterials can be engineered for encapsulating therapeutic drugs, whose tumoricidal property remains unaltered.[2,3] The organic-based nanocarriers include polymeric, dendrimeric, cell membrane-derived, lipid and carbon-based platforms, whereas inorganic counterparts comprise iron oxide, gold, copper, silver, silica, and hydroxyapatite (HXAp). Intensive investigations of inorganic nanocarriers have been widely conducted due to their favourable surface properties, appreciable drug loading capacity, minimal toxicity, bioavailability, controlled or sustained drug release, and stability toward organic solvents.[4-6]

Due to the structural and compositional similarities with biological tissues such as bone and teeth, HXAp has been extensively considered for medical applications. In general, nanoparticles inherit salient features as compared to their bulk counterparts in terms of their reactivity, surface reconstruction, structure-related sensitivity, and adsorption property. Similarly, the nanostructured HXAp material possesses a higher surface area, biocompatibility, high adsorption property, and higher affinity for chemical species. These inherent nanoscale properties of HXAp can be exploited for drug delivery application in cancer nanomedicines.[7-10] Integration of the bioimaging property into therapy is an effective approach in monitoring and interpretation of the mode and site of nanocarrier distribution. Based on luminescence, probing of the therapy can be achieved through the usage of quantum dots, carbon nanomaterials, upconversion nanoparticles, metal nanoclusters, and incorporation of fluorescent dyes.[11,12] Out of these, metal nanoclusters are a new class of emerging fluorophores having a size closely approaching to Fermi wavelength of electrons and possess discrete energy levels. Among nanoclusters, copper nanoclusters (CuNCs) have attained substantial attention due to their size-tunable luminescent emission between near UV to near-infrared region, water solubility, high photoluminescence, and negligible renal retention.[13-15] Using CuNCs, image-guided therapeutic analysis can be achieved with negligible cytotoxicity after incorporating them into biocompatible nanomaterials such as HXAp.[16]

Among the naturally occurring compounds, polyphenols are a group of therapeutically important agents toward treatment of various disease conditions. Quercetin among them is uniquely positioned due to its anti-cell proliferative nature, intrinsic potency of angiogenesis

inhibition, and apoptosis. However, its pharmaceutical usages have been limited due to poor bioavailability and poor water solubility. Therefore, it is essential to harness its applications using an effective strategy such as loading it to suitable drug delivery vehicles for cancer therapy.[17-19]

Herein, we report the loading of quercetin into CuNC doped HXAp nanoparticles (Cu-HXNPs) for checking the potentiality of the nanocarrier in releasing the anticancer drug to be applied effectively for anti-cell proliferative activity. Being a suitable host, HXNPs could be successfully doped with CuNCs, with further loading of quercetin.[16,20] About 72% of quercetin could be loaded into Cu-HXNPs. The quercetin-loaded Cu-HXNPs after interacting with HeLa cells inhibited their growth via triggered generation of reactive oxygen species (ROS). Doping with metal ions such as copper could enhance the clinical effect of anticancer drugs such as quercetin through HXNPs, with the generation of ROS, leading to oxidative damage, probably through the transition-metal based pathway. [21,22] Moreover, with the aid of Cu-HXNPs as nanocarriers, the ROS generation through transition metal-flavone complexation could induce apoptosis, possibly via altering the mitochondrial membrane function.[23-25] Importantly, the cell cycle pattern was affected and eventual apoptosis killed the treated HeLa cells. While investigating the effect of quercetin-loaded Cu-HXNPs on the viability of the HEK-293 cell line, minimal growth inhibition was observed at lower concentrations with gradual reduction in cell viability toward higher concentrations. Importantly, the current study has also included the employment of 3D spheroids of the HeLa cell line, which bridge the gap between the 2D monolayer culture and animal model and mimic the tumor microenvironment *in vivo*[26] (**Figure 3.1**). The luminescent property of quercetin-loaded Cu-HXNPs also aided in confirmation of cellular uptake of the entire nanocarrier.

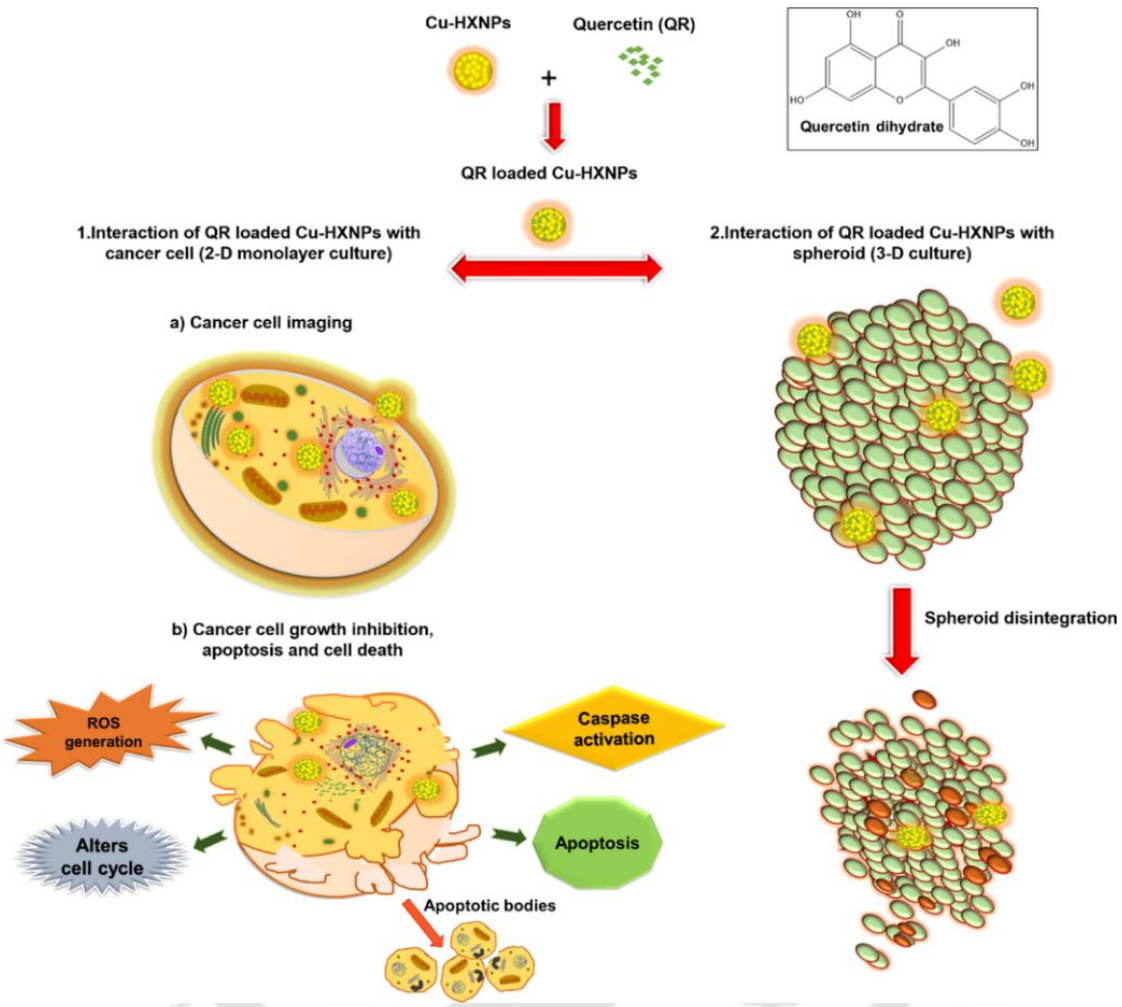

Figure 3.1. Schematic representation of quercetin loading into Cu-HXNPs followed by bioimaging and therapeutic application in cancer cells such as 2D monolayer culture and 3D spheroids of HeLa

3.2. Materials and Methods

3.2.1. Chemicals

For the experimental purpose, the following chemicals were used as-purchased: calcium chloride dihydrate (Merck), strontium nitrate pure (Merck), potassium dihydrogen phosphate (Merck), poly ethylene glycol (PEG) 400 (Merck), polyvinyl alcohol 87-89% hydrolyzed (Sigma-Aldrich), glacial acetic acid (Rankem), ammonia 25% (Merck), copper(II) sulfate pentahydrate pure (Merck), bovine serum albumin (Himedia), sodium hydroxide pellet (Rankem), hydrazine hydrate 80% (Merck), quercetin dihydrate (Sisco Research Laboratories),

and dimethyl sulfoxide (DMSO, Merck). Milli-Q grade water (>18 MΩ cm-1, Millipore) was used in all the experiments.

3.2.2. Synthesis of HXNPs (Undoped HXNPs), CuNCs, and CuNC-Doped HXNPs (Cu-HXNPs)

The entire synthesis procedures have been adopted from our previous report[16] out of which, synthesis of CuNC-doped HXNPs (Cu-HXNPs) has been explained briefly here. To synthesize Cu-HXNPs, in 3 mL of water, 0.2 M calcium chloride dihydrate and 0.12 M strontium nitrate were mixed and 7 mL of PEG 400 was added and stirred. The pH was brought to 11, followed by the addition of synthesized CuNC dispersion. Furthermore, 3 mL of 0.12 M potassium dihydrogen phosphate was added. The first set of dispersion was mixed with the second set of poly (vinyl alcohol) solution containing 2.5% diluted glacial acetic acid and 0.5% ammonia, whose pH was already adjusted to 11. Finally, the whole reaction mixture was heated at 85 °C for 2 min. After the synthesis, centrifugation was carried out twice at 5000 rpm. The final dispersion was stored at 4 °C for experimental purpose.

3.2.3. Drug Loading Efficiency

To check the quercetin loading efficiency of Cu-HXNPs, 500 µL of 5 mM quercetin was added to 500 µL of Cu-HXNPs (having a calcium concentration of 0.76 mg/mL) and incubated for 2 h at 37 °C. After incubation, centrifugation was carried out at 5000 rpm for 5 min to remove the supernatant. The pellet was dispersed in 1 mL of water, and the loading efficiency was checked using fluorescence spectroscopy (PerkinElmer LS55 spectrofluorometer). The fluorescence was recorded at an excitation and emission wavelength of 370 and 535 nm respectively. Using the following formula, the loading efficiency was calculated.

$$\% \text{ of loading efficiency} = \frac{QR_i - QR_f}{QR_i} \times 100$$

Here, QR_i denotes the initial concentration of quercetin used for loading and QR_f denotes the concentration of quercetin in the supernatant.

3.2.4. Study on Quercetin Release from Cu-HXNPs

The quercetin release profile was carried out in pH 4 (acetate buffer) and pH 7.4 [phosphate buffered saline (PBS) buffer]. After the addition of 500 µL of 5 mM quercetin into 500 µL of Cu-HXNPs, incubation was conducted for 2 h at 37 °C. Following the incubation, centrifugation was carried out at 5000 rpm for 5 min and the supernatant was removed. After dispersing the pellet in different pH buffers, release study was performed and the samples were periodically removed at different time intervals (0^{th}, 3^{rd}, 6^{th}, 9^{th}, 12^{th}, 24^{th}, 36^{th}, 48^{th}, 72^{nd}, and 96^{th} h). Furthermore, the withdrawn samples were centrifuged and their supernatant was collected to analyze the release profile by fluorescence spectroscopy. The fluorescence measurements were taken at an excitation of 370 nm and at an emission of 535 nm. The cumulative release was calculated using the formula given as follows.

$$\text{Cumulative release } \% = \frac{\text{QR released in supernatant}}{\text{QR loaded in nanocarrier}} \text{x } 100$$

3.2.5. UV-Visible Spectroscopy

A UV-visible spectrophotometer (Jasco V-630) was used to record the absorbance profile of quercetin, quercetin-loaded Cu-HXNPs, Cu-HXNPs, HXNPs, and CuNCs in the UV-visible range.

3.2.6. Luminescence Measurements

The luminescence measurements were conducted with the help of fluorescence spectrophotometer (PerkinElmer LS55 spectrofluorometer and Fluorolog Horiba).

Time-resolved photoluminescence (TRPL) analysis was carried out for CuNCs and Cu-HXNPs using a FluroMax-4 spectrofluorometer.

3.2.7. TEM

The as-synthesized CuNCs, undoped HXNPs, Cu-HXNPs were viewed using a transmission electron microscope, having a maximum accelerating voltage of 200 keV (JEM 2100; JEOL, Peabody, MA). Transmission electron microscopy (TEM) imaging was carried out by drop-

casting 7 µL of the sample to a carbon-coated copper grid. The sample was air dried overnight. Prior to drop-casting, the samples were sonicated in an ultrasonic bath (Telsonic) for 40 min.

3.2.8. FESEM

To study the morphology of quercetin-loaded Cu-HXNPs and undoped HXNPs, field emission scanning electron microscopy (FESEM) (JEOL JSM-7610F) was conducted. About 20 µL of the sample was drop-casted to an aluminum foil-covered glass slide and air-dried. Before drop-casting, sonication of the sample was carried out for 40 min.

To understand the cell surface morphology, the treated and control cells of HeLa and HEK-293 were imaged using FESEM. For analysis, the cells (HeLa or HEK-293) were treated with quercetin-loaded Cu-HXNPs. Incubation of both treated and control cells was carried out at 37 °C for 24 h. Furthermore, the cells were washed using PBS and trypsinized. The fixation of the cells was carried out with 0.1% formaldehyde followed by washing the cells with PBS. To an aluminium foil-covered glass slide, 20 µL of the diluted culture was drop-casted and air-dried overnight.

3.2.9. Zeta Potential

The zeta potential analysis of Cu-HXNPs, quercetin, and quercetin-loaded Cu-HXNPs was performed using a Malvern Zetasizer Nano ZS.

3.2.10. LCMS

The interaction of quercetin with Cu-HXNPs was confirmed through liquid chromatography mass spectrometry (LCMS) (Q-Tof premier). The study was conducted for quercetin and quercetin-loaded Cu-HXNPs.

3.2.11. Cell Culture

For performing cell culture studies, HeLa (human cervical carcinoma) and HEK-293 (human embryonic kidney-293) cells were procured from National Centre for Cell Sciences (NCCS), Pune, India.

For culturing the cells, Dulbecco's modified Eagle's medium (DMEM) supplemented with L-glutamine (4 mM), penicillin (50 units per mL), streptomycin (50 mg/mL, Sigma-Aldrich), and fetal bovine serum (10% v/v, PAA Laboratories, Austria) was used. The cells were grown in a 5% CO_2 humidified incubator at 37 °C.

3.2.12. Cell Viability Assay

The cell viability assay using MTT [3-(4,5-dimethylthiazol-2-yl)-2,5-diphenyltetrazolium bromide] was carried out on HeLa cells and HEK-293 (normal cell line). For the assay, 1×10^4 HeLa or HEK-293 cells/well were seeded into a 96-well plate, cultured in DMEM media and incubated in a 5% CO_2-humidified incubator at 37 °C for 24 h. The cells were treated with Cu-HXNPs (quercetin concentration, 0 µM) and quercetin-loaded Cu-HXNPs of varying quercetin concentrations (ranging from 100 to 500 µM) and quercetin (concentrations ranging from 100 to 500 µM) and incubated at 37 °C for 48 h. For the entire study, quercetin was dissolved in DMSO with the concentration of DMSO not exceeding 0.1% in cell culture medium. At the end of 48 h treatment, the MTT assay was carried out. The respiratory mitochondrial enzyme in the viable cells causes reduction of MTT leading to formation of formazan product which can be measured at 570 nm by fixing reference filter at 655 nm. The amount of formazan formed is directly proportional to the amount of viable cells. The percentage (%) of cell viability was calculated as follows.

$$\% \text{ of viable cells} = \frac{(\text{A570-A655}) \text{of treated cells}}{(\text{A570-A655}) \text{of control cells}} \text{x } 100$$

3.2.13. Generation of 3D Spheroids

Initially, HeLa cells were grown as monolayers until confluency was obtained, followed by trypsinization and resuspension in DMEM media. For the formation of spheroids, the 96-well plates were precoated with 1.5% agarose-containing serum-free DMEM media. Once solidified, HeLa cells at a density of 15,000 cells per well were seeded followed by centrifuging at 700 rcf for 10 min. Furthermore, the 96-well plates were incubated at 37 °C inside a 5% CO_2 humidified incubator for 96 h. Once the generation of spheroids is achieved, they were used for further studies.

3.2.14. Viability Study on 3D Spheroids

The viability study was carried out by treating spheroids with Cu-HXNPs (quercetin concentration, 0 μM) and quercetin-loaded Cu-HXNPs of varying quercetin concentrations (ranging from 200 to 1000 μM) and quercetin (concentrations ranging from 200 to 1000 μM) for 48 h at 37 °C. At the end of treatment, the viability was assessed using almarBlue assay by recording the absorbance at 570 nm, fixing the reference filter at 655 nm. The cell viability (%) was determined using the given formula.

$$\% \text{ of viable cells} = \frac{(\text{A570-A655}) \text{of treated cells}}{(\text{A570-A655}) \text{of control cells}} \text{x } 100$$

3.2.15. Confocal Laser Scanning Microscopy

The confocal experiment was carried out by treating the HeLa cells with Cu-HXNPs, quercetin-loaded Cu-HXNPs, and free quercetin at the IC_{50} concentration of quercetin-loaded Cu-HXNPs and incubating for 3 h at 37 °C. The samples were imaged using a Zeiss LSM 880 microscope (at a laser excitation of 405 nm).

For understanding the subcellular localization property, lysosomal staining assay was conducted using a cytopainter green lysosomal staining kit (Abcam). After the treatment of HeLa cells with quercetin-loaded Cu-HXNPs for 3 h, manufacturer's instructions were followed, where staining was carried out for one and half hour. The fixed cells were further visualized at an excitation of 405 nm (quercetin loaded Cu-HXNPs) and 488 nm (cytopainter green).

In the case of spheroids, live/dead cell imaging was carried out using the acridine orange/propidium iodide staining method. After being subjected to treatment with Cu-HXNPs, quercetin-loaded Cu-HXNPs, and free quercetin for 48 h, the spheroids were viewed under a Zeiss LSM 880 microscope. The treatment of spheroids with the given samples was carried out at a concentration in which quercetin-loaded Cu-HXNPs exerted 50% (approx.) viability reduction.

3.2.16. Determination of ROS Generation

The ROS generation from the cells treated with Cu-HXNPs, quercetin-loaded CuHXNPs, and free quercetin was studied using a microplate reader (Tecan) and epi-fluorescence microscopy (Nikon ECLIPSE, TS100, Tokyo). Primarily, the treatment of cells with quercetin-loaded Cu-HXNPs and free quercetin was carried out in a 96-well plate for 3 h. By the completion of the treatment, the cells were incubated with 1 mM DCFH-DA (2,7-dichlorofluoresceindiacetate) for 10 min. The cells were replenished with fresh media. The non-fluorescent DCFH-DA after the diffusion into the cells is hydrolyzed to DCFH, which upon oxidation gets converted into green-emitting DCF (dichlorofluorescein). The ROS generation was confirmed at an excitation of 488 nm and an emission of 530 nm.

3.2.17. Cell Cycle Analysis

For cell cycle analysis, HeLa cells (1×10^5 cells) were seeded in a six-well plate. The grown cells were treated with Cu-HXNPs, quercetin-loaded Cu-HXNPs, and free quercetin for 48 h. After the completion of the treatment, the media and the PBS of both control and treated cells were separately collected and the cells were trypsinized. The media, PBS, and the trypsinized cells were centrifuged at 650 rcf for 5 min, and cells were collected. Under constant and careful vortexing, the cells were fixed using 70% of ice cold ethanol and stored at 4 °C. Furthermore, the cells were centrifuged and washed using ice cold PBS after which they were treated with RNase for 1 h at 55 °C. To the RNase-treated cells, 10 µL of PI (1 mg/mL) was added and incubated in the dark at 37 °C for 30 min. Finally, all the samples were analyzed in a FacsCalibur (BD Biosciences, NJ) flow cytometer. For each sample, 15000 cells were analysed for recording PI fluorescence using the CellQuest program (BD Biosciences).

3.2.18. Cleaved Caspase 3 Assay

Here, HeLa cells (1×10^5 cells) were grown and treated with Cu-HXNPs, quercetin-loaded Cu-HXNPs, and quercetin for 48 h. The control and treated cells were trypsinized and centrifuged at 650 rcf for 5 min. Using 0.1% formaldehyde, the cells were fixed for 15 min. The fixed cells were centrifuged, and the pellet was redispersed in PBS. Upon the addition of 0.5% Tween 20, the cells were incubated in the dark for 20 min. Thereafter, the cells were centrifuged and

washed thrice using PBS. Furthermore, 10 µL of the PE-conjugated anticaspase-3 antibody was added, and the cells were incubated at 37 °C for 30 min. The cleaved caspase 3 assay was carried out in a FacsCalibur flow cytometer (BD Biosciences, NJ). Fluorescence data of every sample were recorded for 15000 cells through the CellQuest program (BD Biosciences).

3.3. Results and Discussion

3.3.1. Synthesis and Characterisations

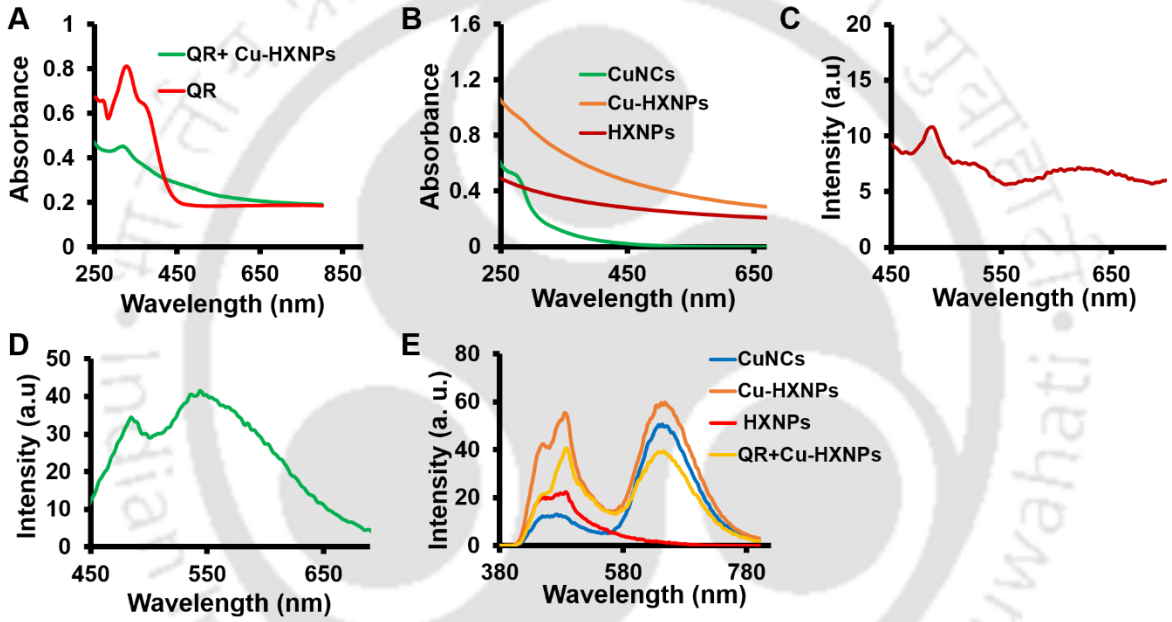

Figure 3.2. (A) UV-visible absorption spectra of quercetin (QR)-loaded Cu-HXNPs and free quercetin. (B) UV-visible absorption spectra of CuNCs, Cu-HXNPs and undoped HXNPs. Emission spectra of (C) quercetin loaded Cu-HXNPs (emission peaks at 490 and 535 nm) and (D) quercetin (emission peaks at 490 and 540 nm). The excitation wavelength was set at 370 nm. (E) Emission spectra of CuNCs, Cu-HXNPs, undoped HXNPs and quercetin-loaded Cu-HXNPs with their emission peaks at 650 nm (excitation at 365 nm).

The as-synthesized Cu-HXNPs were loaded with anticancer drug quercetin. The loading of quercetin into Cu-HXNPs was further confirmed by UV-visible and fluorescence spectroscopy methods. UV-visible spectroscopy revealed the presence of a peak at around 330 nm and 332 nm in the case of quercetin-loaded Cu-HXNPs and free quercetin, respectively. A weaker peak at 377 nm was also observed in the case of free quercetin (**Figure 3.2A**). A weak shoulder at 377 nm further supported the incorporation of quercetin in the Cu-HXNPs. This concurs with the earlier reports, which suggest that quercetin has an absorption peak in the range between

320 and 380 nm.[27] Furthermore, the analysis on CuNCs and Cu-HXNPs through UV-visible spectroscopy signified the presence of a peak at around 280 nm corresponding to the bovine serum albumin (BSA) template present in CuNCs. No surface plasmon resonance peak was found in the visible region discounting the formation of bigger-sized copper nanoparticles in both CuNCs and Cu-HXNPs. Additionally, no significant peak was observed throughout the scanned range in the case of HXNPs (**Figure 3.2B**). When quercetin-loaded Cu-HXNPs were excited at 370 nm, a sharp emission peak at 490 nm and a broader peak at around 535 nm attributed to quercetin were observed.[28] In the case of free quercetin, emission peaks at 490 and 540 nm were observed (**Figure 3.2C and D**). Moreover, at an excitation of 365 nm, the CuNCs, Cu-HXNPs, and quercetin-loaded Cu-HXNPs exhibited an emission peak around 650 nm that attributes to CuNCs. A slight reduction in the fluorescence intensity of quercetin-loaded Cu-HXNPs was observed, probably due to the covalent binding of quercetin with BSA protein, which was used as a template in CuNCs.[29] In the case of undoped HXNPs, fluorescence emission was negligible at 650 nm (**Figure 3.2E**). At an excitation of 370 nm, quercetin exhibited an emission wavelength in a range of 535-540 nm, which is not inclusive within the red region of the visible spectrum. Therefore, the red fluorescence-emitting CuNCs, doped in Cu-HXNPs, can be specifically applied in the imaging of biological cells and tissue. An emission obtained in the region of such a longer wavelength not only permits deeper tissue penetration but also diminishes autofluorescence from the cellular milieu.[30] Being a bioimaging material, to further understand the intrinsic property of our nanocarrier, a TRPL analysis was conducted. The study indicated the lifetime of CuNCs to be 4.25 µs, whereas Cu HXNPs were found to have an average lifetime of 5.37 µs. The lifetime of both CuNCs and Cu-HXNPs was recorded at an excitation/emission of 365/650 nm (**Figure 3.3**).

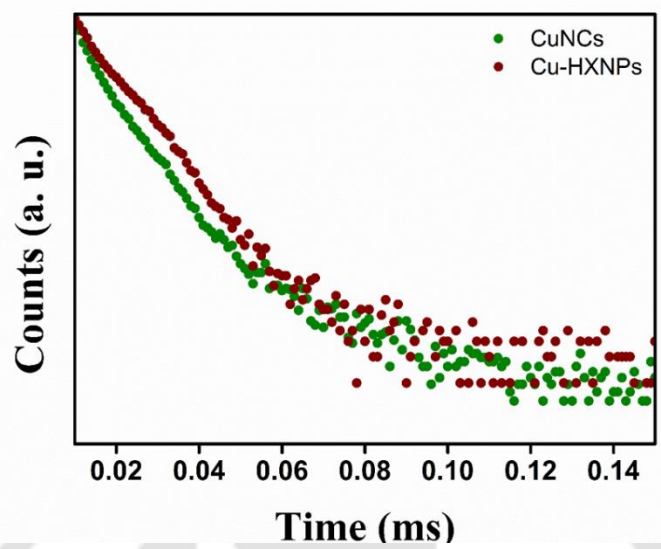

Figure 3.3. Time resolved photoluminescence (TRPL) spectra of CuNCs (χ^2 – 0.99, average lifetime- 4.25 µs) and Cu-HXNPs (χ^2 – 0.99, average lifetime- 5.37 µs) at an excitation of 365 nm and an emission of 650 nm.

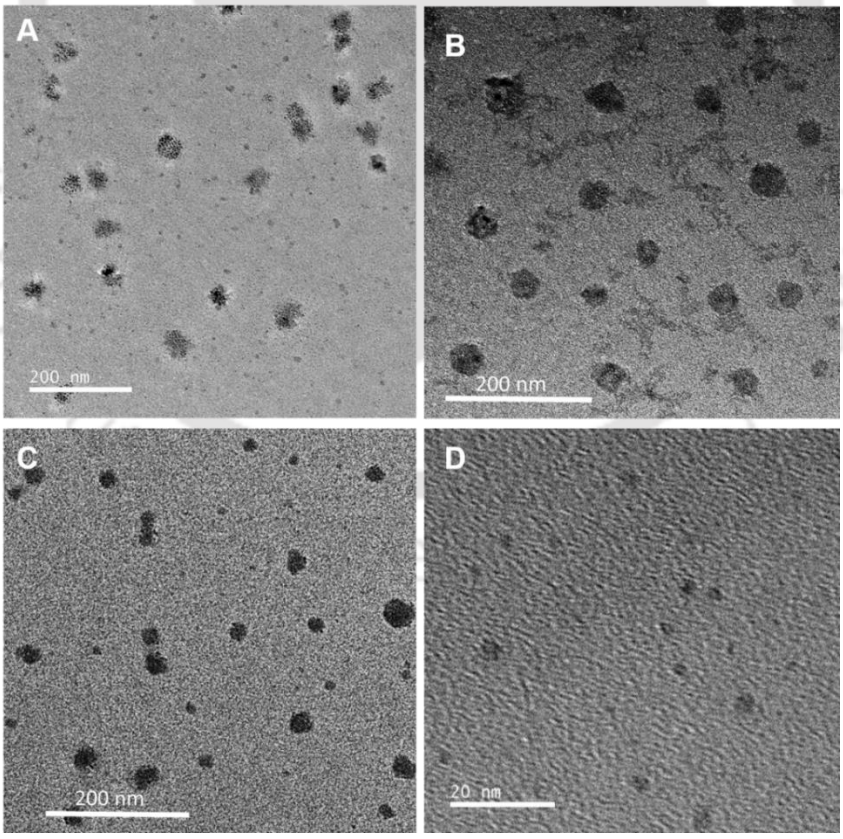

Figure 3.4. (A) TEM image of quercetin-loaded Cu-HXNPs at a scale bar of 200 nm. TEM image of (B) Cu-HXNPs (scale bar at 200 nm), (C) undoped HXNPs (scale bar at 200 nm) and (D) CuNCs (scale bar at 20 nm).

Furthermore, the TEM analysis revealed the quercetin-loaded Cu-HXNPs to be having an average size of 36.2 ± 4.3 nm (**Figure 3.4A**). Likewise, the average size of Cu-HXNPs, HXNPs, and CuNCs was calculated to be 32.2 ± 5.9, 24.2 ± 6.0, and 1.7 ± 0.7 nm respectively (**Figure 3.4B-D**). Size calculations of nanoparticles and nanoclusters were carried out using Image J software. The selected area electron diffraction patterns obtained suggested the crystalline nature of the quercetin-loaded Cu-HXNPs with planes (210) and (420) that correspond to the planes of HXNPs as previously reported[31] (**Figure 3.5A**). Thus, it implies that the crystalline properties of Cu-HXNPs were found to be unaltered and intact even after having the quercetin-loaded into them. Similarly, the high resolution TEM image also suggested the presence of lattice spacing of 0.47 nm that corresponds to the (110) plane of HXAp[32,33] (**Figure 3.5B**).

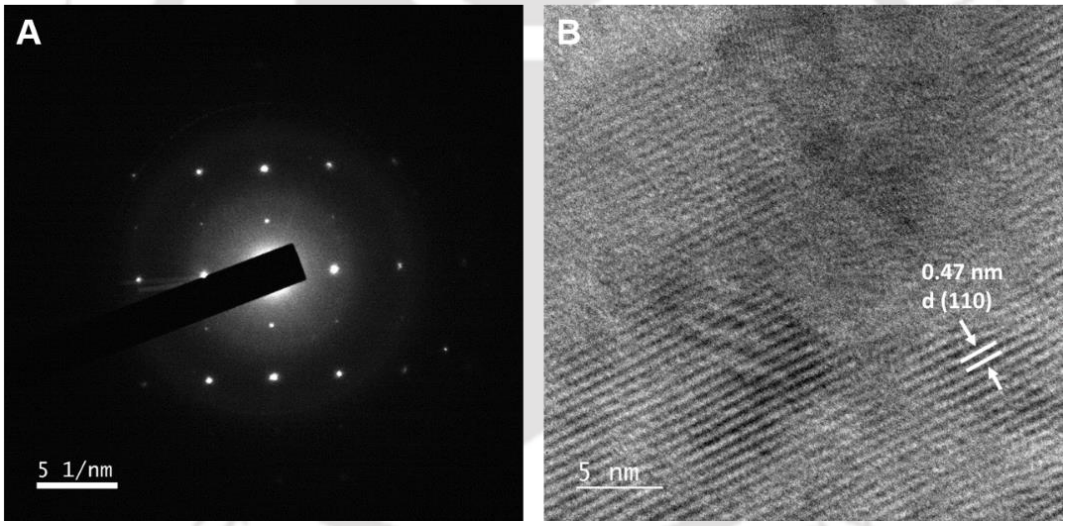

Figure 3.5. (A) SAED pattern and (B) HRTEM of quercetin loaded Cu-HXNPs (scale bar of 5 nm).

Additionally, the FESEM images obtained were in accordance with the TEM results where the size of the quercetin-loaded Cu-HXNPs was found to be 36.0 ± 8.9 nm. The FESEM analysis suggested the undoped HXNPs to be having an average size of 24.5 ± 2.8 nm, which corresponds to the TEM images of undoped HXNPs (**Figure 3.6A and B**).

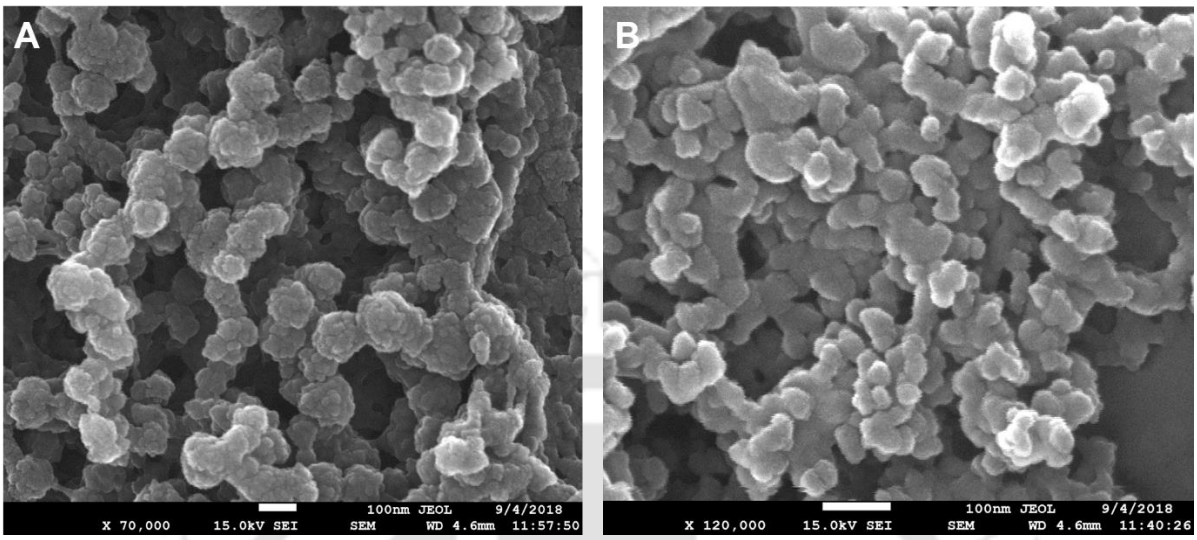

Figure 3.6. FESEM images of (A) quercetin loaded Cu-HXNPs and (B) undoped HXNPs (scale bar at 100 nm).

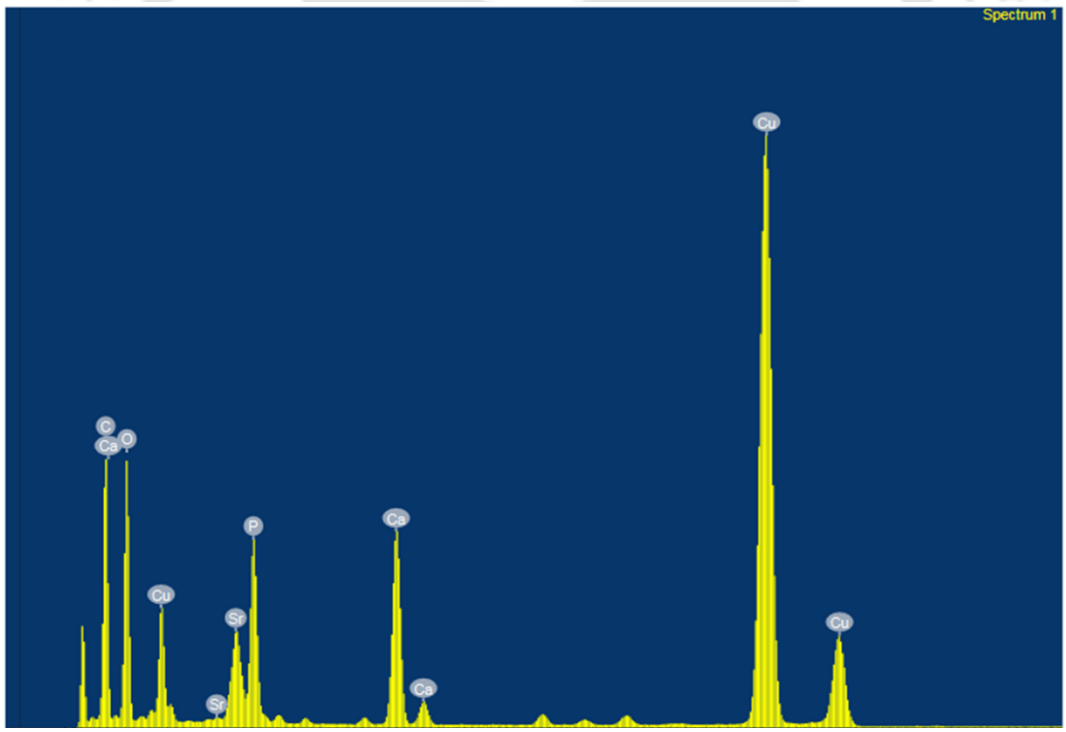

Figure 3.7. EDX spectrum showing elemental composition of quercetin loaded Cu-HXNPs

The energy-dispersive X-ray spectroscopy (EDX) confirmed the presence of individual ions such as calcium, phosphorous, strontium, copper, carbon, and oxygen in quercetin-loaded Cu-HXNPs (**Figure 3.7**). For the determination of surface charges, the zeta potential analysis was conducted, which confirmed that the quercetin-loaded Cu-HXNPs carried a net negative charge

of -20.5 ± 0.2 mV (**Figure 3.8A**). The free quercetin and Cu HXNPs carried net negative charges of -39.1 ± 0.3 and -19.3 ± 0.1 mV, respectively (**Figure 3.8B and C**). The interaction of negatively charged quercetin and negatively charged Cu-HXNPs might be probably due to the influence of positively charged calcium ions present on the planes of HXNPs.[34]

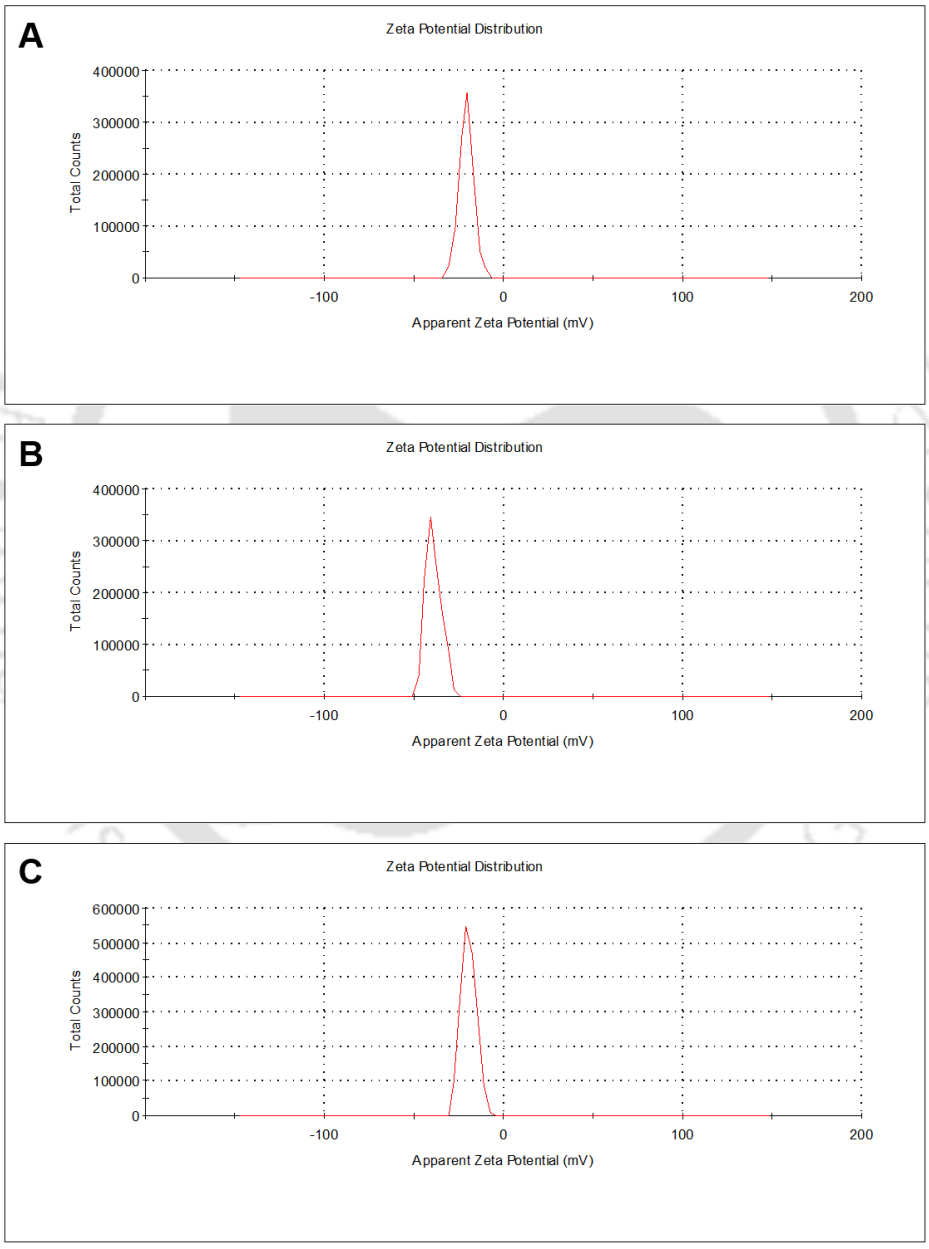

Figure 3.8. Zeta potentials of (A) quercetin loaded Cu-HXNPs, (B) quercetin and (C) Cu-HXNPs dispersions.

The interaction of quercetin with Cu-HXNPs was confirmed by LCMS analysis. The LCMS spectrum of free quercetin (**Figure 3.9A**) showed an m/z value of 301.01, which was clearly evident in the quercetin-loaded Cu-HXNPs (**Figure 3.9B**), showing the presence of quercetin in Cu-HXNPs.[35,36]

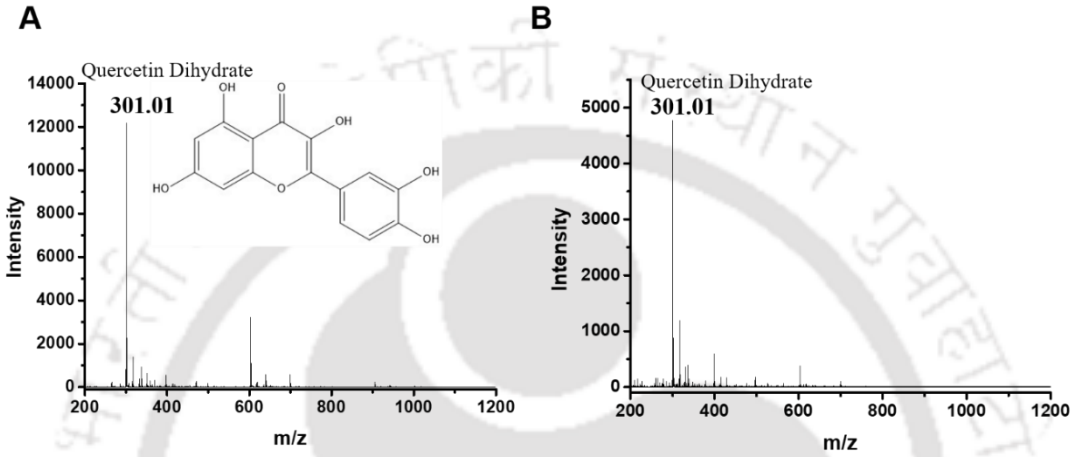

Figure 3.9. LCMS spectra of (A) free quercetin (structure of quercetin is given) and (B) quercetin loaded Cu-HXNPs. Free quercetin showed an m/z value of 301.01, which was also evident in quercetin loaded Cu-HXNPs.

3.3.2. Drug Release Profile

Using fluorescence spectroscopy, the loading efficiency was found to be 72% and the concentration of quercetin-loaded within the Cu-HXNPs was thus calculated to be 3.6 mM. The cumulative release of quercetin from Cu-HXNPs at different time intervals was analysed *in vitro* where maximum release was observed in an acidic environment (acetate buffer, pH 4) as compared to the physiological environment (PBS buffer, pH 7.4). In pH 4, the release profile exhibited a slow and steady increase of drug release up to 12th h, where there occurred an initial burst release of 65% of drug with further 53% release at 24th h. Toward 48th h, the drug release was slowly declined, followed by displaying a steady pattern with 26% of drug release (**Figure 3.10A**). In pH 7.4, the release was suggested to be comparatively less with a maximum of 17% at 12th h followed by a gradual increase toward 48th h, showing 19% of release (**Figure 3.10B**). Thus, a pH-responsive release pattern could be observed with maximum release occurring in an acidic environment. Furthermore, by checking the release study up to 96 h, it was confirmed that the release of total drug loaded might require more than 48 h, as there was 12 and 13% of

quercetin released from quercetin-loaded Cu-HXNPs at 72nd and 96th h, respectively, at pH 4 (**Figure 3.10C**). Similarly, at pH 7.4, a release of 19 and 20% of quercetin was observed at 72nd and 96th h, respectively (**Figure 3.10D**).

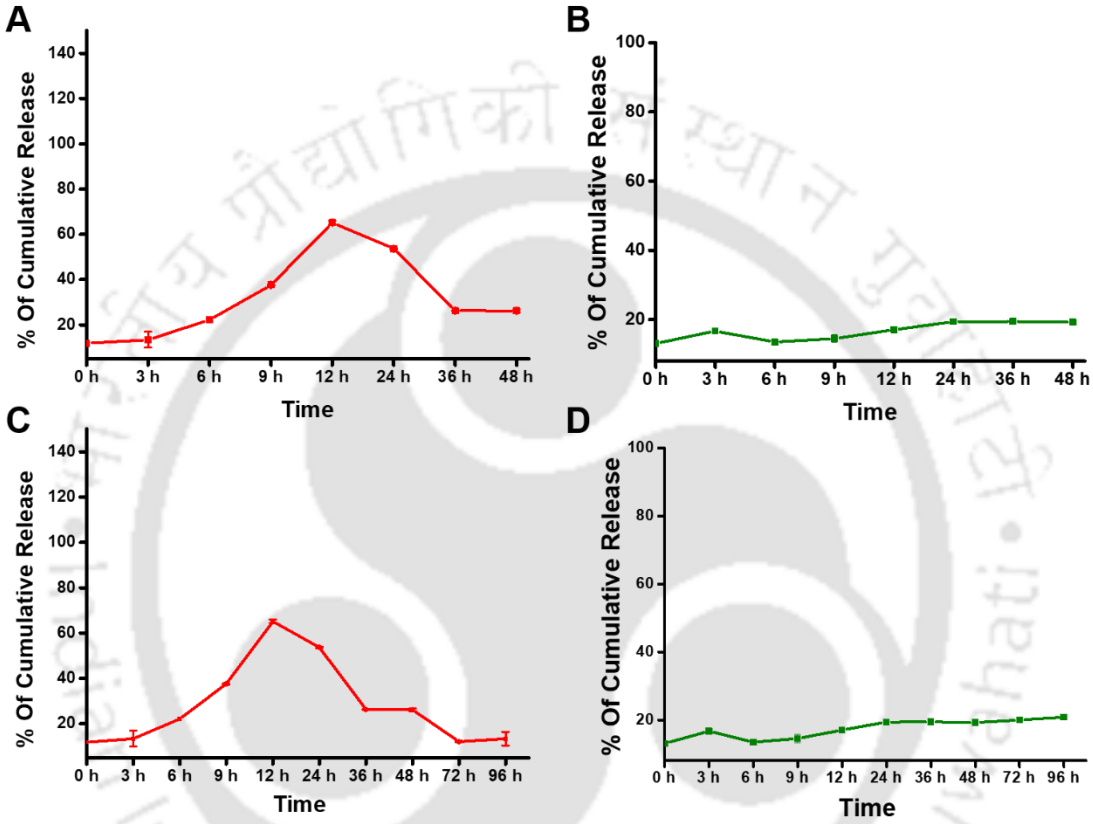

Figure 3.10. Study on the release pattern of quercetin from quercetin-loaded Cu-HXNPs carried out at (A) pH 4 (acetate buffer) and (B) pH 7.4 (PBS buffer) up to 48 h. At pH 4, an initial burst release of 65% was obtained at 12th h followed by 53% of release at 24th h. Toward 48th h, the drug release was gradually reduced to 26% in a slow and sustained manner. The release profile of quercetin at pH 7.4 exhibited initially a maximum release of 17% at 12th h, with a slow increase to 19% of release at 48th h. Release study conducted up to 96 h at (C) pH 4 and (D) pH 7.4. At pH 4, 12% and 13% of quercetin release from quercetin loaded Cu-HXNPs was obtained at 72nd and 96th h respectively. At pH 7.4, 19% and 20% of quercetin was released at 72nd and 96th h respectively.

3.3.3. Confocal Microscopic Analysis

The uptake of quercetin-loaded Cu-HXNPs by HeLa cells was confirmed by confocal studies carried out at an excitation of 405 nm and at two different emission wavelengths (650 and 530 nm).

In brief, **Figure 3.11A** depicts quercetin-loaded Cu-HXNP-treated HeLa cells at an emission of 650 nm which corresponds to CuNCs and **Figure 3.11B** depicts quercetin-loaded Cu-HXNP-treated HeLa cells at an emission of 530 nm that corresponds to quercetin. The representative bright-field image of HeLa cells treated with quercetin-loaded Cu-HXNPs is presented in **Figure 3.11C**. **Figure 3.11D** corresponds to the merged image of HeLa cells treated with quercetin-loaded Cu-HXNPs with emissions at 650 and 530 nm. The cellular intake of quercetin-loaded Cu-HXNPs was evident through the luminescence emitted from Cu-HXNPs and quercetin at their respective emission wavelength. The biocompatibility of HXNPs and the luminescence property of CuNCs can be contemplated as the attractive features in qualifying the entire nanoformulation to be a suitable diagnostic probe in cancer theranostics. Similarly, the uptake of Cu-HXNPs (**Figure 3.12A-D**) and free quercetin (**Figure 3.13A-D**) was analyzed, and the images are given. The internalization of Cu-HXNPs and free quercetin by cells was clearly understood from the depth projection image of treated cells.

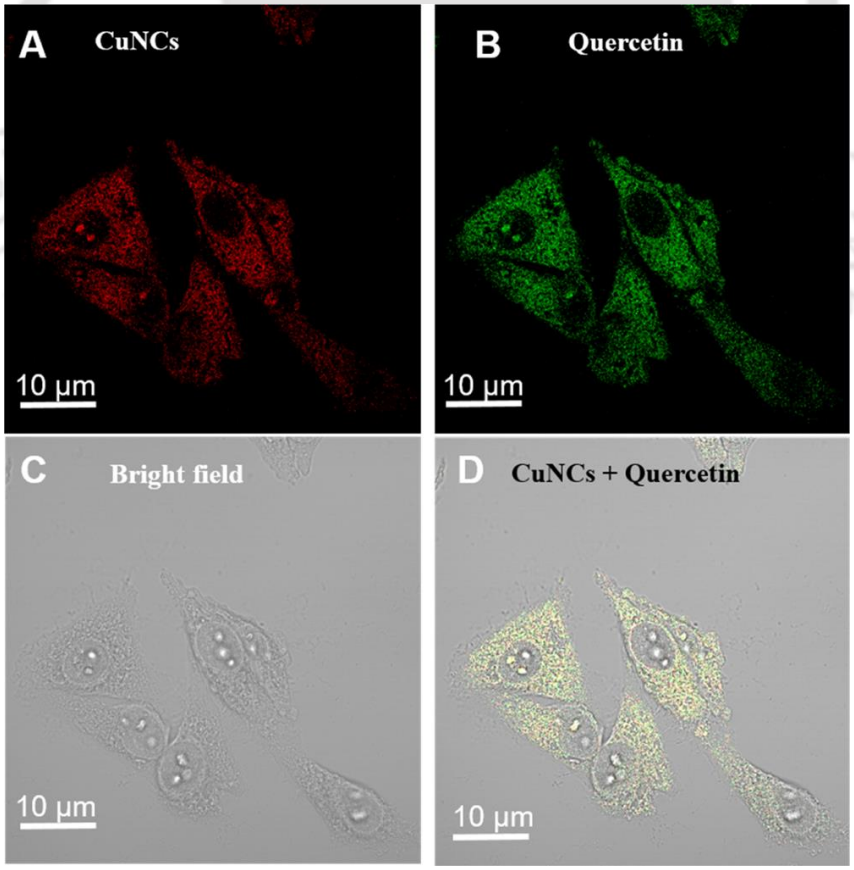

Figure 3.11. Confocal images showing HeLa cell uptake of quercetin-loaded Cu-HXNPs. (A) Confocal image of HeLa cells treated with quercetin-loaded Cu-HXNPs (emission at 650 nm

that corresponds to CuNCs doped in HXNPs) and (B) confocal image of quercetin-loaded Cu-HXNP-treated HeLa cells (emission set at 530 nm that corresponds to quercetin). (C) Bright field image of HeLa cells treated with quercetin-loaded Cu-HXNPs and (D) merged image of HeLa cells treated with quercetin-loaded Cu-HXNPs. The HeLa cells were treated at IC_{50} concentration of quercetin-loaded Cu-HXNPs. The laser excitation was kept at 405 nm. The scale bar is 10 µm.

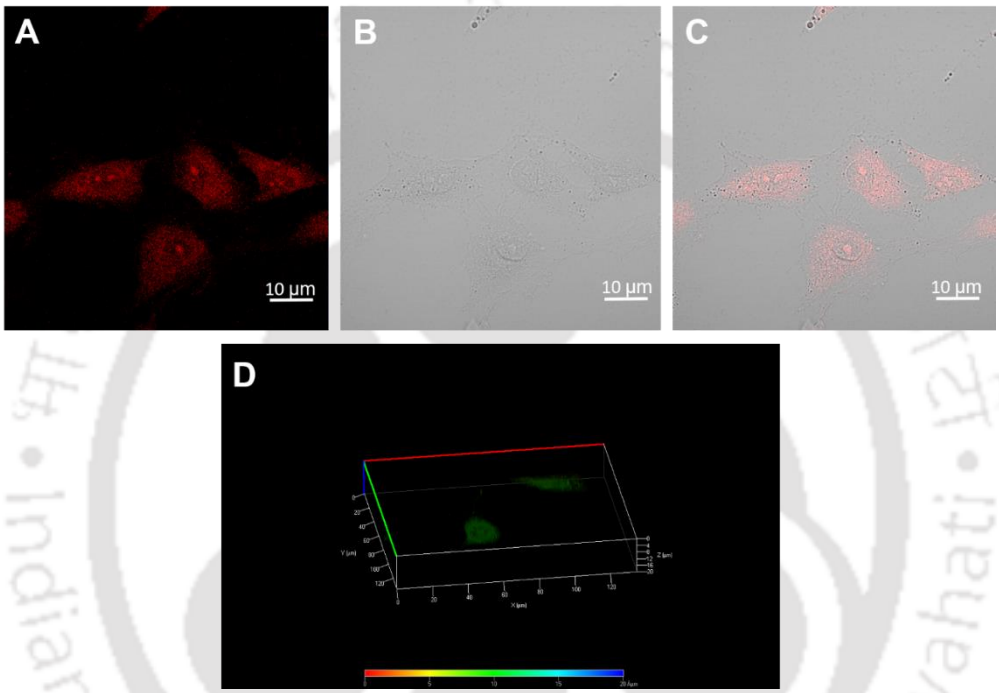

Figure 3.12. Confocal images of HeLa cells treated with Cu-HXNPs. (A) Confocal image, (B) bright field image, (C) merged image and (D) depth projection image showing internalization of Cu-HXNPs in HeLa cells. The scale bar is 10 µm.

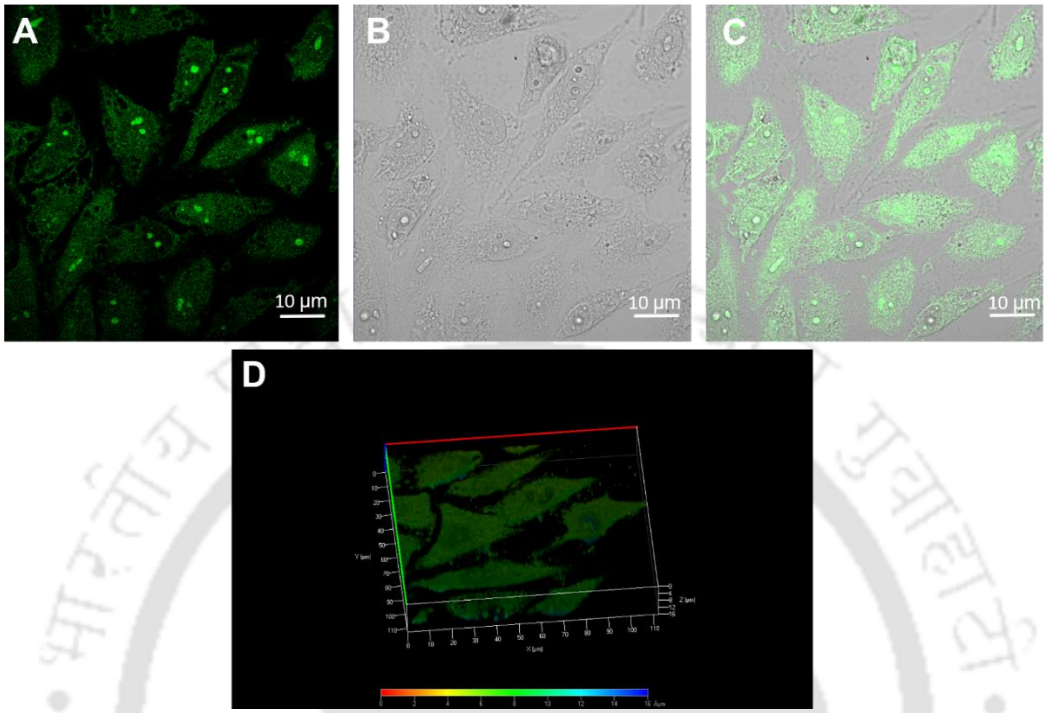

Figure 3.13. Confocal images of HeLa cells treated with free quercetin. (A) Confocal image, (B) bright field image, (C) merged image and (D) depth projection image showing internalization of free quercetin in HeLa cells. Scale bar is kept at 10 µm.

Additionally, to explore the subcellular localization attribute of quercetin-loaded Cu-HXNPs, a cytopainter green lysosomal staining experiment was performed (**Figure 3.14A-D**). From the merged image of confocal microscopy obtained, it was revealed that the quercetin-loaded Cu HXNPs were internalized and finally localized into lysosomal compartments (validated by the presence of yellow spots in the merged image, (**Figure 3.14D**).

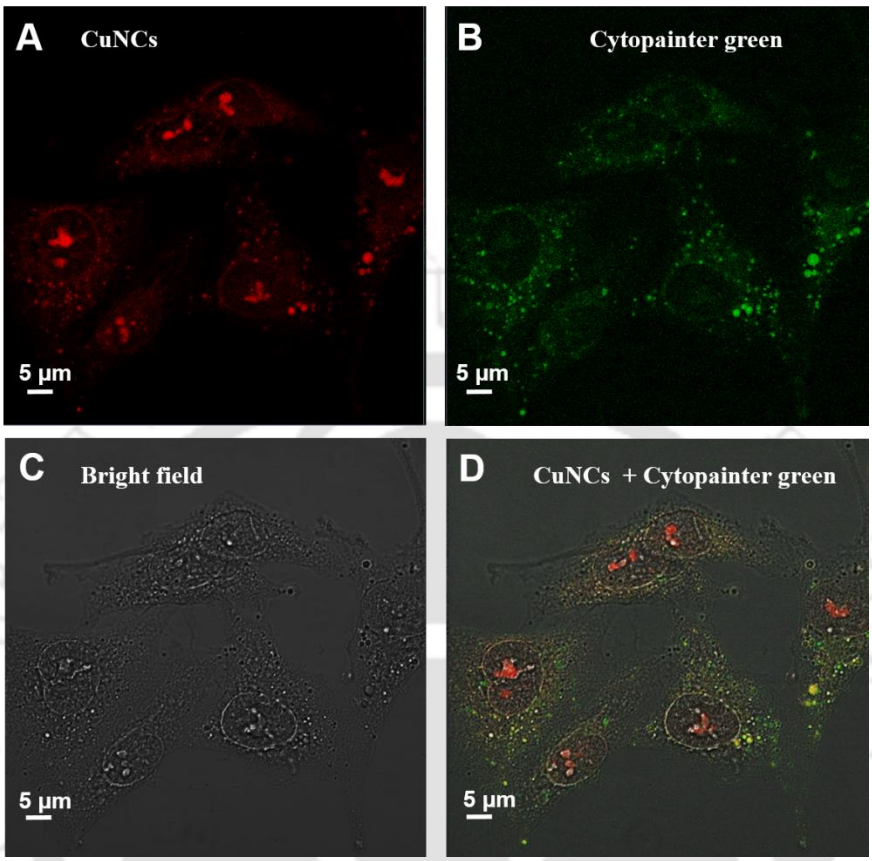

Figure 3.14. (A) Confocal image exhibiting red fluorescence of quercetin loaded Cu-HXNPs in HeLa cells treated with quercetin loaded Cu-HXNPs and cytopainter green lysosomal staining kit, (B) confocal image showing green fluorescence in HeLa cells treated with quercetin loaded Cu-HXNPs and cytopainter green lysosomal staining kit, (C) bright field image of HeLa cells treated with quercetin loaded Cu-HXNPs and cytopainter green lysosomal staining kit and (D) merged image of HeLa cells treated with quercetin loaded Cu-HXNPs and cytopainter green lysosomal staining kit.

3.3.4. Anti-Cell Proliferative Studies

The cell viability study of quercetin-loaded Cu-HXNPs on HeLa cells was assessed by MTT assay through which their anti-cell proliferative efficiency was compared with only Cu-HXNPs and free quercetin. The MTT assay suggested that at 200 µM quercetin, the quercetin-loaded Cu-HXNPs exhibited IC_{50}, whereas free quercetin exhibited IC_{50} at 300 µM. In the case of only Cu-HXNPs, minimal killing was observed (**Figure 3.15A**). The MTT results suggest the ability of Cu-HXNPs to release quercetin, which could potentially enter the cells bringing about conformational variations, propelling cell cycle modifications and apoptosis. Similarly, MTT

assay was carried out for normal cell line such as HEK-293, which evinced negligible sensitivity toward free quercetin and Cu-HXNPs. At lower concentrations tested, the inhibitory action of quercetin-loaded Cu-HXNPs was found to be less on HEK-293 as compared to their action on HeLa. Toward the higher concentration of quercetin such as 500 µM, quercetin-loaded Cu-HXNPs gradually reduced the viability of HEK-293 cells to around 53% (**Figure 3.15B**).

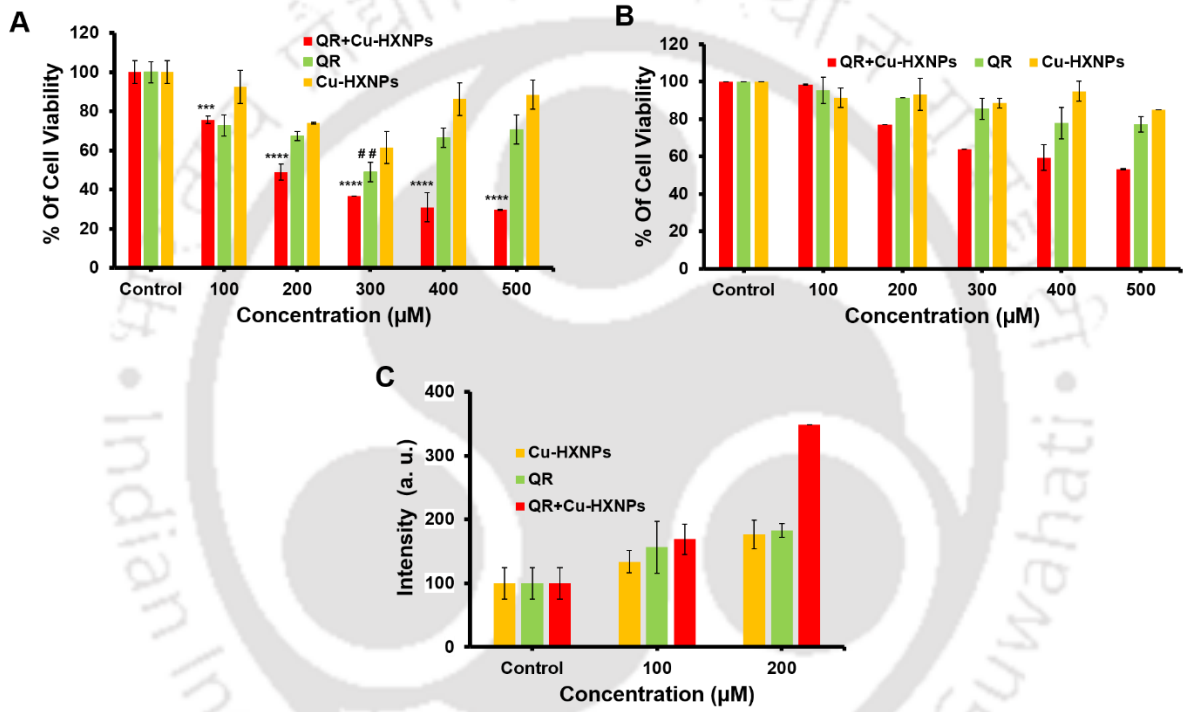

Figure 3.15. (A) Cell viability assay on HeLa cells treated with quercetin-loaded Cu-HXNPs, free quercetin and Cu-HXNPs. At a concentration of 200 µM quercetin, quercetin-loaded Cu-HXNPs showed their IC_{50}, whereas free quercetin showed an IC_{50} at 300 µM. The ANOVA test revealed statistical significance of quercetin-loaded Cu-HXNPs and free quercetin with respect to the control. Statistical significance is represented by ## ($p < 0.005$), *** ($p < 0.001$) and **** ($p < 0.0001$). The values are represented as mean ± standard deviation (SD) of three individual experiments. (B) Viability assay on HEK-293 cells treated with quercetin-loaded Cu-HXNPs, free quercetin and Cu-HXNPs. Data represented are based on three separate experiments conducted. (C) Graph representing the intensity of ROS generation in HeLa cells treated with Cu-HXNPs, free quercetin and quercetin-loaded Cu-HXNPs. The graph depicts the averaged intensity value from triplicate experiments.

The anti-cell proliferative activity in HeLa cells was found to be enhanced by the generation of ROS, which could be substantiated by DCFH-DA study (**Figure 3.15C**). In this study, we could confirm that there was an appreciable amount of ROS generated from cells treated with quercetin-loaded Cu-HXNPs in contrast to the control cells, which generated a minimal amount of ROS. At 200 µM, there was maximum generation of ROS by cells treated with quercetin-loaded Cu-HXNPs as compared to free quercetin and Cu-HXNPs. Quercetin is generally understood to be an antioxidant. However, studies suggest that flavonoids including quercetin can act as a pro-oxidant at its higher concentration and be driven to enhance the ROS production in the presence of transition metals such as copper. Now, our nanosystem such as Cu-HXNPs contains copper, which is a transition metal that is understood to initiate ROS formation through flavones.[37,38] Thus, the ROS generation is probably intensified from the quercetin once it is successfully loaded into Cu-HXNPs and applied for the cellular treatment *in vitro*. Therefore, we suppose that under various conditions, quercetin tends to behave as an ambivalent compound, where it induces ROS generation rather than exhibiting the antioxidant property.[39]

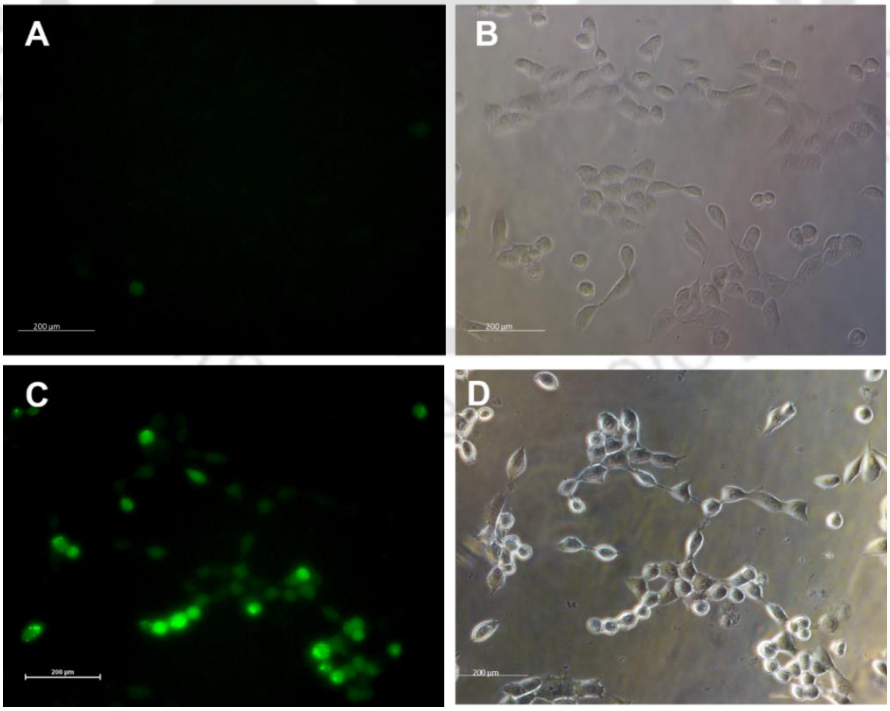

Figure 3.16. Epifluorescence images showing DCF fluorescence indicating the generation of ROS in HeLa cells. (A) Fluorescent image and (B) bright field image of control cells. (C) Fluorescent image and (D) bright field image of cells treated with quercetin loaded Cu-HXNPs.

Through epifluorescence spectroscopy (**Figure 3.16A-D**), it was evident that the control cells emitted negligible DCF fluorescence, whereas cells treated with quercetin-loaded Cu-HXNPs emitted a considerable amount of DCF fluorescence due to the generation of ROS. This was in consonance with MTT assay, which suggested that the viability of cells was almost halved at 200 µM quercetin loaded in quercetin-loaded Cu-HXNPs with further reduction at higher concentration such as 500 µM quercetin. Generation of ROS could possibly play a major role in the reduction of cell proliferation where the cancer cells become more sensitive toward the enhanced intracellular ROS.[40]

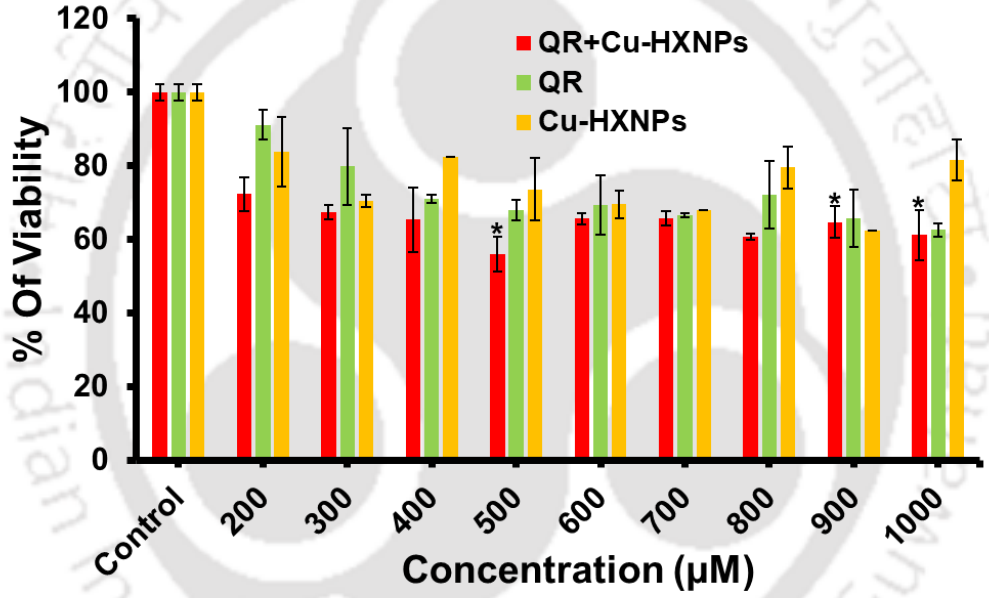

Figure 3.17. Viability assay on 3D spheroids after the treatment with quercetin-loaded Cu-HXNPs, free quercetin and Cu-HXNPs. Upon treatment of spheroids with quercetin-loaded Cu-HXNPs, approximately 50% viability reduction was observed at 500 µM quercetin. Statistical significance of quercetin-loaded Cu-HXNPs with respect to the control is denoted by * ($p < 0.05$). Data are represented as mean ± SD of three individual experiments.

The 3D spheroids are understood to be better representative systems that mimic the *in vivo* tumor microenvironment.[41] Therefore, the therapeutic ability of our present system on 3D spheroids was evaluated using alamarBlue-based viability assay. While analyzing the effect of quercetin-loaded Cu-HXNPs on 3D spheroids, approximately 50% of viability reduction was obtained at 500 µM quercetin up to which there was a gradual decease in cell proliferation. With the increase in the concentration up to 1000 µM, the therapeutic effect of quercetin-loaded Cu-HXNPs on 3D spheroids was found to remain almost constant.

The sensitivity of 3D spheroids toward free quercetin and Cu-HXNPs was milder in comparison to quercetin-loaded Cu-HXNPs (**Figure 3.17**).

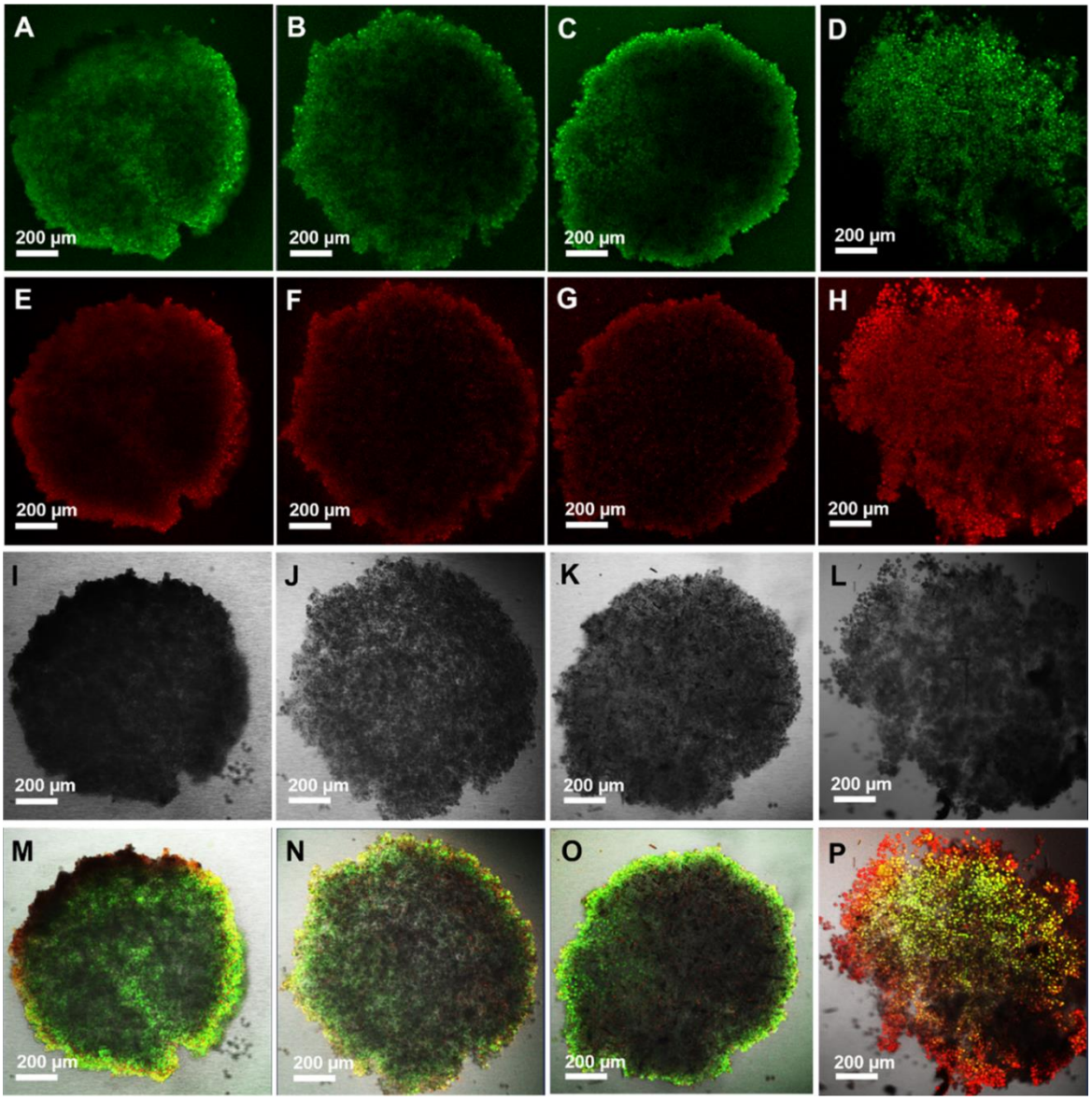

Figure 3.18. Live/dead cell staining assay. Confocal images of the AO-stained (A) control, (B) Cu-HXNP-treated, (C) quercetin-treated and (D) quercetin-loaded Cu-HXNP-treated spheroid, showing green fluorescence. Confocal images of the PI-stained (E) control, (F) Cu-HXNP-treated, (G) quercetin-treated and (H) quercetin-loaded Cu-HXNP-treated spheroid, showing red fluorescence. Corresponding bright field images of the (I) control, (J) Cu-HXNP-treated, (K) quercetin-treated and (L) quercetin-loaded Cu-HXNP-treated spheroid. Merged images of the (M) control, (N) Cu-HXNP-treated, (O) quercetin-treated and (P) quercetin-loaded Cu-HXNP-treated spheroid. The scale bar is 200 µm.

To gain further insights into the efficiency of our present drug-loaded nanosystem, live/dead cell staining assay was carried out on the spheroids treated with Cu-HXNPs, free quercetin, and quercetin-loaded Cu-HXNPs (**Figure 3.18A-P**). As shown in **Figure 3.18M-P**, the untreated spheroid was found to have an intact morphology with significant green fluorescence due to AO-stained live cells. The spheroid treated with free quercetin and Cu-HXNPs exhibited minimal disintegration and a minimum number of dead cells due to low fluorescence intensity emerging from red-emitting PI-stained cells. However, upon treatment with quercetin-loaded Cu-HXNPs, there was significant disintegration manifested in the entire spheroid with predominant red fluorescence emitted from a large number of PI-stained dead cells. Thus, the analysis suggests that Cu-HXNPs could successfully deliver quercetin deep within the spheroid, leading to appreciable disorganization of the 3D multicellular system.

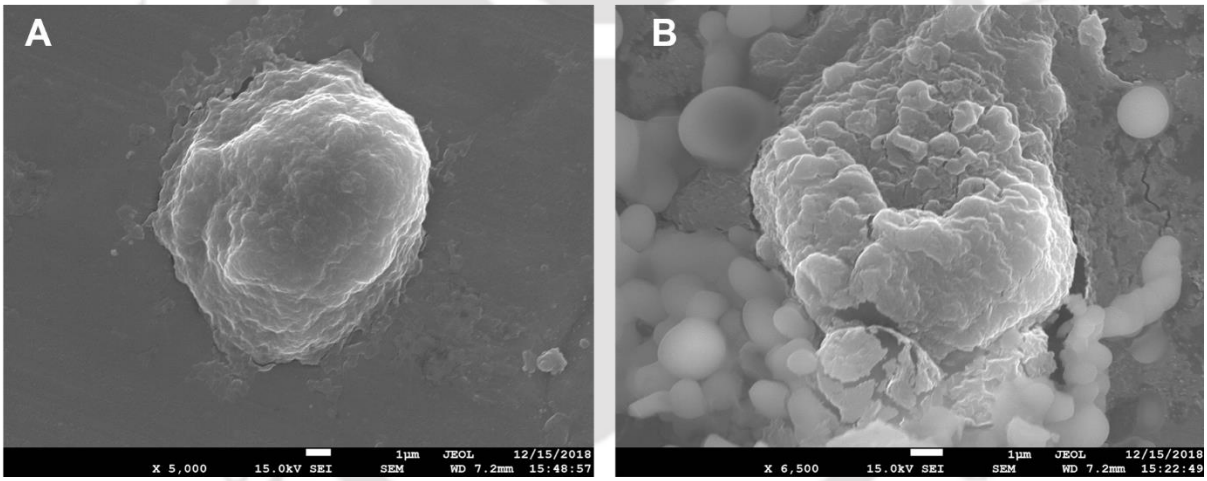

Figure 3.19. FESEM images of HeLa cell treated with quercetin loaded Cu-HXNPs at 200 µM. (A) Control cell and (B) treated cell. Scale bar is kept at 1 µm.

Using FESEM analysis, the morphological evaluation of 2D monolayer culture of HeLa cells treated with quercetin-loaded Cu-HXNPs (200 µM) was carried out, where the disrupted cell membrane was significantly evident as compared to the untreated cells (**Figure 3.19A and B**). The mechanism behind such an alteration can be possibly due to the accumulation of ROS, which leads to disruption of protein and lipid bilayer, resulting in loss of cell membrane integrity. Moreover, ROS can act as common mediators of apoptosis, which is distinguished by morphological changes such as shrinkage, breakage, and blebbing of the membrane.[42-44]

This suggests quercetin-loaded Cu-HXNPs to be a suitable nanocarrier in bringing about significant intracellular changes that are partially manifested through morphological deformation of treated cells. When HEK-293 cell lines were treated with quercetin-loaded Cu-HXNPs at 200 µM, no significant morphological changes were observed as compared to control cells, which implies the lower cytotoxic effect of the present drug-loaded nanocarrier to normal cell lines in comparison to treated HeLa cells (**Figure 3.20A and B**).

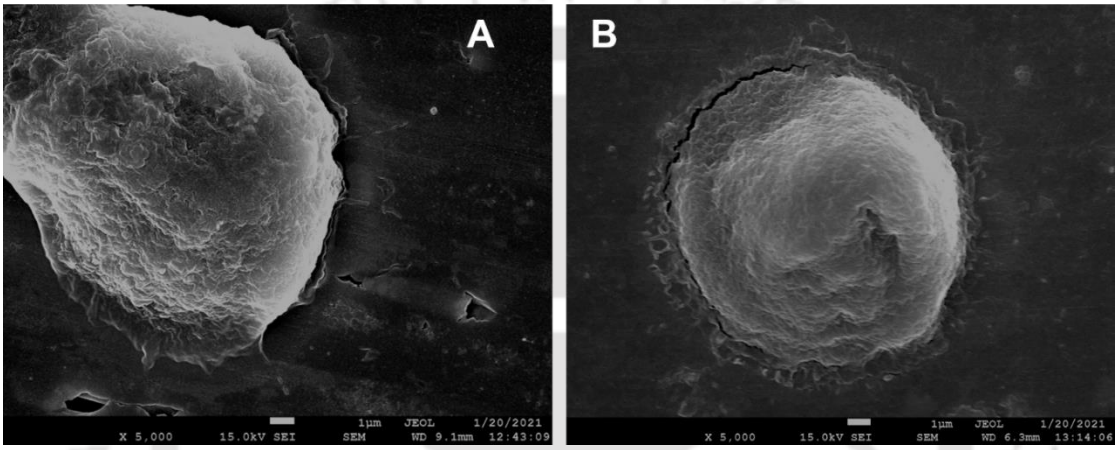

Figure 3.20. FESEM images of HEK-293 cell. (A) Control cell and that of (B) treated cell (treated with quercetin loaded Cu-HXNPs at 200 µM). The scale bar is at 1 µm.

The cell cycle study suggested the high anti-cell proliferative activity of quercetin-loaded Cu-HXNPs with the increase in the sub G0/G1 population (8.14%) compared to the control (0.73%) with subsequent changes in the other phases of the cell cycle such as G0/G1, S, and G2/M phases (**Figure 3.21A and Figure 3.21B (I-IV**). The drug-treated cells also showed a slight increase in the sub G0/G1 population (6.25%) with changes in the other phases, whereas the only Cu-HXNP-treated cells exhibited similar cell population to that of the control in all the stages. We suppose that the action of quercetin released from quercetin-loaded Cu-HXNPs would have probably involved in the upregulation of tumor suppressor genes and downregulation of genes involved in cell proliferation and differentiation.[45] The comparatively higher sub G0/G1 population in cells treated with quercetin-loaded Cu-HXNPs denotes the occurrence of apoptosis. Therefore, to confirm the apoptotic event, cleaved caspase 3-based assay was performed where the cells treated with quercetin-loaded Cu-HXNPs were found to have undergone apoptosis with the increase in the M2 population (53.17%) as compared to cells treated with free quercetin (50.70%). The apoptotic population found in the case of control

cells was only 1.20%. In addition, the cells treated with only Cu-HXNPs did not exhibit significant apoptosis and was almost similar to control cells (**Table 3.1, Figure 3.22A-D**). A quantitative figure depicting the nonapoptotic and apoptotic population of control and treated HeLa cells is also included (**Figure 3.22E**). Thus, quercetin-loaded Cu-HXNPs are suggested to be potential in activating the caspase cascade, which could efficiently trigger the apoptosis process, inhibiting the further cell growth progression.

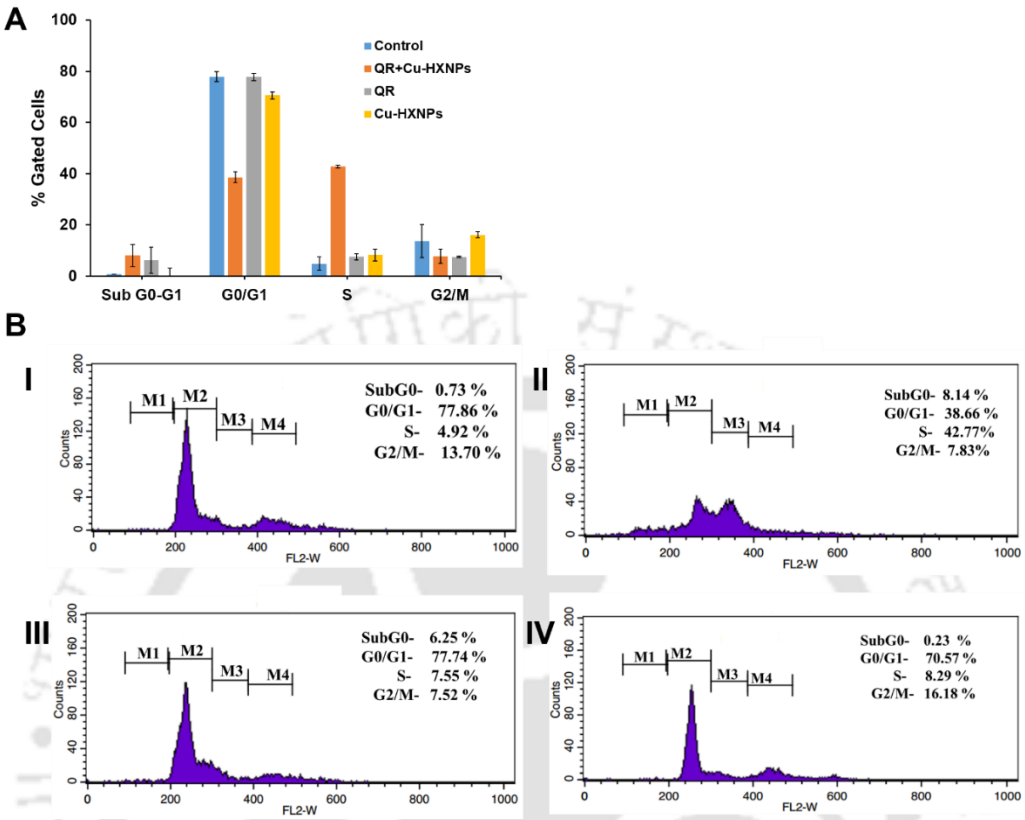

Figure 3.21. (A) Cell cycle analysis of HeLa cells. The analysis was carried out for control cells and cells treated with quercetin loaded Cu-HXNPs, free quercetin and Cu-HXNPs. (B) Flow cytometer representation of (I) control cells, (II) cells treated with quercetin loaded Cu-HXNPs, (III) cells treated with free quercetin and (IV) cells treated with Cu-HXNPs.

Sample	M1 (%) (Non-apoptotic population)	M2 (%) (Apoptotic population)
Control	98.83	1.20
QR + Cu-HXNPs	47.07	53.17
QR	49.67	50.70
Cu-HXNPs	96.77	3.38

Table 3.1. Data representing the M1 (non-apoptotic) and M2 (apoptotic) population of control cells and cells treated with quercetin loaded Cu-HXNPs, free quercetin and Cu-HXNPs.

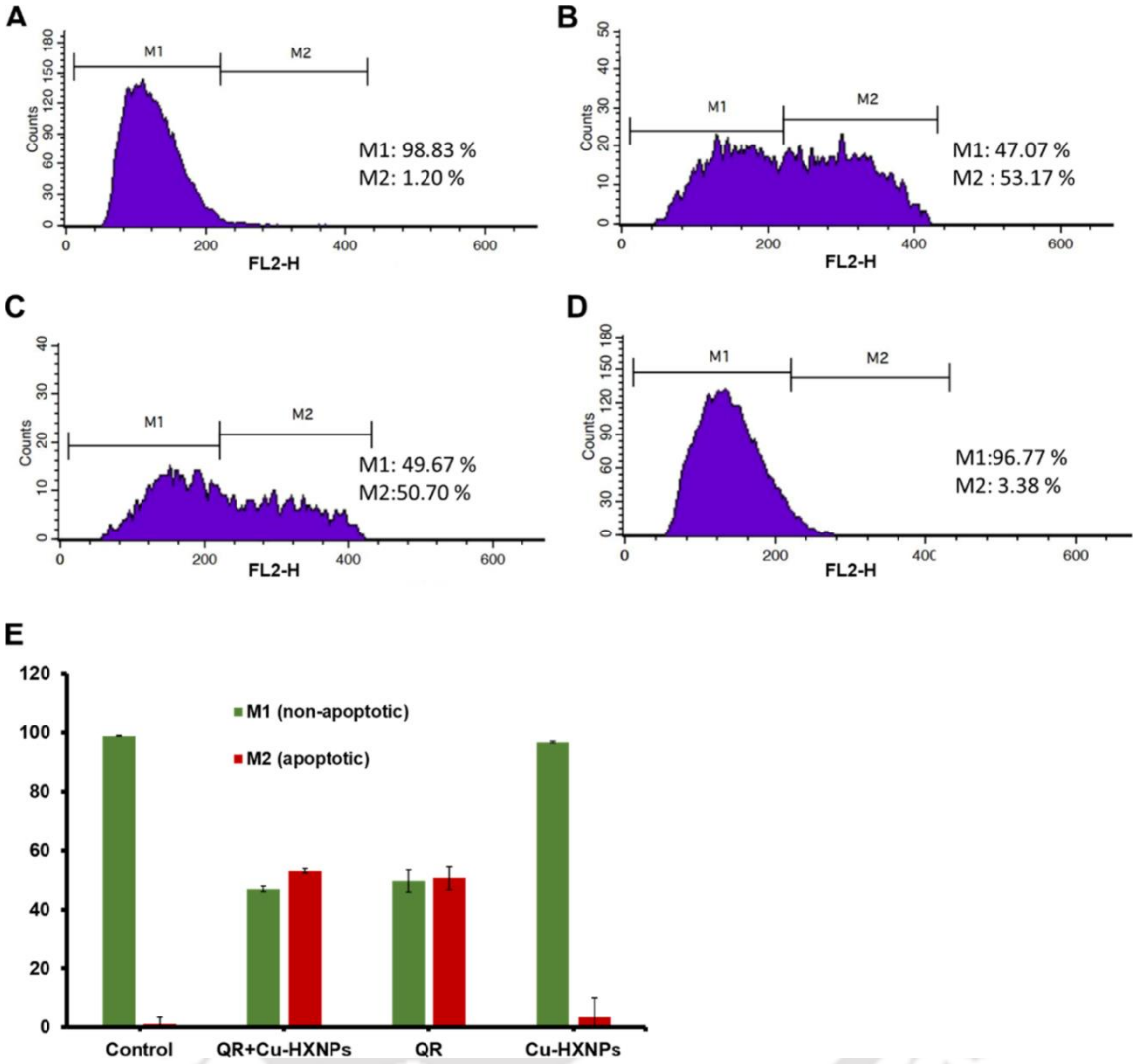

Figure 3.22. Cleaved caspase 3 assay for analysing the percentage of apoptosis in HeLa cells. The figures represent results from (A) control, (B) quercetin-loaded Cu-HXNP, (C) free quercetin and (D) Cu-HXNP treatments. (FL2-H represents the fluorescence signal height). (E) Graphical representation of assay showing M1 and M2 population of control and treated cells. The M1 population represents the non-apoptotic population and M2 population represents the apoptotic population.

3.4. Conclusions

Briefly, Cu-HXNPs were synthesized and an anticancer drug quercetin was loaded for investigating the anti-cell proliferative activity as a nanocarrier. Cu-HXNPs were found to be efficient in loading the anticancer drug quercetin, which upon interacting with HeLa cells reduced their viability and survival. The quercetin-loaded Cu-HXNPs potentially modified the

cell cycle pattern and induced apoptosis. Having the luminescent property, quercetin-loaded Cu-HXNPs exhibited the bioimaging property, which was found to be beneficial for confirming their cellular uptake. Upon checking with the normal cell line such as HEK-293, the present drug-loaded nanocarrier produced comparatively lower cytotoxicity with respect to HeLa cells. Interestingly, on analysing the therapeutic significance of quercetin-loaded Cu-HXNPs on HeLa 3D spheroids, substantial disruption of the multicellular spheroid could be observed. Based on the performed studies and the subsequent outcome, it has been concluded that the formulated luminescent drug delivery vehicle has the potential for therapeutic and imaging application in the forthcoming cancer-related investigation.

3.5. References

1. Namiki, Y.; Fuchigami, T.; Tada, N.; Kawamura, R.; Matsunuma, S.; Kitamoto, Y.; Nakagawa, M. Nanomedicine for Cancer: Lipid-Based Nanostructures for Drug Delivery and Monitoring. *Accounts Chem Res* **2011,** *44* (10), 1080-1093.
2. Sun, Q.; Zhou, Z.; Qiu, N.; Shen, Y. Rational Design of Cancer Nanomedicine: Nanoproperty Integration and Synchronization. *Adv Mater* **2017,** *29* (14), 1606628.
3. Liu, Z.; Jiang, W.; Nam, J.; Moon, J. J.; Kim, B. Y. S. Immunomodulating Nanomedicine for Cancer Therapy. *Nano Lett* **2018,** *18* (11), 6655-6659.
4. Jabr-Milane, L.; van Vlerken, L.; Devalapally, H.; Shenoy, D.; Komareddy, S.; Bhavsar, M.; Amiji, M. Multi-functional nanocarriers for targeted delivery of drugs and genes. *J Control Release* **2008,** *130* (2), 121-8.
5. Bjornmalm, M.; Thurecht, K. J.; Michael, M.; Scott, A. M.; Caruso, F. Bridging Bio-Nano Science and Cancer Nanomedicine. *Acs Nano* **2017,** *11* (10), 9594-9613.
6. Senapati, S.; Mahanta, A. K.; Kumar, S.; Maiti, P. Controlled drug delivery vehicles for cancer treatment and their performance. *Signal Transduct Target Ther* **2018,** *3*, 7.
7. Munir, M. U.; Ihsan, A.; Javed, I.; Ansari, M. T.; Bajwa, S. Z.; Bukhari, S. N. A.; Ahmed, A.; Malik, M. Z.; Khan, W. S. Controllably Biodegradable Hydroxyapatite Nanostructures for Cefazolin Delivery against Antibacterial Resistance. *Acs Omega* **2019,** *4* (4), 7524-7532.
8. Sau, T. K.; Rogach, A. L.; Jackel, F.; Klar, T. A.; Feldmann, J. Properties and applications of colloidal nonspherical noble metal nanoparticles. *Adv Mater* **2010,** *22* (16), 1805-25.
9. Geuli, O.; Miller, M.; Leader, A.; He, L.; Melamed-Book, N.; Tshuva, E. Y.; Reches, M.; Mandler, D. Electrochemical Triggered Dissolution of Hydroxyapatite/Doxorubicin Nanocarriers. *ACS Applied Bio Materials* **2019,** *2* (5), 1956-1966.

10. Qi, C.; Zhu, Y.J.; Lu, B.Q.; Zhao, X.-Y.; Zhao, J.; Chen, F. Hydroxyapatite nanosheet-assembled porous hollow microspheres: DNA-templated hydrothermal synthesis, drug delivery and protein adsorption. *J Mater Chem* **2012,** *22* (42), 22642-22650.
11. Dasgupta, A.; Biancacci, I.; Kiessling, F.; Lammers, T., Imaging-assisted anticancer nanotherapy. *Theranostics* **2020,** *10* (3), 956-967.
12. Bai, X.; Wang, S.; Xu, S.; Wang, L. Luminescent nanocarriers for simultaneous drug or gene delivery and imaging tracking. *TrAC Trends in Analytical Chemistry* **2015,** *73*, 54-63.
13. Bhattacharyya, K.; Mukherjee, S. Fluorescent Metal Nano-Clusters as Next Generation Fluorescent Probes for Cell Imaging and Drug Delivery. *Bulletin of the Chemical Society of Japan* **2017,** *91* (3), 447-454.
14. Tao, Y.; Li, M.; Ren, J.; Qu, X. Metal nanoclusters: novel probes for diagnostic and therapeutic applications. *Chemical Society reviews* **2015,** *44* (23), 8636-63.
15. Ghosh, R.; Goswami, U.; Ghosh, S. S.; Paul, A.; Chattopadhyay, A. Synergistic anticancer activity of fluorescent copper nanoclusters and cisplatin delivered through a hydrogel nanocarrier. *ACS Appl Mater Interfaces* **2015,** *7* (1), 209-22.
16. Simon, A. T.; Dutta, D.; Chattopadhya, A.; Ghosh, S. S. Copper Nanocluster-Doped Luminescent Hydroxyapatite Nanoparticles for Antibacterial and Antibiofilm Applications. *Acs Omega* **2019,** *4* (3), 4697-4706.
17. Hu, K.; Miao, L.; Goodwin, T. J.; Li, J.; Liu, Q.; Huang, L. Quercetin Remodels the Tumor Microenvironment To Improve the Permeation, Retention, and Antitumor Effects of Nanoparticles. *Acs Nano* **2017,** *11* (5), 4916-4925.
18. Srivastava, S.; Somasagara, R. R.; Hegde, M.; Nishana, M.; Tadi, S. K.; Srivastava, M.; Choudhary, B.; Raghavan, S. C. Quercetin, a Natural Flavonoid Interacts with DNA, Arrests Cell Cycle and Causes Tumor Regression by Activating Mitochondrial Pathway of Apoptosis. *Sci Rep* **2016,** *6*, 24049.
19. Hashemzaei, M.; Delarami Far, A.; Yari, A.; Heravi, R. E.; Tabrizian, K.; Taghdisi, S. M.; Sadegh, S. E.; Tsarouhas, K.; Kouretas, D.; Tzanakakis, G.; Nikitovic, D.; Anisimov, N. Y.; Spandidos, D. A.; Tsatsakis, A. M.; Rezaee, R. Anticancer and apoptosis inducing effects of quercetin in vitro and in vivo. *Oncol Rep* **2017,** *38* (2), 819-828.
20. Syamchand, S. S.; Sony, G., Multifunctional hydroxyapatite nanoparticles for drug delivery and multimodal molecular imaging. *Microchimica Acta* **2015,** *182* (9), 1567-1589.
21. Weerasuriya, D. R. K.; Wijesinghe, W.; Rajapakse, R. M. G., Encapsulation of anticancer drug copper bis(8-hydroxyquinoline) in hydroxyapatite for pH-sensitive targeted delivery and slow release. *Materials science & engineering. C, Materials for biological applications* **2017,** *71*, 206-213.
22. Chen, M. H.; Hanagata, N.; Ikoma, T.; Huang, J. Y.; Li, K. Y.; Lin, C. P.; Lin, F. H., Hafnium-doped hydroxyapatite nanoparticles with ionizing radiation for lung cancer treatment. *Acta biomaterialia* **2016,** *37*, 165-73.

23. Wang, H.; He, L.; Zhang, P.; Zhang, J.; Chen, Z.; Ren, X.; Mei, X., Folate-modified hydroxyapatite nanorods induce apoptosis in MCF-7 cells through a mitochondrial-dependent pathway. *New Journal of Chemistry* **2019,** *43* (37), 14728-14738.
24. Ikeda, N. E.; Novak, E. M.; Maria, D. A.;Velosa, A. S.; Pereira, R. M., Synthesis, characterization and biological evaluation of Rutin-zinc(II) flavonoid -metal complex. *Chem Biol Interact* **2015,** *239*, 184-91.
25. Zhao, H.; Wu, C.; Gao, D.; Chen, S.; Zhu, Y.; Sun, J.; Luo, H.; Yu, K.; Fan, H.; Zhang, X., Antitumor Effect by Hydroxyapatite Nanospheres: Activation of Mitochondria-Dependent Apoptosis and Negative Regulation of Phosphatidylinositol-3-Kinase/Protein Kinase B Pathway. *ACS Nano* **2018,** *12* (8), 7838-7854
26. Wang, J.; Zhang, X.; Li, X.; Zhang, Y.; Hou, T.; Wei, L.; Qu, L.; Shi, L.; Liu, Y.; Zou, L.; Liang, X., Anti-gastric cancer activity in three-dimensional tumor spheroids of bufadienolides. *Sci Rep* **2016,** *6*, 24772.
27. Patra, M.; Mukherjee, R.; Banik, M.; Dutta, D.; Begum, N. A.; Basu, T. Calcium phosphate-quercetin nanocomposite (CPQN): A multi-functional nanoparticle having pH indicating, highly fluorescent and anti-oxidant properties. *Colloids and Surfaces B: Biointerfaces* **2017,** *154*, 63-73.
28. Mezzetti, A.; Protti, S.; Lapouge, C.; Cornard, J. P. Protic equilibria as the key factor of quercetin emission in solution. Relevance to biochemical and analytical studies. *Physical Chemistry Chemical Physics* **2011,** *13* (15), 6858-6864.
29. Chen, Z.; Qian, S.; Chen, J.; Chen, X. Highly fluorescent gold nanoclusters based sensor for the detection of quercetin. *J Nanopart Res* **2012,** *14* (12), 1264.
30. Oliveira, E.; Bertolo, E.; Nunez, C.; Pilla, V.; Santos, H. M.; Fernandez-Lodeiro, J.; Fernandez-Lodeiro, A.; Djafari, J.; Capelo, J. L.; Lodeiro, C. Green and Red Fluorescent Dyes for Translational Applications in Imaging and Sensing Analytes: A Dual-Color Flag. *ChemistryOpen* **2018,** *7* (1), 9-52.
31. Farzadi, A.; Bakhshi, F.; Solati-Hashjin, M.; Asadi-Eydivand, M.; Osman, N. A. a. Magnesium incorporated hydroxyapatite: Synthesis and structural properties characterization. *Ceram Int* **2014,** *40* (4), 6021-6029.
32. Lin, K.; Liu, X.; Chang, J.; Zhu, Y. Facile synthesis of hydroxyapatite nanoparticles, nanowires and hollow nano-structured microspheres using similar structured hard-precursors. *Nanoscale* **2011,** *3* (8), 3052-3055.
33. Sheikh, F. A.; Kanjwal, M. A.; Macossay, J.; Barakat, N. A.; Kim, H. Y. A simple approach for synthesis, characterization and bioactivity of bovine bones to fabricate the polyurethane nanofiber containing hydroxyapatite nanoparticles. *Express Polym Lett* **2012,** *6* (1), 41-53.
34. Okada, M.; Matsumoto, T. Synthesis and modification of apatite nanoparticles for use in dental and medical applications. *Japanese Dental Science Review* **2015,** *51* (4), 85-95.

35. Vacek, J.; Papoušková, B.; Vrba, J.; Zatloukalová, M.; Křen, V.; Ulrichová, J. LC–MS metabolic study on quercetin and taxifolin galloyl esters using human hepatocytes as toxicity and biotransformation in vitro cell model. *Journal of Pharmaceutical and Biomedical Analysis* **2013,** *86*, 135-142.

36. Tanaka, S.; Trakooncharoenvit, A.; Nishikawa, M.; Ikushiro, S.; Hara, H. Comprehensive Analyses of Quercetin Conjugates by LC/MS/MS Revealed That Isorhamnetin-7- O-glucuronide-4'- O-sulfate Is a Major Metabolite in Plasma of Rats Fed with Quercetin Glucosides. *J Agric Food Chem* **2019,** *67* (15), 4240-4249.

37. Galluzzo, P.; Martini, C.; Bulzomi, P.; Leone, S.; Bolli, A.; Pallottini, V.; Marino, M., Quercetin-induced apoptotic cascade in cancer cells: antioxidant versus estrogen receptor alpha-dependent mechanisms. *Mol Nutr Food Res* **2009,** *53* (6), 699-708.

38. Cao, G.; Sofic, E.; Prior, R. L., Antioxidant and prooxidant behavior of flavonoids: structure-activity relationships. *Free Radic Biol Med* **1997,** *22* (5), 749-60.

39. De Marchi, U.; Biasutto, L.; Garbisa, S.; Toninello, A.; Zoratti, M., Quercetin can act either as an inhibitor or an inducer of the mitochondrial permeability transition pore: A demonstration of the ambivalent redox character of polyphenols. *Biochimica et Biophysica Acta (BBA) - Bioenergetics* **2009,** *1787* (12), 1425-1432.

40. Dharmaraja, A. T. Role of Reactive Oxygen Species (ROS) in Therapeutics and Drug Resistance in Cancer and Bacteria. *J Med Chem* **2017,** *60* (8), 3221-3240.

41. Edmondson, R.; Broglie, J. J.; Adcock, A. F.; Yang, L., Three-dimensional cell culture systems and their applications in drug discovery and cell-based biosensors. *Assay Drug Dev Technol* **2014,** *12* (4), 207-218.

42. Perillo, B.; Di Donato, M.; Pezone, A.; Di Zazzo, E.; Giovannelli, P.; Galasso, G.; Castoria, G.; Migliaccio, A., ROS in cancer therapy: the bright side of the moon. *Exp Mol Med* **2020,** *52* (2), 192-203.

43. Redza-Dutordoir, M.; Averill-Bates, D. A., Activation of apoptosis signalling pathways by reactive oxygen species. *Biochim Biophys Acta* **2016,** *1863* (12), 2977-2992.

44. Rameshthangam, P.; Chitra, J. P., Synergistic anticancer effect of green synthesized nickel nanoparticles and quercetin extracted from Ocimum sanctum leaf extract. *Journal of Materials Science & Technology* **2018,** *34* (3), 508-522.

45. Bishayee, K.; Ghosh, S.; Mukherjee, A.; Sadhukhan, R.; Mondal, J.; Khuda-Bukhsh, A. R. Quercetin induces cytochrome-c release and ROS accumulation to promote apoptosis and arrest the cell cycle in G2/M, in cervical carcinoma: signal cascade and drug-DNA interaction. *Cell Prolif* **2013,** *46* (2), 153-63.

Chapter 4

In Vitro Therapeutic Attributes of Luminescent Hydroxyapatite Nanoparticles in Co-Delivery Approach

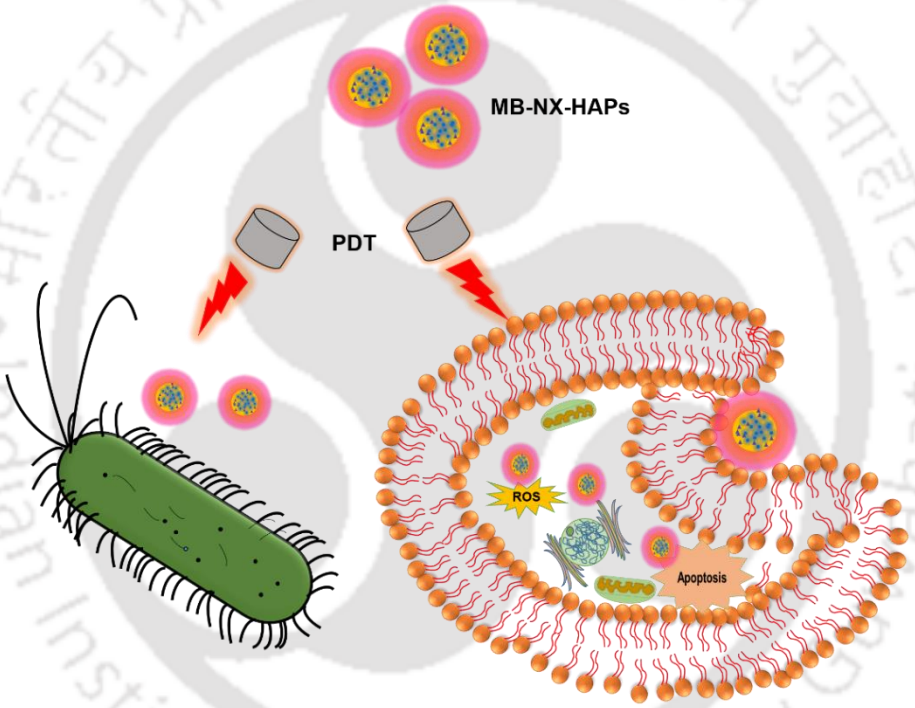

Chapter 4

In Vitro Therapeutic Attributes of Luminescent Hydroxyapatite Nanoparticles in Co-Delivery Approach

Abstract

Pivotal objectives of clinical importance have been accomplished through diverging treatment modalities, implemented through nanoscale platforms. In the present study, hydroxyapatite nanoparticles doped with copper nanoclusters (HAPs) were explored for co-delivery of hydrophobic drug namely norfloxacin (NX) and hydrophilic photosensitizer such as methylene blue (MB). NX and MB were successfully homed into HAPs (MB-NX-HAPs), which further exhibited a pH dependent release of NX and MB. With the objective of attaining enhanced effect, MB-NX-HAPs were evaluated for combination therapy, involving chemotherapy and photodynamic therapy (PDT) with irradiation at 640 nm. The combinatorial therapy approach was initially applied for antibacterial therapy, which suggested a considerable reduction in bacterial growth of Gram negative strain *Pseudomonas aeruginosa* MTCC 2488. Thereafter, the antiproliferative study performed in cancer cell lines (HeLa and MCF-7) revealed the efficiency of MB-NX-HAPs in bestowing combinatorial effect through chemotherapy and PDT (irradiation at 640 nm). The combined effect exerted through MB-NX-HAPs subsequently induced ROS generation, cell cycle alteration and apoptosis activation in cancer cells. The biocompatible nature of MB-NX-HAPs was appreciably shown through their minimal effect in normal cell line (HEK-293). Additionally, HAPs through luminescence of copper nanoclusters were suggested to aid in bioimaging of cancer cell lines.

4.1. Introduction

Co-delivery is a potential avenue for attaining combinatorial effect in therapeutic realm. Monotherapy involving single drug, individual techniques like radiation therapy, phototherapy, immunotherapy and chemotherapy have been always clinically implemented for different kinds

of ailments. However, with the advancement of severity in diseases due to mutation, molecular complexity and multidrug resistance (MDR), many alternate strategies have been devised. One of the newly conceived approaches is the combinatorial therapy, a standard regimen for treating hypertension, rheumatoid arthritis, pathogenic infections and even different kinds of cancer. Combinatorial therapy employs multiple mechanisms or the usage of two or more pharmacologically active compounds for the treatment procedure.[1-3] One of the mechanisms, adopted in combinatorial treatment is photodynamic therapy (PDT), which is a light induced external stimuli for treatment of varieties of infirmities. PDT is a non-invasive treatment modality, that entails three essential elements such as photosensitizer, suitable light source and oxygen. Upon excitation under light of suitable wavelength, photosensitizer transfers its energy to endogenous dissolved oxygen, which generates reactive oxygen species (ROS). Combining drug based therapy in conjugation with PDT is understood to intensify the treatment impact, compensating their drawbacks exhibited, when applied individually.[4-6]

Cancer therapy has explored numerous classes of drugs, among which non-cancer drugs through reprofiling have emerged out to render promising divergence for management of the disease. Fluoroquinolones (FQ) represent the most notable therapeutic class of compounds in medicinal chemistry, for the treatment of broad range of bacterial infections, including MDR *Mycobacterium tuberculosis*.[7,8] Upon deactivating DNA topoisomerase II or DNA gyrase, FQ interrupt DNA transcription and replication in bacteria. Besides antibacterial properties, FQ have been admired for other clinical implications such as anti-inflammatory, antiviral, antifungal and even anticancer. This interesting transition from antibacterial to anticancer agents is mostly attributed to their recognition of topoisomerases, that share sequence homology in both prokaryotes and eukaryotes. Studies suggest that complexation of FQ with metal ions such as copper, enhances antiproliferative activity, potentially triggering cascade of apoptosis.[9-11] Norfloxacin (NX), known to be one of the second generation FQ is documented to be lysosomotropic and dissipate membrane potential with induction of ROS generation in cancer cell lines. Therefore, employment of NX in combination with a suitable photosensitizer for PDT would possibly augment combinatorial therapy, with limited dosage in contrast to conventional curative approach.[12,13]

However, administration of free form of drugs or photosensitizers in any clinical regimen might amplify systemic toxicity, promote agglomeration, non-specific biodistribution and premature drug degradation. These concerns can be resolved through encapsulating them into suitable nano systems. The drug delivery nano platforms solve the aforementioned apprehensions with improved payload lodging time, leading to superior pharmacokinetics with negligible peripheral toxicity. The tailorable physiochemical properties and ease of functionalization have positioned inorganic nanomaterials as drug delivery nanocarrier in combinatorial therapy.[14-18] The leaky vasculature and inadequate lymphatic drainage nature of tumour sites facilitate enhanced permeation and retention effect (EPR), which drives reflux targeting of numerous well-formulated inorganic nanocarriers, for combinatorial therapy. Usually, the compromised sites in various diseases are always characterized by abnormal biochemical microenvironment with inflammatory infiltrates and varying pH gradient. Interestingly, this complex nature involving factors such as redox, enzyme and pH has been scrutinized for fabricating efficient inorganic nanocarriers for intrinsic stimuli triggered drug release.[19-24]

Considering the inevitable significance of presenting a biocompatible inorganic nanocarrier for therapy, innumerable expeditions have been carried out in various inorganic resources. Hydroxyapatite nanoparticles, due to their resemblance to mineral phase of hard tissues have aroused curiosity in applying for drug delivery. Apart from pharmacological characteristics they acquire, hydroxyapatite nanoparticles are found to be capable of accommodating both hydrophilic and hydrophobic molecules, unlike most of the documented organic nanocarriers.[25-27] In addition to therapy, bioimaging is an integral part of diagnosis for intracellular monitoring and analysis of any disease condition, presence and distribution of uptaken nanocarrier. Bioimaging can be achieved by amalgamating luminescent entities with the suitable nanocarriers. Copper nanoclusters are excellent luminescent material, with their tunable emission property and stability, alongside enhancing the overall therapeutic effect through copper ions. Moreover, red emitting copper nanoclusters hold significant importance for *in vivo* imaging, due to excellent membrane penetrability, physiological tolerance and low protein adsorption.[28]

The current work details the development of copper nanocluster doped hydroxyapatite nanoparticles (HAPs), by slightly modifying our previously reported protocol.[29]

The entire nanoformulation was investigated for combinatorial therapy by co-delivering a hydrophobic drug and a hydrophilic photosensitizer namely NX and methylene blue (MB) respectively (**Figure 4.1)**. Encapsulation of 73 % of NX and loading of 69 % of MB could be achieved in the currently synthesised HAPs (MB-NX-HAPs). Along with chemotherapeutic approach, PDT technique was introduced, aiming to attain the combined treatment effect through MB-NX-HAPs in antibacterial and anticancer application. Antibacterial application carried out in *Pseudomonas aeruginosa* MTCC 2488, suggested the effect of combinatorial therapy in reducing their viability. Similarly, the antiproliferative study attempted in HeLa and MCF-7 cell lines, revealed the combined outcome of chemotherapy and PDT through MB-NX-HAPs by significantly inhibiting the proliferation, with minimal effect on normal cell line such as HEK-293. The current combination therapy could enhance ROS generation, modify cell cycle pattern and induce apoptosis in cancer cells. Also, the luminescent property inherited by HAPs through doping with copper nanoclusters was evaluated for bioimaging purpose in cancer cell lines.

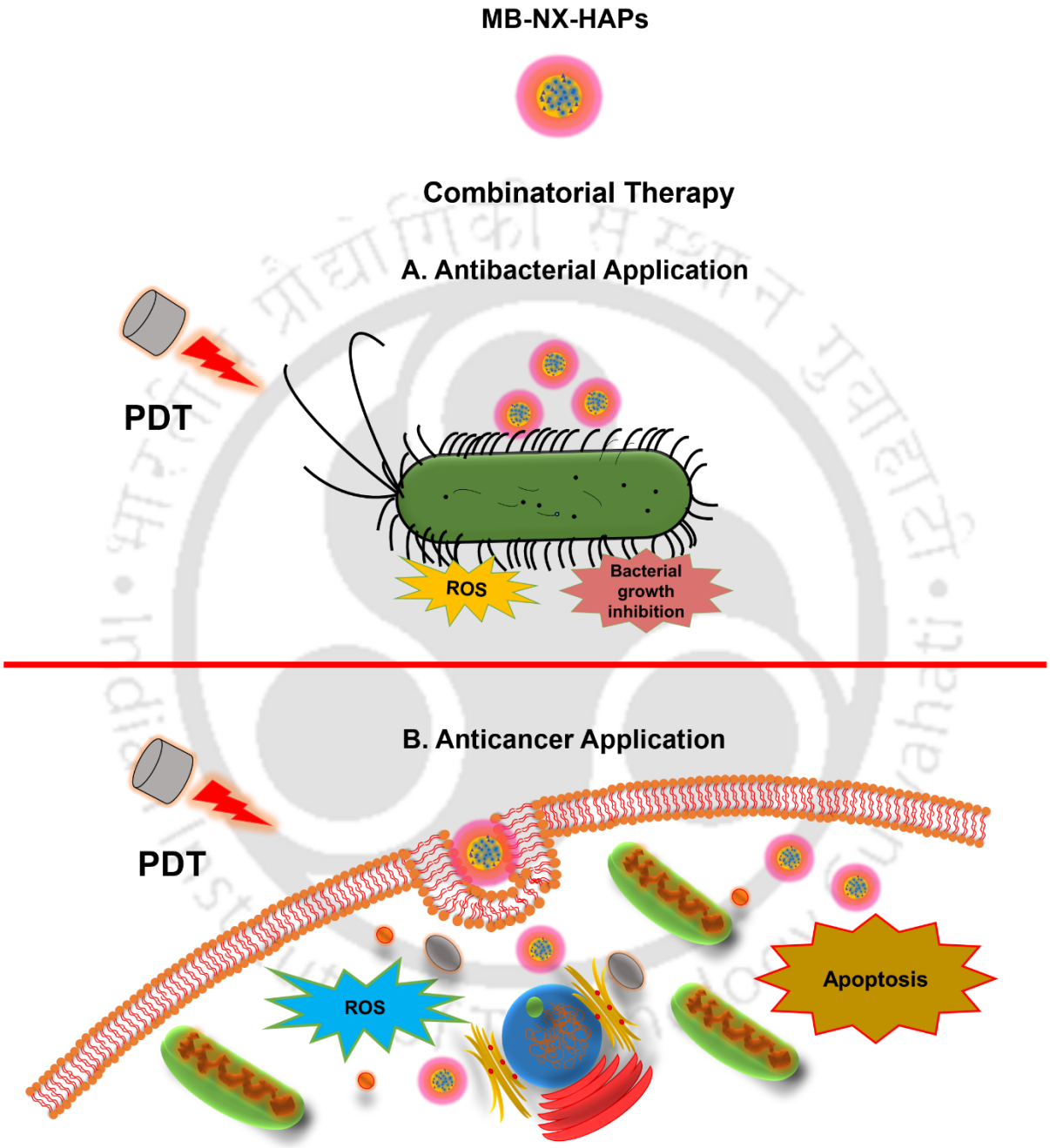

Figure 4.1. Copper nanocluster doped hydroxyapatite nanoparticles (HAPs) for combined therapy (chemotherapy and PDT) in bacterial and cancer cell treatment by co-delivering norfloxacin (NX) and methylene blue (MB).

4.2. Materials and Methods

4.2.1. Chemicals

Our experimental methods included the usage of following chemicals as-purchased: calcium chloride dihydrate (Merck), strontium nitrate pure (Merck), potassium dihydrogen phosphate (Merck), PEG (poly ethylene glycol) 400 (Merck), polyvinyl alcohol 87-89% hydrolysed (Sigma-Aldrich), glacial acetic acid (Rankem), ammonia 25% (Merck), copper (II) sulfate pentahydrate pure (Merck), bovine serum albumin (Himedia), sodium hydroxide pellet (Rankem), hydrazine hydrate 80% (Merck), norfloxacin (Sisco Research Laboratories), methylene blue (Qualigens), brain heart infusion (BHI) broth (Himedia) and nutrient broth (NB) (Himedia). Milli-Q grade water (> 18 MΩ cm^{-1}, Millipore) was used in all the experiments.

4.2.2. Preparation of Norfloxacin Encapsulated Copper Nanocluster Doped Hydroxyapatite Nanoparticles (NX-HAPs) and Methylene Blue Loaded NX-HAPs (MB-NX-HAPs)

Initially, to 1.5 mL of 0.2 M calcium chloride dihydrate and 0.12 M of strontium nitrate, 0.5 mL of PEG 400 was added. The pH of the solution was adjusted to pH 11 using 1M NaOH. To the stirring mixture, 4.5 mL of copper nanocluster dispersion was added, whose synthesis method had been already detailed in our previous report.[29] Further, 1.5 mL of 0.12 M potassium dihydrogen phosphate was added, resulting into turbid dispersion. A second set of solution containing 1 mL of PVA with 2.5% diluted glacial acetic acid and 0.5% ammonia was kept under stirring, into which NX was added dropwise. The pH of the later set of solution was brought to 11. Subsequently, the second set was mixed with first set and the whole reaction mixture was kept under stirring for 1 hr at room temperature in dark. The final concentration of NX added to the total reaction mixture was 40 µg/mL. At the end of an hour, the dispersion was introduced to heating at 85 °C for 2 min. Once cooled, the dispersion was centrifuged at 5000 rpm for 10 min. The obtained pellet was redispersed and stored at 4 °C for further analysis.

Loading of MB into NX-HAPs was done as follows. At the completion of NX-HAPs synthesis, followed by initial centrifugation, 20 µM of MB was added to the dispersion and stirred for an hour in dark. At the end of stirring, the MB loaded NX-HAPs (MB-NX-HAPs) were centrifuged at 5000 rpm. The redispersed composite was stored at 4 °C and used for various analysis.

4.2.3. Study on Drug Loading Efficiency

After the encapsulation of NX and loading of MB into MB-NX-HAPs was completed as mentioned, their efficiency was analysed using fluorescence spectroscopy (Perkin - Elmer LS55 spectrofluorometer) and calculated by the following formula.

$$\% \text{ of encapsulation efficiency} = \frac{NX_i - NX_f}{NX_i} x100$$

$$\% \text{ of loading efficiency} = \frac{MB_i - MB_f}{MB_i} x100$$

Here, NX_i or MB_i denotes initial amount of added NX or MB respectively and NX_f or MB_f denotes amount of unloaded NX or MB respectively.

In case of NX, the encapsulation efficiency was checked at an excitation and emission of 272 nm and 445 nm respectively. Similarly, the amount of MB loaded was checked at an excitation/emission of 665 nm/685 nm

4.2.4. Release Study

The release profile of both NX and MB was conducted in pH 4 (acetate buffer) and pH 7.4 (PBS buffer), that mimic the pH of tumour and physiological sites respectively. Once the encapsulation and loading of NX and MB was sequentially achieved, release study was performed with MB-NX-HAPs. The samples were incubated in acetate and PBS buffer with their serial withdrawal at various time period (0^{th}, 3^{rd}, 6^{th}, 9^{th}, 12^{th} and 24^{th} h). Further, the samples were centrifuged to recover the supernatant and analysed by fluorescence spectroscopy. The fluorescence measurements were recorded at an excitation/emission of 272

nm/445 nm and 665 nm/685 nm for NX and MB respectively. The cumulative release of both NX and MB was calculated using the formula given below.

$$\text{Cumulative release \%} = \frac{\text{Drug (NX or MB) released in supernatant}}{\text{Drug ((NX or MB) loaded in nanocarrier}} \text{x } 100$$

4.2.5. UV Visible Spectroscopy

The optical characteristics of MB, HAPs and MB-NX-HAPs were studied by a UV-visible spectrophotometer (Jasco V-630) in the UV-visible range.

4.2.6. Luminescence Measurements

All the luminescence spectra measurements were analysed with the help of fluorescence spectrophotometer (by using a Perkin - Elmer LS55 spectrofluorometer and fluoromax).

4.2.7. Singlet Oxygen Detection Study Using 1,3-Diphenylizobenzofuran (DPBF)

The singlet oxygen generation was analysed by mixing 100 µL of MB-NX-HAPs and 100 µL of 0.08 mM DPBF. The reaction mixture was subjected to irradiation using an LED array having an emission peak at 640 nm (2.5 mW/cm^2) for a time period of 0 to 4 min. The luminescence of DPBF was monitored and recorded using fluorescence spectrophotometer. Similarly, the experiment was compared with control samples such as MB-NX-HAPs and DPBF without irradiation (dark) as well as only DPBF under irradiation at 640 nm.

4.2.8. Transmission Electron Microscopy (TEM)

The as synthesized NX-HAPs and MB-NX-HAPs were imaged under a transmission electron microscope, having a maximum accelerating voltage of 200 keV (JEM 2100; JEOL, Peabody, MA). For imaging, 7 µL of sample was drop-cast to a carbon coated copper grid and air dried. Prior to drop-casting, all the samples were sonicated in ultrasonicate bath (TELSONIC) for 40 min.

4.2.9. Field Emission Scanning Electron Microscopy (FESEM).

Images of NX-HAPs and MB-NX-HAPs were recorded by FESEM (Sigma 300). After sonicating for 40 min, 20 µL of sample was drop cast and kept under air drying overnight.

To understand the morphological features of control and treated bacterial cells, the bacteria were treated with NX-HAPs (at the MIC of NX in NX-HAPs) and incubated for 10 h. The control and treated bacteria were centrifuged at 5000 rpm for 2 min and resuspended in sterile water. 20 µL of the diluted samples was drop cast and air dried overnight for analysis.

The morphology of treated HeLa and MCF-7 cells was analysed using FESEM. Initially, the cultured cells (HeLa or MCF-7) were treated with MB-NX-HAPs (at a concentration of NX and MB where 50% of viability reduction was observed) for 8 h and then irradiated at 640 nm (2.5 mW/cm^2) for 30 min. Both the treated and untreated cells (control) were incubated for another 4 h (a total 12 h incubation). At the end of incubation, the cells were trypsinized and fixed using 0.1% formaldehyde. After a final wash with PBS, suitable dilution of cell samples was drop cast to an aluminium foil covered glass slide. Air dried samples were analysed under electron microscope.

4.2.10. Zeta Potential

The zeta potential of MB, NX, HAPs, NX-HAPs and MB-NX-HAPs was measured through Malvern Zetasizer Nano ZS.

4.2.11. Antibacterial Studies

The antibacterial studies were performed using the Gram positive strain (*Staphylococcus aureus* MTCC 96) and Gram negative strain (*Pseudomonas aeruginosa* MTCC 2488). *Staphylococcus aureus* MTCC 96 and *Pseudomonas aeruginosa* MTCC 2488 were grown in BHI and NB respectively at 37 °C for 12 h (180 rpm). *Pseudomonas aeruginosa* MTCC 2488 was treated with different concentrations of free NX (0.05 µg/mL to 10 µg/mL), NX-HAPs (with NX concentration ranging from 0.05 µg/mL to 10 µg/mL) and HAPs (NX -0 µg/mL) to check the MIC (minimum inhibition concentration) and MBC (minimum bactericidal concentration). *Staphylococcus aureus* MTCC 96 was treated with free NX (10 µg/mL to 400 µg/mL), NX-HAPs (having NX concentration from 10 µg/mL to 400 µg/mL) and HAPs (NX - 0 µg/mL). Monitoring of bacterial growth was done by measuring the optical density (OD) in UV-visible spectroscopy (Jasco V-630) at 595 nm. All the measurements were taken in triplicates.

Additionally, MIC and MBC of NX and NX-HAPs for *Pseudomonas aeruginosa* MTCC 2488 were double confirmed by plating method. To a nutrient agar plate, 100 µL of culture treated with MIC and MBC of each sample was spread-plated and incubated for 12 h at 37 °C.

4.2.12. Growth Kinetics Study

The study on bacterial growth kinetics was conducted for *Pseudomonas aeruginosa* MTCC 2488, once subjected to treatment with the MIC and MBC of NX and NX-HAPs. Periodical recording of OD at different time intervals was carried out for 12 h at 37 °C. Each measurement was recorded in triplicates.

4.2.13. Antibacterial Photodynamic Therapy (PDT)

Bacterial cells ($1x10^8$ CFU/mL) from overnight culture were treated with HAPs (NX - 0 µg/mL, MB - 0 µM), NX (0.05 µg/mL), NX-HAPs (NX - 0.05 µg/mL), free MB (5 µM), and MB-NX-HAPs (NX - 0.05 µg/mL, MB - 5 µM). Further, all the bacterial samples including untreated (control) culture were pre-incubated for 3 h in dark. Following incubation, bacterial samples treated with MB-NX-HAPs and free MB were subjected to PDT through irradiation at 640 nm (2.5 mW/cm^2), using a customized LED array for 30 min. Bacterial cells treated with remaining samples were kept covered with aluminium foil for 30 min as the PDT group. The bacteria treated with free MB and MB-NX-HAPs, without irradiation (dark) were also maintained for the study. After 30 min, all the samples were diluted in PBS and 100 µL of culture was plated on nutrient agar plates and incubated at 37 °C overnight, for counting the CFU (colony forming unit). The initial antibacterial PDT study on bacteria treated with different concentrations of free MB (2 µM, 5 µM and 10 µM) under irradiation and non-irradiation (dark) was conducted in the similar way. The percentage of survival inhibition was calculated as per following formula.[30]

$$\% \text{ of survival inhibition} = \frac{B_c - B_t}{B_c} x100$$

Here, B_c denotes CFU/mL of bacteria without any treatment and B_t denotes CFU/mL of bacteria under treatment groups.

4.2.14. Cell Culture Studies

Cell Culture

The cell culture studies were performed in HeLa (human cervical carcinoma), MCF-7 (human breast cancer) and HEK-293 (human embryonic kidney-293) cells. All these cell lines were purchased from National Centre for Cell Sciences (NCCS), Pune, India. The cells were maintained in Dulbecco's Modified Eagle's Medium supplemented with L-glutamine (4 mM), penicillin (50 units per mL), streptomycin (50 mg/mL, Sigma-Aldrich) and fetal bovine serum (10% v/v, PAA Laboratories, Austria). The cells were cultured under 5% CO_2 humidified incubator at 37 °C.

4.2.15. Cell Viability Assay

The cell viability assay on HeLa, MCF-7 and HEK-293 cells was conducted using MTT [3-(4,5-dimethylthiazol-2-yl)-2,5-diphenyltetrazolium bromide]. Initially, $1x10^4$ HeLa or MCF-7 or HEK-293 cells /well were seeded into a 96 well plate and grown in DMEM media inside a 5% CO_2 humidified incubator at 37 °C for 24 h. The cells were treated with HAPs (NX - 0 µg/mL and MB- 0 µM), NX-HAPs of varying NX concentrations (0.4, 0.6, 0.8, 2 and 4 µg/mL), MB-NX-HAPs (with NX concentrations at 0.4, 0.6, 0.8, 2 and 4 µg/mL and MB concentrations at 0.11, 0.17, 0.23, 0.57 and 1.15 µM), free NX (0.4, 0.6, 0.8, 2 and 4 µg/mL) and free MB (0.11, 0.17, 0.23, 0.57 and 1.15 µM). After 8 h of incubation, the cell samples to be irradiated (free MB and MB-NX-HAPs treated cells) were exposed to 640 nm light (2.5 mW/cm^2) for 30 min. Following irradiation, the cells were further incubated with other treatment groups for 24 h at 37 °C in 5% CO_2 humidified incubator. Free MB and MB-NX-HAPs treated cells without irradiation (dark) were also compared for the viability assay. With the completion of incubation, the MTT assay was conducted. The formazan product obtained from the reduction of MTT through respiratory mitochondrial enzyme in viable cells is spectrophotometrically detected at 570 nm with the reference filter at 655 nm. The resultant formazan product is directly proportional to the viable cells present. The percentage (%) of cell viability was calculated as follows.

$$\% \text{ of viable cells} = \frac{(\text{A570-A655}) \text{of treated cells}}{(\text{A570-A655}) \text{of control cells}} \text{x } 100$$

4.2.16. Cellular Uptake Study

To confirm the internalization in HeLa and MCF-7 cells, the cells were seeded at a density of $1x10^5$ cells in six well plates. Treatment of each cell line was done with HAPs, NX-HAPs and MB-NX-HAPs for 5 h. The treated cells were washed in PBS and harvested by trypsinization. The resuspended cells were then analysed in a flow cytometer (Cytoflex, Beckman Coulter), for the uptake.

4.2.17. Confocal Laser Scanning Microscopy

The bioimaging property of HAPs and NX-HAPs was analysed in HeLa and MCF-7 cells. The cells ($1x10^5$) were initially seeded on a sterile cover slip placed inside a 35 mm tissue culture petri dish. The grown cells were treated with samples (at concentration of NX, where 50% viability reduction was obtained in NX-HAPs) and kept under incubation for 5 h. Further, untreated (control) and treated cells were fixed using 0.1% formaldehyde and 70% ice cold ethanol. The cover slip containing cells was then carefully placed on a microscopic glass slide and sealed in all the four sides. All the samples were visualized under confocal microscope (Zeiss LSM 880) at a laser excitation of 405 nm.

4.2.18. DCFH-DA Based ROS Study

To study ROS generation in HeLa and MCF-7, $1x10^5$ cells of each cell line were seeded. The grown cells were treated with HAPs, NX-HAPs, MB-NX-HAPs, free NX and free MB (at concentration of NX and MB in MB-NX-HAPs, where cell viability was reduced to 50%) and incubated for 8 h. After incubation, the cells to be irradiated (free MB and MB-NX-HAPs treated cells) were subjected to 640 nm LED array of light for 30 min. Cells treated with free MB and MB-NX-HAPs without irradiation (dark) were also maintained for analysis. By the completion of the irradiation, the cells were incubated with 10 µM of DCFH-DA (2,7-dichlorofluoresceindiacetate) for 30 min. Further, the cells were trypsinized and replenished with fresh media. Subsequently, the analysis for DCF fluorescence in cells was performed in a flow cytometer (Cytoflex, Beckman Coulter).

4.2.19. Cell Cycle Analysis

For cell cycle analysis, HeLa or MCF-7 cells ($1x10^5$ cells) were seeded in six well plates. The mode of treatment in cells was similar to the method conducted for MTT assay. At the end of treatment and incubation, accumulation of media and PBS of control and treated cells were separately done, followed by trypsinization of cells. The cells were centrifuged at 650 rcf for 5 min. The cells collected from centrifugation were fixed in 70% of ice cold ethanol, with careful vortexing and stored at 4 °C. For analysis, the cells were carefully washed using ice cold PBS and incubated with RNase at 55 °C. The RNase treated cells were stained with 1 mg/mL of PI (propidium iodide) and incubated at 37 °C in dark for 30 min. Finally, cell cycle analysis was carried out for all the samples in a flow cytometer FacsCalibur (BD Biosciences, NJ) and PI fluorescence was recorded with the help of CellQuest programme (BD Biosciences).

4.2.20. Apoptosis Assay

HeLa cells or MCF-7 cells ($1x10^5$ cells) were cultured followed by treatment, similar to that carried out for MTT assay. After the treatment procedure, the cells were trypsinized and centrifuged at 650 rcf for 5 min. The trypsinized cells were incubated with annexin-v FITC antibody in a staining buffer and finally analysed in a flow cytometer (Cytoflex, Beckman Coulter).

4.3. Results and Discussion

4.3.1. Synthesis and Characterisations

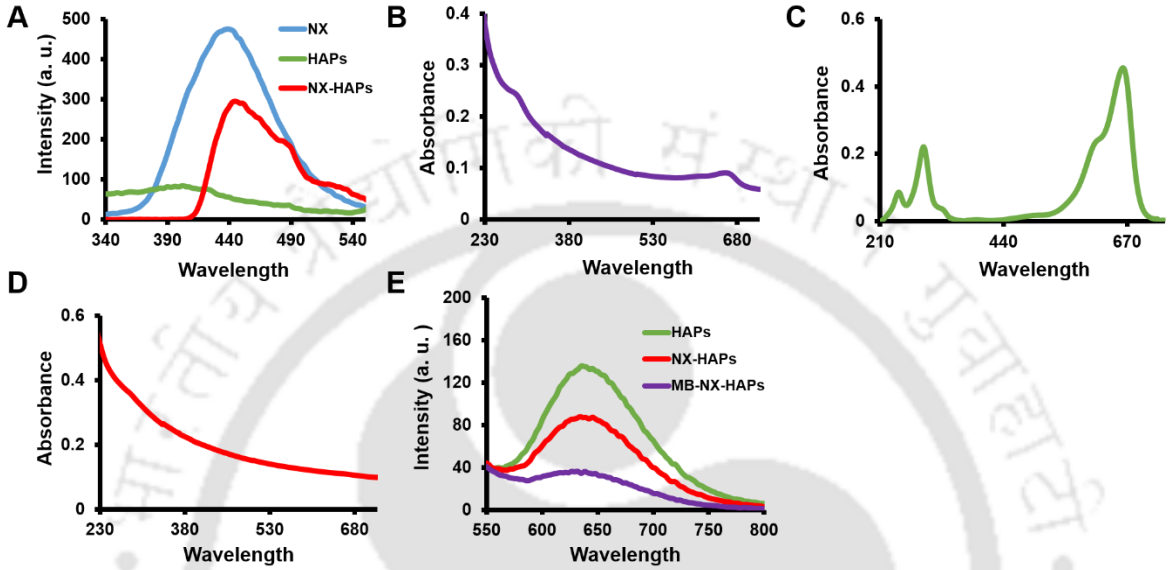

Figure 4.2. (A) Fluorescence spectra of NX, HAPs and NX-HAPs (excitation at 272 nm). UV-visible absorbance of (B) MB-NX-HAPs, (C) MB and (D) HAPs. (E) Fluorescence spectra of HAPs, NX-HAPs and MB-NX-HAPs (excitation at 365 nm)

Hydroxyapatite nanoparticles doped with copper nanoclusters were synthesised by slightly modifying our previously presented method[29], with the encapsulation of NX during synthesis. The encapsulation of NX into NX-HAPs was assessed by fluorescence spectroscopy, which suggested the presence of NX with its peak approximately at 445 nm, similar to the peak observed for free NX, while exciting at 272 nm.[31-33] In case of HAPs, there was no significant peak at corresponding spectral region (**Figure 4.2A**). Followed by the synthesis of NX-HAPs, the nanoformulation was loaded with MB, a phenothiazine photosensitizer, whose presence was characterized by UV-visible spectroscopy. The absorbance spectra of MB-NX-HAPs indicated the loading of MB with its peak approximately at 665 nm, identical to the peak of free MB[34] (**Figure 4.2B and C**). The obtained spectral features were compared with absorbance spectra of HAPs (**Figure 4.2D**). Further, the luminescence property due to the presence of doped copper nanoclusters was evaluated in HAPs, NX-HAPs and MB-NX-HAPs. By keeping excitation centred at 365 nm, an emission peak at 650 nm was obtained for the given samples, with the intensity of NX-HAPs slightly reduced as compared to HAPs.

Such reduction in intensity of NX-HAPs might be probably due to the entropy driven hydrophobic bonding of NX with BSA, which is present as template in copper nanoclusters.[35] Though the intensity was comparatively reduced, MB-NX-HAPs also exhibited a weaker emission peak at 650 nm (**Figure 4.2E**). For better understanding the photophysical properties, a fluorescence lifetime study was conducted. The study revealed the lifetime of HAPs, NX-HAPs and MB-NX-HAPs to be 1.51 µs, 1.24 µs and 1.00 µs respectively (**Figure 4.3A- C**).

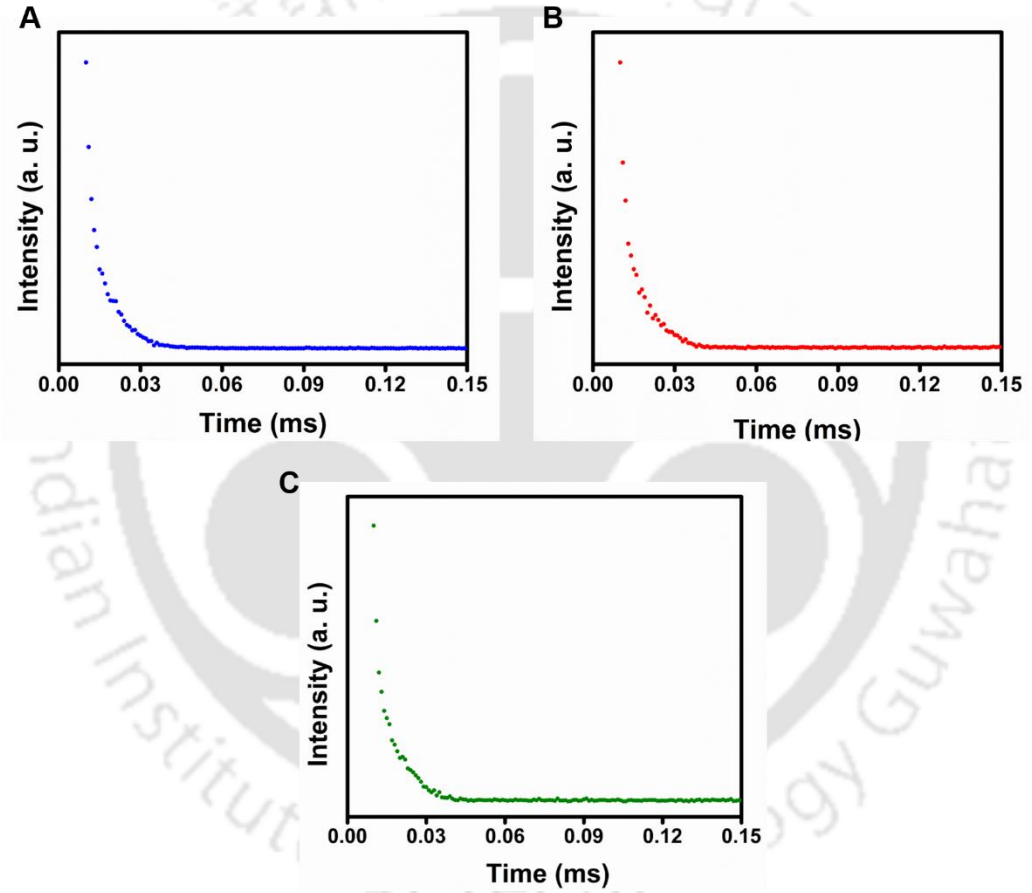

Figure 4.3. Time resolved photoluminescence (TRPL) spectra of (A) HAPs ($\chi 2$ – 0.99, average lifetime- 1.51 µs), (B) NX-HAPs ($\chi 2$ – 0.99, average lifetime- 1.24 µs) and (C) MB-NX-HAPs ($\chi 2$ – 0.99, average lifetime- 1.00 µs). The analysis was carried out at an excitation of 365 nm and an emission of 650 nm.

Further, the formulation of NX-HAPs and MB-NX-HAPs was validated by TEM imaging. The obtained images suggested NX-HAPs (**Figure 4.4A**) and MB-NX-HAPs (**Figure 4.4B**) to be of roughly spherical, having a size of 67.2± 7.8 nm and 60.8 ± 8.4 nm respectively. To elucidate the crystalline nature of NX-HAPs and MB-NX-HAPs, selective area electron diffraction

(SAED) analysis was carried out. The revealed characteristic planes of NX-HAPs (410), (510), (400) and MB-NX-HAPs (002), (004), (510) were understood to be representing the planes of hydroxyapatite as reported earlier[36] (**Figure 4.4C and D**). The high resolution TEM (HRTEM) suggested a lattice spacing of 0.30 nm and 0.27 nm for NX-HAPs (**Figure 4.4E**) and MB-NX-HAPs (**Figure 4.4F**) respectively, corresponding to (210) and (300) planes of hydroxyapatite nanomaterial.[37]

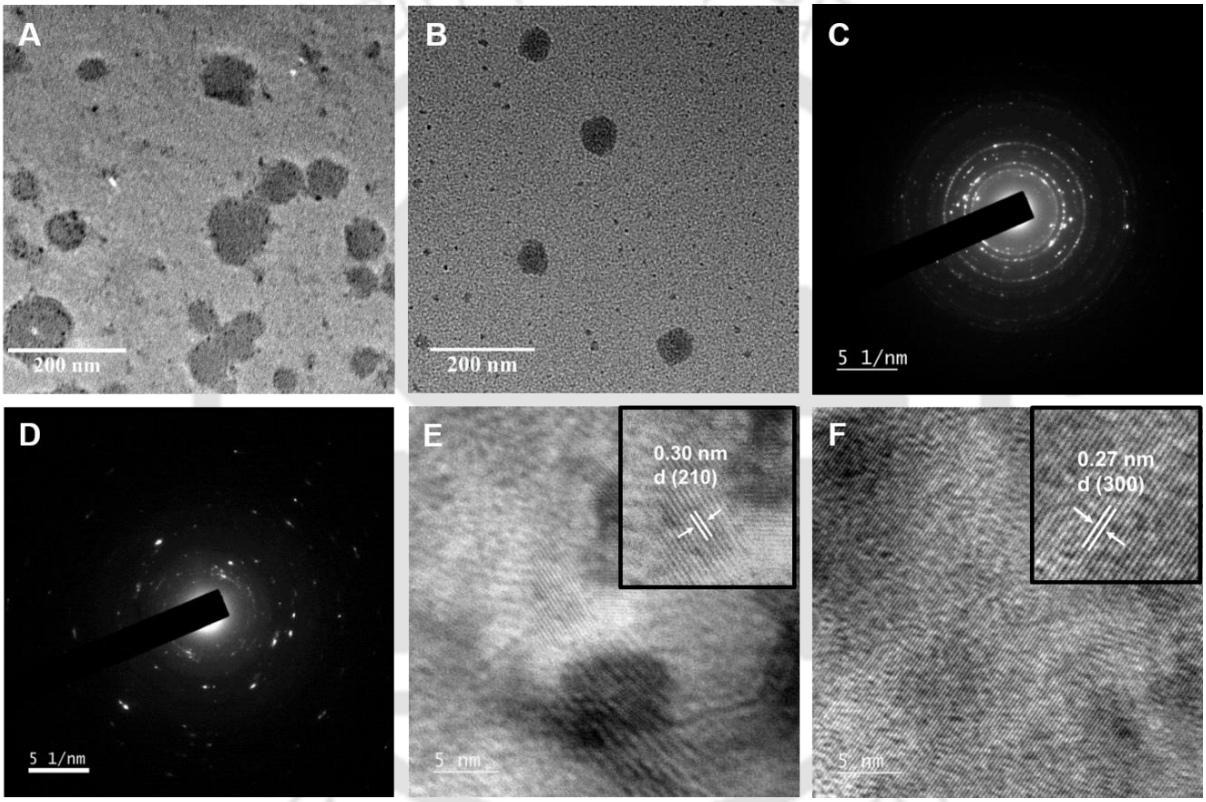

Figure 4.4. TEM image of (A) NX-HAPs (scale bar at 200 nm) and (B) MB-NX-HAPs (scale bar at 200 nm). SAED of (C) NX-HAPs and (D) MB-NX-HAPs. HRTEM pattern of (E) NX-HAPs (scale bar at 5 nm) and (F) MB-NX-HAPs (scale bar at 5 nm).

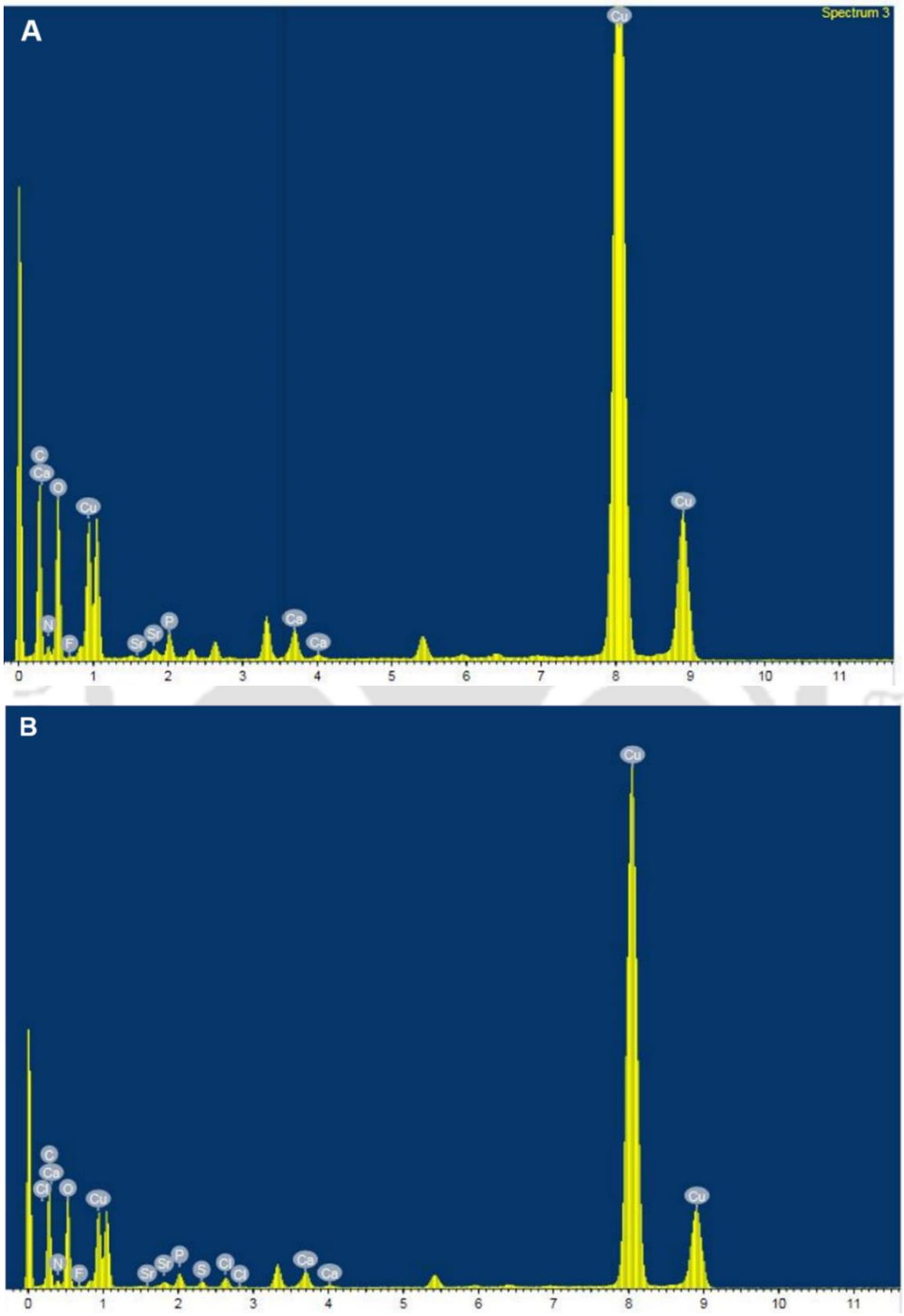

Figure 4.5. EDX spectra of (A) NX-HAPs and (B) MB-NX-HAPs

Additionally, the energy dispersive X-ray (EDX) investigation displayed the elemental composition of the as-synthesised NX-HAPs and MB-NX-HAPs (**Figure 4.5A and B**). Moreover, characterization using FESEM conveyed the size of NX-HAPs to be 67.5± 6.4 nm and of MB-NX-HAPs to be 60.5 ± 3.5 nm, in support to the TEM data obtained (**Figure 4.6A and B**). The size calculation of both the TEM and FESEM data was performed using Image J software.

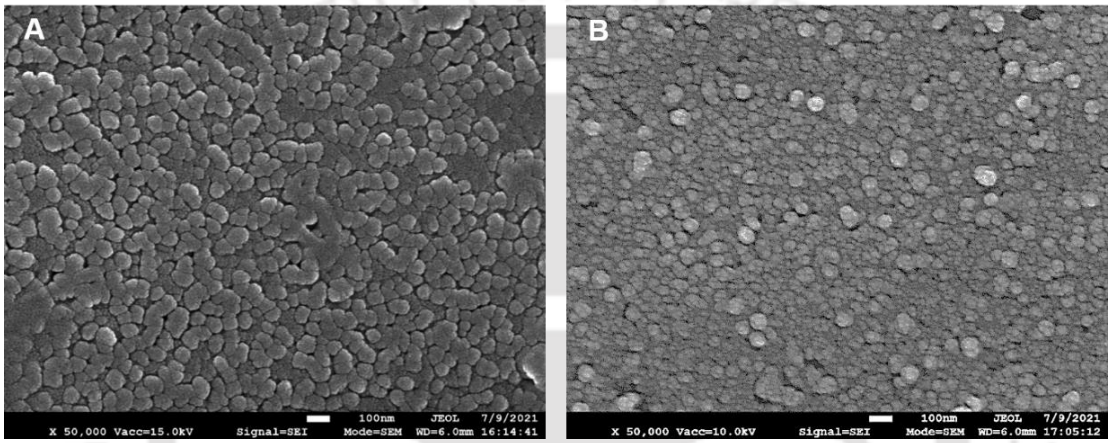

Figure 4.6. FESEM image of (A) NX-HAPs and (B) MB-NX-HAPs

Surface charge is one of the important influencing factors in cellular uptake event. Therefore, to study the net surface charge and interaction of NX and MB with our present nanocarrier, zeta potential analysis was conducted (**Figure 4.7A-F**). In the analysis, HAPs exhibited a surface charge of -15.4 ± 3.04 mV. Upon encapsulation with the positively charged NX (6.49 ± 0.24 mV), the NX-HAPs were found to have a net charge of -14.3 ± 2.89 mV. With the subsequent loading of positively charged MB (8.46 ± 0.64 mV), the final surface charge of MB-NX-HAPs was suggested to be -12.6 ± 3.85 mV. As per various reports, the uptake of negatively charged nanoparticles is mostly attributed to the non-specific interaction with plasma membrane receptors. The interaction of nanoparticles with physiological protein is to be seriously governed for drug delivery application. It is documented that negatively charged nanoparticles are negligibly adsorbed by serum opsonin proteins, benefiting for long term circulation and prevention of rapid systemic clearance, promoting therapeutic efficacy.[38-42]

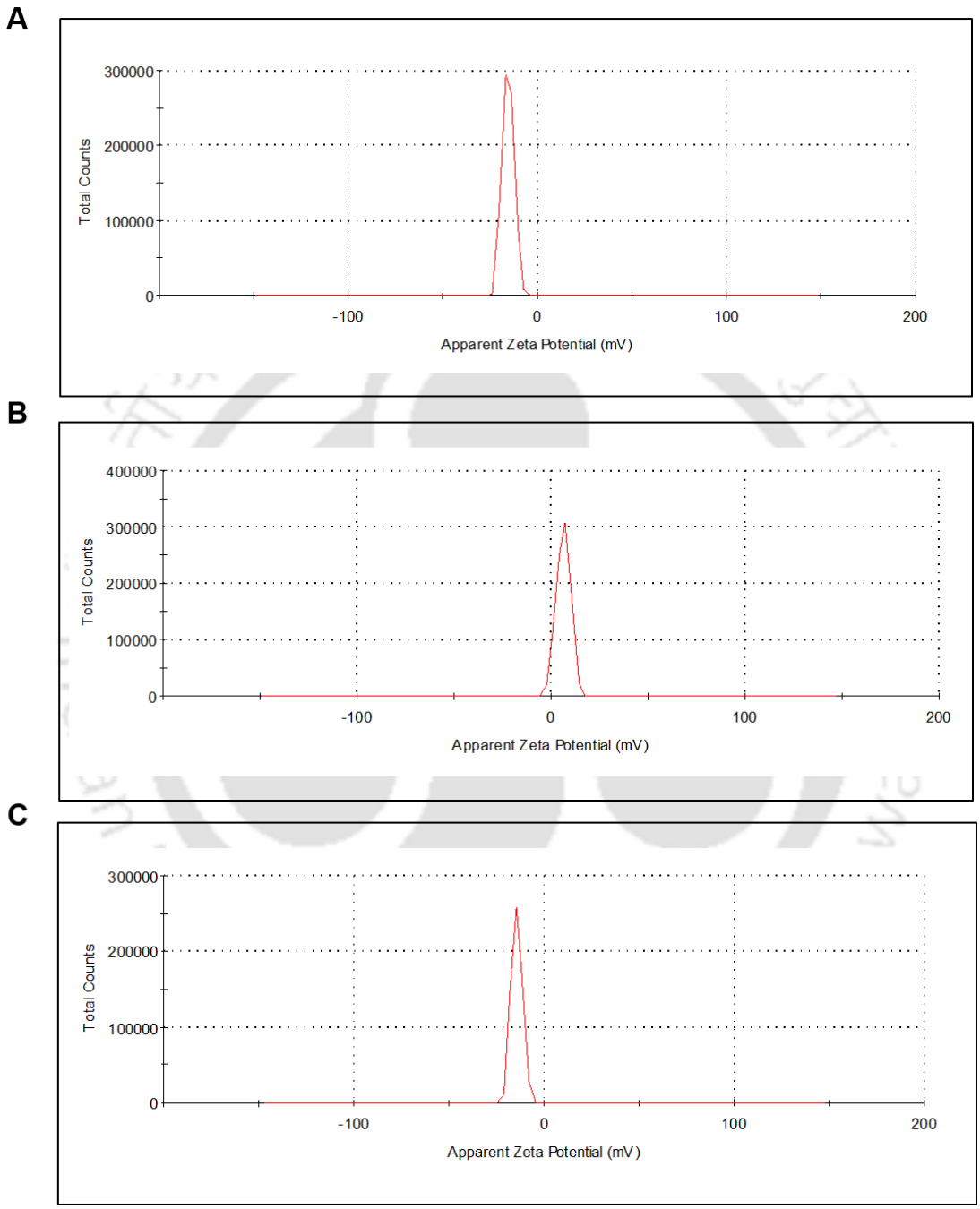

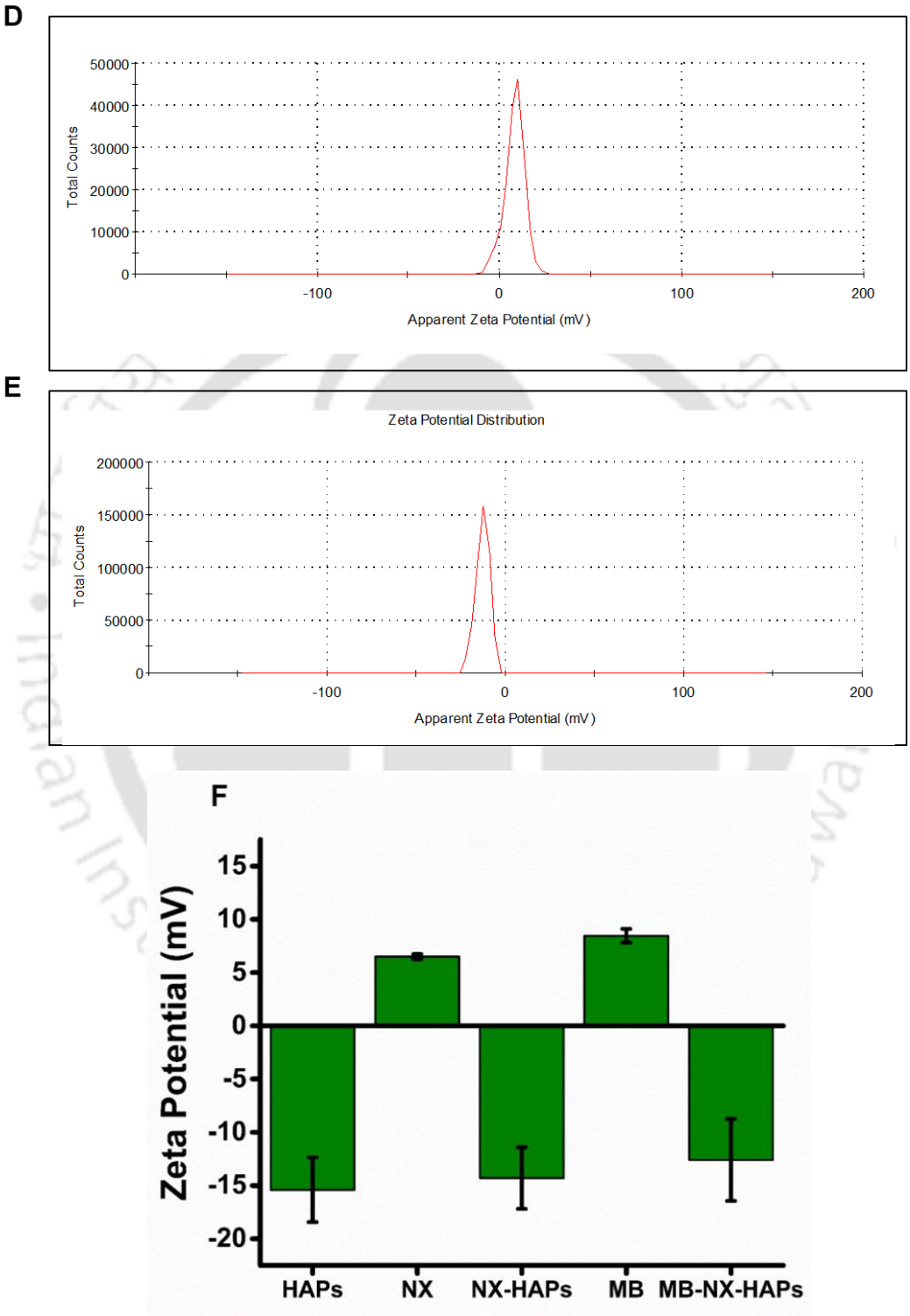

Figure 4.7. Zeta potential of (A) HAPs, (B) NX, (C) NX-HAPs, (D) MB and (E) MB-NX-HAPs. (F) Graphical representation of zeta potentials.

4.3.2. Drug Release Study

With the aid of fluorescence spectroscopy, the encapsulation and loading efficiency had been checked, where MB-NX-HAPs suggested an encapsulation of 73% of NX, with a total concentration of 29.2 µg/mL of NX. Likewise, in case of MB, a loading efficiency of 69% was exhibited by MB-NX-HAPs, with its total concentration calculated to be 13.8 µM. Once the successful entrapment of therapeutic compounds was achieved, the release profile of both NX and MB from MB-NX-HAPs was investigated in different pH buffers [pH 4 (acetate buffer) and pH 7.4 (PBS)] for a time period of 24 h (**Figure 4.8A-D**). In case of NX at pH 4, there was a slow and gradual increase in the release pattern until 9th h, where 47% of release was obtained. Thereafter, almost a steady and sustained drug release was observed until 24th h, with a release of 48% of NX. However, at physiologic pH 7.4, the amount of NX released from MB-NX-HAPs was observed to be comparatively less, with a maximum release of 27% at 12th h, which sustained up to 24th h. The release profile of MB from MB-NX-HAPs in acidic pH was observed to be almost steady until 6th h, followed by which, there was a continuous increment until 24th h at which, 65% of MB was released. At pH 7.4, a very slow and steady pattern was followed until 12th h, showing an increase towards 24th h with 41% of release. The current release profile of NX and MB from MB-NX-HAPs indicated a pH dependent event, with maximum release occurring at acidic pH than physiological pH. This would probably facilitate accumulation of drug at acidic environment, mostly prevalent in certain disease conditions, with minimal systemic exposure. Moreover, it is documented that hydroxyapatite is highly soluble in acidic condition, favouring the release of loaded drug molecules at compromised regions, thus making the whole nanocarrier biodegradable.[43,44]

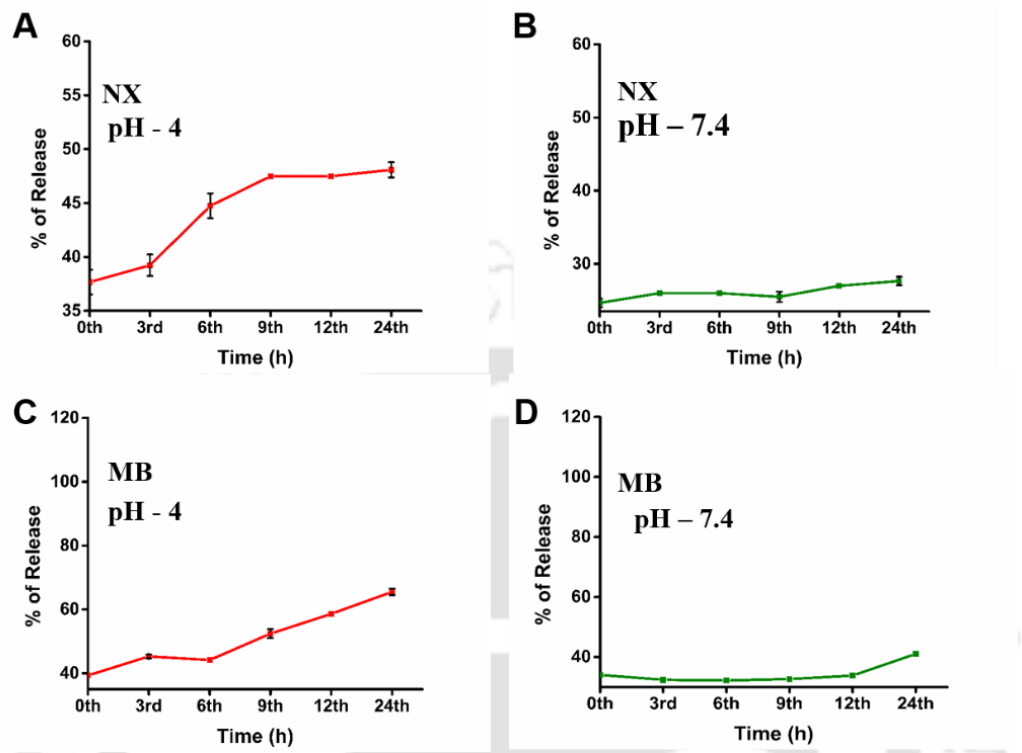

Figure 4.8. Drug release profile showing release of NX from MB-NX-HAPs (A) at pH 4 (acetate buffer) and (B) at pH 7.4 (PBS buffer). Drug release pattern of MB from MB-NX-HAPs (C) at pH 4 (acetate buffer) and (D) pH 7.4 (PBS buffer). At pH 4, the NX released from MB-NX-HAPs suggested a pattern of gradual increase up to 9th h, where 47% of NX was released, following which a sustained release pattern was observed until 24th h with 48% of release. At pH 7.4, the NX released from MB-NX-HAPs was less in amount with 27% of release at 12th h, which continued until 24th h. In case of MB released from MB-NX-HAPs at pH 4, a steady increase from 6th h was observed, which continued up to 24th h with 65% of release. At pH 7.4, the MB released from MB-NX-HAPs was found to be comparatively less, maintaining a steady pattern till 12th h with a sudden spike at 24th h with 41% of release.

4.3.3. Antibacterial Study

Once the encapsulation was done, NX-HAPs were initially evaluated for antibacterial activity towards Gram positive strain *S. aureus* MTCC 96 and Gram negative strain *P. aeruginosa* MTCC 2488. Through monitoring the cultural turbidity, the effect of NX-HAPs on the growth of both the strains was assessed and compared with free NX and HAPs. The concentration at which, there was no visible cultural turbidity was considered to be the MIC. Further, reinoculation of culture from visually clear culture tubes to fresh medium evinced MBC. In case of *P. aeruginosa* MTCC 2488, the MIC of NX in NX-HAPs was suggested to be 2 µg/mL

and MBC obtained was 8 µg/mL. The MIC and MBC of free NX was found to be 0.8 µg/mL and 2 µg/mL respectively. However, no MIC could be obtained for bacteria treated with HAPs, which exhibited only minimal effect on treated bacteria (**Figure 4.9A**). The growth kinetics depicting the effect of free NX, HAPs and NX-HAPs on *P. aeruginosa* MTCC 2488 is given (**Figure 4.9B**).

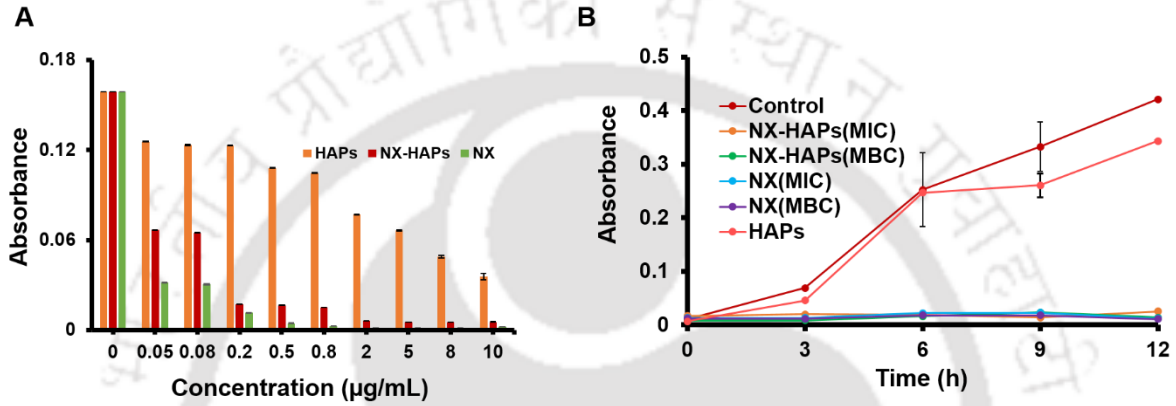

Figure 4.9. (A) Optical density (at 595 nm) of bacteria (*P. aeruginosa* MTCC 2488) treated with HAPs, NX and NX-HAPs. (B) Growth curve study on *P. aeruginosa* MTCC 2488. The MIC and MBC of NX in NX-HAPs was 2 µg/mL and 8 µg/mL respectively. Free NX exhibited its MIC and MBC at a concentration of 0.8 µg/mL and 2 µg/mL respectively. No MIC was found for only HAPs on treated bacteria.

Upon checking the activity of NX, HAPs and NX-HAPs towards *S. aureus* MTCC 96, no significant inhibitory activity was observed for HAPs and NX-HAPs at the tested concentrations. While checking the activity of free NX towards higher concentration, an MIC close to 80 µg/mL was found (**Table 4.1**).

Samples	Concentration range of NX tested (µg/mL)	MIC obtained (µg/mL)
NX	10-400	80
HAPs	Without NX	No MIC
NX-HAPs	10-400	No MIC

Table 4.1. MIC of the samples applied for *S. aureus* MTCC 96 treatment.

Based on the results acquired, the remaining antibacterial study was carried out in *P. aeruginosa* MTCC 2488. For further confirmation of MIC and MBC on *P. aeruginosa* MTCC 2488, plating method was opted. The plating method revealed a very few colonies at MIC of NX-HAPs, with no single colonies at their MBC. Similar pattern of results was observed for MIC and MBC of free NX on *P. aeruginosa* MTCC 2488 (**Figure 4.10A-E**). To gain better insight on the morphological feature of *P. aeruginosa* MTCC 2488 treated with NX-HAPs, an FESEM analysis was performed (**Figure 4.11A and B**). The treated bacterial cells were found to have lost its native morphology, with rough and protruded membrane, as compared to untreated bacteria, which had a smooth and intact morphology. Such membrane alteration might be the result of ROS generation by NX, that gradually leads to disruption of intracellular component and bacterial cell death.[45]

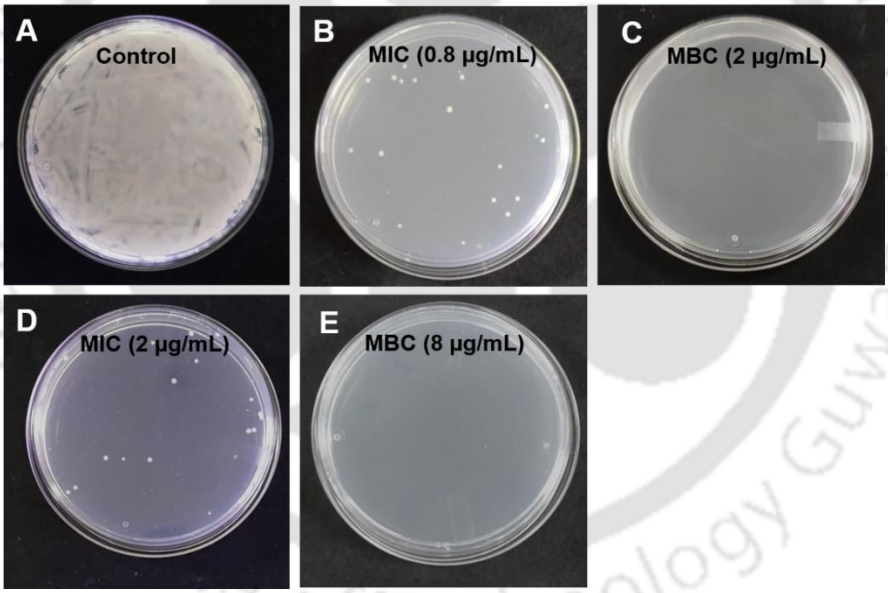

Figure 4.10. *P. aeruginosa* MTCC 2488 grown on nutrient agar plate. (A) Control, bacteria treated at (B) MIC (0.8 µg/mL) and (C) MBC (2 µg/mL) of free NX. Bacteria treated at (D) MIC (2 µg/mL) and (E) MBC (8 µg/mL) of NX in NX-HAPs.

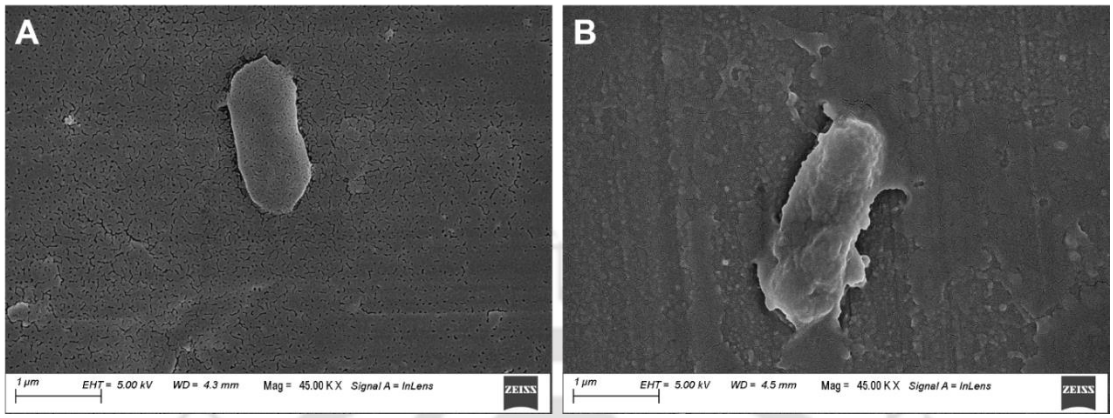

Figure 4.11. FESEM image of (A) control (untreated) and (B) NX-HAPs treated bacteria (*P. aeruginosa* MTCC 2488).

Further, to explore the PDT effect of MB-NX-HAPs on *P. aeruginosa* MTCC 2488, the activity of free MB (2 µM, 5 µM and 10 µM) was initially checked in dark as well as under irradiation with light source at 640 nm. The results suggested a concentration dependent antibacterial PDT activity of MB, under dark and irradiation condition (**Figure 4.12A**). Based on the data obtained with regards to inhibitory effect of MB (**Figure 4.12A**) and NX (**Figure 4.9A**), antibacterial PDT was conducted by fixing concentration of MB at 5 µM and NX at 0.05 µg/mL for combinatorial effect (**Figure 4.12B**). As per the survival data obtained, some amount of inhibition in bacterial growth was observed, following the treatment with HAPs, NX-HAPs and MB-NX-HAPs. However, there was considerable reduction in the number of bacterial colonies, in case of irradiated bacterial culture subjected to MB-NX-HAPs treatment, in comparison to other tested samples (**Figure 4.13A-H**). The growth inhibition of bacteria treated with free MB (irradiated and non-irradiated) as well as free NX was also analysed. The photoinactivation property exhibited under irradiation, provides the perception on the feasibility of MB-NX-HAPs, for being explored more in antibacterial PDT to eradicate infective agents.

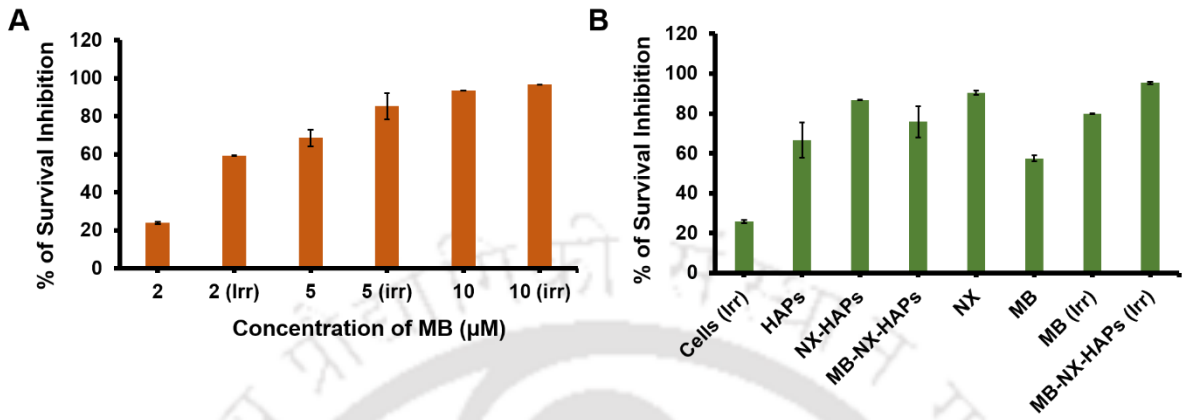

Figure 4.12. (A) Antibacterial PDT showing survival inhibition (%) at different concentrations of free MB on *P. aeruginosa* MTCC 2488 under irradiation at 640 nm (2.5 mW/cm^2) and without irradiation (dark). The data are represented as mean ± standard deviation (SD) of three individual experiments. (B) Antibacterial PDT performed on *P. aeruginosa* MTCC 2488 using MB-NX-HAPs (NX-0.05 µg/mL, MB- 5 µM) and free MB (5 µM) under irradiation at 640 nm. The effect was compared with other samples such as HAPs (NX-0 µg/mL, MB-0 µM), free NX (0.05 µg/mL), NX-HAPs (NX-0.05 µg/mL), MB-NX-HAPs (NX-0.05 µg/mL, MB-5 µM) and free MB (5 µM) in dark. The values are represented as mean ± standard deviation (SD) of three individual experiments.

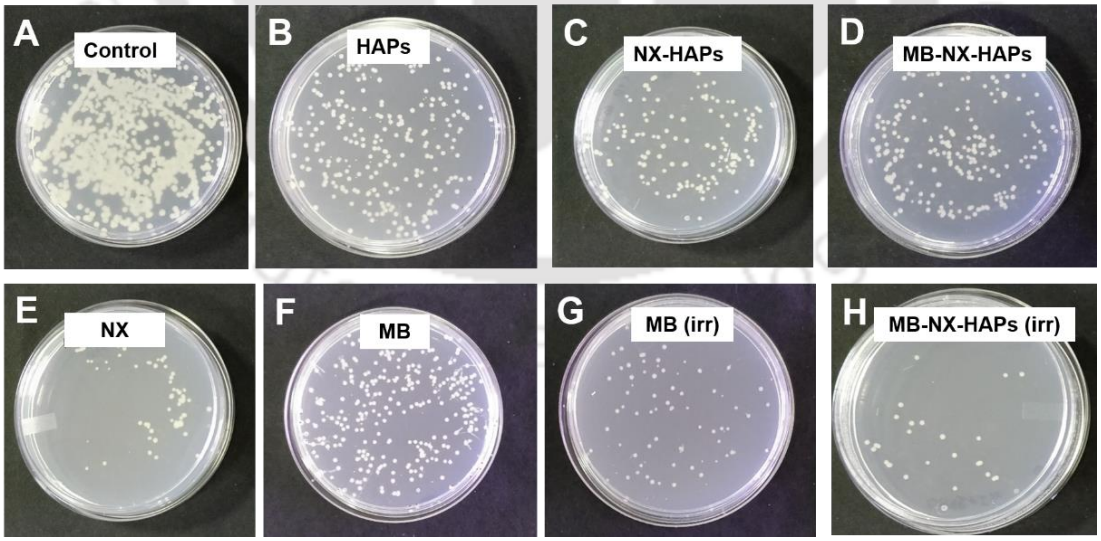

Figure 4.13. Antibacterial PDT on *P. aeruginosa* MTCC 2488 under irradiation at 640 nm and without irradiation (dark). (A) Control, bacteria treated with (B) HAPs (NX-0 µg/mL, MB-0 µM), (C) NX-HAPs (NX-0.05 µg/mL), (D) MB-NX-HAPs (NX-0.05 µg/mL, MB-5 µM), (E) free NX (0.05 µg/mL), (F) free MB (5 µM), (G) free MB (irradiated) (5 µM) and (H) MB-NX-HAPs (irradiated) (NX-0.05 µg/mL, MB-5 µM).

4.3.4. Uptake Study

Assessment of HAPs, NX-HAPs and MB-NX-HAPs for cancer cell applications was performed in cervical cancer (HeLa) and breast cancer (MCF-7) cell lines. Initially, using flow cytometry, uptake study was conducted. The study suggested that both HeLa and MCF-7 cells could internalize HAPs, NX-HAPs and MB-NX-HAPs upon treatment for 5 h (**Figure 4.14A-D**).

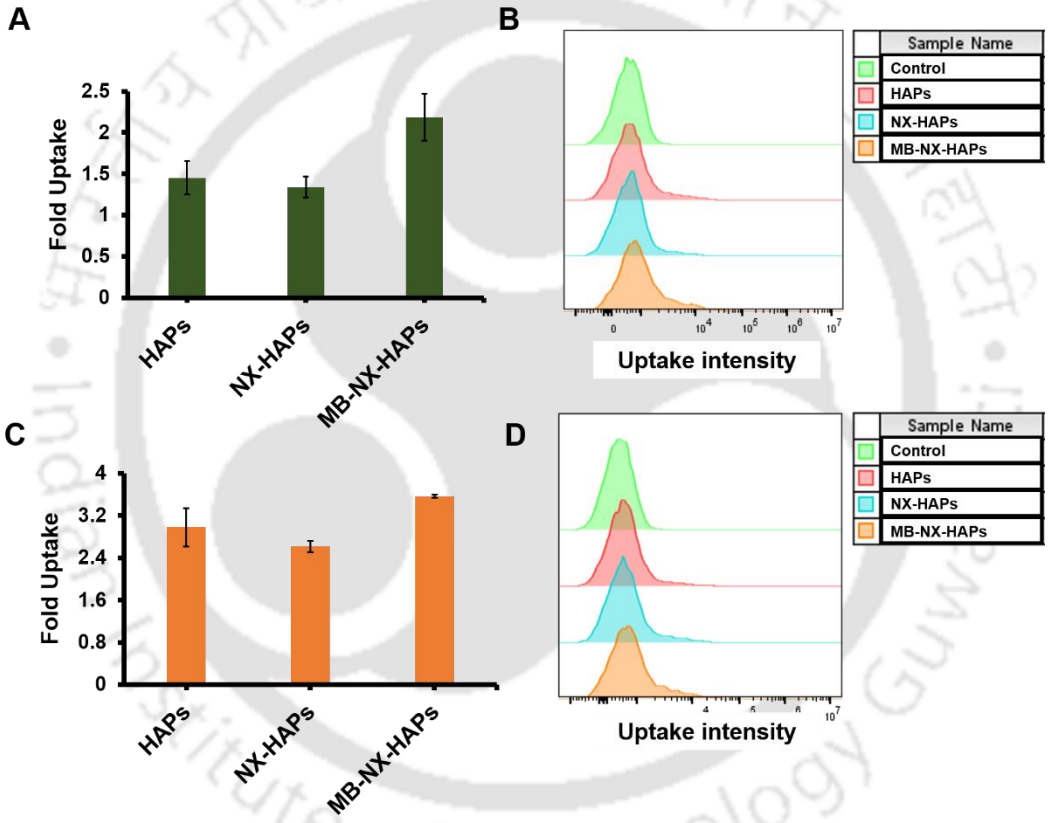

Figure 4.14. Uptake study on HeLa and MCF-7. (A) Fold uptake of HAPs, NX-HAPs and MB-NX-HAPs by HeLa cells and (B) histogram showing uptake of samples by HeLa cells. (C) Graphical representation showing fold uptake of HAPs, NX-HAPs and MB-NX-HAPs by MCF-7 cells and (D) histogram of sample uptake by MCF-7 cells.

4.3.5. Bioimaging Study

Bioimaging property was confirmed for both HAPs and NX-HAPs using confocal microscopy. **Figure 4.15A-C** depicts the fluorescence property of HAPs in HeLa and images of their corresponding control cells (untreated) are shown in **Figure 4.15D-F.** Confocal images of MCF-7 cells showing HAPs fluorescence, along with their control cells (untreated) are given

in **Figure 4.16A-F**. Further, **Figure 4.17A-D** represents the imaging efficiency of NX-HAPs in HeLa cells, at two different emissions such as 445 nm and 650 nm with respect to NX and HAPs fluorescence respectively. **Figure 4.17A** shows the image of cells, corresponding to NX fluorescence and **Figure 4.17B** corresponds to HAPs fluorescence. Representative bright field and merged image of HeLa cells treated with NX-HAPs are given in **Figure 4.17C and D**. Similar study was conducted in MCF-7 cell lines. The bioimaging property of NX-HAPs in MCF-7 cells was obtained at two different emission wavelengths, corresponding to NX and HAPs. The cells exhibited blue fluorescence and red fluorescence in **Figure 4.17E and F** respectively. **Figure 4.17G** depicts the bright field image of NX-HAPs treated MCF-7 cells. The respective merged image of MCF-7 cells treated with NX-HAPs is shown in **Figure 4.17H**. Confocal study was carried out for untreated cells (control) of both HeLa and MCF-7 cells with emissions kept at blue (445 nm) and red region (650 nm) (**Figure 4.18A-H**). All the confocal analysis were performed at an excitation of 405 nm. Thus, the currently synthesised red emitting HAPs bestow the bioimaging attributes in cancer cell lines, which facilitate in monitoring their distribution along with their loaded molecules intracellularly.

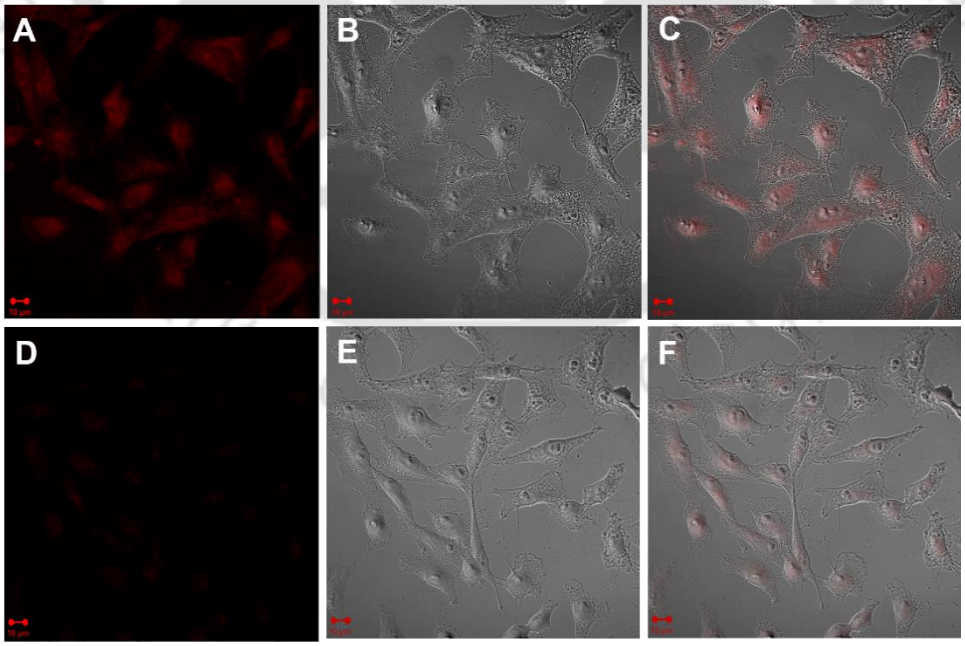

Figure 4.15. (A) Confocal image of HeLa cells treated with HAPs. (B) Bright field and (C) merged image of HeLa cells treated with HAPs. (D) Confocal, (E) bright field and (F) merged of untreated HeLa cells. The laser excitation was done at 405 nm (scale bar is at 10 µm).

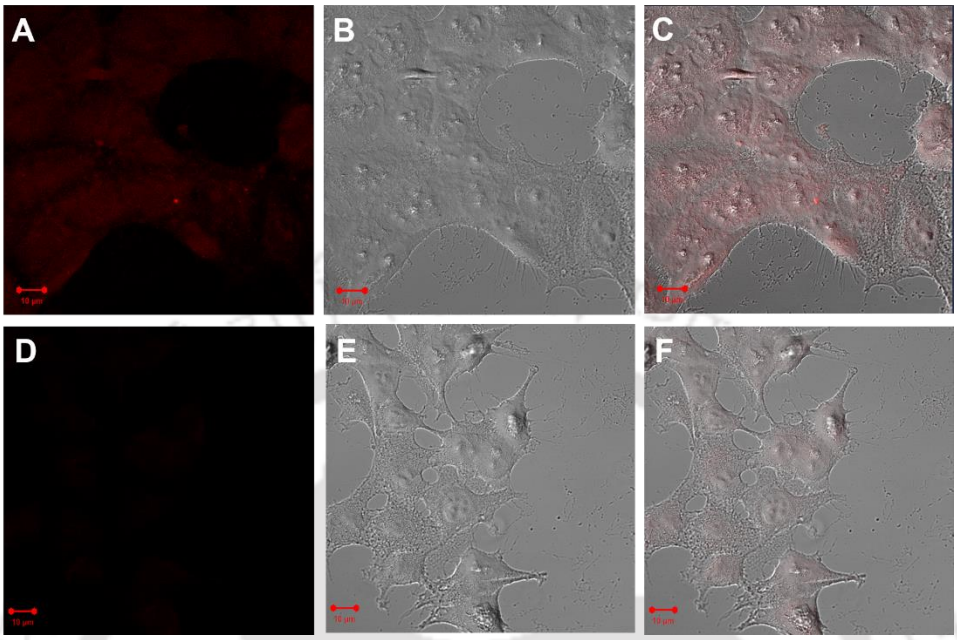

Figure 4.16. (A) Confocal image of HAPs treated MCF-7 cells. (B) Bright field and (C) merged image of MCF-7 cells treated with HAPs. (D) Confocal, (E) bright field and (F) merged of untreated MCF-7 cells. Excitation of laser was done at 405 nm and the scale bar is kept at 10 µm

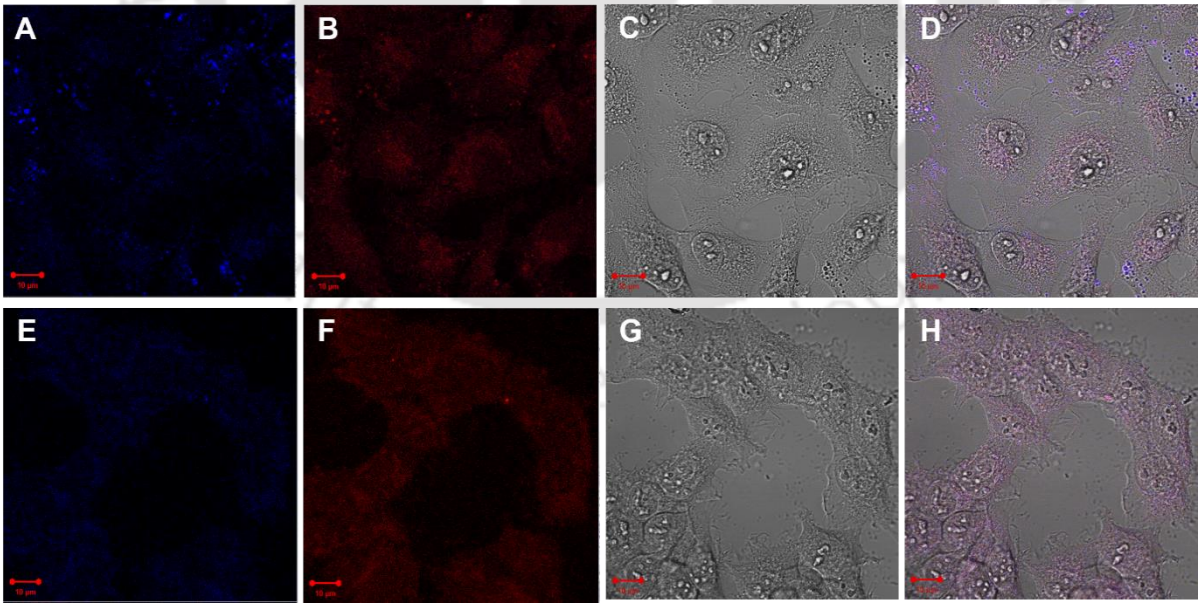

Figure 4.17. Confocal images of NX-HAPs treated HeLa cells showing (A) NX fluorescence (445 nm) and (B) HAPs fluorescence (650 nm). (C) Bright field image and (D) merged image of HeLa cells treated with NX-HAPs. Fluorescence image of NX-HAPs treated MCF-7 cells showing emissions corresponding to (E) NX (445 nm) and (F) HAPs (650 nm). (G) Bright field

image and (H) merged image of MCF-7 cells treated with NX-HAPs. The laser excitation for confocal experiment was kept at 405 nm (scale bar at 10 µm).

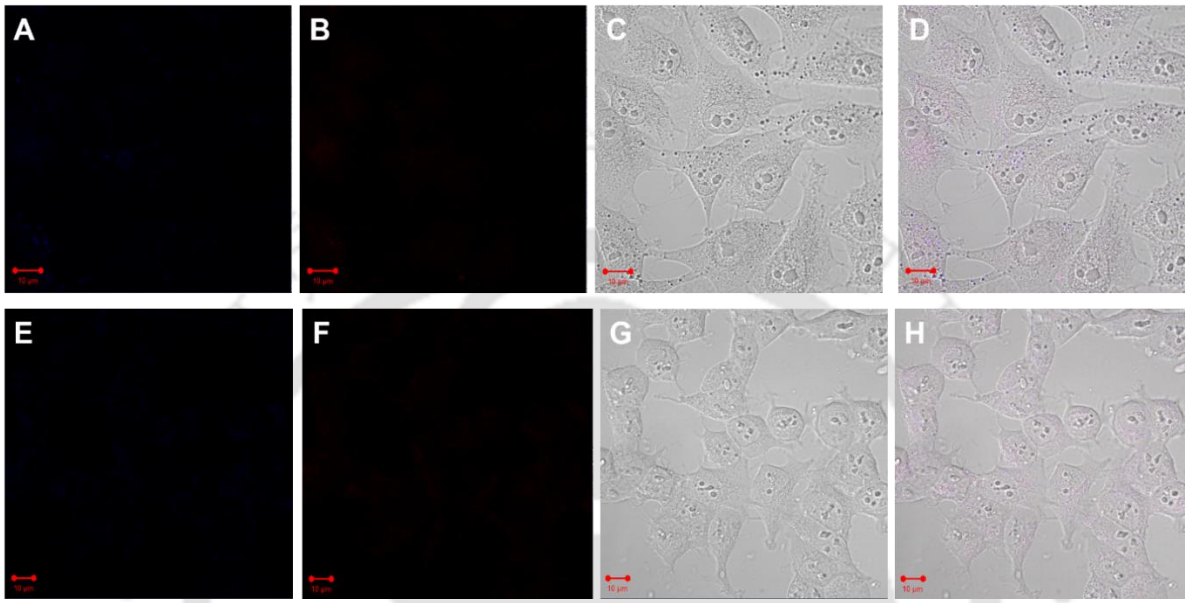

Figure 4.18. Confocal images of untreated HeLa cells corresponding to fluorescence of (A) NX and (B) HAPs. (C) Bright field and (D) merged image of untreated HeLa cells. (E) & (F) Confocal images of untreated MCF-7 cells with respect to NX and HAPs fluorescence respectively. (G) Bright field and (H) merged image of untreated MCF-7 cells. The study has been performed in comparison to NX-HAPs treated HeLa and MCF-7 cells. Laser excitation was at 405 nm and scale bar is at 10 µm.

4.3.6. Anti-Cell Proliferative Study

Viability study of HAPs, NX-HAPs and MB-NX-HAPs, with the conjugation of chemotherapy and PDT was analysed in HeLa and MCF-7 cells primarily through MTT assay. Now, PDT in cancer therapy is understood to potentiate and improve the overall activity of nanocarriers or individual drug molecules.[46] Therefore, in the present study, PDT approach was explored through MB-NX-HAPs along with chemotherapy for combinatorial effect in cancer cell lines. Initially, HeLa cells were subjected to treatment with NX-HAPs, HAPs and NX, which suggested that NX-HAPs could reduce the viability to half maximum at a concentration of 2 µg/mL of NX (**Figure 4.19A**). HAPs were also found to reduce the cell viability at their higher copper concentration as close to 20 µg/mL. Free NX at similar concentration did not show significant killing on treated HeLa cells.

In order to establish the efficacy of MB-NX-HAPs through PDT, HeLa cells treated with MB-NX-HAPs were exposed to irradiation at 640 nm for 30 min. The outcome suggested significant reduction in proliferation, showing 50% viability reduction at concentration of 0.6 µg/mL of NX and 0.17 µM of MB in MB-NX-HAPs (**Figure 4.19B**). Under dark condition, cells treated with MB-NX-HAPs (2 µg/mL of NX and 0.57 µM of MB), exhibited almost similar inhibition pattern as that of NX-HAPs. Also, minimal reduction in proliferation was observed in HeLa cells treated with free MB under dark and irradiation treatment in the present study.

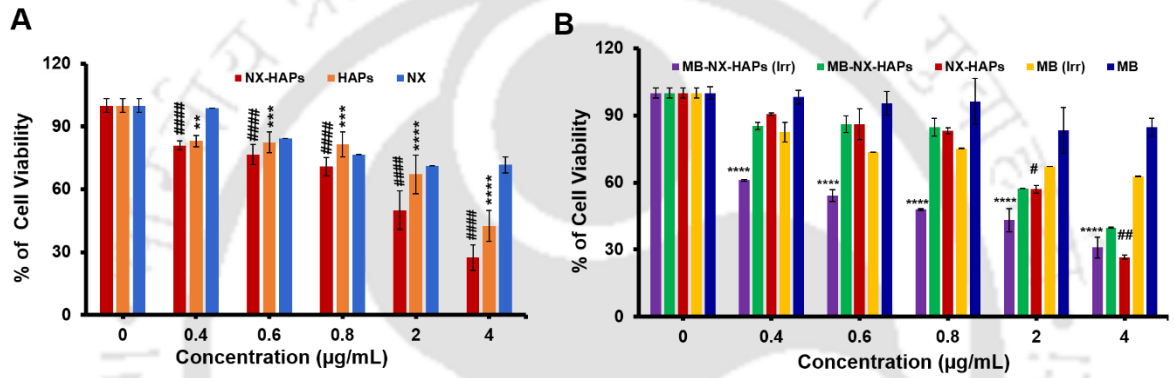

Figure 4.19. MTT assay on (A) HeLa cells after treatment with NX-HAPs, HAPs and free NX. At a concentration of 2 µg/mL of NX, NX-HAPs could reduce the HeLa cell proliferation to 50%. Only HAPs also exhibited cell viability reduction to almost 50% at a copper concentration of 20 µg/mL. The values given are the mean ± standard deviation (SD) of three different experiments. Statistical significance is represented by #### ($p < 0.0001$), ** ($p < 0.005$), *** ($p < 0.001$) and **** ($p < 0.0001$). (B) Combined chemotherapy and PDT on HeLa cells. At a concentration of 0.6 µg/mL of NX and 0.17 µM of MB, MB-NX-HAPs under irradiation at 640 nm reduced the viability of HeLa cells to 50%. MB-NX-HAPs (dark) at a concentration of 2 µg/mL of NX and 0.57 µM of MB could bring about 50% viability reduction in HeLa cells. All the values are represented as mean ± standard deviation (SD) of three individual experiments. The ANOVA test suggested statistical significance of MB-NX-HAPs (irradiation at 640 nm) and NX-HAPs with respect to control. Statistical significance is represented by # ($p < 0.05$), ## ($p < 0.005$), and **** ($p < 0.0001$).

While checking the viability reduction in MCF-7 cells treated with NX-HAPs, HAPs and NX, it was revealed that the viability of MCF-7 was reduced to half maximum at a concentration of 4 µg/mL of NX in NX-HAPs (**Figure 4.20A**). There was no considerable viability reduction in case of free NX treated and HAPs treated MCF-7 cells. Upon irradiation of MCF-7 cells following treatment with MB-NX-HAPs, the viability was reduced to 50% at a concentration

of 0.8 µg/mL of NX and 0.23 µM of MB in MB-NX-HAPs (**Figure 4.20B**). Without irradiation, 50% viability reduction was obtained at 4 µg/mL of NX and 1.15 µM of MB in MB-NX-HAPs treated MCF-7 cells. The inhibition observed in MB treated MCF-7 cells under dark and irradiation was not evident as irradiated sample of MB-NX-HAPs treated cells.

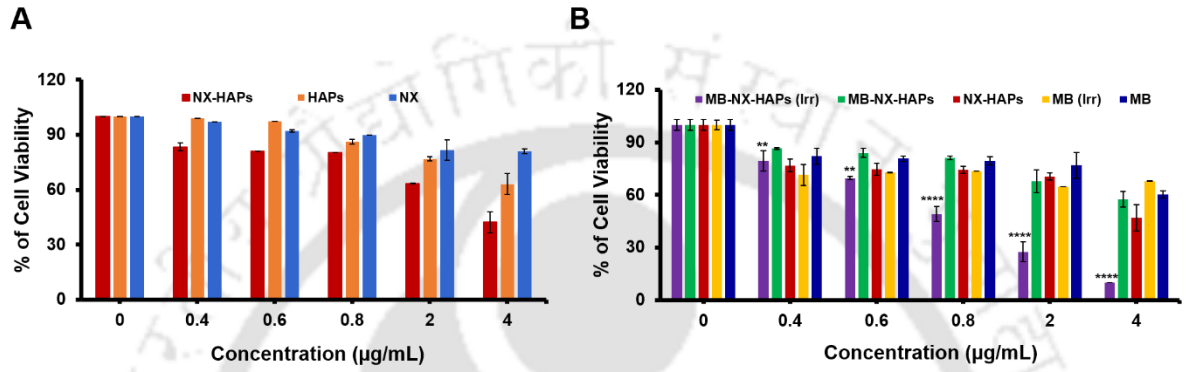

Figure 4.20. MTT assay on (A) MCF-7 cells treated with NX-HAPs, HAPs and free NX. The viability of MCF-7 cells was reduced to 50% at a concentration of 4 µg/mL of NX in NX-HAPs. The data represented are the mean ± standard deviation (SD) of three individually performed experiments. (B) Viability data showing combined treatment effect on MCF-cells. The 50% viability reduction in MB-NX-HAPs treated MCF-cells, subjected to irradiation was observed at 0.8 µg/mL of NX and 0.23 µM of MB. In case of MB-NX-HAPs treated cells (dark), the viability was reduced to 50% at 4 µg/mL of NX and 1.15 µM of MB. Data represented are based on three individual experiments performed. Statistical significance of MB-NX-HAPs (irradiation) with respect to control is denoted as ** ($p < 0.005$) and **** ($p < 0.0001$).

While analysing the viability activity on normal cell line such as HEK-293, no substantial toxicity was observed in case of NX-HAPs, HAPs and NX (**Figure 4.21A**). Similarly, under dark and irradiation treatment, MB-NX-HAPs and free MB did not show significant inhibitory effect on HEK-293, suggesting the biocompatible nature of our present nanocarrier ((**Figure 4.21B**). Moreover, only cells irradiated without nanocarrier or drug pre-treatment were found to be viable up to more than 85% in HeLa, MCF-7 and HEK-293 (**Figure 4.22A-C**).

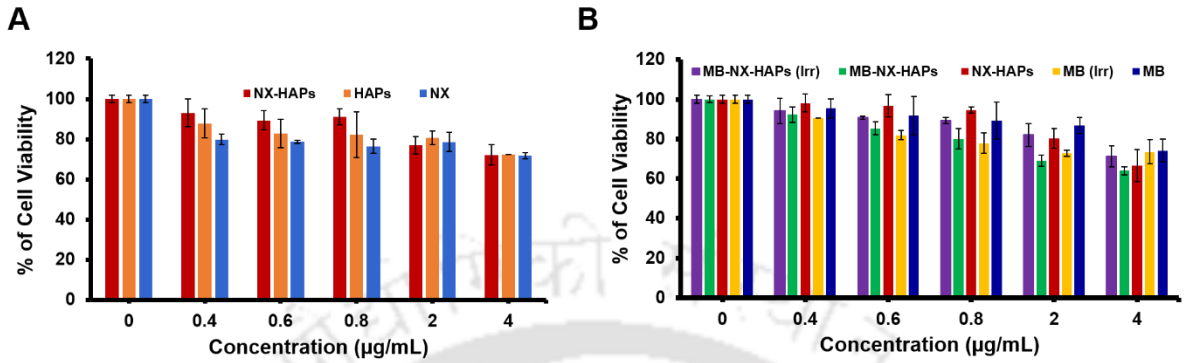

Figure 4.21. Viability assay on (A) HEK-293 cells. (B) Combined treatment effect on HEK-293. The values are presented as mean ± standard deviation (SD) of three individual experiments.

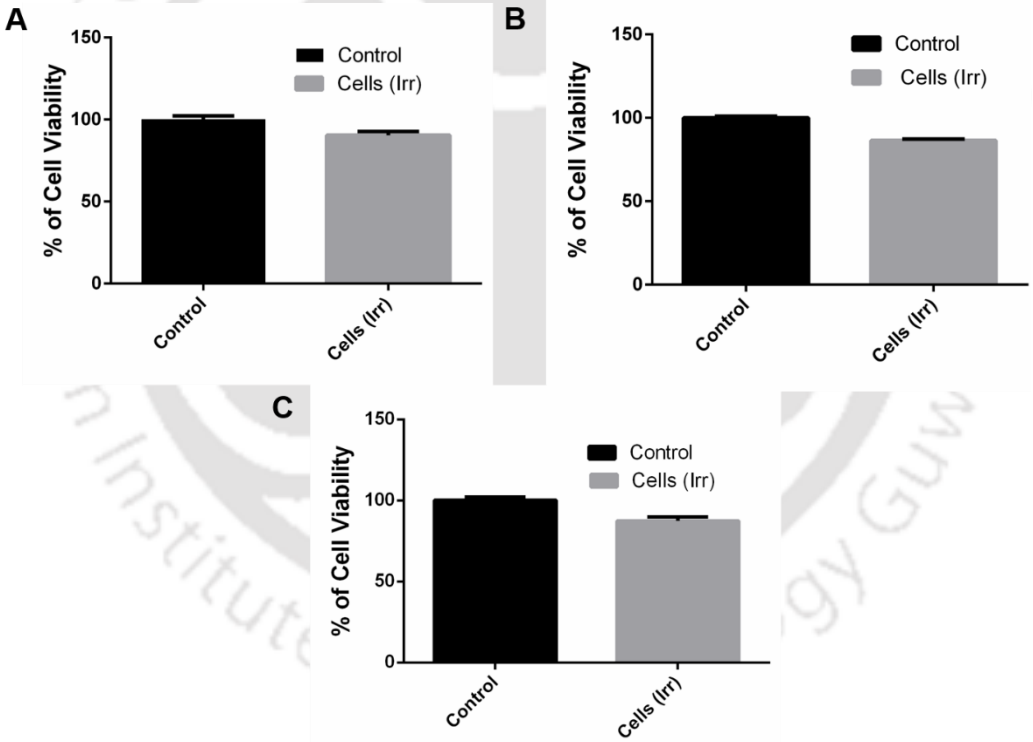

Figure 4.22. (A) HeLa cells, (B) MCF-7 cells and (C) HEK-293 cells irradiated under 640 nm light

The antiproliferative study executed in both HeLa and MCF-7 cells indicated the combinatorial effect of PDT using MB as photosensitizer, in combination with NX loaded in our present nanocarrier. Both drug and PDT based approach could sum the merits of individual therapeutic component, enhancing the treatment effect at lower dosages and avoiding unwanted side effects.

Additionally, the copper ions doped in the present nanocarrier can augment the inhibitory activity along with NX. Metal complexation with FQ has been reported to accelerate the biological activities like inhibiting efflux pump, facilitating the DNA binding and destabilization, enhancing apoptotic effect and improving antiproliferative activity in cancer cells [47-50]. Also, the PDT implemented in combined therapeutic approach can elevate ROS production in cancer cells, which could possibly help in inducing selective cellular toxicity. Subsequently, the role of ROS in declining the cancer cell proliferation was evaluated in the current study. Initially, the ability of singlet oxygen generation by MB-NX-HAPs, triggered through irradiation was analysed by DPBF assay. The DPBF fluorescence was recorded in the presence of irradiated MB-NX-HAPs (at 640 nm) and non-irradiated MB-NX-HAPs (**Figure 4.23A and B**). For comparison, fluorescence of irradiated DPBF (at 640 nm) was also analysed as control (**Figure 4.23C**). In case of irradiated MB-NX-HAPs, the obtained data suggested the gradual quenching of DPBF fluorescence with increase in time. This is possibly due to the degradation of DPBF by singlet oxygen, generated from MB-NX-HAPs upon irradiation, thus indicating their efficacy in light activated generation of singlet oxygen. In presence of non irradiated MB-NX-HAPs and irradiated DPBF, the fluorescence quenching of DPBF was found to be minimal with increase in time.

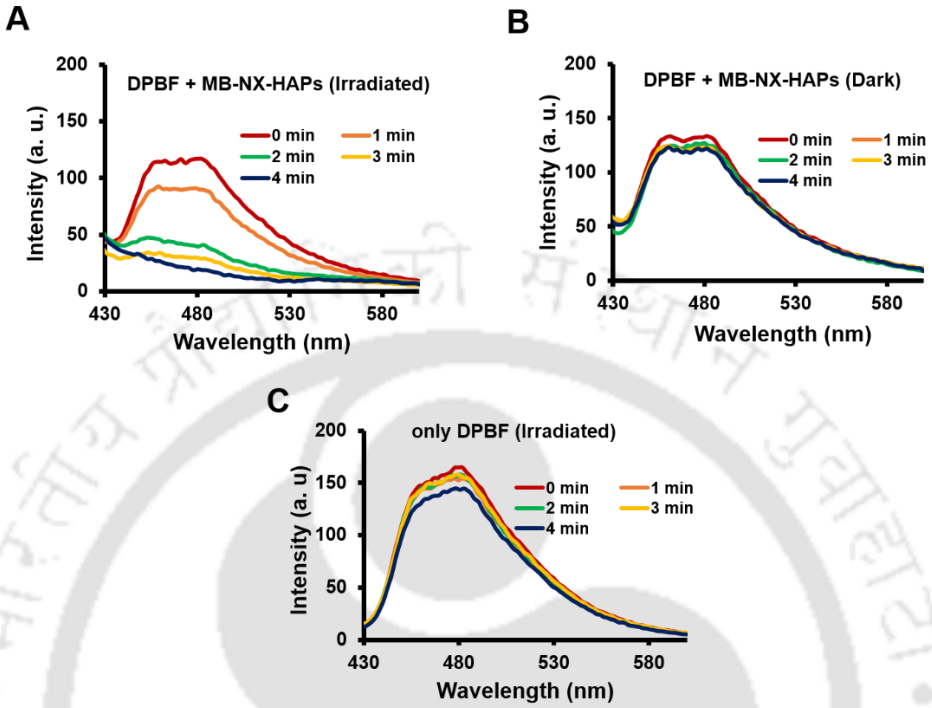

Figure 4.23. DPBF fluorescence with (A) MB-NX-HAPs after irradiation at 640 nm, (B) MB-NX-HAPs (dark). (C) Fluorescence of only DPBF irradiated at 640 nm.

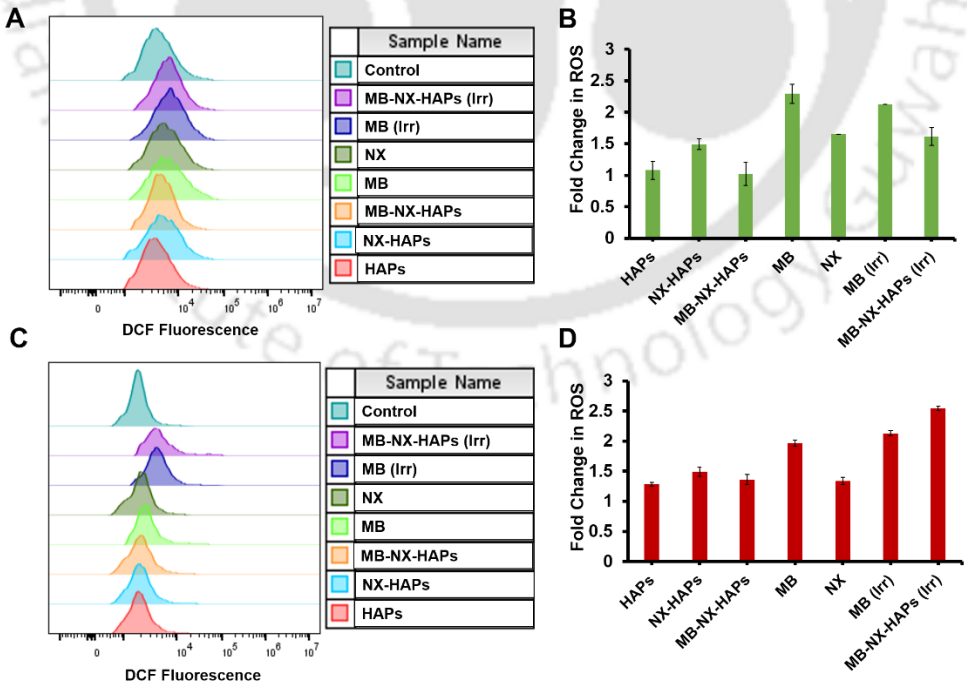

Figure 4.24. DCFH-DA study conducted on HeLa and MCF-7 cells. (A) Histogram showing DCF fluorescence in HeLa cells. (B) Graphical representation of ROS production in HeLa cells.

(C) Histogram presenting DCF fluorescence generated in MCF-7 cells. (D) Graphical representation of ROS produced in MCF-cells.

Further, using DCFH-DA assay, intracellular ROS generation was checked in HeLa and MCF-7 cells through flow cytometry (**Figure 4.24A-D**). The analysis revealed that both HeLa and MCF-7 could generate appreciable amount of ROS in irradiated cells, treated with MB-NX-HAPs. The amount of ROS generated in HeLa and MCF-7 cells, treated with other given samples is also shown in **Figure 4.24**. To morphologically evaluate cancer cell ablation caused by MB-NX-HAPs under irradiation, FESEM analysis was performed in HeLa and MCF-7 (**Figure 4.25A-D**). As compared to control, the images of treated HeLa and MCF-7 cells indicated cell membrane disruption and shrinkage, associated with ROS generation and subsequent apoptotic event.

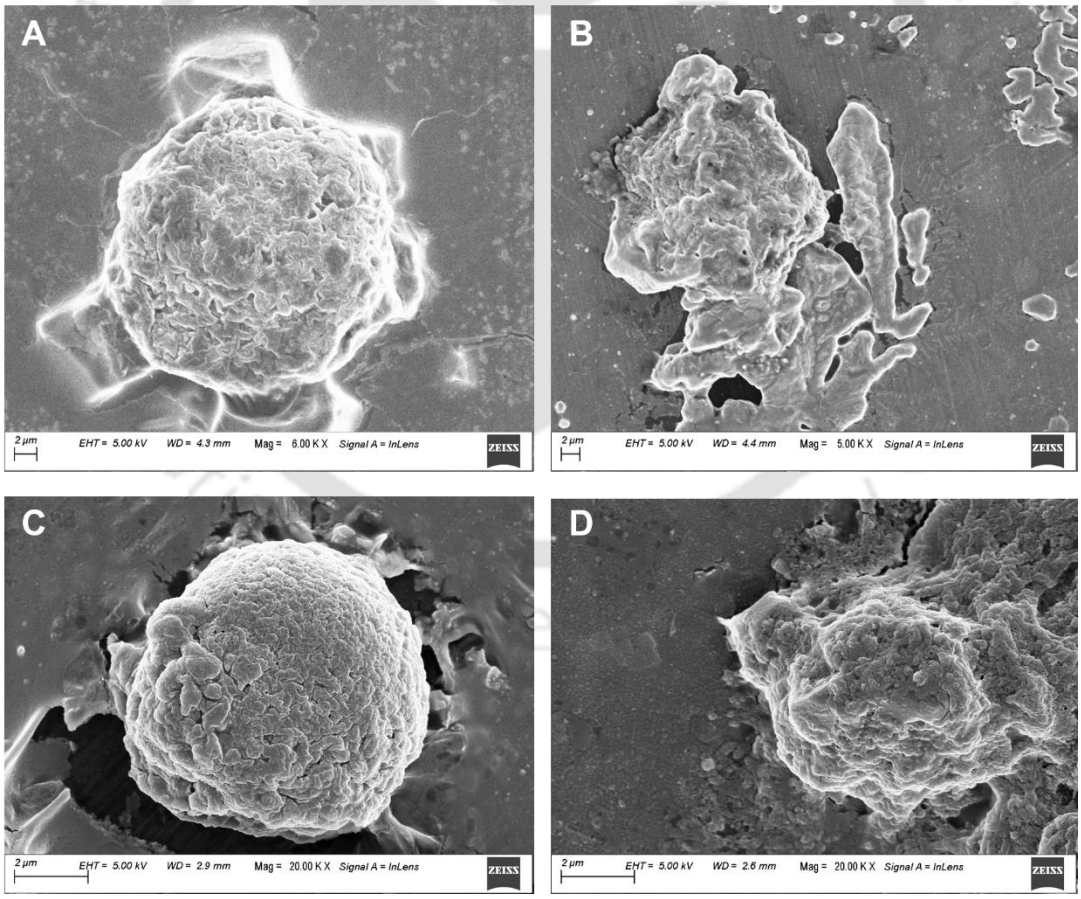

Figure 4.25. Irradiated HeLa cells treated with MB-NX-HAPs (0.6 µg/mL of NX and 0.17 µM of MB). (A) Control and (B) treated cell of HeLa (scale bar at 2 µm). Irradiated MCF-7 cells treated with MB-NX-HAPs (0.8 µg/mL of NX and 0.23 µM of MB). (C) Control and (D) treated MCF-7 cell (scale bar at 2 µm).

Using PI staining method, the cell cycle analysis was conducted in HeLa and MCF-7 cells (**Figure 4.26A and B**). In HeLa cells, among all the other samples, the sub G0/G1 population (6.57%) was found to be higher in irradiated cells treated with MB-NX-HAPs, with subsequent changes in population of other phases (G0/G1, S and G2/M). The population obtained for cells treated with remaining samples is also given. Similarly, the MCF-7 cells also exhibited higher sub G0/G1 population (10.13%) in irradiated cell sample of MB-NX-HAPs treatment as compared to remaining samples, with corresponding changes in the cell population of other cell cycle phases. The higher sub G0/G1 population is indicative of apoptosis induced cell death.

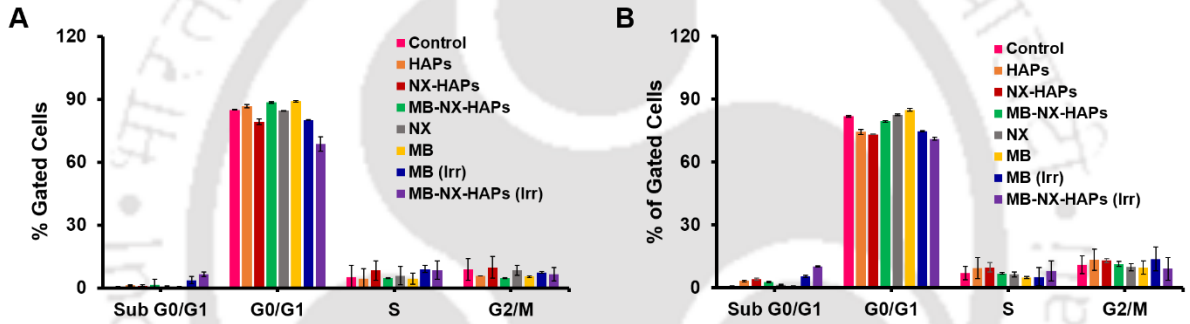

Figure 4.26. Cell cycle analysis carried out in (A) HeLa cells and (B) MCF-7 cells after treatment with HAPs, NX-HAPs, MB-NX-HAPs (both under irradiation at 640 nm and dark), free MB (both under irradiation at 640 nm and dark) and free NX.

Therefore, to substantiate the occurrence of apoptosis, annexin V-FITC based apoptosis assay was conducted. From the assay on HeLa, the apoptotic population obtained was 15.05% in case of irradiated sample of MB-NX-HAPs treated cells (**Figure 4.27A-H**). The percentage of apoptotic population of cells treated with different samples was shown in **Table 4.2.** Likewise, in MCF-7 cells, the irradiated cells of MB-NX-HAPs treatment exhibited considerable apoptotic cell population with 11.43%, among the remaining treatment samples (**Figure 4.28A-H**, **Table 4.3**). Incorporation of PDT was found to potentially enhance the effect of MB-NX-HAPs in deactivating the proliferation of cancer cells, with minimal effect on normal cell line. From the various experiments conducted, it was thus evident that MB-NX-HAPs, through co-delivery approach could appreciably intensify their therapeutic potential in both bacterial and cancer therapy, with the combination of chemotherapy and PDT aspect.

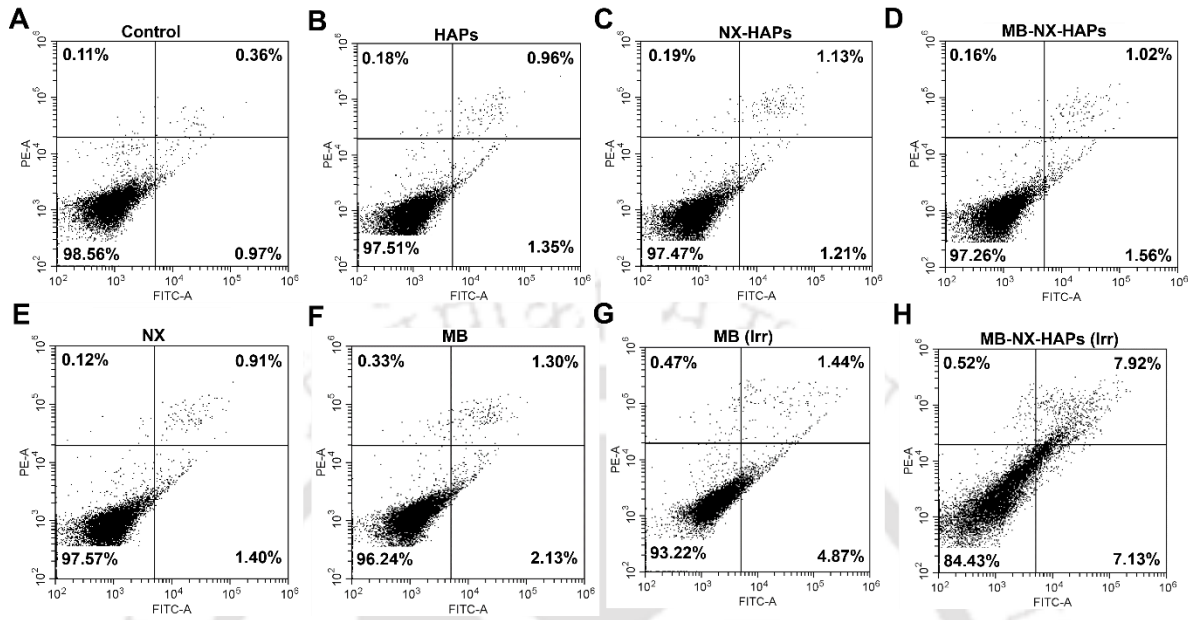

Figure 4.27. Annexin V-FITC assay performed in HeLa. (A) Control cells, (B) HAPs, (C) NX-HAPs, (D) MB-NX-HAPs (dark), (E) free NX, (F) free MB (dark), (G) free MB (irradiated at 640 nm) and (H) MB-NX-HAPs (irradiated at 640 nm) treated cells showing apoptotic and non-apoptotic population.

Sample	Apoptotic Population (%)
Control	1.33
HAPs	2.31
NX-HAPs	2.34
MB-NX-HAPs	2.58
NX	2.31
MB	3.43
MB (Irr)	6.31
MB-NX-HAPs (Irr)	15.05

Table 4.2. Apoptotic population (%) of HeLa cells after treatment with different samples.

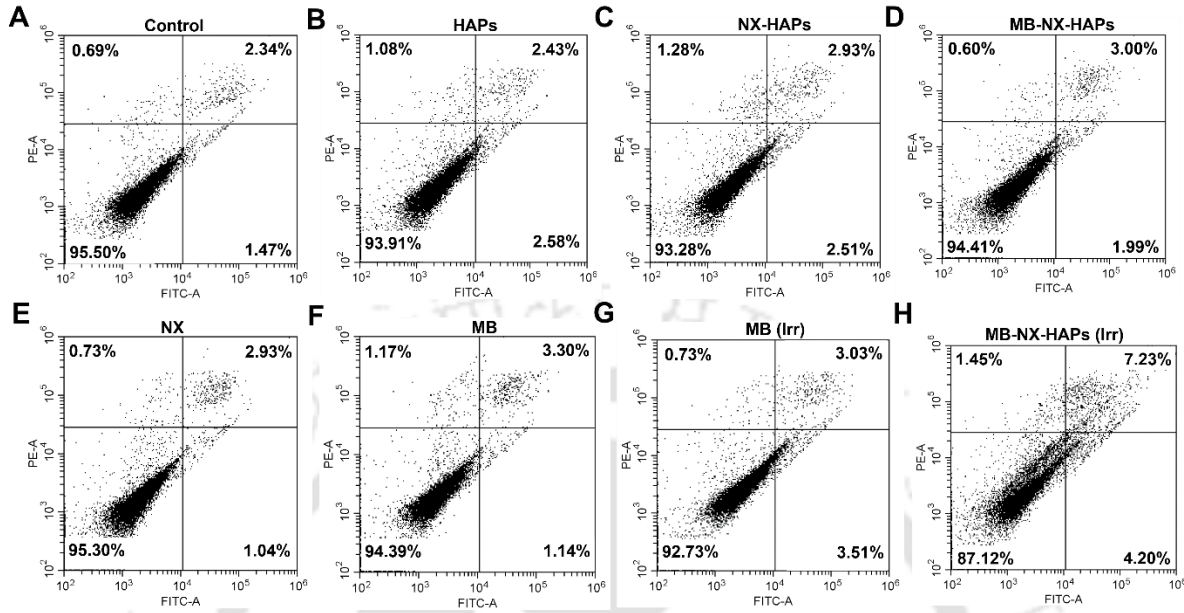

Figure 4.28. Annexin V-FITC assay conducted in MCF-7 cells. (A) Control cells, (B) HAPs, (C) NX-HAPs, (D) MB-NX-HAPs (dark), (E) free NX, (F) free MB (dark), (G) free MB (irradiated at 640 nm) and (H) MB-NX-HAPs (irradiated at 640 nm) treated MCF-7 cells showing population of apoptotic and non-apoptotic cells.

Sample	Apoptotic Population (%)
Control	3.81
HAPs	5.01
NX-HAPs	5.44
MB-NX-HAPs	4.99
NX	3.97
MB	4.44
MB (Irr)	6.54
MB-NX-HAPs (Irr)	11.43

Table 4.3. Percentage of apoptotic population in MCF-7 cells treated with various samples.

4.4. Conclusions

To summarize, a co-delivery approach was implemented through the fabricated MB-NX-HAPs for antibacterial and anticancer therapy. By encapsulation of drug NX, followed by loading a photosensitizer such as MB into HAPs, the nanoformulation was assessed for combinatorial therapy, conjugating chemotherapeutic and PDT technique.

Antibacterial therapy was performed in Gram negative strain such as *P. aeruginosa* MTCC 2488. The study suggested that along with antibacterial drug NX and photosensitizer MB entrapped in MB-NX-HAPs, they could appreciably decline the bacterial growth under irradiation (at 640 nm) as compared to other control samples applied for treatment. For cancer cell application in HeLa and MCF-7, the uptake study was conducted, revealing notable internalisation of MB-NX-HAPs by cells, following treatment. Upon evaluating their antiproliferative efficacy in cancer cell lines such as HeLa and MCF-7, MB-NX-HAPs were suggested to exhibit anti-cell proliferative activity under irradiation using LED light at 640 nm, with no significant toxicity towards normal cells such as HEK-293. Through integration of chemotherapy with PDT, MB-NX-HAPs could elevate the ROS production and alter cell cycle in HeLa and MCF-7 cells, along with significant apoptosis mediated cell death. Hence, the present nanocarrier with its biocompatible characteristics is suggested to be a suitable platform for combinatorial therapy with promising curative potentiality in bacterial and cancer treatment.

4.5. References

1. Jo, M. J.; Jin, I. S.; Park, C. W.; Hwang, B. Y.; Chung, Y. B.; Kim, J. S.; Shin, D. H., Revolutionizing technologies of nanomicelles for combinatorial anticancer drug delivery. *Arch Pharm Res* **2020,** *43* (1), 100-109.
2. Walvekar, P.; Gannimani, R.; Govender, T., Combination drug therapy via nanocarriers against infectious diseases. *Eur J Pharm Sci* **2019,** *127*, 121-141.
3. Xu, Y.; Yao, Y.; Wang, L.; Chen, H.; Tan, N., Hyaluronic Acid Coated Liposomes Co-Delivery of Natural Cyclic Peptide RA-XII and Mitochondrial Targeted Photosensitizer for Highly Selective Precise Combined Treatment of Colon Cancer. *Int J Nanomedicine* **2021,** *16*, 4929-4942.
4. Shi, Z.; Zhou, Y.; Fan, T.; Lin, Y.; Zhang, H.; Mei, L., Inorganic nano-carriers based smart drug delivery systems for tumor therapy. *Smart Materials in Medicine* **2020,** *1*, 32-47.
5. Kwiatkowski, S.; Knap, B.; Przystupski, D.; Saczko, J.; Kędzierska, E.; Knap-Czop, K.; Kotlińska, J.; Michel, O.; Kotowski, K.; Kulbacka, J., Photodynamic therapy - mechanisms, photosensitizers and combinations. *Biomed Pharmacother* **2018,** *106*, 1098-1107.
6. Yi, X.; Dai, J.; Han, Y.; Xu, M.; Zhang, X.; Zhen, S.; Zhao, Z.; Lou, X.; Xia, F., A high therapeutic efficacy of polymeric prodrug nano-assembly for a combination of photodynamic therapy and chemotherapy. *Commun Biol* **2018,** *1*, 202.

7. Yadav, V.; Talwar, P., Repositioning of fluoroquinolones from antibiotic to anti-cancer agents: An underestimated truth. *Biomed Pharmacother* **2019,** *111*, 934-946.
8. Abdel-Aal, M. A. A.; Abdel-Aziz, S. A.; Shaykoon, M. S. A.; Abuo-Rahma, G. E. A., Towards anticancer fluoroquinolones: A review article. *Arch Pharm (Weinheim)* **2019,** *352* (7), e1800376.
9. Lleonart, M. E.; Grodzicki, R.; Graifer, D. M.; Lyakhovich, A., Mitochondrial dysfunction and potential anticancer therapy. *Med Res Rev* **2017,** *37* (6), 1275-1298.
10. Sharma, P. C.; Goyal, R.; Sharma, A.; Sharma, D.; Saini, N.; Rajak, H.; Sharma, S.; Thakur, V. K., Insights on fluoroquinolones in cancer therapy: chemistry and recent developments. *Materials Today Chemistry* **2020,** *17*, 100296.
11. Fedorowicz, J.; Sączewski, J., Modifications of quinolones and fluoroquinolones: hybrid compounds and dual-action molecules. *Monatshefte für Chemie - Chemical Monthly* **2018,** *149* (7), 1199-1245.
12. Boya, P.; Andreau, K.; Poncet, D.; Zamzami, N.; Perfettini, J. L.; Metivier, D.; Ojcius, D. M.; Jäättelä, M.; Kroemer, G., Lysosomal membrane permeabilization induces cell death in a mitochondrion-dependent fashion. *The Journal of experimental medicine* **2003,** *197* (10), 1323-34.
13. Idowu, T.; Schweizer, F., Ubiquitous Nature of Fluoroquinolones: The Oscillation between Antibacterial and Anticancer Activities. *Antibiotics (Basel, Switzerland)* **2017,** *6* (4).
14. Kemp, J. A.; Shim, M. S.; Heo, C. Y.; Kwon, Y. J., "Combo" nanomedicine: Co-delivery of multi-modal therapeutics for efficient, targeted, and safe cancer therapy. *Advanced Drug Delivery Reviews* **2016,** *98*, 3-18.
15. Xiao, B.; Ma, L.; Merlin, D., Nanoparticle-mediated co-delivery of chemotherapeutic agent and siRNA for combination cancer therapy. *Expert Opin Drug Deliv* **2017,** *14* (1), 65-73.
16. Singh, A.; Talekar, M.; Tran, T.-H.; Samanta, A.; Sundaram, R.; Amiji, M., Combinatorial approach in the design of multifunctional polymeric nano-delivery systems for cancer therapy. *Journal of Materials Chemistry B* **2014,** *2* (46), 8069-8084.
17. Niu, X.; Chen, J.; Gao, J., Nanocarriers as a powerful vehicle to overcome blood-brain barrier in treating neurodegenerative diseases: Focus on recent advances. *Asian Journal of Pharmaceutical Sciences* **2019,** *14* (5), 480-496.
18. Lin, G.; Revia, R. A.; Zhang, M., Inorganic Nanomaterial-Mediated Gene Therapy in Combination with Other Antitumor Treatment Modalities. **2021,** *31* (5), 2007096.
19. Afzal, M.; Ameeduzzafar; Alharbi, K. S.; Alruwaili, N. K.; Al-Abassi, F. A.; Al-Malki, A. A. L.; Kazmi, I.; Kumar, V.; Kamal, M. A.; Nadeem, M. S.; Aslam, M.; Anwar, F., Nanomedicine in treatment of breast cancer - A challenge to conventional therapy. *Seminars in cancer biology* **2021,** *69*, 279-292.

20. Bjarnsholt, T.; Whiteley, M.; Rumbaugh, K. P.; Stewart, P. S.; Jensen, P. O.; Frimodt-Moller, N., The importance of understanding the infectious microenvironment. *Lancet Infect Dis* **2021**.
21. Whiteside, T. L., The tumor microenvironment and its role in promoting tumor growth. *Oncogene* **2008,** *27* (45), 5904-12.
22. Persi, E.; Duran-Frigola, M.; Damaghi, M.; Roush, W. R.; Aloy, P.; Cleveland, J. L.; Gillies, R. J.; Ruppin, E., Systems analysis of intracellular pH vulnerabilities for cancer therapy. *Nat Commun* **2018,** *9* (1), 2997.
23. Yang, S.; Han, X.; Yang, Y.; Qiao, H.; Yu, Z.; Liu, Y.; Wang, J.; Tang, T., Bacteria-Targeting Nanoparticles with Microenvironment-Responsive Antibiotic Release To Eliminate Intracellular Staphylococcus aureus and Associated Infection. *ACS Appl Mater Interfaces* **2018,** *10* (17), 14299-14311.
24. Shariatinia, Z., Big family of nano- and microscale drug delivery systems ranging from inorganic materials to polymeric and stimuli-responsive carriers as well as drug-conjugates. *Journal of Drug Delivery Science and Technology* **2021,** *66*, 102790.
25. Gao, P.; Nie, X.; Zou, M.; Shi, Y.; Cheng, G., Recent advances in materials for extended-release antibiotic delivery system. *J Antibiot (Tokyo)* **2011,** *64* (9), 625-34.
26. Barbosa, A. A.; Junior, S. A.; Mendes, R. L.; de Lima, R. S.; de Vasconcelos Ferraz, A., Multifunctional hydroxyapatite with potential for application in theranostic nanomedicine. *Materials science & engineering. C, Materials for biological applications* **2020,** *116*, 111227.
27. Murugan, E.; Geetha Rani, D. P.; Srinivasan, K.; Muthumary, J., New surface hydroxylated and internally quaternised poly(propylene imine) dendrimers as efficient biocompatible drug carriers of norfloxacin. *Expert Opin Drug Deliv* **2013,** *10* (10), 1319-34.
28. An, Y.; Ren, Y.; Bick, M.; Dudek, A.; Hong-Wang Waworuntu, E.; Tang, J.; Chen, J.; Chang, B., Highly Fluorescent Copper Nanoclusters for Sensing and Bioimaging. *Biosens. Bioelectron.* **2020,** *154*, 112078.
29. Simon, A. T.; Dutta, D.; Chattopadhyay, A.; Ghosh, S. S., Copper Nanocluster-Doped Luminescent Hydroxyapatite Nanoparticles for Antibacterial and Antibiofilm Applications. *ACS Omega* **2019,** *4* (3), 4697-4706.
30. Hasanin, M. S.; Abdelraof, M.; Fikry, M.; Shaker, Y. M.; Sweed, A. M. K.; Senge, M. O., Development of Antimicrobial Laser-Induced Photodynamic Therapy Based on Ethylcellulose/Chitosan Nanocomposite with 5,10,15,20-Tetrakis(m-Hydroxyphenyl)porphyrin. **2021,** *26* (12), 3551.
31. Lee, H. B.; Peart, T. E.; Svoboda, M. L., Determination of ofloxacin, norfloxacin, and ciprofloxacin in sewage by selective solid-phase extraction, liquid chromatography with fluorescence detection, and liquid chromatography--tandem mass spectrometry. *Journal of chromatography. A* **2007,** *1139* (1), 45-52.

32. Salahuddin, N.; Abdelwahab, M.; Gaber, M.; Elneanaey, S., Synthesis and Design of Norfloxacin drug delivery system based on PLA/TiO2 nanocomposites: Antibacterial and antitumor activities. *Materials Science and Engineering: C* **2020,** *108*, 110337.
33. Tofan, T.-G.; Cheregi, M.-C.; David, I.-G.; David, V., Spectrofluorimetric Analyses of Ciprofloxacin and Norfloxacin. **2019,** *29* (1), 29.
34. Selvam, S.; Sarkar, I., Bile salt induced solubilization of methylene blue: Study on methylene blue fluorescence properties and molecular mechanics calculation. *Journal of pharmaceutical analysis* **2017,** *7* (1), 71-75.
35. Kamat, B. P., Study of the interaction between fluoroquinolones and bovine serum albumin. *Journal of Pharmaceutical and Biomedical Analysis* **2005,** *39* (5), 1046-1050.
36. Farzadi, A.; Bakhshi, F.; Solati-Hashjin, M.; Asadi-Eydivand, M.; Osman, N. A. a., Magnesium incorporated hydroxyapatite: Synthesis and structural properties characterization. *Ceram. Int.* **2014,** *40*, 6021.
37. In, Y.; Amornkitbamrung, U.; Hong, M.-H.; Shin, H., On the Crystallization of Hydroxyapatite under Hydrothermal Conditions: Role of Sebacic Acid as an Additive. *ACS Omega* **2020,** *5* (42), 27204-27210.
38. Zhang, D.; Wei, L.; Zhong, M.; Xiao, L.; Li, H.-W.; Wang, J., The morphology and surface charge-dependent cellular uptake efficiency of upconversion nanostructures revealed by single-particle optical microscopy. *Chemical Science* **2018,** *9* (23), 5260-5269.
39. Patil, S.; Sandberg, A.; Heckert, E.; Self, W.; Seal, S., Protein adsorption and cellular uptake of cerium oxide nanoparticles as a function of zeta potential. *Biomaterials* **2007,** *28* (31), 4600-4607.
40. Ahn, S.; Seo, E.; Kim, K.; Lee, S. J., Controlled cellular uptake and drug efficacy of nanotherapeutics. *Sci Rep* **2013,** *3*, 1997.
41. Hillaireau, H.; Couvreur, P., Nanocarriers' entry into the cell: relevance to drug delivery. *Cellular and molecular life sciences : CMLS* **2009,** *66* (17), 2873-96.
42. Nandhakumar, S.; Dhanaraju, M. D.; Sundar, V. D.; Heera, B., Influence of surface charge on the *in vitro* protein adsorption and cell cytotoxicity of paclitaxel loaded poly(ε-caprolactone) nanoparticles. *Bulletin of Faculty of Pharmacy, Cairo University* **2017,** *55* (2), 249-258.
43. Gao, W.; Chan, J. M.; Farokhzad, O. C., pH-Responsive Nanoparticles for Drug Delivery. *Molecular Pharmaceutics* **2010,** *7* (6), 1913-1920.
44. Du, M.; Chen, J.; Liu, K.; Xing, H.; Song, C., Recent advances in biomedical engineering of nano-hydroxyapatite including dentistry, cancer treatment and bone repair. *Composites Part B: Engineering* **2021,** *215*, 108790.
45. Martínez, S. R.; Durantini, A. M.; Becerra, M. C.; Cosa, G., Real-Time Single-Cell Imaging Reveals Accelerating Lipid Peroxyl Radical Formation in Escherichia coli Triggered by a Fluoroquinolone Antibiotic. *ACS Infectious Diseases* **2020,** *6* (9), 2468-2477.

46. de Freitas, L. M.; Soares, C. P.; Fontana, C. R., Synergistic effect of photodynamic therapy and cisplatin: A novel approach for cervical cancer. *Journal of Photochemistry and Photobiology B: Biology* **2014,** *140*, 365-373.
47. Akinremi, C.; Obaleye, J.; Amolegbe, S.; Adediji, J.; Bamigboye, M. O., Biological activities of some Fluoroquinolones-metal complexes. *International Journal of Medicine and Biomedical Research* **2012,** *1*, 24-34.
48. Bykowska, A.; Starosta, R.; Jezierska, J.; Jeżowska-Bojczuk, M., Coordination versatility of phosphine derivatives of fluoroquinolones. New CuI and CuII complexes and their interactions with DNA. *RSC Advances* **2015,** *5* (98), 80804-80815.
49. Singh, R.; Jadeja, R. N.; Thounaojam, M. C.; Patel, T.; Devkar, R. V.; Chakraborty, D., Synthesis, DNA binding and antiproliferative activity of ternary copper complexes of moxifloxacin and gatifloxacin against lung cancer cells. *Inorganic Chemistry Communications* **2012,** *23*, 78-84.
50. Patitungkho, S.; Adsule, S.; Dandawate, P.; Padhye, S.; Ahmad, A.; Sarkar, F. H., Synthesis, characterization and anti-tumor activity of moxifloxacin–Copper complexes against breast cancer cell lines. *Bioorganic & Medicinal Chemistry Letters* **2011,** *21* (6), 1802-1806.

Chapter 5

Conclusions and Future Prospects

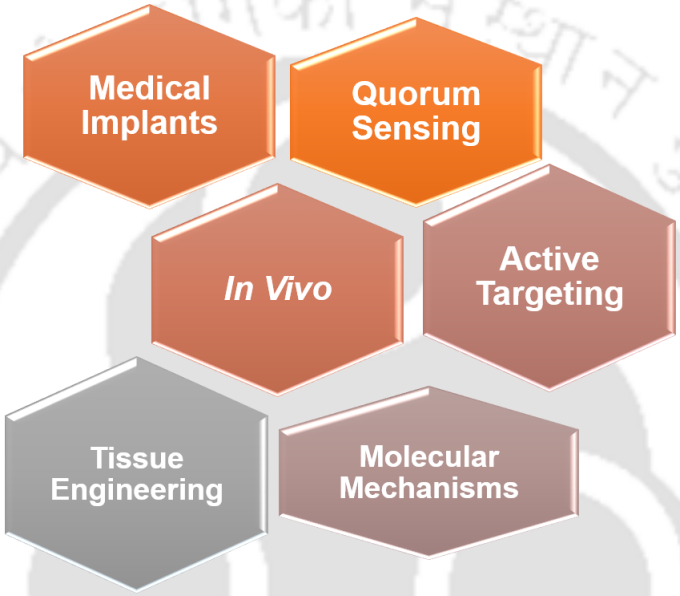

Chapter 5

Conclusions and Future Prospects

5.1. Conclusions

The whole dissertation compiles the synthesis of a drug delivery carrier based on hydroxyapatite, which contains calcium and phosphate as its basic composition. Having the similar constituent of human body tissues, the nanocarriers were biocompatible. Along with therapy as the major application, imaging and tracking of internally distributed nanocarriers were made possible through doping with luminescent copper nanoclusters.

The current thesis details the synthesis and characterisations of hydroxyapatite nanoparticles doped with copper nanoclusters. The copper nanocluster doped hydroxyapatite nanoparticles loaded with antibacterial drug kanamycin were explored for antibacterial and antibiofilm applications. The nanocarrier which exhibited sustained release of drug was found to be active against the growth of Gram negative bacteria. Also, they were found to be active in eradication of pathogenic biofilm formed by *Pseudomonas aeruginosa*. In addition to therapeutic effect, the bacterial cells could be imaged due to luminescent copper nanoclusters present in hydroxyapatite nanoparticles.

Further, copper nanocluster doped hydroxyapatite nanoparticles were explored for cancer therapy in monolayer and tumour spheroids of cancer cells. The nanocarrier loaded with anticancer drug quercetin, could significantly inhibit the proliferation of monolayer cancer cells with generation of ROS. The cell cycle pattern of cancer cells was found to be altered and event of apoptosis induced cell death was observed. Also, bioimaging efficiency of copper nanocluster doped hydroxyapatite nanocarrier was evident in cancer cells. The anticancer property of drug loaded copper nanocluster doped hydroxyapatite nanoparticles was appreciably effective against 3-D tumour spheroids of cervical cancer cells. The drug loaded nanosystem prompted significant disintegration of spheroid system by probably delivering drug molecules internally within its core.

Another therapeutic approach implemented through copper nanocluster doped hydroxyapatite nanoparticles was by evaluating combinatorial effect for bacterial and cancer

therapy. A combination of chemotherapeutic and PDT approach was applied through the nanoformulation by co-delivering an antibacterial drug (norfloxacin) and a photosensitizer (methylene blue). Such a combination of drug based therapy and PDT was understood to upgrade inhibitory effect in case of antibacterial study than when applied individually. Similarly, in case of cancer cells, chemotherapy in combination with PDT significantly reduced the viability of cells at a very lower doses. With significant generation of ROS, the developed nanocarrier exhibited anti-cell proliferative activity, induced apoptosis mediated cells death, with minimal effect on normal cell line.

5.2. Future Prospects

Based on the various findings observed from the present study, following prospects can be considered for the future investigation.

- Hydroxyapatite nanomaterials to be studied for coating medical implants such as catheter for preventing implants mediated infections.
- Functionalization with suitable ligands for recognizing specific cellular components and intracellular sites to execute active targeting and enhanced therapy.
- Quorum sensing targeted therapy for deactivating the genes responsible for cell to cell communication, to improve the eradication of pathogenic biofilms.
- Unveiling of detailed molecular mechanisms to understand the actual mode of action responsible for curative events.
- *In vivo* studies for better understanding the physiological and biochemical characteristics following drug delivery.
- Utilizing the bioinspired nature of hydroxyapatite for wide range of tissue engineering applications.

Publications and patent

Publications from Thesis work

1. **Anitha T. Simon**, Deepanjalee Dutta, Arun Chattopadhyay and Siddhartha Sankar Ghosh; Copper nanocluster doped luminescent hydroxyapatite nanoparticles for antibacterial and antibiofilm applications; ***ACS Omega*, 4, 3, 4697–4706, 2019**
2. **Anitha T. Simon,** Deepanjalee Dutta, Arun Chattopadhyay and Siddhartha Sankar Ghosh; Quercetin-Loaded Luminescent Hydroxyapatite Nanoparticles for Theranostic Application in Monolayer and Spheroid Cultures of Cervical Cancer Cell Line *In Vitro*; ***ACS Applied Bio Materials*, 4, 5, 4495–4506**, **2021**
3. **Anitha T. Simon,** Arun Chattopadhyay and Siddhartha Sankar Ghosh; *In vitro* Therapeutic Attributes of Luminescent Hydroxyapatite Nanoparticles in Co-Delivery Approach. (**Manuscript under preparation**)

Publications from collaborative work

1. Deepanjalee Dutta, Sunil Kumar Sailapu, **Anitha T. Simon**, Siddhartha Sankar Ghosh and Arun Chattopadhyay; Gold-Nanocluster-Embedded Mucin Nanoparticles for Photodynamic Therapy and Bioimaging; ***Langmuir*, 35, 32, 10475–10483, 2019**
2. Sunil Kumar Sailapu, Deepanjalee Dutta, **Anitha T. Simon**, Siddhartha Sankar Ghosh and Arun Chattopadhyay; Smartphone controlled interactive portable device for theranostics in vitro; ***Biosensors and Bioelectronics*, 146, 15, 111745, 2019.**
3. Tamanna Bhuyan, **Anitha T. Simon**, Surjendu Maity, Amit Kumar Singh, Siddhartha Sankar Ghosh,and Dipankar Bandyopadhyay; Magnetotactic T-Budbots to Kill-n-Clean Biofilms. ***ACS Applied Materials and Interfaces*, 12, 39, 43352–43364, 2020.**

Patent filed from collaborative work

- Arun Chattopadhyay, Sunil Kumar Sailapu, Deepanjalee Dutta, Siddhartha Sankar Ghosh, **Anitha T Simon**. Wirelessly Operated LED Device for Photodynamic Therapy and Subsequent Monitoring of Therapeutic Succes (2017). Indian Patent Application No.201731031603 (Patent).

Conferences and Workshops Attended

1. NWNTD (National Workshop on Nanoelectronics and Theranostic devices) 2016-2019 held by Centre for Nanotechnology, IIT Guwahati.
2. Participated in Biomedical Device Technology on 5th International Conference on Advanced Nanomaterials and Nanotechnology (ICANN-2017), organised by Centre for Nanotechnology, IIT Guwahati
3. Participated in model presentation at Research Conclave'18 (2018), organised by IIT Guwahati
4. Presented poster on International Conference on Biotechnology and Biological Science (Biospectrum-2019), organised Department of Biotechnology by University of Engineering and Management
5. Presented poster on International Conference on Advanced Nanomaterials and Nanotechnology (ICANN-2019), organised by Centre for Nanotechnology, IIT Guwahati.
6. Delivered oral presentation on National Conference on "Chemistry of Chalcogenides" (NC3-2021), organised by Department of Applied Chemistry, Defence Institute of Advanced Technology, Pune.

Permissions

Figure 1.2

SPRINGER NATURE LICENSE
TERMS AND CONDITIONS
Jan 11, 2022

This Agreement between Ms. Anitha Simon ("You") and Springer Nature ("Springer Nature") consists of your license details and the terms and conditions provided by Springer Nature and Copyright Clearance Center.

License Number	5221370002961
License date	Jan 03, 2022
Licensed Content Publisher	Springer Nature
Licensed Content Publication	Environmental Chemistry Letters
Licensed Content Title	Nanocarriers for drug delivery applications
Licensed Content Author	Munusamy Chamundeeswari et al
Licensed Content Date	Nov 21, 2018
Type of Use	Thesis/Dissertation
Requestor type	academic/university or research institute
Format	print and electronic
Portion	figures/tables/illustrations
Number of figures/tables/illustrations	1
Will you be translating?	no
Circulation/distribution	1 - 29
Author of this Springer Nature content	no
Title	Luminescent Composites of Hydroxyapatite Nanoparticles for Theranostic Applications
Institution name	IIT Guwahati
Expected presentation date	Jan 2022
Portions	Figure 1
Requestor Location	Ms. Anitha Simon IIT Guwahati Guwahati, 781039 India Attn: IIT Guwahati
Total	0.00 USD

Figure 1.3

JOHN WILEY AND SONS LICENSE
TERMS AND CONDITIONS
Jan 11, 2022

This Agreement between Ms. Anitha Simon ("You") and John Wiley and Sons ("John Wiley and Sons") consists of your license details and the terms and conditions provided by John Wiley and Sons and Copyright Clearance Center.

License Number	5221370937449
License date	Jan 03, 2022
Licensed Content Publisher	John Wiley and Sons
Licensed Content Publication	Chemistry - A European Journal
Licensed Content Title	Biological and Medical Applications of Calcium Phosphate Nanoparticles
Licensed Content Author	Viktoriya Sokolova, Matthias Epple
Licensed Content Date	Mar 16, 2021
Licensed Content Volume	27
Licensed Content Issue	27
Licensed Content Pages	18
Type of use	Dissertation/Thesis
Requestor type	University/Academic
Format	Print and electronic
Portion	Figure/table
Number of figures/tables	1
Will you be translating?	No
Title	Luminescent Composites of Hydroxyapatite Nanoparticles for Theranostic Applications
Institution name	IIT Guwahati
Expected presentation date	Jan 2022
Portions	Figure 1
Requestor Location	Ms. Anitha Simon IIT Guwahati Guwahati, 781039 India Attn: IIT Guwahati
Publisher Tax ID	EU826007151
Total	0.00 USD

Figure 1.4

ELSEVIER LICENSE
TERMS AND CONDITIONS
Jan 11, 2022

This Agreement between Ms. Anitha Simon ("You") and Elsevier ("Elsevier") consists of your license details and the terms and conditions provided by Elsevier and Copyright Clearance Center.

License Number	5221380076875
License date	Jan 03, 2022
Licensed Content Publisher	Elsevier
Licensed Content Publication	Journal of Water Process Engineering
Licensed Content Title	A review on the synthesis of hydroxyapatite, its composites and adsorptive removal of pollutants from wastewater
Licensed Content Author	Shraddha Pai,Srinivas M Kini,Raja Selvaraj,Arivalagan Pugazhendhi
Licensed Content Date	Dec 1, 2020
Licensed Content Volume	38
Licensed Content Issue	n/a
Licensed Content Pages	1
Start Page	101574
End Page	0
Type of Use	reuse in a thesis/dissertation
Portion	figures/tables/illustrations
Number of figures/tables/illustrations	1
Format	both print and electronic
Are you the author of this Elsevier article?	No
Will you be translating?	No
Title	Luminescent Composites of Hydroxyapatite Nanoparticles for Theranostic Applications
Institution name	IIT Guwahati
Expected presentation date	Jan 2022
Portions	Figure 3
Requestor Location	Ms. Anitha Simon IIT Guwahati Guwahati, 781039 India Attn: IIT Guwahati
Publisher Tax ID	GB 494 6272 12

Total	0.00 USD

Figure 1.5

ELSEVIER LICENSE
TERMS AND CONDITIONS
Jan 11, 2022

This Agreement between Ms. Anitha Simon ("You") and Elsevier ("Elsevier") consists of your license details and the terms and conditions provided by Elsevier and Copyright Clearance Center.

License Number	5221380569051
License date	Jan 03, 2022
Licensed Content Publisher	Elsevier
Licensed Content Publication	Ceramics International
Licensed Content Title	Bioactive, luminescent erbium-doped hydroxyapatite nanocrystals for biomedical applications
Licensed Content Author	Sudip Mondal,Van Tu Nguyen,Sumin Park,Jaeyeop Choi,Le Hai Tran,Myunggi Yi,Joong Ho Shin,Chang-Yong Lee,Junghwan Oh
Licensed Content Date	Jul 1, 2020
Licensed Content Volume	46
Licensed Content Issue	10
Licensed Content Pages	12
Start Page	16020
End Page	16031
Type of Use	reuse in a thesis/dissertation
Portion	figures/tables/illustrations
Number of figures/tables/illustrations	1
Format	both print and electronic
Are you the author of this Elsevier article?	No
Will you be translating?	No
Title	Luminescent Composites of Hydroxyapatite Nanoparticles for Theranostic Applications
Institution name	IIT Guwahati
Expected presentation date	Jan 2022
Portions	Figure 1
Requestor Location	Ms. Anitha Simon IIT Guwahati Guwahati, 781039 India Attn: IIT Guwahati
Publisher Tax ID	GB 494 6272 12
Total	0.00 USD

Figure 1.7

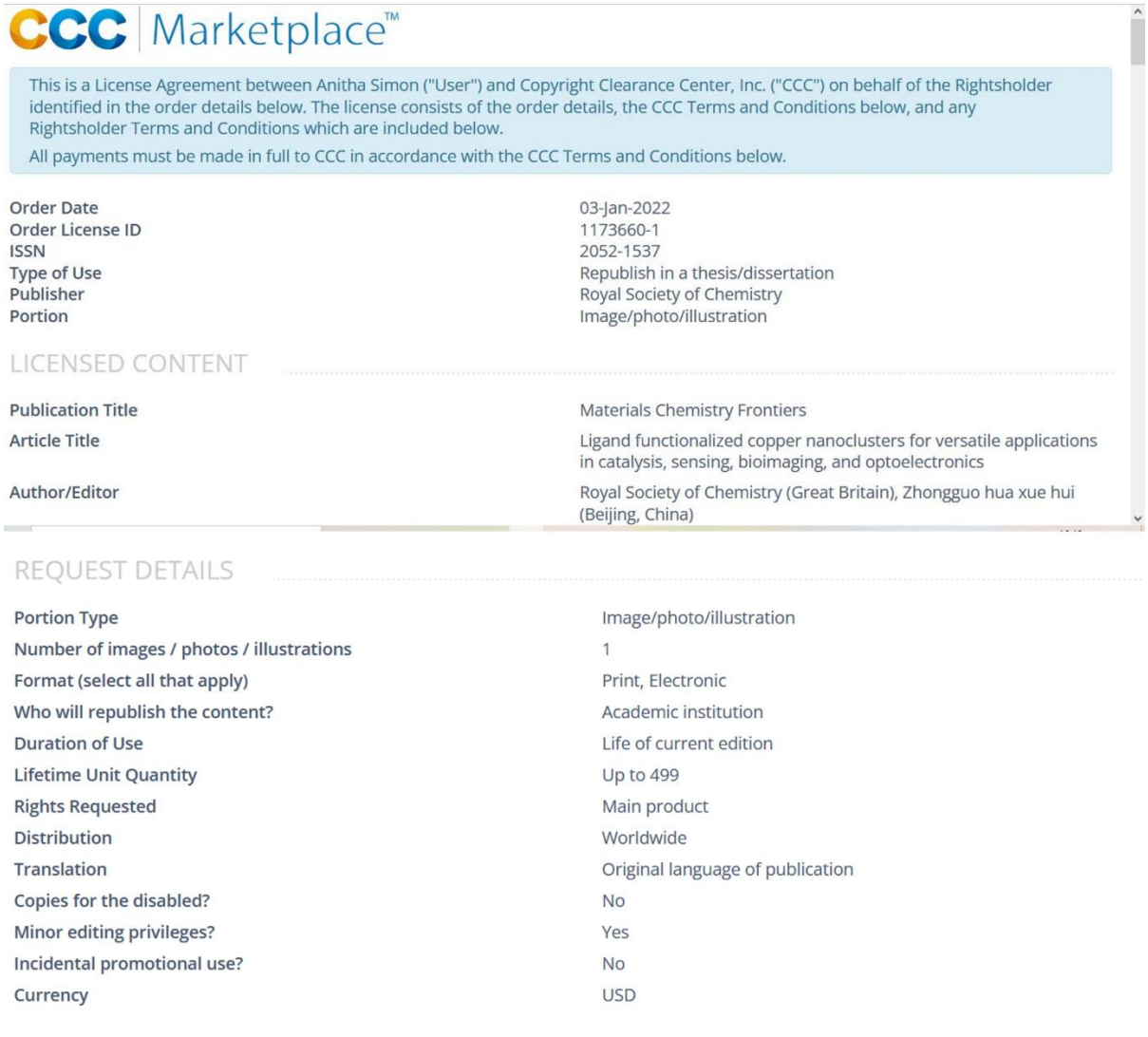

CCC Marketplace™

This is a License Agreement between Anitha Simon ("User") and Copyright Clearance Center, Inc. ("CCC") on behalf of the Rightsholder identified in the order details below. The license consists of the order details, the CCC Terms and Conditions below, and any Rightsholder Terms and Conditions which are included below.

All payments must be made in full to CCC in accordance with the CCC Terms and Conditions below.

Order Date	03-Jan-2022
Order License ID	1173660-1
ISSN	2052-1537
Type of Use	Republish in a thesis/dissertation
Publisher	Royal Society of Chemistry
Portion	Image/photo/illustration

LICENSED CONTENT

Publication Title	Materials Chemistry Frontiers
Article Title	Ligand functionalized copper nanoclusters for versatile applications in catalysis, sensing, bioimaging, and optoelectronics
Author/Editor	Royal Society of Chemistry (Great Britain), Zhongguo hua xue hui (Beijing, China)

REQUEST DETAILS

Portion Type	Image/photo/illustration
Number of images / photos / illustrations	1
Format (select all that apply)	Print, Electronic
Who will republish the content?	Academic institution
Duration of Use	Life of current edition
Lifetime Unit Quantity	Up to 499
Rights Requested	Main product
Distribution	Worldwide
Translation	Original language of publication
Copies for the disabled?	No
Minor editing privileges?	Yes
Incidental promotional use?	No
Currency	USD

Figure 1.8

This is a License Agreement between Anitha Simon ("User") and Copyright Clearance Center, Inc. ("CCC") on behalf of the Rightsholder identified in the order details below. The license consists of the order details, the CCC Terms and Conditions below, and any Rightsholder Terms and Conditions which are included below.

All payments must be made in full to CCC in accordance with the CCC Terms and Conditions below.

Order Date	03-Jan-2022
Order License ID	1173666-1
ISSN	2040-3372
Type of Use	Republish in a thesis/dissertation
Publisher	RSC Pub
Portion	Image/photo/illustration

LICENSED CONTENT

Publication Title	Nanoscale
Article Title	Protein-directed synthesis of pH-responsive red fluorescent copper nanoclusters and their applications in cellular imaging and catalysis.
Author/Editor	National Center for Nanoscience and Technology., Royal Society of Chemistry (Great Britain)

REQUEST DETAILS

Portion Type	Image/photo/illustration
Number of images / photos / illustrations	1
Format (select all that apply)	Print, Electronic
Who will republish the content?	Academic institution
Duration of Use	Life of current edition
Lifetime Unit Quantity	Up to 499
Rights Requested	Main product
Distribution	Worldwide
Translation	Original language of publication
Copies for the disabled?	No
Minor editing privileges?	No
Incidental promotional use?	No
Currency	USD

Figure 1.10

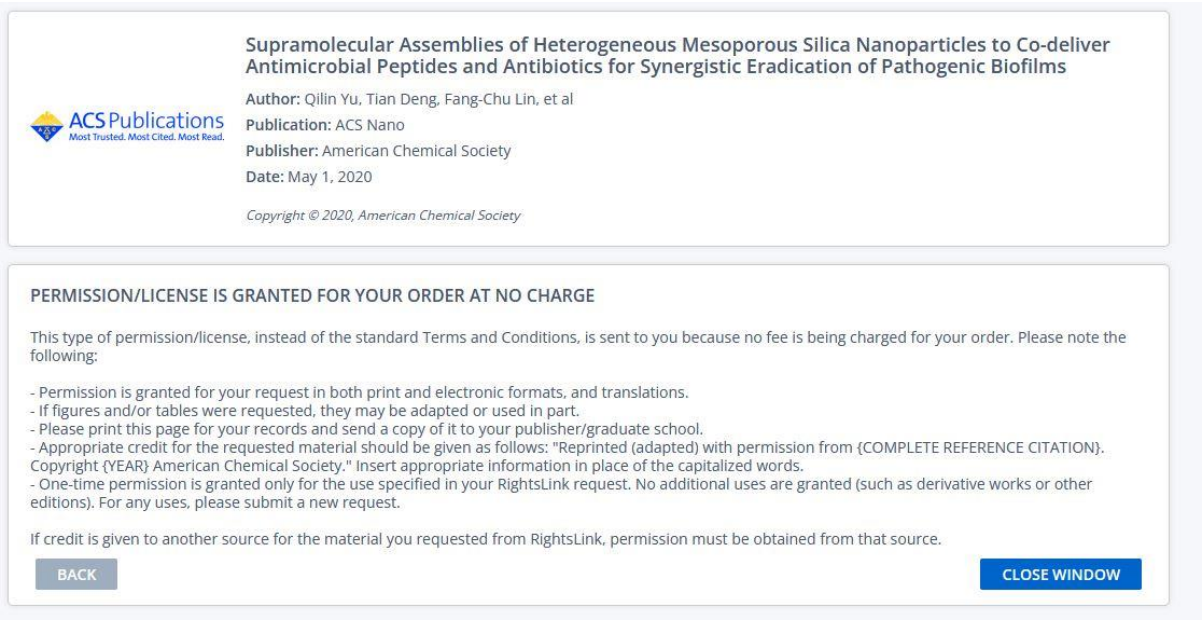

ACS Publications
Most Trusted. Most Cited. Most Read.

Supramolecular Assemblies of Heterogeneous Mesoporous Silica Nanoparticles to Co-deliver Antimicrobial Peptides and Antibiotics for Synergistic Eradication of Pathogenic Biofilms

Author: Qilin Yu, Tian Deng, Fang-Chu Lin, et al
Publication: ACS Nano
Publisher: American Chemical Society
Date: May 1, 2020

Copyright © 2020, American Chemical Society

PERMISSION/LICENSE IS GRANTED FOR YOUR ORDER AT NO CHARGE

This type of permission/license, instead of the standard Terms and Conditions, is sent to you because no fee is being charged for your order. Please note the following:

- Permission is granted for your request in both print and electronic formats, and translations.
- If figures and/or tables were requested, they may be adapted or used in part.
- Please print this page for your records and send a copy of it to your publisher/graduate school.
- Appropriate credit for the requested material should be given as follows: "Reprinted (adapted) with permission from {COMPLETE REFERENCE CITATION}. Copyright {YEAR} American Chemical Society." Insert appropriate information in place of the capitalized words.
- One-time permission is granted only for the use specified in your RightsLink request. No additional uses are granted (such as derivative works or other editions). For any uses, please submit a new request.

If credit is given to another source for the material you requested from RightsLink, permission must be obtained from that source.

BACK CLOSE WINDOW

Figure 1.12

ELSEVIER LICENSE
TERMS AND CONDITIONS
Jan 11, 2022

This Agreement between Ms. Anitha Simon ("You") and Elsevier ("Elsevier") consists of your license details and the terms and conditions provided by Elsevier and Copyright Clearance Center.

License Number	5221440658495
License date	Jan 03, 2022
Licensed Content Publisher	Elsevier
Licensed Content Publication	Biomaterials
Licensed Content Title	Mitochondria and nuclei dual-targeted heterogeneous hydroxyapatite nanoparticles for enhancing therapeutic efficacy of doxorubicin
Licensed Content Author	Hui Xiong,Shi Du,Jiang Ni,Jianping Zhou,Jing Yao
Licensed Content Date	Jul 1, 2016
Licensed Content Volume	94
Licensed Content Issue	n/a
Licensed Content Pages	14
Start Page	70
End Page	83
Type of Use	reuse in a thesis/dissertation
Portion	figures/tables/illustrations
Number of figures/tables/illustrations	1
Format	both print and electronic
Are you the author of this Elsevier article?	No
Will you be translating?	No
Title	Luminescent Composites of Hydroxyapatite Nanoparticles for Theranostic Applications
Institution name	IIT Guwahati
Expected presentation date	Jan 2022
Portions	Scheme 1
Requestor Location	Ms. Anitha Simon IIT Guwahati Guwahati, 781039 India Attn: IIT Guwahati
Publisher Tax ID	GB 494 6272 12
Total	0.00 USD

Figure 1.13

SPRINGER NATURE LICENSE
TERMS AND CONDITIONS
Jan 11, 2022

This Agreement between Ms. Anitha Simon ("You") and Springer Nature ("Springer Nature") consists of your license details and the terms and conditions provided by Springer Nature and Copyright Clearance Center.

License Number	5221441135180
License date	Jan 03, 2022
Licensed Content Publisher	Springer Nature
Licensed Content Publication	Photochemical & Photobiological Sciences
Licensed Content Title	Increased photoluminescence and photodynamic therapy efficiency of hydroxyapatite-β-cyclodextrin-methylene blue@carbon powders with the favor of hydrogen bonding effect
Licensed Content Author	Kaijie Zhang et al
Licensed Content Date	Sep 25, 2021
Type of Use	Thesis/Dissertation
Requestor type	academic/university or research institute
Format	print and electronic
Portion	figures/tables/illustrations
Number of figures/tables/illustrations	1
Will you be translating?	no
Circulation/distribution	1 - 29
Author of this Springer Nature content	no
Title	Luminescent Composites of Hydroxyapatite Nanoparticles for Theranostic Applications
Institution name	IIT Guwahati
Expected presentation date	Jan 2022
Portions	Scheme 1
Requestor Location	Ms. Anitha Simon IIT Guwahati Guwahati, 781039 India Attn: IIT Guwahati
Total	0.00 USD

Chapter 2

Thank you for contacting ACS Publications Support.

Your permission request is granted and there is no fee for this reuse.
In your planned reuse, you must cite the ACS article as the source, add this direct link: https://pubs.acs.org/doi/10.1021/acsomega.8b03076, and include a notice to readers that further permissions related to the material excerpted should be directed to the ACS.

Please do not hesitate to contact us if you need any further assistance.

Sincerely,

Vojin Vucic
ACS Publications Support
Customer Services & Information
Website: https://acs.service-now.com/acs
Email: support@services.acs.org
Phone: 800-227-9919 | 202-872-(HELP) 4357

Case Information:

Case: CSCSI0046222

Created On: 01-11-2022 05:12:21 AM EST

Title: Request for using the entire article for thesis

Description: Respected sir/madam

This is to kindly seek your permission for reusing the full article whose details are given below, for my thesis and I am the original author of the entire content. Thank you

https://pubs.acs.org/doi/pdf/10.1021/acsomega.8b030<https://pubs.acs.org/doi/pdf/10.1021/acsomega.8b03076>

Copper Nanocluster-Doped Luminescent Hydroxyapatite Nanoparticles for Antibacterial and Antibiofilm Applications.

Regards
Anitha T Simon

Chapter 3

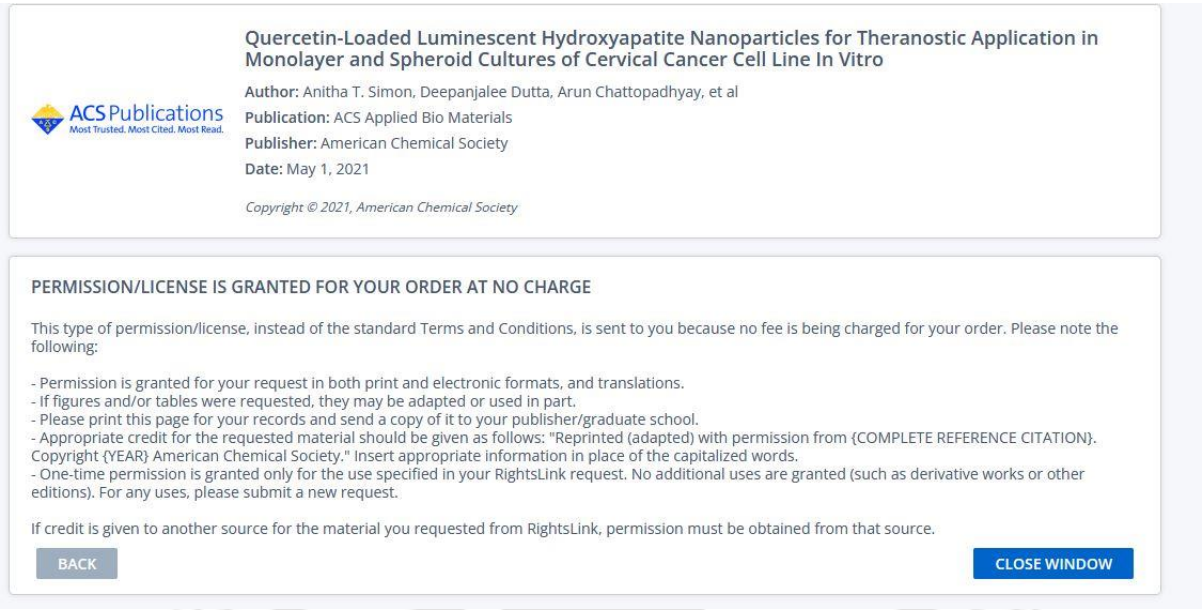

Quercetin-Loaded Luminescent Hydroxyapatite Nanoparticles for Theranostic Application in Monolayer and Spheroid Cultures of Cervical Cancer Cell Line In Vitro

Author: Anitha T. Simon, Deepanjalee Dutta, Arun Chattopadhyay, et al

Publication: ACS Applied Bio Materials

Publisher: American Chemical Society

Date: May 1, 2021

PERMISSION/LICENSE IS GRANTED FOR YOUR ORDER AT NO CHARGE

This type of permission/license, instead of the standard Terms and Conditions, is sent to you because no fee is being charged for your order. Please note the following:

- Permission is granted for your request in both print and electronic formats, and translations.
- If figures and/or tables were requested, they may be adapted or used in part.
- Please print this page for your records and send a copy of it to your publisher/graduate school.
- Appropriate credit for the requested material should be given as follows: "Reprinted (adapted) with permission from {COMPLETE REFERENCE CITATION}. Copyright {YEAR} American Chemical Society." Insert appropriate information in place of the capitalized words.
- One-time permission is granted only for the use specified in your RightsLink request. No additional uses are granted (such as derivative works or other editions). For any uses, please submit a new request.

If credit is given to another source for the material you requested from RightsLink, permission must be obtained from that source.

BACK CLOSE WINDOW